2015

Towards the Realization of Systematic, Self-Consistent Typical Medium Theory for Interacting Disordered Systems

Chinedu Ekuma Ekuma
Louisiana State University and Agricultural and Mechanical College, cekuma1@lsu.edu

TOWARDS THE REALIZATION OF SYSTEMATIC, SELF-CONSISTENT TYPICAL MEDIUM THEORY FOR INTERACTING DISORDERED SYSTEMS

A Dissertation

Submitted to the Graduate Faculty of the
Louisiana State University and
Agricultural and Mechanical College
in partial fulfillment of the
requirements for the degree of
Doctor of Philosophy

in

The Department of Physics and Astronomy

by
Chinedu E. Ekuma
B.S., Ebonyi State University, Nigeria, 2007
M.S., Southern University and A&M College, 2010
May 2015

Dedicated to my Wife, Janefrances for her love and patience,

my Daughter Prudencia, for her love and patience,

my mum, Roseline (of Blessed Memory) for her inspirations,

my sisters and brothers, for their prayers,

and above all, to God for His immeasurable EVERYTHING that is good.

Acknowledgments

The completion of this Ph.D. has been a wonderful and often overwhelming experience. Overall, this is a journey grappling with the physics itself, which has been the real learning experience, and the add-ons of how to write a paper give a coherent talk, work as a team, code intelligibly, stay up until the night birds start singing, and... be,... focused.

I am very privileged to have worked with the most intuitive, dynamic, unassuming, and supportive advisor, anyone could ask for, in the person of Dr. Mark Jarrell. With an almost no coding background, he nurtured me to develop a large-scale coding skill that made me appreciate science more. Mark has the ability to tackle diverse physical problems from many perspective with extraordinary ideas that I will always admire. I have learned a great deal of physics and career in science in general from him. Most importantly, I have learned how to do a real research. Even in his busy schedules, he certainly fosters a friendly, collaborative research group and he definitely knows how and when to give the needed push in the forward direction when the zeal goes downhill. I will forever cherish those unscheduled group meetings, talks, and afternoon chalkboard lecturers. I also want to thank my conjunct Advisor Dr. Juana Moreno, who is very nice and considerate.

The diverse nature of Mark's research group comprising of other students and post-docs, both past and present made this experience even more worthwhile. The dynamics of bouncing ideas off so many excellent minds are priceless. The list goes on, but there are a few that cannot be in the etc., Z.-Y. Meng, K.-M. Tam, H. Terletska, N.S. Vidhyadhiraja, and S.-X. Yang. Mark gave me the opportunity of interacting with many external collaborators. To mention, but a few, I am grateful to Dr. David Singh, Oak Ridge National Laboratory, TN. With my initial background in the density functional theory (DFT) from my M.Sc, David worked me through the deep valley of the capabilities of DFT to correctly inform and guide in the design of materials. Dr. Wei Ku,

Brookhaven National Laboratory, Upton, NY. In the era of many beyond DFT methods incorporating many-body effects, Wei held my hands through the paths of downfolding and unfolding of electronic band structures to extract effective Hamiltonian for realistic many-body simulations. Dr. Vladimir Dobrosavljevic, Department of Physics, Florida State University. Having pioneered the incorporation of typical medium theory to the coherent potential approximation, we had many stimulating discussions. Dr. Diola Bagayoko, Department of Physics, Southern University, Baton Rouge, LA. Diola was my MSc thesis advisor. In fact, he has never taken his eyes off me. I have continued to collaborate with him and, of course, I still apply the law of human performance. To all the experimental groups, both within LSU and beyond whom I have shared ideas, co-authored papers and some provided computational data. I also want to thank Dr. Mark Jarell, Dr. Juana Moreno, Dr. John Perdew, Dr. Diola Bagayoko, Dr. John DiTusa, Dr. David Singh, and Dr. Konstantin Busch for devoting their precious time to serve on my committee. I am also indebted to the Good people of Ebonyi, Nigeria who by the award of overseas postgraduate studies made this dream.

Our group's secretary Carol Duran is surely the kindest, coolest and most witty person one could possibly hope to spend a lunch-break gossiping with. Shelley Lee, you have been like a sister. There are countless others who have been there for me throughout my time at LSU. From the physics general office (one name rings bell Arnell) to all my friends scattered in other departments, you all have been wonderful. To my brothers and sisters (Emmanuel, Kelechi, Beatrice, Felicia, Catherine, and Chigozie) for their unwavering support. My mom, Mrs. Roseline Ekuma of blessed memory. You will always have a special place in my heart. Even though you are no more, the thoughts of having you as a mother is the key reason for all my strides. I will fulfill all the dreams and aspirations you had for me. Finally, Janefrances (the love of my life) and Prudencia (my Jewel) has been my rock and love. Janefrances you have seen my best and the worst, and provided the support, hugs, and energy in this journey. Prudencia for the past few months, the sight of you and the pebbling voice of 'daddy' have made me focus more.

Table of Contents

List of Tables

List of Figures

Statement of Originality

The research work in this dissertation was carried out unless otherwise stated, by the author in collaboration with his advisors Dr. Mark Jarrell and Dr. Juana Moreno. Results and ideas from other authors have been properly cited. This dissertation has not been previously submitted for a degree to any other university or educational institution. However, part of it has been published in co-authorship in the following articles:

Large portion of Chapter 6 appears in

> "Effective Cluster Typical Medium Theory for Diagonal Anderson Disorder Model in One- and Two-Dimensions", C. E. Ekuma, *et al.* , J. Phys.: Condens. Matter **26**, 274209 (2014) [1].

Large portion of Chapter 7 have appeared in the following paper:

> "Typical Medium Dynamical Cluster Approximation for the Study of Anderson Localization in Three Dimensions", C. E. Ekuma, *et al.* , Phys. Rev. B **89**(R), 081107 (2014) [2];

Chapter 8 appears in its entirety as

> "Study of off-diagonal disorder using the typical medium dynamical cluster approximation", H. Terletska, C. E. Ekuma, *et al.* , Phys. Rev. B **90**, 094208 (2014) [3].

Finally, most of Chapter 10 appears in the manuscript

> "Metal-Insulator Transitions in Interacting Disordered Systems", C. E. Ekuma, *et al.* , `http://arxiv.org/abs/1503.00025`.

Electronic preprints of most of the papers are available on the Internet at the following URL: `http://arXiv.org/a/ekuma_c_1`.

Publication List

In the course of my Ph.D. program, aside the core research towards my Ph.D. dissertation, I was involved in various collaborations not limited to First-principles ab-initio simulations of realistic materials using density functional theory. As such, the list below involves other publications aside those pertaining to my Ph.D.

1. *"Metal-Insulator-Transition in a Weakly interacting Disordered Electron System "* **C. E. Ekuma**, S.-X. Yang, H. Terletska, K.-M. Tam, N. S. Vidhyadhiraja, J. Moreno, and M. Jarrell `http://arxiv.org/abs/1503.00025`.
2. *"Finite cluster typical medium theory for disordered electronic systems "* **C. E. Ekuma**, H. Terletska, C. Moore, K.-M. Tam, N. S. Vidhyadhiraja, J. Moreno, and M. Jarrell. Manuscript in preparation.
3. *"Two-Particle Theory for Disordered Electron Systems "* **C. E. Ekuma** *et al.* Manuscript in preparation.
4. *"Metal-Insulator-Transitions in Weakly Interacting Disordered Two-Dimensional Electron Systems "* **C. E. Ekuma** *et al.* Manuscript in preparation.
5. *"Competing magnetic states, disorder, and the magnetic character of Fe_3Ga_4 "* J. H. Mendez, **C. E. Ekuma**, Y. Wu, B. W. Fulfer, J. C. Prestigiacomo, W. A. Shelton, M. Jarrell, J. Moreno, D. P. Young, P. W. Adams, A. Karki, R. Jin, Julia Y. Chan, J. F. DiTusa. Phys. Rev. B. **91**, 144409 (2015). doi: 10.1103/PhysRevB.91.144409.
6. *"A Typical Medium Dynamical Cluster Approximation for the Study of Anderson Localization in Three Dimensions "* **C. E. Ekuma**, H. Terletska, K.-M. Tam, Z.-Y. Meng, J. Moreno, and M. Jarrell. Phys. Rev. B Rapid Commun. **89** 081107 (2014). doi: 10.1103/PhysRevB.89.081107.
7. *"Study of off-diagonal disorder using the typical medium dynamical cluster approximation "* H. Terletska, **C. E. Ekuma**, C. Moore, K.-M. Tam, J. Moreno, and M. Jarrell. Phys. Rev. B **90**, 094208 (2014). doi: 10.1103/PhysRevB.90.094208.
8. *"Effective Cluster Typical Medium Theory for Diagonal Anderson Disorder Model in One- and Two-Dimensions "* **C. E. Ekuma**, H. Terletska, Z.-Y. Meng, J. Moreno, M. Jarrell, S. Mahmoudian, and V. Dobrosavljević. J. Phys.: Condens. Matter **26** 274209 (2014). doi: 10.1088/0953-8984/26/27/274209.

9. *"Electronic Structure and Spectra of CuO "* **C. E. Ekuma**, V. I. Anisimov, J. Moreno, and M. Jarrell, The Euro. Phys. J. B **87** 23 (2014). doi: 10.1140/epjb/e2013-40949-5.

10. *"Electronic, transport, optical, and structural properties of rocksalt CdO"*, **C. E. Ekuma**, J. Moreno, and M. Jarrell. J. Appl. Phys. **114**(15) 3705 (2013). doi: 10.1063/1.4825312.

11. *"First-principles Wannier function analysis of the electronic structure of PdTe: weaker magnetism and superconductivity "* **C. E. Ekuma**, Chia-Hui Lin, J. Moreno, W. Ku, and M. Jarrell. J. Phys.: Condens. Matter **25** 405601 (2013). doi: 10.1088/0953-8984/25/40/405601.

12. *"Re-examining the Electronic Structure of Ge: A first Principle Study"* **C. E. Ekuma**, D. Bagayoko., J. Moreno, and M. Jarrell. Phys. Lett. A, **377**(34-36), 2172–2176 (2013). doi: 10.1016/j.physleta.2013.05.043.

13. *"Ab-Initio Calculation of Electronic Properties of InP and GaP"* Y. Malozovsky, L. Franklin, **C. E. Ekuma**, G. L. Zhao, and D. Bagayoko. Inter. J. Mod. Phys. B **27**(5), 1362013-1 – 1362013-8 (2013). doi: 10.1142/S0217979213620130

14. *"Density functional theory description of electronic properties of wurtzite zinc oxide"* L. Franklin, **C. E. Ekuma**, G. L. Zhao, and D. Bagayoko. J. Phys. and Chem. Solids **74**(5), 729 – 736 (2013). doi: 10.1016/j.jpcs.2013.01.013.

15. *"Physical Properties of $Ba_2Mn_2Sb_2O$ Single Crystals"* J. Li, **C. E. Ekuma**, I. Vekhter, M. Jarrell, J. Moreno, S. Stadler, A. Karki, and R. Jin. Phys. Rev. B **86**, 195142 (2012). doi: 10.1103/PhysRevB.86.195142.

16. *"First Principle Local Density Approximation Description of the Electronic Properties of Ferroelectric Sodium Nitrite"* **C. E. Ekuma**, M. Jarrell, J. Moreno, L. Franklin, G. L. Zhao, J. T. Wang, and D. Bagayoko, Mater. Chem. and Phys., **136**, 1137 – 1142 (2012). doi: 10.1016/j.matchemphys.2012.08.066.

17. *"Electronic, Structural, and Elastic Properties of Metal Nitrides XN (X = Sc, YN): A first Principle Study"* **C. E. Ekuma**, J. Moreno, M. Jarrell, and D. Bagayoko. AIP Advances, **2**, 032163 (2012). doi: 10.1063/1.4751260.

18. *"First Principle Electronic, Structural, Elastic, and Optical Properties of Strontium Titanate"* **C. E. Ekuma**, M. Jarrell, J. Moreno, and D. Bagayoko. AIP Advances, **2**, 012189 (2012). doi: 10.1063/1.3700433 .

19. *"Optical Properties of PbTe and PbSe"* **C. E. Ekuma**, David J. Singh, J. Moreno, and M. Jarrell. Phys. Rev. B **85**, 085205 (2012). doi: 10.1103/PhysRevB.85.085205.

20. *"Ab-initio Electronic and Structural Properties of Rutile Titanium Dioxide"* **C. E. Ekuma** and D. Bagayoko. Jpn. J. Appl. Phys. **50**, 101103 (2011). doi: 10.1143/JJAP.50.101103.

Notation and Abbreviations

- $\hbar = 1; e = 1; m = 1$.
- $\overline{G}(\mathbf{K}, \omega)$ is the coarse-grained cluster Green function of the lattice.
- $\overline{M}(K) = \dfrac{N_c}{N} \sum_{\tilde{k}} M(K + \tilde{k})$ is the coarse-graining of a function M.
- $G(R_i, R_j, \omega) \xrightarrow{FT} G(\mathbf{K}, \mathbf{K}, \omega)$ is the fully dressed cluster Green function.
- (R_i, R_j) and $(\mathbf{K}, \mathbf{K}')$ is site and momenta indices, respectively.
- $k = \mathbf{K} + \tilde{k}$ is the cluster momenta while B is the full bare bandwidth.
- G$(\mathbf{K}, \omega)$ and $\Sigma(\mathbf{K}, \omega)$ is the cluster Green function and self-energy, respectively.
- N_c and $N_0^c(\mathbf{K}, \varepsilon)$ is the cluster size and bare partial density of states, respectively.
- W and U is the strength of disorder and interaction, respectively.
- $\bar{\varepsilon}_{\mathbf{K}}$ is the coarse-grained bare dispersion and t_{ij} is the hopping matrix element.
- $\mathcal{G}(\mathbf{K}, \omega)$ is the cluster-excluded Green function and $\Gamma(\mathbf{K}, \omega)$ is the hybridization rate.
- $c_i^\dagger (c_i)$ and n_i is the creation (annihilation) and number operator, respectively.
- W_c (β) is the critical disorder strength (order parameter critical exponent).
- MIT: Metal insulator transitions
- ALT: Anderson localization transitions
- TMDCA: Typical medium dynamical cluster approximation
- DCA: Dynamical cluster approximation; CPA: Coherent potential approximation
- SOPT: Second-order perturbation theory

Abstract

This work is devoted to the development of a systematic method for studying electron localization. The developed method is Typical Medium Dynamical Cluster Approximation (TMDCA) using the Anderson-Hubbard model. The TMDCA incorporates non-local correlations beyond the local typical environment in a self-consistent way utilizing the momentum resolved typical-density-of-states and the non-local hybridization function to characterize the localization transition.

For the (non-interacting) Anderson model, I show that the TMDCA provides a proper description of the Anderson localization transition in one, two, and three dimensions. In three-dimensions, as a function of cluster size, the TMDCA systematically recovers the re-entrance behavior of the mobility edge and obtains the correct critical disorder strength for the various disorder configurations and the associated *universal order-parameter-critical-exponent* β and in lower-dimensions, the well-knowing scaling relations are reproduced in agreement with numerical exact results. The TMDCA is also extended to treat diagonal and off-diagonal disorder by generalizing the local Blackman-Esterling-Berk and the importance of finite cluster is demonstrated. It was further generalized for multiband systems.

Applying the TMDCA to weakly interaction electronic systems, I show that incorporating Coulomb interactions into disordered electron system result in two competing tendencies: the suppression of the current due to correlations and the screening of the disorder leading to the homogenizing of the system. It is shown that the critical disorder strength (W_c^U), required to localize all states, increases with increasing interactions (U); implying that the metallic phase is stabilized by interactions. Using the results, a soft pseudogap at the intermediate W close to W_c^U is predicted independent of filling and dimension, and I demonstrate in three-dimensions that the mobility edge is preserved as long as the chemical potential, μ, is at or beyond the mobility edge energy (ω_ε). A

two-particle formalism of electron localization is also developed within the TMDCA and used to calculate the direct-current conductivity, enabling direct comparison with experiments.

Note significantly, the TMDCA benchmarks well with numerical exact results with a dramatic reduction in computational cost, enabling the incorporation of material's specific details as such provide an avenue for the possibility of studying electron localization in real materials.

Chapter 1

Structure of Dissertation

The overall aim of this dissertation is to develop a formalism capable of properly characterizing disordered electron systems including disordered systems with off-diagonal disorders, and competing diagonal disorder and Coulomb interactions in one, two, and three dimensions. The developed method is the typical medium dynamical cluster approximation (TMDCA) and it has been applied to study diverse disorder configurations. Even though there is remarkable amount of works already in the current literature employing computational techniques of varying complexity for studying disordered electronic systems and its variants, there are still many glaring issues that are not properly understood. I will explain this assertion in details in Chapter 2.

I will give a general Introduction in Chapter 2. Here, key concepts of disorder, interactions, the general concept of quantum transport, the scaling theory of localization based on the single-parameter theory, and the justification for using the typical density of states as an appropriate order parameter for characterizing not just disordered system, but when both disorders and interactions are present at the same time, will be discussed. Most significantly, I will show from physical point of view based on multifractal analysis that geometrical averaging of the disordered system is a robust representation of the most probable (typical) value.

In Chapter 4, I will give an insight into the different models for studying disordered and/or interacting electronic system. Emphasis will be on the models used in this dissertation. The local typical medium theory will also be discussed here and its deficiencies will be given. I will in Chapter 5 give the details of the typical medium dynamical cluster approximations (TMDCA). I will further discuss the steps in formulating a proper TMDCA for characterizing localization in electronic systems especially, the issue of cluster self-averaging and how to avoid it. The self-consistency and implementation of the TMDCA will also be discussed.

After the above introductory and formalism development in Chapters 2 to 3, this dissertation falls naturally into five parts, which are relatively independent:

- Study of the disordered electron system in lower (one and two) and three dimensions will be given in Chapters 6 and 7, respectively.
- The application of the dynamical cluster approximation (DCA) and the typical medium DCA to the study of both diagonal and off-diagonal disorder will be presented in Chapter 8.
- In Chapter 9, I will present the results for the generalization of the TMDCA for the study of the disordered multi-band system and then present the study of a two-band species.
- The results of the initial effects electron interactions on disordered electronic systems will be presented in Chapter 10.
- To make connection with experiments, I will in Chapter 11, present a two-particle formulation that will be used to calculate the direct current conductivity within the typical medium dynamical cluster approximation.
- Some key information that will aid in the general understanding of the dissertation are presented in Appendices B–E.

Chapter 2

General Introduction

2.1 Introduction

The property of some materials being conductors and others not is one of the highly researched areas of condensed matter physics. Many experimental studies show that a slight variation of an external parameter like pressure, chemical composition, temperature, etc., can induce a metal-insulator-transition, i.e., turning a highly conducting metal into an insulator and vice-versa. A phenomenon referred to as electronic localization. The physics of electron localization remains one of the most intriguing concepts in modern condensed matter and material physics community. Generally, a well-defined metal-insulator-transition (MIT) is observed in three-dimensional systems even for the non-interacting electrons, as demonstrated by the single-parameter scaling theory [4]. The physics, however, is drastically different in lower (one and two) dimensions as the single-parameter scaling theory of localization (SPSTL) predicts the absence of delocalized phase for the non-interacting electrons. The problem of electron localization is even more interesting in the two-dimensions systems since it is the lower critical dimension for the Anderson localization transitions. As a consequence of this, key interest is to use the two-dimensional system to assist in understanding the physics of strongly correlated quasi-2D systems, such as high-Tc superconductors. Several authors (see e.g., Refs [5–11]) especially, at half-filling for the two-dimensional system have carried out extensive theoretical and numerical studies to explore the possibility of a metallic phase. Most of these results generally agree that in the absence of any symmetry breaking field, the two-dimensional system is always localized. While the above descriptions of the physics of electron localization are at half-filling, the situation seems to be different away from half-filling. For the Hubbard model, while a strong repulsive Hubbard interaction can induce a phase transition

in a three-dimensional, non-disordered systems at half-filling from a metal to insulator, away from half-filling, it remains metallic [5, 12–14].

The central question in the two-dimensional systems is whether Coulomb interactions can induce a metal-insulator transitions by enhancing the conductivity of an interacting disordered system. This conjecture is supported by experiments, which showed that interactions or any symmetry breaking field could induce an insulator-metal transition, and hence are very important. Early experiments on thin films and mesoscopic Aharonov-Bohm experiments on disordered rings demonstrated the validity of the coherent backscattering effects in two dimensions [15–17]. Ma and Fradkin using $1/N$ expansion in $2+\varepsilon$ dimensions found a new "interacting" fixed point in their study on localization and interactions in a disordered electron gas [18]. Subsequently, Finkel'stein and co-workers, using renormalization group arguments, predicted the existence of a quantum critical point in two dimensions (2D) [19]. The SPSTL [4] was modified into a two-parameter scaling theory [19], the validity of which was confirmed by experiments in 2D Si-metal-oxide-semiconductor field-effect transistors [20]. Several other authors [21, 21–28] supports that repulsive electron interactions can enhance the conductivity of an interacting disordered electron system in two-dimensions leading to an MIT. The main problem in detecting a clear metal-insulator transitions in two-dimensions in numerical studies have largely been due to the fact that the localization length grows exponentially [5, 29] making it difficult to distinguish the localized phase from the extended ones.

In three-dimensions, the pioneering work of Altshuler and Aronov, employing perturbation theory to the lowest order in U and ignoring all crossing diagrams showed that interactions can induce a square-root singularity at the Fermi level and hence strongly renormalize a disordered Fermi liquid [30]. Recent work using exact diagonalization predicts a robust zero-bias anomaly in the strong coupling, large disorder regime [31]. Quantum Monte-Carlo (QMC) [32, 33] and renormalization group techniques [34] both show no evidence of a metallic phase in one-dimension even in the presence of Coulomb interactions.

2.2 General Concepts of Disordered Systems

The understanding of the electronic and related properties of strongly correlated electron systems are one of the most important problems in condensed matter physics. Strongly correlated systems are challenging and comprises a wide class of materials (not limited to the transition metal oxides) with unusual (often technologically useful) properties. It remains one of the most intensively studied areas of research in current condensed matter physics. While no single, generally acceptable definition can be ascribed to the term *strongly correlated* electronic materials, it can be loosely said to mean the behavior of electrons in materials that is generally not well described by simple one-electron models or theories such as the Hartree-Fock theory or the generally used density functional theory and its variants.

Fundamental structures of strongly correlated materials are made from simple building blocks. They have electronic degrees of freedom that produce exotic properties. For example, in materials with poor screening properties, such as the doped transition metal oxides, the interaction energy between valence electrons can overwhelm their kinetic energy, causing a strongly coupled many-body ground state. As a result of this strong electron correlation, these materials display a range of emergent properties, including high-temperature superconductivity (that can conduct electricity without any resistance below a critical temperature), spintronics (also known as the magnetic semiconductors that have the possibility to manipulate both the spin and the charge degrees of freedom), exotic phases, the heavy fermions (with effective electron mass greater than its bare mass), colossal magnetoresistance (materials that can induce a change in the resistivity by orders of magnitudes due to the application of a few Tesla's magnetic field), and an extreme sensitivity to external perturbations (e.g., magnetic field or doping). Due to many competing phases (spin, charge, lattice, and orbital degrees of freedom) involved in these systems, many complex phases can emerge. Collective states of these complex systems are generally hard to understand by using quantum mechanical single-quasiparticle approximation. While these various degrees of freedom can be fine-tuned via external parameters to produce new materials and even improve on already existing ones, such exotic electronic orderings, frequently observed in strongly correlated electron

systems, remain poorly understood. Understanding the properties of strongly correlated systems remain a "Grand Challenge". These materials do not obey the conventional laws of solid state physics as such, new "smart" ideas are highly needed. We are, therefore, faced with two options: to radically amend the existing laws of physics or to abandon them, and come up with new ones.

The fundamental parameters controlling the behavior of correlated systems are the hybridization (escape) rate (a measure of the tunneling amplitude of particle hopping between sites), on-site Coulomb repulsion energy, and the density of charge carriers or the filling factors. Disordered electron systems including the competition between disorder and interactions provide a good yardstick for exploring some of the exotic properties of (strongly correlated) electron systems especially since disorder is ubiquitous and unavoidable. The interplay of disorder [4, 35–37] and Coulomb interactions [38, 39] is an important problem in diverse fields not limited to the physics of cold atoms, photonic and bosonic systems, and optical lattices [40–43]. It has been actively studied both theoretically [17, 28, 44–50] and experimentally (see for e.g., the metal-insulator transition of doped semiconductors [39, 51–53] and some perovskite compounds [54–58]) for the past few decades.

Further, exact numerical computations have been of tremendous assistant in elucidating the properties of disordered systems as they have been successfully used to study localization. However, these exact numerical methods are severely limited. They require rather a large cluster and almost all known popular numerical methods, including the transfer-matrix, Kernel polynomial, and exact diagonalization methods are difficult (almost impossible) to incorporate interactions (even an interaction as simple as a single impurity coupling) as such, eliminates the possibility of incorporating chemically specific details. An alternative approach is offered by mean-field theories such as the coherent potential approximation and its extensions. They generally map the lattice onto a relatively small self-consistently embedded clusters and these methods have been successfully extended to the treatment of interactions as well as disorder and to chemically realistic models. Unfortunately, these methods have been woeful in the treatment of Anderson localization due mainly to the averaging procedure utilized and improvements in the environment describing the effective medium have been limited to single sites.

The difficulty in formulating a mean-field theory for studying strongly correlated systems are easy to guess. The two limits: a good metal and a good insulator and the intermediate regime, are generally very different physical systems that can be characterized by subtle elementary excitations with different energy scales. For insulators, these are long-lived (collective) bosonic excitations such as spin waves and phonons; and for metals, they are generally quasiparticles similar to the electrons are excited above the Fermi sea. At the intermediate regime of the metal-insulator transitions (MIT), both types of excitations coexist leading to a non-trivial density of states. As such, a "simple" theoretical formalisms fail as they are not capable of distinguishing between the delocalized and localized phases in the gapless single-particle spectra of the correlated Anderson insulator. Conceptually, these are features of a typical quantum critical point (QCP) but with an additional bottleneck. Taking a typical QCP involving spin or charge ordering as an example, the criticality can easily be described by examining the fluctuations associated with the order parameter due to an appropriate symmetry breaking. This is strikingly different in the case of the MIT since it is more suitably described as a dynamical transition and a straightforward order parameter theory is not available. As a consequence of these, the intermediate regime between the metal and the insulator has remained very hard to understand both from the practical and conceptual standpoint.

2.3 Fundamentals of Quantum Transport

The phenomenon of localization transition is a typical example of quantum transport where coherent multiple backscattering interference effects of electron states propagating in a disordered medium may inhibit their propagation across the sample. To understand how this happens, it is intuitive to describe the manifestation of quantum interference in good metals with the disorder. The basic microscopic ideas of quantum transport are quite understood [59,60]. As emphasized by Schrödinger, the four noble truths about quantum states are superposition, interference, nonclonability and uncertainty (no quantum copier machine), and entanglement [61, 62]. The scattering of electrons off a random impurity can be characterized by three energy-dependent length scales vis-à-vis three energy-dependent time scales ($\tau(k) = l/\upsilon$, where $\upsilon = \nabla_k \varepsilon(k)$, $\varepsilon(k)$ is the dispersion

relation). For a single electron scattering off impurity states, the renormalized k-wave states can be described as quasiparticles in the proximity of the impurity states with a finite lifetime $\tau_s(k)$. Hence, single scattering processes define the first length scale, known as the scattering *mean-free path*, $l_s = \upsilon_s \tau_s$ which is the typical length an electron travels before it loses the memory of its initial state. It generally describes the decay length of the average single-particle Green's function [63].

The multiple scattering processes defines the second length scale in the scattering of electrons in a disordered medium. This length scale characterizes the typical length scale traveled by the electrons before losing the memory of its initial direction. This length scale is generally known as the *transport (Boltzmann) mean-free path*, l_B. The fundamental difference between l_s and l_B is that the latter is the length over which the momentum transfer becomes uncorrelated and involves extra factor $(1 - cos\theta)$ [63]. It is an important length scale in the description of Anderson localization transition (ALT). It is directly proportional to the multiple backscattering processes that drive ALT where in general within the l_B, the ballistic electron trajectories become diffusive. In general, $l_B > l_s$, but are equal in the white-noise limit (here wavelength is smaller than the typical size of the impurities), and the disorder can be said to be a set of randomly distributed Dirac peaks [64] with an isotropic scattering (the so-called isotropic limit is a case where there is no p-spherical harmonic and the $\cos\theta$ averages to zero). In this limit, the electron loses simultaneously, the memory of its initial state and initial direction of propagation.

While the Boltzmann mean-free path l_B characterizes the typical length scale traveled by the electrons before losing the memory of its initial direction, it does not define the length scale of the return of the electrons to its initial state as embedded in the return probability of the electrons on site l after time τ, $P(\tau) = \left\langle |G(l,l,\tau)|^2 \right\rangle$, where $G(l,l,\tau)$ is the local Green function. Diffusive transport permits the electrons return to their initial positions via loop paths in a 'constructive' interference setting. Since each of the loops can be traveled in either way, two multiple-scattering paths with exactly the same phase develops during a successive scattering process. The coherent nature of the above described scenario, which is generic for any disordered potential guarantees that it survives disorder averaging. Also, the coherent nature of the multiple-scattering processes ensures that the two paths are in phase and hence 'constructive' interference which significantly enhances the

return probability of the electrons. This generally leads to the well-known coherent backscattering and hence localization. In cases where the coherent backscattering is in the presence of nominal disorder strength, weak localization with significant diffusive transport exists [36]. However, in the strong disorder regime, the diffusive transport is completely quenched, a scenario referred to as strong or Anderson localization [35, 65]. At this point, the probability distribution of the electrons exhibit spatially exponential decay. This defines the third typical length scale known as the *localization length*, l_τ which defines the ALT.

Chapter 3

Metal Insulator Transitions

In this Chapter, I will give a brief review of the various mechanisms described in details in Chapter 4 that are the major players in the localization of electron systems. Generally in fermionic systems, there are two basic routes to electronic localization: randomness (or disorder) generally referred to as the Anderson localization or due to electron interactions known as the Mott localization transitions. At this point, it is important to make distinction between metal-insulator transitions and other forms of transitions that occur in materials. The metal-insulator transitions is a phase transition strictly occurring at zero temperature $T = 0$. As such, it is a quantum phase transition. A material is a metal when the direct current (DC) conductivity $\sigma(T)$ remains finite as $T \to 0$ and it is an insulator, when $\sigma(0) = 0$. Hence, the electron localization in this sense involve a transition from a delocalized to localized states, and vice-versa. In contrary, band-like transitions [66, 67] as in Bloch transitions are due to energetic separation of initially overlapping bands or the Perls transitions [68], which is due to lattice distortion.

3.1 Ideal Material: Perfect Crystal System

The perfect periodicity in real solids is an idealization rather than a rule. In general, there are imperfections in real materials and are of great importance for transport properties. The broken translational symmetry makes the system deviate from the extended Bloch wave nature, and in some cases, to localized states. As such, model of ordered systems cannot be used to understand disordered materials [69]. The problem of quantum localization in a random potential (commonly known as Anderson localization [35]) has proven to be surprisingly rich and remains one of the most fascinating mesoscopic phenomena (for a review, see Refs. [44, 60, 69, 70]) in condensed

matter physics. In spite of the overwhelming collective effects of the scholarly researchers, the problems associated with Anderson localization are recently understood and the phenomenon continues to generate new ideas.

In general due to computational or experimental limitations, the disorder is usually viewed as non-desirable, and may be neglected in order to deal with generic models. In most cases, this approach is often successful in describing macroscopic properties where microscopic disorder is treated as a source of uncertainty in physical measurements. However, it is now well-known that in some cases, a disorder can have dramatic effects even at the macroscopic scale [46, 69, 71, 72]. An emblematic and fascinating example is Anderson localization, in which disorder can turn a piece of metal into an insulator; and as explained above, a typical disorder configurations may locally favor one or another of the many competing "exotic" phases of matter.

3.2 Anderson Localization Transitions

The Anderson localization transitions are basically induced by disorder (or randomness). As explained in Chapter 2, Section 3.1, the idea of a perfect crystal is an idealization. Real materials inevitably contain one form of disorder or other forms of lattice imperfections and/or disorder [36] and the presence of disorder can dramatically alter the Bloch states, which is always extended. Disorder-driven metal-insulator-transitions remains one of the most fascinating and studied phenomena in disordered systems not limited to the "traditional condensed matter physics community" but have actively been studied in other fields [35, 40–43, 73–94]. As has been previously explained in Chapter 2 Section 3.5, the dynamics of Anderson localization transitions rely on coherent backscattering due to the restoration of coherent phase (interference effects). This effect if sustained alters the eigenmodes of the electrons in the system from extended to localized states due to the trapping of electrons into long-lived resonant states. The ALT is characterized by the vanishing of the hybridization paths accompanying the quantum localization of the wavefunctions as a consequence of the coherent backscattering off random impurities. Here, the charge carriers do not generally vanishing and no opening of a gap in the single-particle spectra.

While Anderson localization will be highlighted in most part of this dissertation as it is one of the main topics being investigated, it is imperative to note that the Anderson metal-insulator-transitions is quite different from the metal-insulator-transitions (MIT) that occurs in periodic systems. In the latter, only partially, filled bands carry current, i.e., there is a gap opening in the single particle spectra even if all states are extended [95] while in the former, at the transition, the spectra is gapless [96] and no current propagates through the entire system. [1]

The Anderson localization transition is normally manifested as the impeding of electronic diffusion and hence, localized states emerges whose properties are described by a characteristic length, localization length (cf. Chapter 4 Section 2.3) that determines the degree of localization [36, 93]. At an intermediate stage of electron diffusion (weak disorder), localization is weak and acts as a precursor to Anderson (strong) localization [36, 44, 94]. An avalanche of research following the 1958 seminal paper of Anderson [35] has explored many aspects of localization transitions, all generally with the same aim of trying to understand the role of disorder in materials. As search for new improved materials continues, key fundamental questions among the various open issues in characteristic disordered systems are to understand the role of disorder and how to effectively control localized modes in achieving metal-insulator-transitions. The ability to understand this phenomenon is not only important in our quest for new insights on the dynamics of electronic localization, but will aid in identifying new areas of applicability of disordered systems.

3.3 Mott Localization Transitions

A system with dominant electron correlation as compared to the kinetic energy, undergoes a transition from a metal to a correlation-induced insulator. This is generally referred to as the Mott MIT [38, 51] where electrons are localized (trapped) in their individual atomic orbitals leading to the opening of a gap in the single-particle spectra. The study of MIT in the so-called correlated systems came to a renewed interest in the last few decades, following the discovery of high-temperature superconductivity (for recent studies and reviews, see Refs. [99–101]).

Assuming a crystal with one valence electron per atom, then, the opening of the gap following

[1] The density of states of Anderson localized state is uncritical at the transitions but the local density of states is critical [2, 36, 97, 98].

Mott transition is due to the competition between the kinetic energy gained by the delocalization of the electron and the activation energy emanating from the creation of electron-hole pair induced by the Coulomb interaction. Unlike the disorder induced metal-insulator-transitions (MIT), the interaction induced MIT is not 'fully' a single-particle mechanism since according to the single-particle picture, a predicted metallic system can become insulating due to electrostatic inter-particle interaction.

Most of the diverse exotic behaviors in correlated materials can be traced to the electron interactions [8, 102–104]. For an insight to the above assertion, we recall that in conventional metals electrons barely interact with each other. In the language of the Fermi liquid theory, there is the tendency to screen local charges such that electrons can be treated as isolated particles in a homogeneous background known as Fermi sea. In contrast, in the presence of electron correlations, these electrons start to interact with each other. This scenario lacks any broadly successful theoretical formalism modeling the behavior. Hence, conventional approaches and/or ideas proved of little significance. However, recent breakthroughs both from experimental and theoretical perspective [52, 60, 105, 106] have led to the avalanche of new and exciting techniques which have enhanced our understanding of the general problem of metal-insulator transitions in correlated materials.

3.4 Disorder and Electron Correlations in Materials

A system with a combined disorder and electron interactions no doubt is more challenging to characterize [44, 69, 104] than when disorder or interactions act independent of each. This is a typical characteristic of real materials. Real materials are always characterized by some electron correlations and numerous kinds of disorder, such as impurities; interstitials, antisites, and topological defects; vacancies, inhomogeneous chemical distribution, and/or nonstoichiometric composition; etc. that give rise to subtle many-body phenomena [30, 44, 46]. In essence, disorder can be said to be ubiquitous, and, in fact, disorder and electron correlation inevitably coexist. Therefore, it is important to *properly* understand the combined effects of disorder and electron interaction. Naively,

since both randomness and Coulomb interactions can independently lead to MIT, one would expect their combined effect to be complimentary in inducing MIT. In general, the opposite has been observed to be the case. Interacting disordered electron systems show strong renormalization of the disorder strength [8]; and concomitant increased inelastic scattering and hence reduction in the effective disorder strength [60] that may inhibit the development of the quasi-coherent energy scale, already in the metallic state [102]. As a consequence of this, there will be non-trivial renormalization of the trajectories of the mobility edge and the critical parameters like the critical disorder strength may be different from those of the "pure" Anderson MIT [12].

While there have been significant efforts to understand the combined effect of disorder and interactions on the local density of states close to the Fermi level, the band edges have received scant attention. Specifically, the effect of weak interactions on the mobility edge has not been discussed thus far. This can be attributed to the difficulty in defining a proper mean-field order parameter capable of distinguishing between the delocalized and localized phases in the gapless single-particle spectra of the correlated Anderson insulator. The presence of interaction will further complicate this already intricate situation due to the quantitatively, different, low energy scales under this coexistence with a nontrivial density of states (DoS) of the Anderson and Mott insulators. This is one of the main issues being addressed in this dissertation, which is to systematically study the *initial effects of electron interactions* on the single-particle excitation; the mobility edge trajectories (the energy separating extended and localized electron states); and the critical behavior of the localization transition of a disordered electron system.

We note that in the past decades, some theoretical and experimental efforts have been made to study the coexistence of disorder and interaction [8,49,55,60,107]. However, unlike these previous computational methods, the results presented here incorporates both nonlocal spatial correlations (by using the newly developed TMDCA [2]) and onsite electron interactions incorporated via nonlocal and frequency dependent self-energy using second order perturbation theory. Also, disorder and interaction are treated as a function of increasing cluster size as such, many "higher order" nonlocal diagrams are self-consistently incorporated beyond a single impurity level in a typical effective medium environment.

3.5 Characteristics of a Localized System

A localized electronic system has a unique property which distinguishes it from a delocalized phase. Here, I will briefly discuss some of these unique characteristics.

3.5.1 Probability Distribution Function and Asymptotic Wavefunction

One of the most important parameter characterizing a localized electronic system is its probability distribution function (PDF) [35]. This is manifested in the complex wavefunction, which generally has a multifractal structure with large amplitude variations in space [37]. Before an electronic system becomes localized, the amplitude of the wavefunction is approximately the same on every site vis-à-vis, the probability distribution function of the local density of states is symmetric with a Gaussian distribution. However, at the localized phase, the wavefunctions have substantial weight on a few sites only, falling off exponentially at large distances with the PDF of the local density of states developing long tails and are extremely asymmetric with a log-normal shape [65]. Most of the weight is concentrated around zero. More precisely, the wavefunction $\psi_\alpha(x)$ for any given eigenstates $|\psi_\alpha\rangle$ of the Hamiltonian H behaves as [97]

$$|\psi_\alpha(x)| \sim e^{-|x-x_0^{(\alpha)}|/\xi} \tag{3.1}$$

where $\xi \equiv \xi(\omega_\alpha)$ is the characteristic localization length, which determines the asymptotic behavior of $\psi_\alpha(x)$, when $|x| \to \infty$ and $x_0^{(\alpha)}$ is the center of the localization of state $|\psi_\alpha\rangle$.

3.5.2 Coherent BackScattering

As explained above, one of the essential ingredients for achieving (weak) localization of electrons is the coherent backscattering. Heuristically, the Feynman paths [30, 108, 109] depict the best way to look at the coherent backscattering [35].

Assuming a good conductor ($\lambda \ll l$), moving from point A to B, with the multiple scattering path, which contains a *loop* with the positions of the disorders constant in time, such that the phases along this path is fixed as depicted in Figure 3.1. The probability $P_{A\to B}$ for a transfer between the

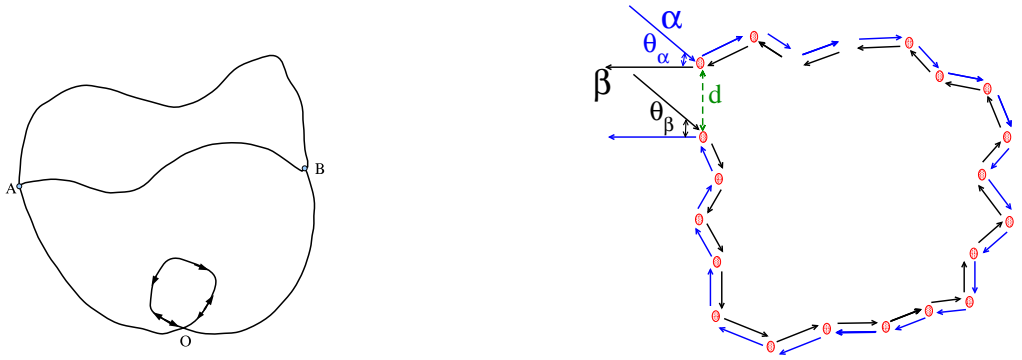

Figure 3.1: Left panel: Possible Feynman paths for a particle to move from point A to B. 'O' denotes point of path self-crossing, which are identical under time reversal. Right panel: Expanding points A to B showing the Coherent backscattering process.

two points can be obtained by squaring the modulus of the sum of the various amplitudes of the probability of the particle to pass through all the possible paths given as

$$P_{\alpha\to\beta\sim\alpha} = \left|\sum_{\alpha} A_\alpha\right|^2 \tag{3.2a}$$

$$|P_{\alpha\to\beta}| = \sum_{\alpha}|A_\alpha|^2 + \sum_{\alpha\neq\beta} A_\alpha A_\beta^* = |A_\alpha e^{i\theta_\alpha} + A_\beta e^{i\theta_\beta}|^2 = A_\alpha^2 + A_\beta^2 + 2A_\alpha A_\beta \underbrace{cos(\theta_\alpha - \theta_\beta)}_{=1 \text{ for } \theta_\alpha=\theta_\beta}. \tag{3.2b}$$

where A_α is the probability amplitude of the Feynman path α. Equation 3.2a depicts the sum of the probabilities of a particle to pass any direction while Equation 3.2b incorporates the interference of the various amplitudes. The physical interpretation of Equation 3.2a is that for most of the paths, interference is destroyed since their lengths differ strongly leading to the wavefunction having different phases on these paths. Hence, these different phases basically cancel out when summed over the various paths. This leads to a classical description of electrons (Boltzmann or diffusive transport). However, if the system is symmetric under time reversal, there are paths of a special kind (self-intersecting paths). Consider two paths *A* (*clockwise*) and *B* (*anti-clockwise*) (cf. Figure 3.1(a)). Then, for each path A_α (α), there exists exactly one path A_β (β), which is the time reversal counterpart of A_α (α) (cf. Figure 3.1(b)). Since these two paths are coherent, hence, in phase, their interference cannot be neglected. Their return probability is thus twice as large as the classical counterpart (cf. Equation 3.2b), and this corresponds to quantum corrections to electron

transport as manifested in the conductivity. Letting $A_\alpha = A_\beta = A$, Equation 3.2 becomes

$$P_{\alpha\to\beta} = \begin{cases} 4A & \text{if } \theta_\alpha = \theta_\beta \quad \text{in phase} \\ 2A & \text{if } \theta_\alpha \neq \theta_\beta \quad \text{out of phase} \end{cases} \tag{3.3}$$

Thus, localization occurs when there is phase coherency in the multiple backscattering trajectories of the electrons with a return probability to their original positions vis-à-vis, the electrons remain at their sites. [2] Since the total probability is normalized, i.e.,

$$\sum_\beta P_{\alpha\to\beta} = 1 \tag{3.4}$$

the quantum correction to the classical (diffusive) regime generally leads to enhanced return probability and hence, reduction to the ability of the particle to propagate [30, 108, 110] corresponding to a reduction in the conductivity of the system. In 3D where there is broad MIT, the return probability is weak and continually decreases with increase in energy such that localization only manifests at sufficiently low energy. This particular picture leads to the development of the mobility edge which separates the diffusive states ($kl_B \gtrsim 1$) from the localized states ($kl_B \lesssim 1$).

3.5.3 Lifshitz Tails

The Lifshitz tails [97, 111] is one of the signatures of a localized state. It has its origin from the emergence of rare configurations of on-site energies with eigenenergies close to the mobility edge spectrum [97, 111, 112]. The Lifshitz states generally emerge, when the disorder strength is strong such that particles with high(low) energies as compared to the average disorder potential are bound within the hills(valleys) of the energy landscape. This is a highly non-trivial quantum effect due to slowly diffusive tunneling by the particles.

Consider the eigenenergies $\omega \sim \omega_0^\pm$ of the eigenstates $\hat{H}$ ($\omega_0^\pm \sim \pm(\varepsilon_i + 2td)$ is the upper(lower) boundary of the energy of $\hat{H}$). This energy scale can only exist when all the on-site energies ε_i are

[2] A note of caution though in low dimensional systems (1 and 2D), the concept of diffusion being a precursor for ALT is strictly not true since, in general, in these dimensions, all states are localized for any arbitrary disorder strength [4] in the absence of any symmetry breaking field.

at a small regime very close to the boundary (edge) of the energy distribution [97, 111]. [3] Hence, states with energies close to the edge (top and bottom of the bands) are strongly localized within this regime due to strongly fluctuations. The probability of finding such rare configurations within a finite region of the lattice is exponentially small.

3.5.4 Mobility Edge

As has been explained in the previous sections, all single-particle spectra become localized above a certain critical value of the disorder strength W_c. However, even before all the states become localized, the states at the top and the bottom of the spectrum are always localized [2, 114, 115] at certain intermediate disorder strength $W < W_c$ (cf. Figure 3.2). The mobility edge is basically the sharp energy ω_c separating the extended and the localized states [116, 117] as depicted with arrows in Figure 3.2. As noted by Mott [51, 118], assuming the coexistence of the localized and the delocalized states at the same energy, then, any arbitrary small perturbations will lead to the mixture of these states leading to the destruction of the localized states. Put differently, the delocalized phase always win over the localized states if both coexist at the same energy.

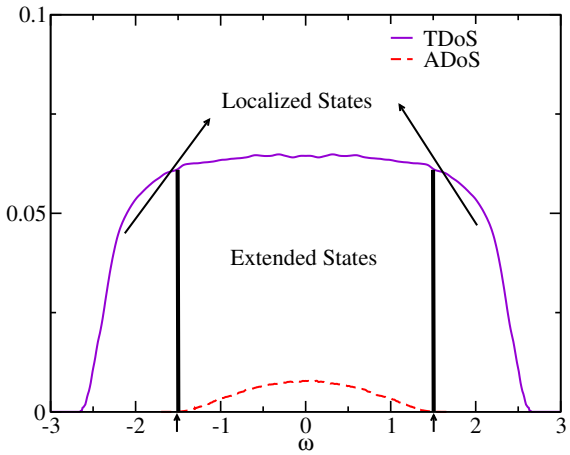

Figure 3.2: The evolution of the typical DoS (dashed line) and the average ADoS (solid line) as a function of energy for the 3D system. While the TDoS does vanish at the mobility, the ADoS remains finite. The position of the arrows denotes the critical regions.

[3] This is generally a signature of a localized state [112, 113].

3.6 The Scaling Theory of Anderson localization Transition

One of the features of Anderson localization is that it is characterized by eigenvalues that are infinitely close to each other, and eigenfunctions that are exponentially localized. Of course, the above description of Anderson localization is more or less a mathematical abstraction as it is not of much usefulness to an experimentalist trying to characterize a localization transitions since, in general, no one can actually measure eigenfunctions in localized realistic systems. The foundation of what is known today as the scaling theory of Anderson localization was by the earlier works of Landau [119] who observed that the transport in the localized regime of a finite system is described by the conductance, G rather than the conductivity, σ as one would generally expect.

$$G = \sigma L^{d-2} \tag{3.5}$$

where d is the dimension of the system.

In some of the earlier works on disordered electron system by Thouless [70,120], he showed that in a finite open media, eigenvalues are repelled by quantization criterion. However, due to leakage through the boundaries, the system achieves a finite width. Further, Thouless and co-workers [70, 120–123] demonstrated that the localization transition occurs when the level separation (the energy related to the average diffusion time a particle needs to propagate through the volume, also known as the Thouless energy,

$$E_T = \hbar/\tau_\phi \tag{3.6}$$

where $\tau_\phi = L_\phi/D$ is the dephasing or Thouless time, and D is the microscopic diffusion constant) is larger than the level width (the averaged energy spacing of two neighboring eigenenergies in the volume, ΔE_s). From Einstein relations,

$$\sigma = e^2 N(\varepsilon_F) D \tag{3.7}$$

where e is the electronic charge, $N(\varepsilon_F)$ is the density of states at the Fermi energy. Combining the

above three equations, one arrives at

$$G = e^2 N(\varepsilon_F) D L^{d-2} = e^2 N(\varepsilon_F) \frac{1}{\tau_\phi} L^d = \frac{e^2}{\hbar} \frac{dN}{dE}(\varepsilon_F) E_T = \frac{e^2}{\hbar} \frac{E_T}{\Delta E_s} \tag{3.8}$$

In general and for convenience, the dimensionless (system dependent, L), universal constant known as the Thouless conductance, g

$$g \equiv \frac{e^2}{\hbar} G = \frac{E_T}{\Delta E_s} \tag{3.9}$$

is used in the description of the conductance of finite systems. Note Equation 3.9 is nothing but the ratio of the two microscopic energy scales: the level width and the level separation. The Thouless conductance is a powerful parameter in the scaling theory of Anderson localization and it has been demonstrated to control 'all' the aspects of localization including statistical fluctuations [4, 70, 120–123]. The inequality '$g < 1$' is the celebrated Thouless criterion for Anderson localization.

Wegner [124, 125] using renormalization group, analyzed the scaling of the mobility edge and showed that an arbitrary small disorder is enough to localize all states in one and two (low) dimensions. In essence, they achieved a complete localization of all states in low dimensions and an existence of a metal-insulator-transitions (MIT) in three dimensions (3D) for the non-interacting disordered system. Contrary to Mott's assumption of minimal conductivity [126], the MIT in 3D is a continuous phase transition with the conductivity obeying the power law [44, 127]:

$$\sigma \sim |E - E_c|^\nu \tag{3.10}$$

where ν is the critical exponent of the conductivity and E_c is the mobility edge energy. The work of Abrahams, Anderson, Licciardello, and Ramakrishnan (the gang of four) [4] put the scaling theory of localization in firm footing The single-parameter scaling theory of the Anderson localization transitions [4] is one of the great milestones in the quest to understand the Anderson localization. Abrahams *et al.* [4] building on the recent developments in the study of Anderson localization [70, 120–123, 127] showed the dimensionless Thouless conductance g is a function of scale length L only such that

$$g = g(L) \equiv g(n.L) = f(n, g(L)) \tag{3.11}$$

where n is a scale factor. Equation 3.11 makes the assumption that in stacking small systems to form a large system, that the conductance of a large system depends only on the conductance of the original small system. The key question that needs to be addressed is how g depends on L. Recall that for a pure metal, the conductance is generally large, $g \gg 1$. In this metallic limit, we know from Ohm's scaling law that $g \approx \sigma L^{d-2} + \ldots$. Also, in the strongly localized regime $g \ll 1$, the conductance drops off exponentially with length as $g \approx e^{-L/\xi}$, where ξ is the localization length. One can obtain the β-function by carefully interpolating between theses two limits. This can be achieved by using the intrinsic property of the problem. Since it basically involves doubling the system size many times, the best way to think about it is to assume a logarithmic scale. Taking the derivatives of the two limits described above as

$$\frac{d\ln g}{d\ln L} = \beta[g(L)] = \begin{cases} (d-2) - \zeta(\frac{1}{g}), & g \gg 1 \\ -\frac{1}{\xi}\frac{dL}{d\ln L} = -\frac{L}{\xi} = \ln g, & g \ll 1 \end{cases} \tag{3.12}$$

where ζ is some unknown constant due to higher order corrections by assuming that there exists an analytic expansion of β in powers of $1/g$. A qualitative, schematic plot of the β-function for the various dimensions is shown in Figure 3.3. With Equation 3.12, one can explore how β is expected to behave in the $\beta - g$ plane in one, two, and three dimensions. In one dimensions,

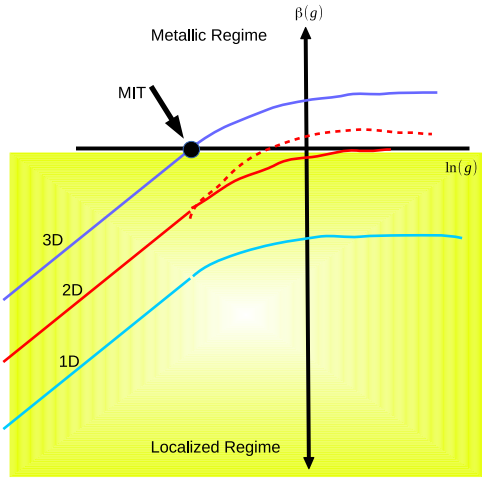

Figure 3.3: A schematic plot of the β for one, two, and three dimensions. For the two-dimensional case, the dotted line shows a system with external field.

from Equation 3.12, neglecting the corrections, β is always negative for $g \gg 1$ implying that the conductance decreases towards 0 and eventually crashes exponentially as g becomes less than unity in the thermodynamic limit ($L \to \infty$). In two dimensions, the asymptotic limit of β for $g \gg 1$ can also be seen to be 0. This implies that in the thermodynamic limit, the conductance of a two-dimensional system is independent of the system size. But the two-dimensional system is a special case since from Equation 3.12, the leading contribution to the β-function vanishes in the Ohmic regime. However, assuming there is a time reversal symmetry breaking field like spin-orbit coupling or say a different universal class [128, 129] aside the orthogonal class, the negative sign of the correction $\beta(g) \sim -1/g$ may change leading to a phase transitions even in two dimensions [16, 37, 65].

In three dimensions, the situation is very different. From Equation 3.12 for $g \gg 1$, the β-function is positive, i.e., $((d-2) = 1)$ while for $g \ll 1$, the β-function goes like $\ln g$. The implication of this from continuity perspective is that on the g-axis, $\beta[g]$ must cross the $\beta = 0$ at some point g_c. Near the transition (i.e., $|(g - g_c)/g_c|$), where one expects the linearization of β to be valid, the localization length scales as

$$\xi \sim |\frac{g - g_c}{g_c}|^{-1/s} = |\frac{g - g_c}{g_c}|^{-\nu} \tag{3.13}$$

where $\nu = 1/s$ is the critical exponent of the correlation length as well known from the theory of critical phenomena [130]. The predictions of the single-parameter scaling have been corroborated by numerical and theoretical studies [36, 131–133], including a generalization to two-parameter scaling theory [19]. However, there are some numerical works reporting its violation [36, 98].

3.7 Scaling Theory of the Typical Density of States

As explained earlier, unlike the conventional continuous phase transitions, the metal-insulator transition is unique since it is more suitably described as a dynamical transitions, as such, an appropriate order parameter for the Anderson localization is difficult. As demonstrated in Ref. [2, 134], the appropriate order parameter characterizing localization transition should satisfy the following

criteria:

1. The order parameter should vanish in the localized (or extended) phases;
2. It should exhibit power law behavior and capture the critical behavior of Anderson localization transitions with the correct critical disorder strength W_c and order parameter critical exponent, β;
3. The order parameter acquires a finite positive value in the localized (or extended) phase.

The typical density of states TDoS meets all of the above requirements and it has been demonstrated as the appropriate order parameter for characterizing the localization transition [2]. For a system near the critical point x_c, the TDoS behaves as

$$TDoS \propto (x_c - x)^{\beta}, \quad \forall x < x_c \tag{3.14}$$

where $\beta = \nu(\alpha_o - d)$ is the *universal* order parameter critical exponent (*typical order parameter exponent*) [135], α_o is the Lipschitz-Hölder exponent [134]. In the TMDCA, Equation 3.14 is characterized by taking the TDoS at the band center while the disorder strength controls the localization transition as

$$TDoS(\omega = 0) = (W_c - W)^{\beta}, \quad \forall W < W_c \tag{3.15}$$

From above, the TDoS will vanish at W_c as such, Equation 3.15 is only valid for $W < W_c$.

3.8 Justification for Typical Density of States as Order Parameter

The local density of states contains all the information about the local amplitudes of the electronic wave functions. As such, its probability distribution functions (PDF) is a natural way to characterize the Anderson localization transition. Unlike the global (average) density of states, which are not critical at the localization transitions, the (unaveraged) local density of states is critical at the transition [35].

The study of disordered systems relies on the PDF of the local variables to measure 'random' quantities of interest [35]. To characterize localization, the most important quantity in the majority of physical or statistical problems is usually the "typical" value of the 'random' variable, which corresponds to the most probable value of the PDF [136]. In most systems the nature of the PDF is not known a priori; as such, we have limited information via the moments or cumulants of the PDFs. Under such situation, the "typical" or the most probable value of the PDF [136] contains important and direct information. Different from some systems where the first moment (the arithmetic average) is a good estimate of the random variable, the Anderson localization is a non-self-averaging phenomenon. Close to the critical point if the system is phase coherent (mesoscopic regime), quantum interference effects cause the strong fluctuation of physical quantities (e.g., LDoS) [137] such that corresponding PDF of the local density of states is very asymmetric with long tails [135, 138] needing infinitely, many moments to describe it [136]. In some cases, the corresponding moments might not even exist especially close to the critical point [139].

Naturally, at the localization transitions, the *typical* local density of states vanishes while the continuous local spectrum becomes sets of delta-function peaks with long-lived resonance states. As a consequence, these long-lived resonance states at a given lattice site, acquire a finite escape rate which, according to the Fermi Golden rule, can be approximated as [35]

$$\tau_\phi \sim 1/(t^2 \rho_i) \tag{3.16}$$

where t is the hopping matrix and ρ is the local density of states in the neighborhood of site i. From Equation 3.16, it is obvious that the *typical* escape rate is dictated by the local density of states (TDoS); implying that the TDoS directly measures the conductivity within the Drude approximation. Based on the above conjecture, the TDoS possess all the essential qualities of a *proper* order parameter for characterizing localization transitions. In the actual computations, the TDoS is generally approximated by the *geometric value*. This can be justified by noting that close to the transition, the pertinent distribution of the TDoS becomes broad, an indication of multifrac-

tality [137] and the desired typical value is well represented by the *geometrical mean* [105]

$$\rho^{c}_{typ}(\omega) = exp\left(\frac{1}{N_c}\sum_{i=1}^{N_c}\langle \ln \rho^{c}_{i}(\omega, Vi)\rangle\right). \tag{3.17}$$

Note, the above assumption is supported by the strong coupling limit (using effective theory) study of localization on a Bethe lattice [138] and independently, by the scaling analysis of the multifractal spectra of the electron wave function near the localization transitions [65, 134].

To prove this, I will use multifractal concept. Recall that the local density of states of a system of size L in the neighborhood of site i is

$$\rho_i(\omega) = \Xi^{-1}(\omega)|\psi(i,\omega)|^2 \tag{3.18}$$

where Ξ is the finite width ($\Xi(\omega) \propto L^{-d}$) broadening parameter and $|\psi(i,\omega)|^2$ is a microcanonical average of squared amplitude at a given energy ω. The spatial average of Equation 3.18 from finite size scaling perspective [65, 134] then becomes

$$\rho_{av} = L^{-d}\int \rho(i,\omega)di \propto L^0 \tag{3.19}$$

Clearly, from Equation 3.19, it is obvious that the average density of states is independent of any external parameter like the disorder strength for an infinite system near the transition point x_c, as such does not qualify as an appropriate order parameter. This is understandable since the average density of states is nothing but the 'global' density of states, which is a smooth function of the external parameter x near x_c.

From statistical point of view, the 'typical' value, Π_{typ} of the distribution of a physical quantity say $\{\Pi_i\}$ is the value where the PDF ($R\ln\Pi$) is a maxima, which is the geometrical mean of $\{\Pi_i\}$ if and only if ($R\ln\Pi$) is symmetrical [134]. Since $\Xi(\omega) \propto L^{-d}$, then, the scaling behavior of the LDoS depends entirely on the wave function such that

$$\langle[\rho_i(\omega)]^q\rangle_L \propto L^{(q-1)d-\tau(q)} \tag{3.20}$$

where $\tau(q)$ is the multifractal mass exponent. For a typical value, Equation 3.20 reduces to

$$\begin{aligned} \rho_{typ} &= exp\left[\langle \ln(\rho_i)\rangle_L\right] \propto L^{d-\alpha_0} \\ &\propto (x_c - x)^{\beta}, \quad \text{for} \quad x < x_c \end{aligned} \tag{3.21}$$

which is the same as Equation 3.17 and it is the form used in this work, where $\beta = \nu(\alpha_0 - d)$ is the typical order parameter exponent, x is an external parameter (e.g., disorder strength or energy), α_0 is the Lipschitz-Hölder exponent which gives the maximum value of the multifractal spectrum and ν is the correlation length critical exponent. Observe now the non-trivial, external parameter dependence of the TDoS.

There is a growing consensus supporting the *log-normal* behavior of the $\rho^c_{typ}(\omega)$ (3.17) close to the localization transition. Based on experiment, theory, and simulations, the local density of state in a disordered system close to transition develops a highly skewed [45], log-normal distribution [52,140,141] with a typical value given by the geometric mean that vanishes at the localization transition, and hence, acts as the order parameter for the localization transition. This is due to the fact that the "typical" value of a "random" variable vis-à-vis the *geometrical value*, corresponds to the most probable value of the probability distribution function [2, 142].

3.9 Experimental Observation of Metal Insulator Transitions

While the present work focuses on the development of an effective mean-field theory and application to the study of electron localizations, to make connect with experiments, it is imperative to justify that metal-insulator-transitions can also be observed experimentally. One of the earliest experimental observation of Anderson localization transitions is on the amorphous semiconductors [36,144,145]. The measurement of temperature dependent conductivity in the localized regime due to electron-phonon coupling is observed to follow Mott's *variable range hopping* [126, 146], i.e., a thermally activated conductivity [147]

$$\sigma(T) \sim \exp\left(-\left(\frac{T_0}{T}\right)^{\frac{1}{d+1}}\right) \tag{3.22}$$

where d is the dimension. Taking three-dimension, for example, exponent in Equation 3.22 changes from $1/4$ to $1/2$ when Coulomb interactions between localized electrons are taken into account as demonstrated by Efros and Shklovskii [148].

One of the most studied system exploring electron localization is the heavily doped semiconductors. Notable among them are the Si:P and Si:B [44, 143, 150–152] where some of the predictions of the one-parameter scaling [4] were experimentally tested. In the pioneering work of Paalanen *et al.* [143] on Si:P, the authors showed that the application of a uniaxial stress, which tunes the concentration at millikelvin temperatures lead to a metal-insulator-transition (cf. Figure 3.4) with a critical exponent $\mu = 0.55 \pm 0.1$ [153] in contrast to the predictions of the single-parameter scaling. However, more recent data where the concentration of P is varied close to MIT by Stupp *et al.* [149] show similar temperature dependence of the conductivity (cf. 3.5(a)) however, the $\sigma(0)$ as a function of reduced concentration $((N-N_c)/N_c)$ [4] for a given concentration $N_c = 3.52 \times 10^{18} cm^{-3}$ inferred from (cf. 3.5(a)) shows a cross-over from $\mu \sim 0.5$ to 1.3 as the concentration decreases towards the critical concentration. This was attributed to the change in sign of the temperature

[4] N_c is used in this section to denote electron concentration. It should not be confused with the cluster size as used in other places.

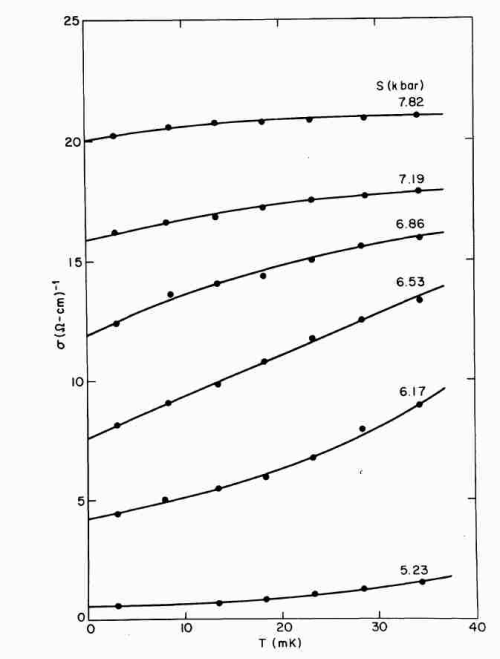

Figure 3.4: The evolution of the conductivity as a function of temperature for various uniaxial stress near MIT for Si:P. Plot is taken from Ref. [143].

coefficient of $\sigma(T)$, m (cf. 3.5(b)) among other things, uncompensated P doping [154].

This seeming exponent puzzle between experimental results, mainly on compensated semiconductors and amorphous alloys with $\mu \approx 1$ and their uncompensated counterpart with $\mu \approx 0.5$ [149, 153, 155, 156], which are believed to belong to the same universality class [37, 157, 158] is still a subject of intensive research. Many explanations have been given by several authors (for e.g., Refs. [37, 149, 156, 158]). For e.g., some believe that this discrepancy is due to wrongful interpretation of experimental data (see discussion in [37, 158]). Stupp *et al.* [149] attributed it to the way the critical regime is chosen. He demonstrated that limiting the critical regime to the small concentration range just above the critical concentration, N_c where $\sigma(T)$ actually decreases with decreasing T leads to $\mu \approx 0.5$ as depicted in Figure 3.5(b). Even at these, strong discrepancy still remains between the experimentally observed values and the numerical ones. Electron-electron interactions have been shown to be important in the full description of MIT in materials [52, 55–58] and, hence, these deviations from theory were interpreted as a consequence of the presence of interaction [37, 46]. Experimentally, there is every indication that the inclusion of interactions or any symmetry breaking field into the theory for electron localization may cause deviations from the predictions of the single-particle scaling theory.

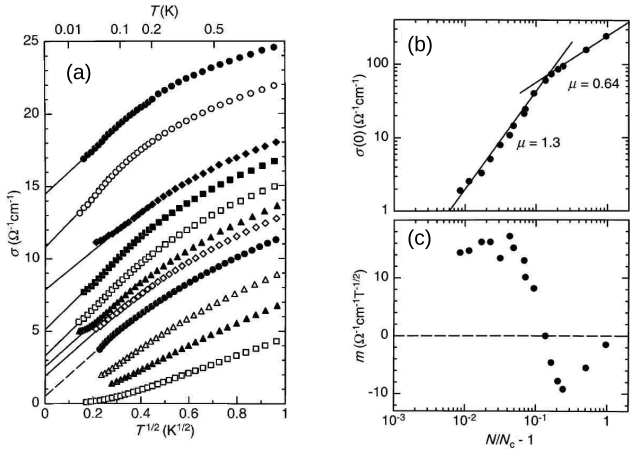

Figure 3.5: (**a**) The electrical conductivity σ versus $\sqrt{(T)}$ of Si:P close to MIT at various P concentrations (in 10^{18} cm^{-3}): 3.38, 3.45, 3.50, 3.52, 3.55, 3.56, 3.58, 3.60, 3.63, 3.67, and 3.69 in going from bottom to the top. The (**b**) zero temperature limit of the conductivity ($\sigma(T \to 0)$) and (**c**) $m = d\sigma/d\sqrt{T}$ versus reduced concentration $(N - N_c)/N_c$ for 3.52 $\times 10^{18} cm^{-3}$. Plot is taken from Ref. [149].

The well-accepted picture of electron localization from the single-parameter scaling theory [4] further came under great scrutiny following the observation of metallic behaviors in low-density silicon metal-oxide-semiconductor field-effect transistors (Si MOSFETs) [27, 53, 159]. While this was initially puzzling and surprising to the condensed matter physics community [26, 159, 160] even with skepticism, the metallic behavior in a two-dimensional system was soon experimentally observed by several other groups [27, 159, 161–169], and even observed in other materials [170–181]. At this point, it became imperative that this is an intrinsic property of a two-dimensional system. As it is evident from the data of Kravchenko *et al.* [53] (cf. Figure 3.6, for low Si concentration, the resistivity increases with decrease in temperature, tending to an insulating states as $T \to 0$. In contrast, for Si concentration above certain threshold (shown with dashed lines in Figure 3.6), the resistivity curves seem to monotonously decrease with decreasing temperature, a

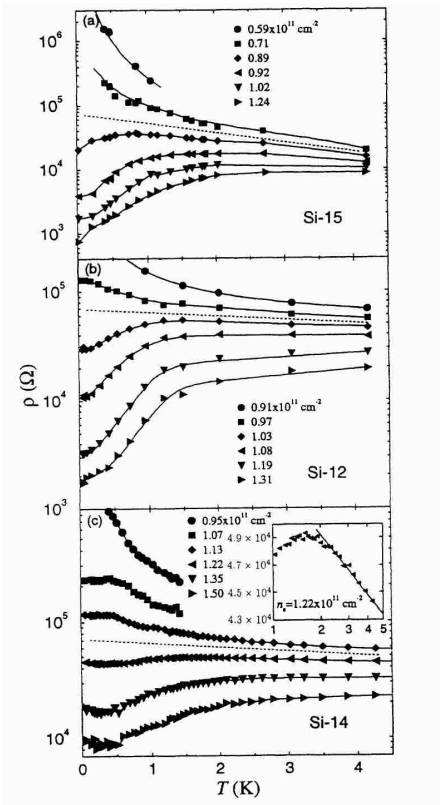

Figure 3.6: The plot of the resistivity vs T for the two-dimensional silicon samples at different silicon concentrations near the critical concentrations. The inset depicts the temperature dependence of the resistivity consistent with weak localization. Plot is taken from Ref. [53].

signature of metallic states. This conundrum implies that if the latter case (low Si concentration) extrapolates to an insulating ground state as $T \to 0$ then, there exists a metal-insulator-transitions in two-dimensions in violation of the predictions of the single-parameter scaling theory [5]. While this is surprisingly, the $1/N$ expansion in $2+\varepsilon$ dimensions by Ma and Fradkin [18] found a new "interacting" fixed point in their study on localization and interactions in a disordered electron gas [18].

Over the years, the conjecture and premise of the above observations and interpretation have been under debate especially from the theoretical point of view since it violates the single-parameter scaling. Notable among them is the question of the relevant temperature scale used in the experiments since the Fermi temperature of the probes used in the experiments is rather low as a consequence of the low sample concentrations. Thus, the observed metallic behavior may be due to finite temperature effects with the insulating states becoming robust at much lower temperatures [26, 176, 182–187]. This is the so-called temperature-dependent screening [188–190]. Temperature dependent disorder scattering [170, 191] and spin-orbit splitting of different spin subbands [192, 193] have also been proposed to explain this puzzle. Another school of thought suggests the modification of the single-parameter scaling theory to two-parameter scaling theory, which permits, within a certain parameter regime, for a metallic solution even in two dimensions [19, 47, 194, 195]. This line of thought was pursued by Finkel'stein and co-workers, using renormalization group arguments, to predict the existence of a quantum critical point in two dimensions (2D) [19], the validity of which was confirmed by experiments in 2D Si-metal-oxide-semiconductor field-effect transistors [20]. In the weak disorder regime, perturbative simulations showed that spin and valley degeneracy [47,196] may be important, which in the limit of an infinite number of valleys, a non-Fermi-liquid metallic state is shown to be stabilized by electron interactions [19,169,181]. The role of electron interactions was also explored and numerical studies have shown that interactions lead to delocalization in two-dimensions [29, 197–201]. Many other theoretical proposals were put forward to explain MIT in 2D. Among them is idea of the admixture of a Fermi liquid and a Wigner crystal [199, 202, 203] at the same energy, a variant of the Wigner-Mott

[5] The possibility of spin-orbit coupling, which breaks time-reversal symmetry can at least be excluded from the experimental data since there is no applied magnetic field or atom with a strong moment.

transition [204, 205]. The role of percolation phenomenon at the MIT [172, 206–209] and local moments [157, 210] have been investigated, and some argue that the emergence of metallic phase in 2D may be a signature of a superconducting phase [211–213] Many other viewpoints were also suggested (see for e.g., [27]), but after many decades of intense research, no generally accepted theory has been formulated for the theoretical description of electron localization not only in two dimensions but also in one and three dimensions. Whatever may be the case, experimental results suggest that for the accurate description of electron localization in materials, a good understand of the interplay between disorder and electron interactions is very central (see for e.g. [52, 55–58]. This will be the focus of Chapter 10.

To further demonstrate the importance of systematic incorporation of electron-electron interactions to the interpretations of an MIT, Richardella *et al.* [52] using scanning tunneling microscopy, visualized the evolution of the local density of states of $Ga_{1-x}Mn_xAs$ samples at various Mn doping. The authors demonstrated that a combined effects of strong spatial variation and electron-electron interactions leads to the suppression of the the tunneling density of states near the Fermi energy. As shown in Figure 3.7 (A-C), spectroscopic maps of the local density of states at the

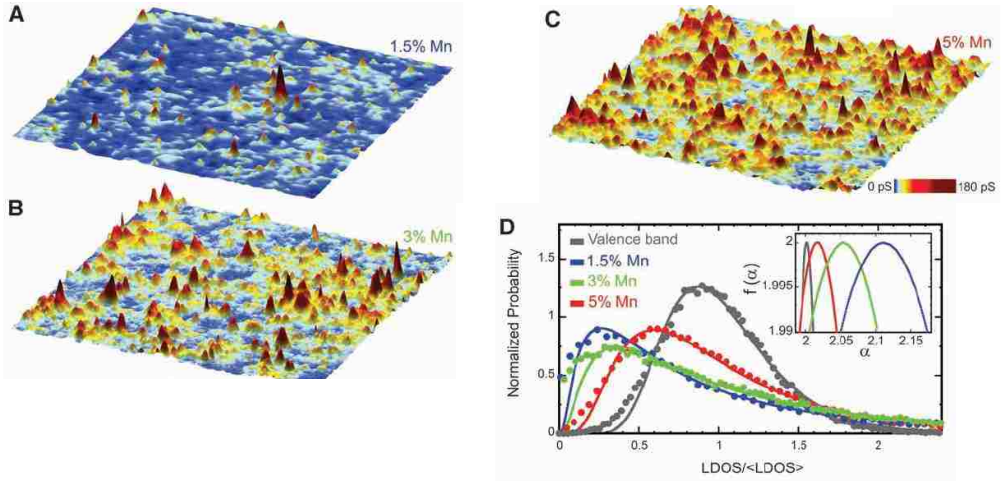

Figure 3.7: The spatial variation of the LDoS in the proximity of the Fermi energy at (**A**) 1.5% Mn doping, $Ga_{0.985}Mn_{0.015}As$, (**B**) 3% Mn doping, $Ga_{0.97}Mn_{0.03}As$, (**C**) 5% Mn doping, $Ga_{0.95}Mn_{0.05}As$. (**D**) The normalized local distribution of the differential conductance. The inset is the multifractal spectrum $f(\alpha)$ near the Lipschitz-Hölder exponent, which gives the maximum of the multifractal spectrum. Plot is taken from Ref. [52].

Fermi energy at different dopings depicts varying spatial variation [141]. For extended states, the distribution of the LDoS are expected to show Gaussian distribution, an indication that the LDoS have equal weight on every site. However, close to the metal-insulator-transitions, different energy scales are expected to emerge especially in the LDoS such that a cross-over from a Gaussian (characteristic of a metal (cf. gray circle in Figure 3.7 (D))) to a log-normal (insulator) behavior starts to emerge even in the weak localization limit [52, 214, 215], but decreasing the doping leads to more skewness of the distribution of the LDoS, i.e., log-normal distribution (Figure 3.7 (D)). The inset of Figure 3.7 (D) shows that even in the presence of electron-electron correlation, the spectrum remains multifractal as in the non-interacting regime.

Chapter 4

Models of Disordered and Interacting Electronic Systems

Over the years, many models have been proposed and developed for the study of disordered and interacting systems, and for studying their combined effects. Prominent amongst them are the Anderson model for disordered electron system [4, 35, 69], which is a tight-binding model for characterizing a disordered electron system. For the study of interacting system, the Hubbard model [216–219] has been rigorously used while to study both the effect of interactions and disorder at the same time, the Anderson-Hubbard model [69, 220] has been consistently used. While there are other various models for studying disordered interacting systems (and their combined effects), in this dissertation, the focus will be on the above mentioned three models. No attempt will be made to cover all the known facts about these models but an overview just enough to interpret the present results will be explained.

4.1 Anderson Model of Disordered Electron System

Before delving into the nitty-gritty of the Anderson model of electron localization, a general overview of the Anderson model will be presented.

Anderson Model: "More is different" [221]; a conjecture pointed out by Anderson [221], when confronted by a change of scale, the behavior of large and complex system might not always be a straightforward extrapolation of the well-known simple behavior of its small-scale components. When increasing the complexity or adding more atoms to a system, its behavior might change drastically in nature: it may undergo a phase transition. The Anderson model of localization is the simplest yet a paradigmatic model for describing electronic transport properties of disordered quantum systems [36, 222]. It has been used successfully used to study amorphous materials such

as alloys [223], semiconductors, and even DNA [224]. Its hallmark is the prediction of a spatial confinement of the electronic motion upon increasing the disorder strength; a phenomenon known as the Anderson localization transitions [35]. In 3D, a metal-insulator-transition occurs as disorder strength W mediates a change of transport properties from metallic behavior at small W via critical behavior at the transition $W_c^{U=0}$ to insulating behavior and strong localization at larger W [36,106].

In particular, in the 1958 seminal paper by Anderson [35], he observed that a large piece of disordered material can become an insulator, even when its elementary blocks have a metallic behavior. This phenomenon has come to be known as Anderson localization. Anderson localization basically results from a subtle interference effect of the backscattered coherent waves propagating in a random medium [225]. While Anderson's prediction remained unappreciated and wasn't fully recognized by the scientific community for up to a decade, it, however, has led to a new paradigm in the way we characterize the transport properties of disordered materials. Anderson localization in general exhibit universality, which has led to the spread of its application in many other fields, which is not limited to the following: the study of condensed matter systems [36, 69, 226], optical and ultra cold atoms [227–233], disordered quantum systems [36, 40], seismic [234, 235], photonic lattices in the form of matter waves [227, 236], electromagnetic absorption in a disordered medium [86, 237], superfluid helium in porous media [238], molecular and biological systems [239–241], and even disordered superconductors [46].

The original Anderson model is a simple model for describing the diffusion or conduction of electrons in the impurity band (disordered system). The Anderson model of disorder has stood the test of time and provides rather accurate, single-particle description of disordered electronic systems. The Anderson model for the non-interacting electrons moving on a lattice with a diagonal on-site random disorder potential is given by the Hamiltonian

$$\hat{H} = -t \sum_{<i,j>} (c_i^\dagger c_j + c_j^\dagger c_i) + \sum_i (V_i - \mu) n_i. \tag{4.1}$$

The disordered part is modeled by a local potential V_i, which is a random quantity distributed according to some specified probability distribution $P(V_i)$. The operators $c_i^\dagger(c_i)$ create (annihilate)

a quasiparticle on site i and $n_i = c_i^\dagger c_i$ is the number operator, μ is the chemical potential, and t is the hopping matrix element between nearest-neighbor $< i, j >$. We set $4t = 1$ as the energy unit. In our analysis, we use different types of disorder distributions. In particular, we consider the box (Bo), Gaussian (Ga), Lorentzian (Lo), and binary (Bi) distributions, respectively, with the distribution functions $P(V_i)$

$$P_{Bo}(V_i) = \frac{1}{2W_{Bo}}\Theta(W_{Bo} - |V_i|), \tag{4.2a}$$

$$P_{Ga}(V_i) = \sqrt{\frac{6}{\pi W_{Ga}^2}} e^{-6V_i^2/W_{Ga}^2}, \tag{4.2b}$$

$$P_{Lo}(V_i) = \frac{W_{Lo}}{\pi(V_i^2 + W_{Lo}^2)}, \tag{4.2c}$$

$$P_{Bi}(V_i) = c_a\delta(V_i - W_A) + c_b\delta(V_i - W_B). \tag{4.2d}$$

where $\Theta(x)$ is a step function, c_a is the concentration of the host A atom, $c_b = 1 - c_a$ is the concentration of the impurity B atom, and the strength of the disorder in units of $4t$ is parameterized by W (W_A and W_B for binary alloy model). We have scaled the W_{Ga} such that the second moments of the P_{Bo} and P_{Ga} agree with each other (i.e., we set the variance of the Gaussian distribution equal to that of the box distribution: $\sigma^2 = W^2/12$) in the event that W_{Bo}=W_{Ga} to enable comparison. Since the Lorentzian distribution lacks second moment, the disorder values cannot be directly compared with that of either the box or Gaussian distributions, respectively. We introduce shorthand notation for disorder averaging $\langle ... \rangle = \int dV_i P(V_i)(...)$.

The Anderson model of a disorder is characterized by two energy scales, t and V_i. For the dimensionless ratio W/t larger than some critical value $(W/t)_c$, all states are said to be localized while below this critical value, there is a mobility edge (cf. Figure 3.2) with the consequence that all states are extended [242].

The Anderson localization transition (ALT) [4, 35] is one of the oldest problem in a disordered electronic system. Already, there have been diverse theoretical studies employing computational techniques of varying complexity not limited to the numerical exact methods (including the exact diagonalization, transfer matrix, and kernel polynomial methods), [106, 132, 243–251] varying

types of renormalization group techniques, [252–254] and various mean field theories [105, 255–261]. We note that the numerical exact methods have been successfully used to study Anderson localization. However, they generally require the treatment of large clusters and the use of powerful computers. As a result, they are difficult to extend to the treatment of interacting systems or chemically specific models. An alternative approach is offered by mean-field theories such as the coherent potential approximation and its extensions. They map the lattice onto relatively small self-consistently embedded clusters so these methods have been successfully extended to the treatment of interactions as well as disorder and to chemically realistic models. Unfortunately, these methods have been woeful in the treatment of Anderson localization due mainly to the averaging procedure utilized and improvements in the environment describing the effective medium have been limited to single sites. We will briefly review below some of the mean-field theories that have been developed for studying disordered electron systems.

4.1.1 The Coherent Potential Approximation

In this section, we will give a general overview of the coherent potential approximation. We will not try to derive nor rigorously review it but will present pertinent descriptions of its applicability and inadequacies for studying the Anderson localization transition. For general reviews and detailed discussions of the CPA, refer to Refs. [258, 261, 262]. The schematic environment is shown in Figure 4.1.

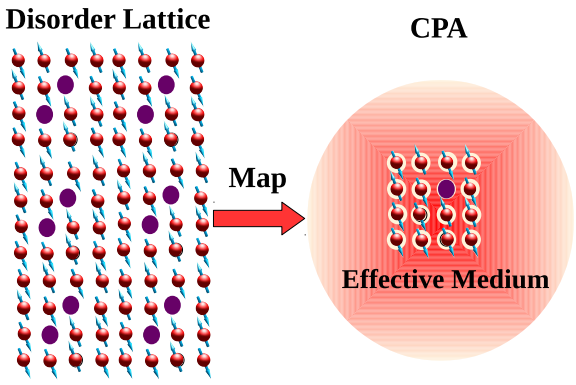

Figure 4.1: A schematic diagram of the CPA environment.

The coherent potential approximation (CPA) [258, 261, 262] is the most commonly used mean-

field theory to study disordered electronic systems. In the CPA implementation, the original infinite disordered lattice is mapped onto an averaged single (momentum-independent) impurity embedded in an effective medium (cf. Fig 4.1). It has been successful in describing some one-particle properties such as the density of states in (substitutional) disordered alloys [258, 261]. However, it has failed to provide adequate physics describing Anderson localization transition (ALT). This failure stems from the local nature of the CPA, as such, it is unable to capture crucial multiple backscattering interference effects that lead to localization and also on the averaging procedure in the self-consistency [2, 36].

4.1.2 Cluster Extensions of Coherent Potential Approximation

Over the years, several efforts have been made to extend the CPA to cluster forms to accommodate spatial corrections that are missing. A typical example of these cluster extensions of the CPA is the dynamical cluster approximation (DCA) [263, 264] and the molecular CPA (MCPA) [265].

We note the problems encountered in early attempts to formulate cluster corrections to the dynamical mean-field approximation are the same as those encountered in the coherent potential approximation (CPA) for disordered systems. As extensively demonstrated by Gonis [266, 267], a successful quantum cluster theory must meet the following criteria

- A successful quantum cluster theory for a disordered system must be able to self-consistently and systematically account for the local fluctuations in the effective environment;
- In the limit of the cluster size being one ($N_c \to 1$), it must recover the CPA;
- In the limit of large cluster size ($N_c \to \infty$, the thermodynamic limit), it must become exact;
- It should be numerically tractable and easy to implement;
- A successful cluster theory must obey translational invariance and preserve the full point-group symmetry of the lattice;
- It should be fully causal so that the self-energy and the associate Green function is analytic in the upper half-plane.

The dynamical cluster approximation has been shown to obey all the above outlined properties of a successful quantum cluster [263, 264, 267]. So far, it remains one of the most successful cluster extension of the CPA. The DCA, unlike the CPA, maps a disordered, infinite lattice to a finite cluster size N_c self-consistently embedded in the effective medium. We will not give detailed explanation of the self-consistent formalism of the DCA until later where we will describe it in our implementation of the DCA-based method for studying the Anderson localization transition.

We remark that, even though, spatial correlations are included in these cluster extensions of the CPA, none of them is adequate for studying Anderson localization transition. The main problem with these methods is that they use algebraic averaging (in the density of states (DoS)) in their self-consistency. The average DoS calculated within such mean-field theories cannot distinguish between extended and localized states and it is not critical at the transition [1, 2, 70, 120]. Hence, such average quantities cannot be used as an order parameter. This is the reason that most mean-field theories like the CPA [262] and its cluster extensions including the DCA [263, 264, 267], fail to provide a proper description of Anderson localization in disordered systems. This failure is intrinsic to these theories as the algebraically averaged quantities, i.e., the averaged density of states, used always favor the metallic state. This can be understood from the fact that in an infinite system of localized states, the average density of states is nothing but the global density of states, which is a smooth function of the disorder strength near the critical point while the local density of states becomes discrete with a non-trivial system size dependence (See for e.g., Refs. [65, 70, 105, 120, 134, 138, 225, 268] for a detailed discussion). I will demonstrate later the failures of finite cluster extensions of the CPA in characterizing the Anderson localization transitions using the DCA.

4.1.3 Algebraic versus Typical Averaging Procedure

Finding a proper single-particle order parameter for the Anderson localization transitions capable of distinguishing between the localized and extended states is a major challenge in the study of disordered electronic systems. The study of disordered systems relies on probability distribution functions (PDFs) to measure 'random' quantities of interest. To characterize localization, the most

important quantity in the majority of physical or statistical problems is usually the "typical" value of the 'random' variable, which corresponds to the most probable value of the PDF [136]. In most systems the nature of the PDF is not known a priori; as such, we have limited information via the moments or cumulants of the PDFs. Under such situation, the "typical" or the most probable value of the PDF [136] contains important and direct information. Different from some systems where the first moment (the arithmetic average) is a good estimate of the random variable, the Anderson localization is a non-self-averaging phenomenon. Close to the critical point the electronic quantities fluctuate strongly and the corresponding PDF of the local density of states is very asymmetric with long tails [135, 138] such that infinitely many moments are needed to describe it [136]. In some cases, the corresponding moments might not even exist especially close to the critical point [139].

The arithmetic average of random one-particle quantities is not critical at the Anderson localization transition. In contrast to the arithmetic average, the geometrical average, [65, 105, 135, 138, 269] gives a better approximation to the most probable value of the local density of states.

4.1.4 The Typical Medium Theory

As explained in Sections 4.1.1 and 4.1.2, the failures of CPA and its cluster extensions to properly characterize the localization transitions stem from the utilization of the algebraic average density of state (DoS) in their self-consistency loop. The average DoS does not vanish at the Anderson localization transition (ALT) as such, not critical [70]. However, the geometrical mean of the local DoS (LDoS) [60, 65, 269], which better approximates the typical value of the LDoS is critical at the ALT.

Dobrosavljević *et al.* [105] incorporated the typical medium theory (TMT) to the study of disorder system, where the typical density of states (TDoS) approximated using the geometrical averaging over disorder configurations are used instead of the arithmetically averaged local density of states. They demonstrated that the TDOS vanishes continuously as the strength of the disorder increases towards the critical point, and it can be used as an effective mean-field order parameter for the Anderson localization. In principle, Dobrosavljević *et al.* [105] showed that the typical density

of states (TDOS) provides a single-particle local order parameter for describing the Anderson localization transitions.

While the single-site TMT has been shown to be successful in describing localized electron states, it still has several drawbacks. In particular, it does not provide a proper description of the critical behavior of the Anderson localization transitions in 3-dimensions (3D). The local TMT underestimates the critical disorder strength with $W_c^{TMT} = 1.65$ instead of the numerical exact value $W_c \approx 2.1$ [37, 131, 247, 270–274] for the box distribution (in the units of our computations). Also, the *universal* order parameter critical exponent, (which has also been called the *typical order parameter exponent*) [135] β obtained in the local TMT is $\beta^{TMT} \approx 1.0$ whereas the recently reported value is $\beta \approx 1.67$ [142, 271]. Another crucial drawback of the single site TMT in three-dimensions is its inability to capture the re-entrance behavior of the mobility edge (energy separating extended and localized electron states) (for the disorder distributions with finite variance e.g., the box, and Gaussian disorder distributions) as seen in exact numerical studies [242, 272, 275]. The TMT also underestimates the extended region in all the disorder distributions studied in this dissertation.

The inadequacies of the local TMT can be remedied by incorporating spatial (non-local) correlations via its cluster extension. This can be achieved by using the DCA schemes, which systematically incorporates the missing non-local effects. This is another task of this dissertation and I will show that a straightforward extension of the local TMT is not just enough as it suffers from cluster self-averaging, which destroys the localization transitions. To avoid such self-averaging issues in the TDoS, a different Typical Medium DCA (TMDCA) method is proposed, which explicitly separates out the local part of the TDoS and treating it with a geometric averaging over disorder configurations. In this way, a proper TDoS that characterizes the ALT in 3D is obtained.

4.2 Hubbard Model

The Hubbard model is the simplest yet versatile model of interacting particles in a lattice. The original formulation of the Hubbard model was to describe electrons in solids [216] but it has since been the center of interest as a model for the high-temperature superconductivity, ultracold

atoms trapped in optical lattices (Bose-Hubbard model) [41, 276, 277], etc. The Hubbard model for interacting electrons moving on a lattice with on-site interaction is given by the Hamiltonian

$$H = -\sum_{\langle ij \rangle} t_{ij}(c_i^\dagger c_j + h.c.) + U\sum_i n_{i\uparrow} n_{i\downarrow}. \tag{4.3}$$

The first term is the energy operator due to hopping of electrons on the lattice. The operator $c_i^\dagger (c_i)$ creates (annihilates) an electron on site i, $n_i = c_i^\dagger c_i$ is the number operator, $t_{ij} = t$ is the hopping matrix element between nearest-neighbor sites. The second term depicts a two-body operator, which is the energy cost, $U > 0$ due to Coulomb repulsion for double occupancy of a site.

4.3 Anderson-Hubbard Model

The Anderson-Hubbard model is a minimal model for studying the interplay between electron–electron interactions and disorder. The Hamiltonian for this model is

$$H = -\sum_{\langle ij \rangle} t_{ij}(c_i^\dagger c_j + h.c.) + \sum_i (V_i - \mu) n_i + U\sum_i n_{i\uparrow} n_{i\downarrow}. \tag{4.4}$$

The first term again is the energy operator due to hopping of electrons on the lattice. The second term represents the disorder part, which is modeled by a local potential V_i randomly distributed according to a probability distribution $P(V_i)$ (cf. Equation 4.2), μ is the chemical potential. The last term is a two-body term, which is the energy cost, $U > 0$ due to Coulomb repulsion for double occupancy of a site just as in the Hubbard model (cf. Equation 4.3). A cartoon of the Anderson-Hubbard model is shown in Figure 4.2.

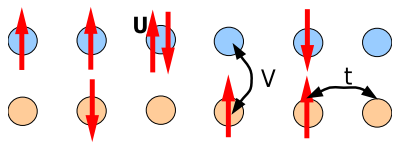

Figure 4.2: A cartoon of the Anderson-Hubbard model, characterized by single-band with near-neighbor hopping t, local potential V, and local repulsive interactions U

Chapter 5

Typical Medium Dynamical Cluster Approximation

In this Chapter, pedagogical steps in formulating a systematic, self-consistent finite cluster mean-field theory for 'proper' characterization of electron localization will be presented.

5.1 Introduction

Decades of efforts to formulate a systematic, self-consistent theory capable of *properly* characterizing the localization transitions in electronic systems have not been overwhelmingly achieved. Aside the single site TMT [105], other variants of the mean-field theories formulated to describe the localization transition have not been successful. However, as explained above, the local TMT has several drawbacks. Among them is the underestimation of the critical disorder strength, order parameter critical exponent, the inability to capture the re-entrance of the mobility edge (in distributions with finite variance), and the underestimation of the extended states in all the disorder distributions explored in this dissertation. One can thus conclude that, even though, the single site TMT gives a qualitative description of the localization transitions, it however fails to describe it quantitatively.

As a consequence of the central importance of an effective mean-field method (that properly describes the Anderson localization transition) to further progress in the study of electron localization, there is a need to formulate a mean-field theory that properly characterizes (both quantitatively and qualitatively) the localization transitions. Furthermore, a well-known long historical dichotomy exists between the mean-field results and the numerical data for the localization transition. Here, we demonstrate that the dichotomy can be reconciled by incorporating spatial fluctuations (in a typical environment) into the mean-field theory offering a solution to this long-standing

problem, by providing a systematic framework in the mean-field theory of Anderson localization including the off-diagonal disorder and interactions.

5.2 Formulation of Typical Medium Dynamical Cluster Approximation

The typical medium dynamical cluster approximation (TMDCA) utilizes the self-consistent framework of the standard dynamical cluster approximation [264, 278] with the important usage of an environment defined by a typical non-local hybridization function $\Gamma(K,\omega)$ (cf. Fig 5.1(a)). In particular, the TMDCA maps the given disordered lattice system into a finite periodic cluster of size $N_c = L_c^d$ which is embedded in an effective self-consistent typical medium (c.f. Figure 5.1(a)). Note that unlike in the usual DCA scheme where the effective medium is constructed via algebraic averaging over disorder configurations, in the TMDCA scheme, geometric averaging is used. By mapping a d-dimensional lattice containing N sites to a finite small cluster containing $N_c = L_c^d$ sites, where L_c is the linear dimension of the cluster, we dramatically reduce the computation effort [267]. The mapping is accomplished by dividing the first Brillouin zone into N_c non-overlapping cells of equal size (cf. Fig 5.2(a)). We show in Fig 5.2(b) how the coarse-graining procedure is achieved for a cluster of size $\mathrm{N}_c = 4$ in 2-dimensions while Fig 5.2(c) depicts the tiling procedure for some clusters.

Unlike the single-site methods commonly used to study disordered systems, such as the coherent potential approximation (CPA) [258, 262] or the local TMT, [105] the TMDCA ensures that non-local, spatial fluctuations, which are neglected in single-site approaches, are systematically incorporated as the cluster size N_c increases. Short length scale correlations inside the cluster are treated exactly up to a range $\xi \lesssim L_c$, while the long length scale correlations are treated within the typical medium (cf. Figure 5.1(a)). At the limit of cluster size $\mathrm{N}_c = 1$, the TMDCA recovers the local TMT, and at the limit of $\mathrm{N}_c \to \infty$, the TMDCA becomes exact. Hence, between these two limits, the TMDCA systematically incorporates non-local correlations into the local TMT.

One of hardest task in developing a (cluster) formalism for characterizing the localization is among other things, the solution to remain causal, fulfill all the essential requirements expected

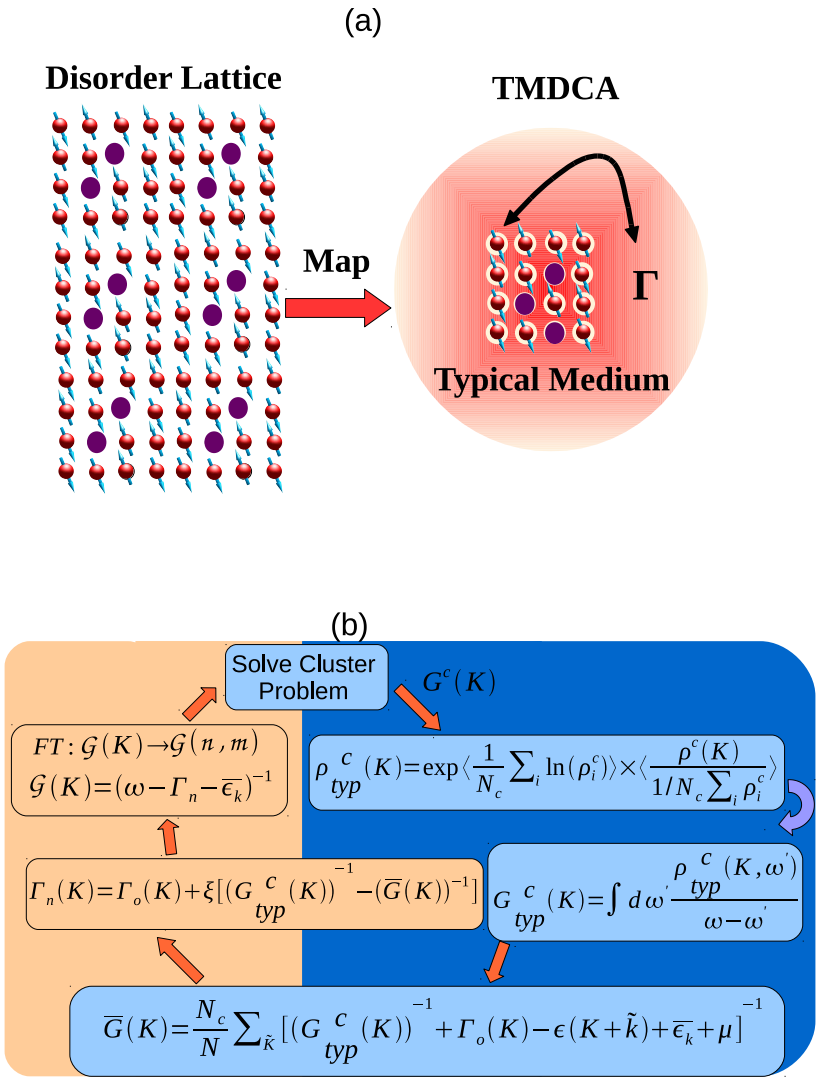

Figure 5.1: (a) A schematic diagram of the environment of the typical medium dynamical cluster approximation (TMDCA). This diagram depicts the mapping of a disordered, infinite lattice to a finite cluster self-consistently embedded in the typical effective medium. (b) The self-consistent loop of the computational procedure of the typical medium dynamical cluster approximation.

of a "successful" cluster theory [266] including causality and translational invariance, and at the same time not suffer from self-averaging [44, 136].

The earlier attempts to formulate a mean-field theory for the localization transitions lacked one or more of the above prescribed requirements for a successful cluster theory and for localization transitions. In the following subsequent sections, I will elaborate on the various attempts in formulating a successful cluster mean-field theory for characterizing localization in details.

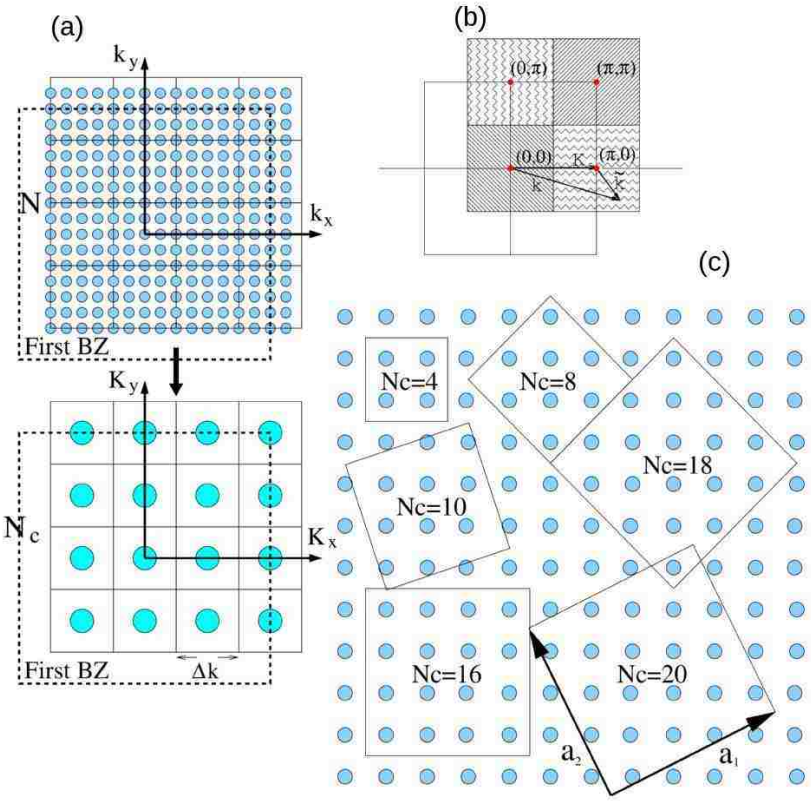

Figure 5.2: (a) An illustration of the coarse-graining procedure used in the TMDCA. (b) A typical $N_c = 4$ cluster cells (shown by different fill patterns) that partition the first Brillouin Zone (dashed line). Each cell is centered on a cluster momentum K (filled circles). Just as in the DCA, to construct the TMDCA cluster, we map a generic momentum in the zone such as k to the nearest cluster point $\mathbf{K}$ = M(k) so that $\tilde{k} = k - \mathbf{K}$ remains in the cell around $\mathbf{K}$. (c) Different tile sizes and orientations. The tiling principal translation vectors, a_1 and a_2, form two sides of each tiling square (as shown for the $N_c = 20$ tiling). For square tile geometries, $a_2 x = -a_1 y$ and $a_2 y = a_1 x$.

5.2.1 Direct Extension of the Local Typical Medium Theory to Finite Cluster

The first attempt at obtaining a cluster formalism capable of quantitatively and qualitatively characterizing localization transition is the obvious extension of the local typical medium theory [105] to its cluster version. Here, the $\rho^c(\mathbf{K},\omega) = -\Im G^c(\mathbf{K},\mathbf{K},\omega)/\pi$ for each cluster disorder configuration is first obtained. Then, using geometric averaging, the cluster-momentum-resolved typical density of states (TDoS) for each $\mathbf{K}$ is

$$\rho^c_{typ}(\mathbf{K},\omega) = \exp\langle \ln \rho^c(\mathbf{K},\omega)\rangle\,. \tag{5.1}$$

As will be elaborated in details in Subsection 5.3.1, defining the typical density of states as in Equation 5.1 suffers from cluster self-averaging as $N_c \to \infty$ in three dimensions. However, it does reproduce the expected behavior in lower (one and two) dimensions as will be shown in Chapter 6.

Further, the inability of the direct extension of the local typical medium theory to finite cluster to fully capture the localization transitions in three dimensions can be inferred from Figure 5.3. While it will eventually converge, it will converge to a critical disorder strength far greater than the numerically known value. A further remark is that the trajectories of the mobility edge is totally missed due to self-averaging. I will elaborate on this later in Subsection 5.3.1.

Another version of the initial attempt to develop cluster theory for the localization transition is the separation of the local densities (typical and algebraic) in such a way that a fraction of their ratio multiples the local typical density while the remaining fraction multiples the algebraic cluster density of states as

$$\begin{aligned}\rho^c_{typ}(\mathbf{K},\omega) &= \left[\left(1.0 - \frac{\exp\left(\frac{1}{N_c}\sum_{i=1}^{N_c}\langle \ln \rho^c_i(\omega,V)\rangle\right)}{\frac{1}{N_c}\sum_{i=1}^{N_c}\left\langle \rho^c_i(\omega,V)\right\rangle}\right) \times \exp\left(\frac{1}{N_c}\sum_{i=1}^{N_c}\langle \ln \rho^c_i(\omega,V)\rangle\right)\right] \\ &+ \left[\left(\frac{\exp\left(\frac{1}{N_c}\sum_{i=1}^{N_c}\langle \ln \rho^c_i(\omega,V)\rangle\right)}{\frac{1}{N_c}\sum_{i=1}^{N_c}\left\langle \rho^c_i(\omega,V)\right\rangle}\right) \times \langle \rho^c(\mathbf{K},\omega,V)\rangle\right]. \end{aligned} \tag{5.2}$$

This again does reproduce the expected behavior in lower dimensions but not in three dimensions due to the same reasons as explained above, it is possible to formulate variants of other definitions of the typical medium, which avoid self-averaging. One of the possibility is just utilizing the local part of the typical density of states as

$$\rho^c_{typ}(K,\omega) = \exp\left(\frac{1}{N_c}\sum_{i=1}^{N_c}\langle \ln \rho^c_i(\omega,V_i)\rangle\right). \tag{5.3}$$

However, while this formulation avoids self-averaging as $N_c \to \infty$, it does not meet some of the criteria of a successful cluster theory. In particular, this formalism does not recover the DCA in the weak coupling limit. This will be demonstrated below. It should be noted that while the first two formulations (cf. Eqs. 5.1 and 5.2), meets all the requirements needed of a successful cluster

theory, it does suffer from cluster self-averaging as $N_c \to \infty$. For all the formulations above, to ensure the causality of the Green function, we carry out the Hilbert transformation of the TDoS to obtain the typical cluster Green function as

$$G^c_{typ}(\mathbf{K},\omega) = \int d\omega' \frac{\rho^c_{typ}(\mathbf{K},\omega')}{\omega - \omega'}. \tag{5.4}$$

5.3 The Typical Medium Dynamical Cluster Approximation

After several attempts and formulating variants of the finite cluster theory for localization transitions, the typical medium dynamical cluster approximation (TMDCA) was developed. The typical medium dynamical cluster approximation scheme is, to the best of my knowledge, a successful, systematic, self-consistent, preserving causality, and numerically efficient effective medium theory to characterizing localization transitions in one, two, and three dimensions. For instance, in the Anderson localization transitions where broad transition exists in three-dimensions, the TMDCA, i) recovers the original single-site TMT scheme at cluster size $N_c = 1$; ii) recovers the DCA results at small disorder strength (when all states are metallic); iii) provides a proper way to separate the energy scales such that the characteristic mobility edge behavior (for the disorder distributions with finite variance) is obtained; iv) captures the critical behavior of Anderson localization transitions with correct critical disorder strength W_c and order parameter critical exponent β, and provides a correct description of the Anderson insulator at large disorder strength (when all states are localized); v) fulfills all the essential requirements expected of a "successful" cluster theory [264, 266].

Before presenting detailed self-consistent algorithm of the TMDCA, an explanation of the origin of the cluster self-averaging in the earlier attempts to develop a cluster version of the typical medium theory will be discussed.

5.3.1 Avoiding Self-Averaging

As it is obvious from above, the averaging procedure used to calculate the typical spectra is not unique. As noted above, a direct extension of the local typical medium theory (TMT) [105] to finite cluster reproduced the expected behavior in one and two dimensions as N_c is increased [1].

However, in three dimension, applying the algorithm directly will lead to effective self-averaging for large clusters. This is due to the fact that close to the criticality, there exist distinct localized and extended states above and below the localization edge given by the TDoS with an energy scale difference that can span an order of magnitude. These energy scales need to be treated differently. This can be seen by investigating the spectra density where the local part of the TDoS is not explicitly separated and treated with geometric averaging over disorder realizations:

$$\rho^c_{typ}(\mathbf{K},\omega) = \exp\langle \ln \rho^c(\mathbf{K},\omega,V_i)\rangle\,. \tag{5.5}$$

In forming the Fourier transform

$$\rho^c(\mathbf{K},\omega,V_i) = \sum_{X,X'} \exp(i\mathbf{K}\cdot(X-X'))\rho^c(X,X',\omega,V_i) \tag{5.6}$$

the average over the cluster coordinates X and X', including the local part, $X = X'$. I.e., the local DoS is first summed over the cluster sites and then Fourier transformed to form the local part of $\rho^c(\mathbf{K},\omega)$. Hence for large clusters, this reduces to linear averaging of the local part instead of geometrical averaging. As a consequence, the host Green function constructed from $\rho^c_{typ}(\mathbf{K},\omega)$ is unaware of the TDoS and thus, it is unable to distinguish between the energies above and below the localization edge.

To avoid such self-averaging in the TDoS, the cluster-momentum-resolved typical density of states (TDoS) for each $\mathbf{K}$ is split into the local and non-local parts. The local part is treated with geometrical averaging over disorder configurations, while the non-local part is treated either with an algebraic (referred to as *linear-log* procedure) or geometric averaging (referred to as *log-log* procedure over the disorder configuration. In the *linear-log* procedure, the local part is treated with a geometrical averaging while the non-local part is approximated algebraically using linear averaging as

$$\rho^c_{typ}(\mathbf{K},\omega) = \exp\left(\frac{1}{N_c}\sum_{i=1}^{N_c}\langle \ln \rho^c_i(\omega,V_i)\rangle\right) \times \left\langle \frac{\rho^c(\mathbf{K},\omega,V_i)}{\frac{1}{N_c}\sum_i \rho^c_i(\omega,V_i)}\right\rangle. \tag{5.7}$$

In the *log-log* procedure, this again involves the treatment of the local part with geometrical averaging but instead, the non-local part is treated with a log averaging as

$$\rho^c_{typ}(\mathbf{K},\omega) = \exp\left(\frac{1}{N_c}\sum_{i=1}^{N_c}\langle \ln \rho^c_i(\omega,V_i)\rangle\right) \times \exp\left(\left\langle \ln \frac{\rho^c(\mathbf{K},\omega,V_i)}{\frac{1}{N_c}\sum_i \rho^c_i(\omega,V_i)}\right\rangle\right). \tag{5.8}$$

It is imperative to note that while there are different behaviors of the two methods around the re-entrance region, both procedure systematically converge to the same critical disorder strength for e.g., $W_c^{N_c\geq 12} \approx 2.1 \pm 0.01$ for the box disorder distribution. However, the former (*linear-log* procedure) is generally more robust than the *log-log* method. The latter is characterized by a slower convergence around the re-entrance region, requiring far larger system size before a convergence of the re-entrance region is achieved in comparison to the numerical experimental results. It may also not be adequate to study localization phenomena in realistic material applications, since it is not obviously clear how a geometrical averaging of the off-diagonal components of the spectral density which is not positive definite will be done. The comparison of the phase diagram obtained using the two procedure: log-log and linear-log formalism is shown in Figure 5.3. As it is evident

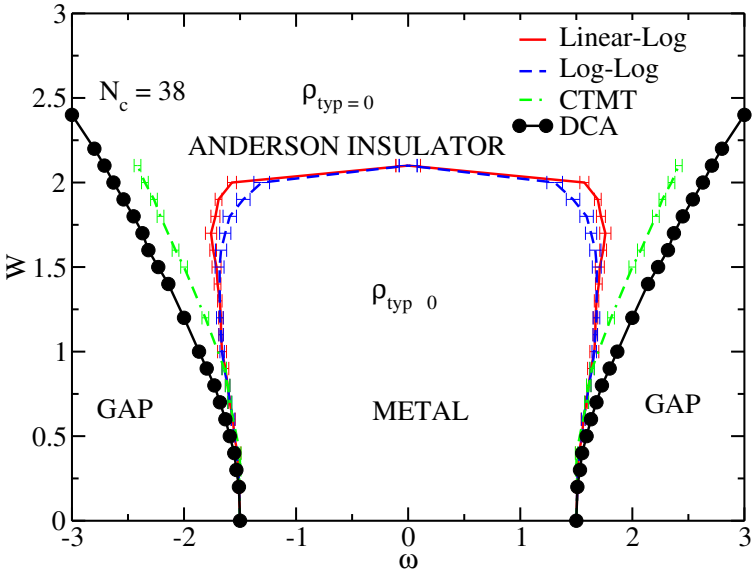

Figure 5.3: A comparison of the phase diagram of the Anderson localization transition for the box disorder distribution in 3D obtained from cluster approximations with $N_c = 38$ using CTMT and the TMDCA (linear-log and log-log) schemes. Observe that in the CTMT, as consequence of self-averaging, the higher disorder behaviors which are captured in our TMDCA are totally missed and the critical disorder strength is also severely over-estimated.

from Fig 5.3, the two new schemes converge to the same critical disorder strength but behave differently around the re-entrance region. For the results presented in the subsequent Chapters of this dissertation, the *linear-log* method is utilized.

Note further that in both the *linear-log* and *log-log* procedures, at small N_c, ≈ 100 self-consistent iterations are required to achieve a convergence while for relatively large N_c, far fewer iterations are required. The convergence criterion for both limits is achieved when the TDoS ($\omega = 0$) does not fluctuate anymore with iteration number within the error bars.

5.3.2 Typical Medium Dynamical Cluster Approximation: The Self-Consistent

The details of the formalism of the typical medium dynamical cluster approximation are described below. The average density of states at each cluster momentum $\mathbf{K}$ within the dynamical cluster approximation is given as

$$\rho^c_{avg}(\mathbf{K},\omega) = \langle \rho^c(\mathbf{K},\omega)\rangle = -\frac{1}{\pi}\langle \Im G^c(\mathbf{K},\mathbf{K},\omega)\rangle, \tag{5.9}$$

where the superscript 'c' denotes cluster and $\langle\rangle$ is the disorder average. The $\mathbf{K}$-dependent cluster Green function is obtained from the site dependent Green function $G_c(i,j,\omega)$ via

$$G^c(\mathbf{K},\mathbf{K},\omega) = \frac{1}{N_c}\sum_{i,j} e^{i\mathbf{K}\cdot(\mathcal{R}_i-\mathcal{R}_j)} G_c(i,j,\omega). \tag{5.10}$$

In the TMDCA, for each cluster configuration, $\rho^c(\mathbf{K},\omega) = -\Im G^c(\mathbf{K},\mathbf{K},\omega)/\pi$ is first obtained and can be shown via the Lehmann representation [279,280], that $\rho^c(\mathbf{K},\omega) \geq 0$ for each $\mathbf{K}$, ω, and disorder configuration. As explained above, the formulation of the TMDCA utilized in this dissertation is the *log-linear* procedure. Here, the local part of the cluster-momentum-resolved typical density of states is separated and treat with geometrical averaging over the cluster and disorder configurations, as to avoid self-averaging as the cluster size increases. The obtained cluster TDoS

is given by

$$\rho^c_{typ}(\mathbf{K},\omega) = \overbrace{\exp\left(\frac{1}{N_c}\sum_{i=1}^{N_c}\langle \ln \rho^c_i(\omega,V)\rangle\right)}^{\text{local TDOS}} \times \underbrace{\left\langle \frac{\rho^c(\mathbf{K},\omega,V)}{\frac{1}{N_c}\sum_i \rho^c_i(\omega,V)}\right\rangle}_{\text{non-local}}. \tag{5.11}$$

The $\rho^c_{typ}(\mathbf{K},\omega)$ possess the following properties: for $N_c = 1$, it reduces to the local TMT scheme with $\rho^c_{typ}(\omega) = \exp\langle \ln \rho(\omega)\rangle$. At low disorder strength, $W \ll W_c$, we find the real space prefactor $\langle \ln \rho_i(\omega,V_i)\rangle \approx \ln\langle \rho_i(\omega,V_i)\rangle$. Then $\rho^c_{typ}(\mathbf{K},\omega)$ reduces to the DoS calculated in DCA scheme, with $\rho^c_{typ}(\mathbf{K},\omega) \approx \langle \rho^c(\mathbf{K},\omega,V)\rangle$. From Equation 5.11, the disorder averaged typical cluster Green function is obtained using the Hilbert transform

$$G^c_{typ}(\mathbf{K},\omega) = \int d\omega' \frac{\rho^c_{typ}(\mathbf{K},\omega')}{\omega-\omega'}. \tag{5.12}$$

A schematic one-dimensional TMDCA self-consistency is shown in Figure 5.1(b). The TMDCA iterative procedure is described:

1. The TMDCA iterative procedure begins by one proposing an initial guess for the hybridization function $\Gamma_o(\mathbf{K},\omega)$, where the subscript o denotes old. The choice of the starting guess for the hybridization function may be based on a priori knowledge, i.e., in case we have information about the self-energy $\Sigma(\mathbf{K},\omega)$ and cluster Green function $G^c(\mathbf{K},\omega)$, $\Gamma_o(\mathbf{K},\omega)$ can be calculated as

$$\Gamma_o(\mathbf{K},\omega) = \omega - \overline{\varepsilon}(\mathbf{K}) + \mu - \Sigma(\mathbf{K},\omega) - 1/G^c(\mathbf{K},\omega) \tag{5.13}$$

   where $\overline{\varepsilon}(\mathbf{K}) = \dfrac{N_c}{N}\sum_{\tilde{k}} \varepsilon(\mathbf{K}+\tilde{k})$ is the coarse-grained bare dispersion with $\tilde{k}$ summed over N/N_c momenta inside the cell centered at the cluster momentum $\mathbf{K}$ [263] (cf. Figure 5.2(b)). However, if nothing is known a priori, the guess $\Gamma_o(\mathbf{K},\omega) \equiv 0$ may serve as the starting point.

2. After setting up the cluster problem, the cluster-excluded Green function $\mathcal{G}(\mathbf{K},\omega)$ is then calculated as

$$\mathcal{G}(\mathbf{K},\omega) = (\omega - \Gamma_o(\mathbf{K},\omega) - \overline{\varepsilon}(\mathbf{K}) + \mu)^{-1}. \tag{5.14}$$

   Since the cluster problem is solved in real space, I then Fourier transform $\mathcal{G}(\mathbf{K},\omega)$ to obtain

$\mathcal{G}_{n,m} = \sum_{\mathbf{K}} \mathcal{G}(\mathbf{K}) \exp(i\mathbf{K} \cdot (r_n - r_m))$.

3. Next, the cluster problem is solved exactly. Here, I stochastically generate random configurations of the disorder potential V. For each disordered configuration, I use the Dyson equation to calculate the new fully disorder dressed cluster Green function

$$G^c(V) = (\mathcal{G}^{-1} - V)^{-1}. \tag{5.15}$$

This is Fourier transformed to $G^c(\mathbf{K}, \mathbf{K}, \omega)$ to obtain the cluster density of states $\rho^c(\mathbf{K}, \omega) = -\frac{1}{\pi}\Im G^c(\mathbf{K}, \mathbf{K}, \omega)$. The typical cluster density of states is then calculated via geometric averaging using Equation 5.11. Then, we calculate the disorder averaged, typical cluster Green function $G^c_{typ}(\mathbf{K}, \omega)$ via Hilbert transform using Equation 5.12. Note the advantage of the stochastic sampling of the disorder configurations. Here, each of the disorder configurations is statistically independent of each other. Thus, instead of sampling the disorder configurations with the very expensive enumeration technique which scales as 2^{Nc}, we instead do a stochastic sampling of the disorder configurations. This greatly reduces the computational cost enabling us to study larger clusters. With this, the number of disorder realizations needed to get a converged solution falls with increased cluster size. Furthermore, since fewer iterations are needed for larger clusters the computational cost does not even scale as N_c^3 as one would expect from Equation 5.15. For a typical 64 site cluster, with box disorder about 500 disorder realizations are enough to produce high-quality data.

4. After solving the cluster problem, I use the typical cluster Green function $G^c_{typ}(\mathbf{K}, \omega)$, to calculate the coarse-grained cluster Green function of the lattice $\overline{G}(\mathbf{K}, \omega)$ as

$$\overline{G}(\mathbf{K}, \omega) = \int \frac{N_0^c(\mathbf{K}, \varepsilon) d\varepsilon}{(G^c_{typ}(\mathbf{K}, \omega))^{-1} + \Gamma(\mathbf{K}, \omega) - \varepsilon_{\mathbf{K}} + \overline{\varepsilon}(\mathbf{K})}, \tag{5.16}$$

where $N_0^c(\mathbf{K}, \varepsilon)$ is the bare partial density of states.

5. The self-consistency is closed by updating the new hybridization function using linear mixing

$$\Gamma_n(\mathbf{K}, \omega) = \Gamma_o(\mathbf{K}, \omega) + \xi[(G^c_{typ}(\mathbf{K}, \omega))^{-1} - (\overline{G}(\mathbf{K}, \omega))^{-1}] \tag{5.17}$$

where the subscripts n and o denote new and old, respectively. The mixing parameter $\xi > 0$ controls the ratio of the new and old $\Gamma(\mathbf{K},\omega)$ entering the next iteration. For very small ξ, convergence may be slowed down unnecessarily, while for very large ξ, oscillations about the self-consistent solution may occur. Instead of linear mixing, the convergence of the computations can be improved by using the Broyden method [281].

6. The above procedure is repeated until the hybridization function converges to the desired accuracy, $\Gamma_o(\mathbf{K},\omega) = \Gamma_n(\mathbf{K},\omega)$. When this happens, the Green functions are also converged, $\overline{G}(\mathbf{K},\omega) = G^c_{typ}(\mathbf{K},\omega)$ within the computational error.

Note the TMDCA just as in the DCA [264, 278] preserves causality. since all the Green functions are causal, both the DoS and the TDoS calculated from them are positive definite. Also, I observe that as N_c increases, the method systematically interpolates between the local TMT and the exact result.

5.3.3 The Pole Procedure

Close to the criticality, the states at the top and bottom (for e.g., a bipartite lattice $(0,0,0)$ and (π,π,π)) of the bands are such that their hybridization rates tend to zero leading to the development of poles in the cluster excluded Green function. Here, I present in detail how to deal with such poles that emerge on the real frequency axis as the critical disorder strength is approached.

When $\Im\Gamma_{typ}(\mathbf{K},\omega)$ becomes very small ($\to 0$), the imaginary part of the cluster-excluded Green function, $\mathcal{G}(\mathbf{K},\omega)$, becomes series of a delta function. To see this clearly, we note that

$$\mathcal{G}(\mathbf{K},\omega) \;=\; (\omega - \Gamma_{typ}(\mathbf{K},\omega) - \overline{\varepsilon}(\mathbf{K}))^{-1} \Longrightarrow \mathcal{P}(\omega-\omega')^{-1} - i\pi\delta(\omega-\omega'), \qquad (5.18)$$

where $\omega' = \overline{\varepsilon}(\mathbf{K}) + \Re\Gamma_{typ}(\mathbf{K},\omega)$ and "$\mathcal{P}$" denotes the principle value. Evidently from Equation 5.18, the poles cannot be represented in the conventional way as a list of frequencies on the computer with a finite frequency resolution $d\omega$. Such difficulty can be avoided by explicitly

replacing each of the $\mathbf{K}-$cells of the $\mathcal{G}(\mathbf{K},\omega)$ with such poles in Equation 5.18 by

$$\mathcal{G}(\mathbf{K},\omega) = \begin{cases} -i\pi/d\omega & : \quad \omega = \omega' \\ \frac{1}{\omega-\omega'} & : \quad \omega \neq \omega'. \end{cases} \tag{5.19}$$

This formulation is referred to as the explicit "*pole-procedure*". With this procedure, the singularity in $\mathcal{G}(\mathbf{K},\omega)$ can be properly captured. An added difficulty is that for a given N_c, as the W_c is approached, $\Im\Gamma_{typ}(\mathbf{K},\omega)$ for individual cells goes to zero at different rates. Hence, I have to determine which of these cells need to be treated with the explicit "pole-procedure". I choose the criterion that for any cell, if $(-1/\pi)\times\Im\Gamma_{typ}(\mathbf{K},\omega') < a\times d\omega'$, then I apply the pole procedure to such cells. Here, $a \gtrsim 1$ is a parameter which measures the minimum number of pixels needed to represent a pole approaching the real frequency axis. Our numerical experience shows that such a criterion works nicely while spurious results are obtained otherwise.

Chapter 6

Application of Typical Medium Dynamical Cluster Approximation to Lower Dimensional Disordered System

Most of the results presented in this chapter has been published in J. Phys.: Condens. Matter **26** *274209 (2014) [1]. My role is the formulation of the model, writing and debugging the code, running the code to generate data and writing the manuscript. The list of the authors, as it appears in the manuscript are C. E. Ekuma, H. Terletska, Z. -Y. Meng, J. Moreno, M. Jarrell, S. Mahmoudian, and V. Dobrosavljević.*

6.1 Introduction

One and two-dimensions provides a unique platform for exploring the localization of electrons. Lower dimensional systems abounds in various realistic systems not limited to metal-oxide-semiconductor field-effect transistor, quantum dots, quasi-one-dimensional materials, etc. For a review of the progress in lower dimensional Anderson localization, see for e.g., Refs. [36, 69, 227, 236, 250, 260, 282–285].

According to the one-parameter scaling theory, [4] there is no delocalized phase in one- and two- dimensions at zero magnetic field and in the absence of spin-orbit coupling, whereas, a metal-insulator-transition (localization/delocalization phase) occurs at finite disorder strength in three-dimensions (3D). Even at this, the 2-dimension (2D) is special since it is the lower critical dimension of the localization phenomenon as such, margninal perturbation e.g., spin-orbit coupling or magnetic field may induce localized states for weak disorder leading to the existence of delocalized states and hence, an MIT. As a consequence, the localization lengths of a disordered 2D system can be quite large, with the implication that numerical approaches can find an MIT

when either a fixed system size with increasing disorder strength or fixed disorder strength for a decreasing system size.

In Section 5.3, I talked about how in the implementation I constructed the typical density of states as in Equation 5.11 to avoid self-averaging as the cluster size is systematically increased. Initially for lower dimensions, I did not separate the local TDoS as in Equation 5.11. I straightforwardly, calculated, using geometric averaging, the cluster-momentum-resolved typical density of states (TDoS) for each **K** as in Equation 5.1, a variant referred to as the cluster typical medium theory (CTMT).

While this works in 1 and 2D, unfortunately, this formalism, when applied with the modest cluster sizes, is unable to fully capture the localization transition in 3D. First, we observe an unsystematic behavior of our formalism in the sense that for a small cluster size, for e.g., N_c=1, 4 and 8, the critical disorder strength W_c, where all states become localized, is underestimated, while for larger cluster sizes, e.g., N_c=24 and 38, it overestimates the critical disorder strength. Of course, in the limit of large N_c, the exact critical behavior around W_c will be recovered. Second, for modest cluster sizes, while the TDoS becomes small as W increases, its width increases monotonically with disorder strength until the critical value is reached. However, in numerical calculations the width first increases and then decreases with disorder strength [275,286,287], indicating that without explicit separation of the local TDoS, the formalism fails to correctly, capture the localization edge for modest cluster sizes. In addition, while the hybridization rates also become small, they do not all vanish at the critical disorder strength W_c. Rather, only the hybridization corresponding to states near the top and bottom of the bands vanish while the states at the band center only vanish for values of the disorder strength much larger than W_c. Apparently, while this particular scenario is able to capture weak localization effects in lower dimensional systems, it is not able to capture the evolution of the localization edge which characterizes the transition in three dimensions until the cluster sizes are very large. A fully causal formalism which is able to efficiently capture the localization transition in 3D is achieved by the re-construction of the TDoS as in Equation 5.11.

Since there is no MIT in the non-interacting 1 and 2 dimensional systems, the above formalism doesn't suffer from any self-averaging as in 3-dimensions. Hence, the first attempt (from

Equation 5.1) and the fully self-consistent TMDCA that works in all dimensions (as explained in Section 5.3) for the lower dimensional cases will eventually converge at the thermodynamic limit but the later will converge faster. The results presented here are for the box disorder configurations distributed according to the distribution function ($P(V_i)$)(4.2a) with a bandwidth of one (for 2D) and a half (for 1D) in the units of the simulations (since $4t = 1$). I apply the CTMT scheme to one- and two-dimensional disordered systems describe by the Hamiltonian (Equation 4.1).

The present study clearly presents the essence of the effective typical medium theory, and the need to systematically go beyond single site approximations for lower dimensional systems. The key result of this chapter is that the TMDCA is a proper mean-field theory that accurately simulates the properties of lower dimensional systems and for $N_c \rightarrow \infty$, the TMDCA correctly shows that an arbitrarily small disorder is enough to localize all states in lower dimensional 'random' Anderson model in agreement with numerical results [4].

6.2 The Nature of the Density of States in one and two Dimensions

In the lower (one and two) dimensions of Anderson model of disorder, there is no delocalization phase [4]. To investigate this, we show in Figure 6.1 shows the local typical density of states

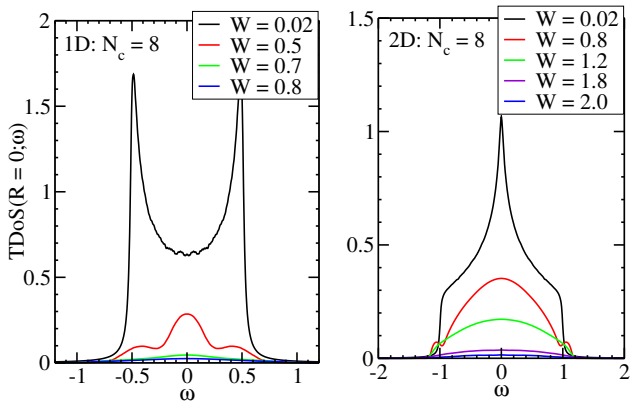

Figure 6.1: The local typical density of states, TDoS(R=0), as a function of frequency for various disorder strengths, W, for clusters of size N_c = 8 for one- (left panel) and two-(right panel) dimensional systems. Observe that in both cases, the TDoS gradually decreases with increasing W. The value of W where the TDoS vanishes reveals the critical disorder strength W_c. Hence, the TDoS behaves as an order parameter for the localization transition. $\Im\ \Gamma(R = 0, \omega)$ (not shown) vanishes at the same critical disorder strength as the TDoS.

(TDoS(R=0)) for a cluster of size N_c = 8 at various disorder strengths. For both one and two dimensions, the TDoS systematically goes to zero as the disorder strength is gradually increased. In 1D, the TDoS is practically zero for all frequencies at a critical disorder strength $W_c \approx 0.8$; whereas in 2D, $W_c \approx 2.3$. Above the critical disorder strength, the electrons are localized. The TDoS calculated in our CTMT scheme indeed provides key information about the Anderson localization transition.

According to the one-parameter scaling theory, [4,35,69,247] in 1D an arbitrary weak disorder strength localizes the electrons; whereas in 2D, the system is also always localized, but with the difference that the conductivity only decreases logarithmically with disorder strength.

As we discussed in preceding sections, mean-field theories, such as the single-site CPA or the DCA, cannot capture the localization transition due to the use of an algebraic averaging scheme in their self-consistency. The single-site TMT, on the other hand, is able to qualitatively describe the localization transition in one, two and three dimensions [286], but with critical disorder strength different from the exact values, i.e., in 1D and 2D, $W_c = 0$ and in 3D $W_c = 2.1$ (in units where $4t = 1$) [105, 131, 286]. This is not surprising as the local TMT completely neglects non-local inter-site correlations. The CTMT gives a better qualitative and quantitative mean-field theory for studying disordered systems in one and two dimensions. We expect that as the cluster sizes increases, the critical disorder strength will systematically converge to the exact value of zero in the thermodynamic limit. This is demonstrated in Figs. 6.2.

6.3 The Evolution of the Local Density of States in one and two Dimensions

Figure 6.2 (Right panel) shows the local typical density of states at the band center, TDoS(R = 0, $\omega = 0$), for a one-dimensional system as a function of disorder strength, W. By increasing the cluster size the critical disorder strength decreases and eventually will go to zero for a reasonably large N_c. Similarly, Figure 6.2 (Right panel) displays the local typical density of states at the band center for a two-dimensional system. The critical disorder strength also decreases as N_c increase. However, the decrease of W_c as a function of N_c is slower than that of the 1D case. This implies

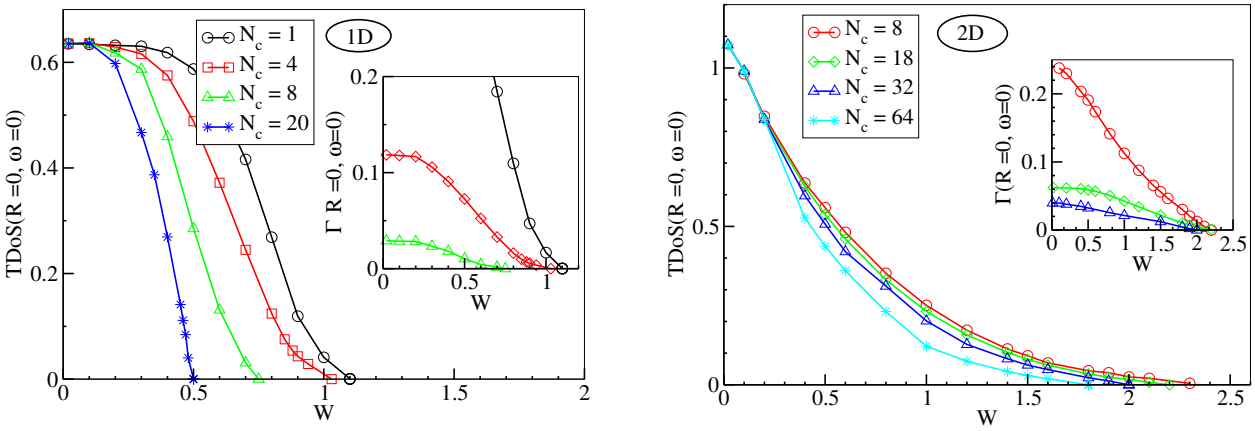

Figure 6.2: The local typical density of states at the band center, TDoS(R = 0, $\omega = 0$), as a function of disorder strength, W/4t, for various cluster sizes for 1D (Left panel) and 2D (Right panel). The critical disorder strength W_c decreases exponentially (in 1D) and logarithmically (in 2D) as cluster size N_c increases. The insets display the local hybridization rate at the band center $\Gamma(R = 0, \omega = 0)$ vs. W/4t. Note that $\Gamma(R = 0, \omega = 0)$ and TDoS(R=0, $\omega = 0$) go to zero at the same critical disorder strength.

that the scaling form of W_c vs N_c (or L_c) for 1D and 2D systems is different. The former follows a power-law whereas the latter has a logarithmic form. This is consistent with the one-parameter scaling theory [4, 35, 69, 247], which shows that a 1D system is strongly localized, while 2D is the lower critical dimension of the Anderson localization transition. The insets of Figs. 6.2 show that the local hybridization rate at the band center, $\Gamma(R = 0, \omega = 0)$, goes to zero at the same value of W than the TDoS.

6.4 Scaling of the Critical Disorder Strength

Figures 6.3 and 6.4 address the scaling of W_c vs N_c. In 1D, the scaling ansatz is $\xi = L_c \sim W_c^{-\nu}$, where ξ is the localization length, and ν is the critical exponent. As shown in Figure 6.3, the power law behavior is nicely captured by our data with $1/\nu = 0.46 \pm 0.10$ in basic agreement with numerical results which reported a value of $1/\nu = 0.5$ [288], and also with the one-parameter scaling theory [4]. The inset of Figure 6.3 is a log log plot of disorder W_c vs cluster size N_c where the power-law behavior $W_c \sim (1/L_c)^{1/\nu}$ is seen as a straight line depicting that W_c goes to zero for large enough cluster size.

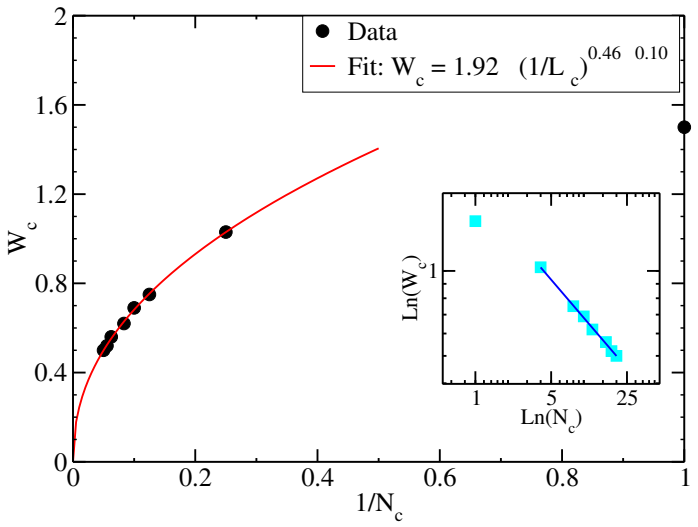

Figure 6.3: The critical disorder strengths W_c for various cluster sizes N_c ($= L_c$) in a 1D disordered system. The data can be fitted with a scaling ansatz: $\xi = L_c \sim W_c^{-\nu}$ or $W_c \sim (1/L_c)^{1/\nu}$, with $1/\nu = 0.46 \pm 0.10$ in agreement with previous numerical results of $1/\nu = 0.5$ [288]. The inset shows the power law behavior in a log-log plot.

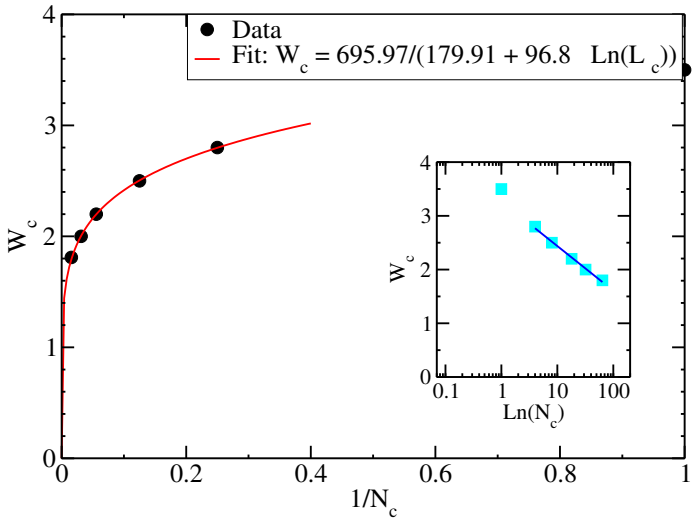

Figure 6.4: The critical disorder strength W_c for various cluster sizes $N_c = L_c^2$ in a 2D disordered system. The data can be fit with a scaling ansatz: $W_c = 695.97/(179.91 + 96.8 \times \ln(L_c))$ in agreement with the results of MacKinnon and Kramer [247]. The inset shows the logarithmic behavior in a semi-log plot.

Figure 6.4 displays the scaling of W_c vs L_c ($N_c = L_c^2$) in a 2D system. Our data can be fit with a logarithmic function, $W_c = 695.97/(179.91 + 96.8 \times \ln(L_c))$. Thus, W_c decreases slowly with N_c and only for very large clusters the system is completely localized. This behavior agrees with the

one-parameter scaling theory [4], as 2D is generally believed to be the lower critical dimension for the ALT [289]. The inset of Figure 6.4 is a semi-log plot of W_c vs ln N_c where the logarithmic behavior is seen as a straight line. We note that our data fit nicely to an exponent form: $L_c = \exp(4.73/W_c^{0.98})/W_c^{0.98}$ in basic agreement with the results of MacKinnon and Kramer [247]. [1]

6.5 The PDF for Lower Dimensional Anderson Localization

As explained in the previous sections, when system becomes localized, the PDFs of the density of states change from Gaussian distribution (where all states are metallic, the PDF is symmetric with the shape of TDoS the same as the ADoS) to a very asymmetric distribution with long tails (where all states are localized, the LDoS strongly fluctuating at all sites, and the TDoS is very different from the ADoS).

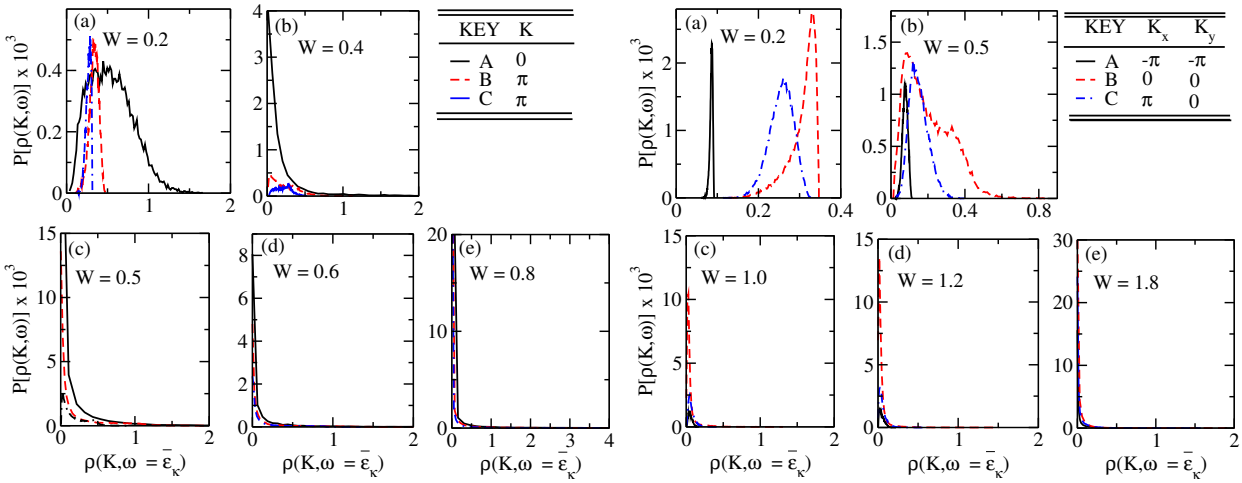

Figure 6.5: The evolution of the probability distribution (PDF[$\rho(\mathbf{K}, \omega = \bar{\varepsilon}_{\mathbf{K}})$]) at different cluster cells with increasing W for a 1D system (Left Panel) and 2D system (Right Panel), the cluster size is $N_c = 8$. The labels A–C correspond to three cluster momenta.

Utilizing large-scale exact diagonalization calculations, Schubert *et al.* [257] have demonstrated that the PDFs close to the Anderson transition in 2D and 3D systems are log-normal. Here, as a proof of principle, we perform similar calculations. Within the CTMT scheme, we obtain the PDFs of the momentum-resolved DoS $\rho(\mathbf{K}, \omega = \bar{\varepsilon}_{\mathbf{K}})$ at different momenta cells centered at cluster

[1] The results obtained from the fully self-consistent, systematic TMDCA where Equation 5.11 is utilized in the self-consistent shows similar trend. However, far smaller disorder strength (for e.g., for 1D at $N_c = 64$, for a disorder strength as small as 0.15,) is needed to localize all the states in agreement with the single-parameter scaling [4]. For comparison, see Figs. 6.6 and 6.7 where the two methods are compared.

momentum point $\mathbf{K}$ and at the averaged energy $\omega = \bar{\varepsilon}_{\mathbf{K}}$ of the cell $\mathbf{K}$. When sampled over large enough number of disorder configurations in our Monte-Carlo procedure, we indeed find as the disorder strength W is increasing, the PDF[$\rho(\mathbf{K}, \omega = \bar{\varepsilon}_{\mathbf{K}})$] (shown in Figs. 6.5 for 1D (Left panel) and 2D (Right panel) systems, respectively) develop log-normal distributions, consistent with the observation in Ref. [257]. Moreover, we find for 1D system, the log-normal distribution happens for all the momentum cells at a very small disorder strength ($W = 0.4, 0.5$) for $Nc = 8$ cluster; and in 2D, the same log-normal distribution for all the cells will only happen at a larger disorder strength ($W = 1.0, 1.2$). This observation is consistent with the fact that 1D systems are much easier to localize (exponential) as compared to 2D systems (logarithmic).

6.6 Fast Convergence of Typical Medium Theory in Lower Dimensions

To demonstrate the difference between the fully self-consistent typical medium dynamical cluster approximation (TMDCA) which works well in all dimensions and the variant developed in the initial attempt to develop a cluster mean-field for the localization transitions (that works in lower dimensions), we show in Figs. 6.6 and 6.7, their comparison plots. Figure 6.6 depicts a comparison plot of the two formalisms in one (Left panel) and two (Right panel) dimensions for the evolution

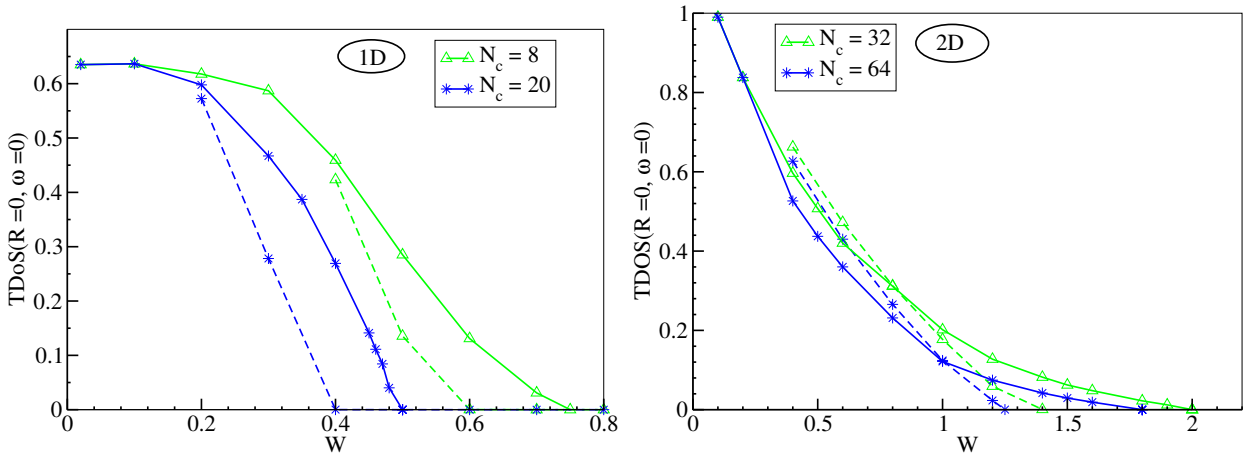

Figure 6.6: A comparison plot of the evolution of the band center of the typical density of states (TDoS($\omega = 0$)) for the TMDCA (dash lines) and the CTMT (solid lines) for the 1 and 2 dimensions. As it is obvious from the plots, the cluster W_c from the TMDCA is far smaller than that from the CTMT.

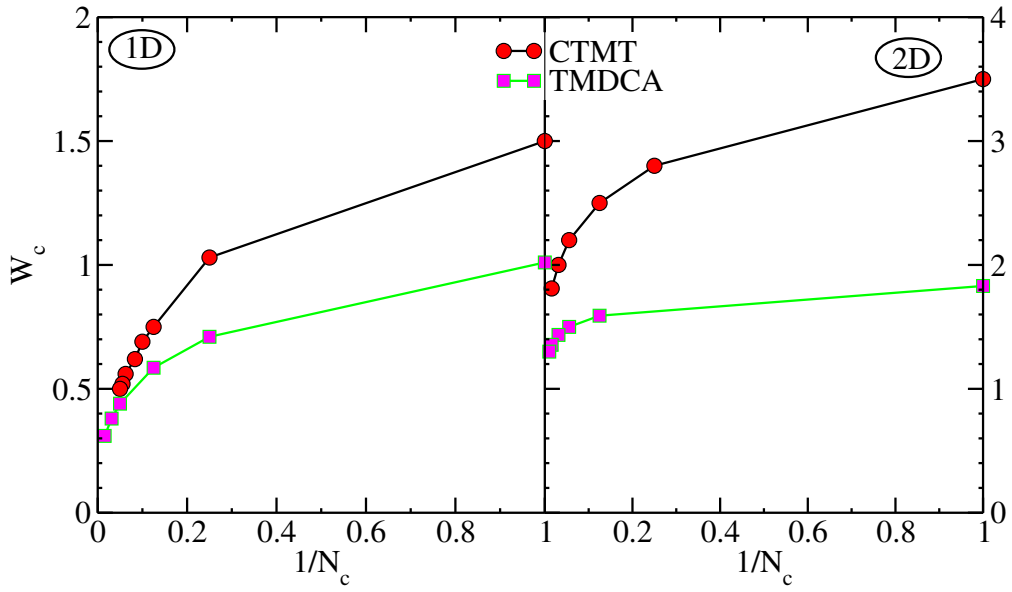

Figure 6.7: A comparison plot of the TMDCA and the CTMT for the critical disorder strength W_c for various cluster sizes N_c in 1 and 2 dimensions. Note the data from the two formalisms fit nicely to an exponential (for 1D) and logarithmic (for 2D) functions, respectively.

of the typical density of states at the band center at increasing disorder strength. As it is obvious from this plot, the TMDCA gives a cluster critical disorder strength (W_c) far smaller than that from the CTMT. Since in both 1 and 2 dimensions, the cluster W_c decreases with N_c, this implies that far smaller cluster size will be needed in the TMDCA to eventually approach the thermodynamic critical disorder strength value which is zero. This becomes more evident in Figure 6.7 where I show a comparison plot of the cluster W_c as a function of $1/N_c$. Even though both fits nicely to an exponential form (for the 1D in the case of the TMDCA, W_c scales linearly with linear cluster size (L_c=N_c): $W_c \sim (1/L_c)^{1/\beta}$ with $1/\beta \sim 0.45 \pm 0.10$ in good agreement with the recent numerical value of $1/\beta = 0.466 \pm 0.095$ [288], single-parameter scaling [4], and the CTMT only differing in the coefficients) and logarithmic form (for the 2D using the TMDCA W_c decreases logarithmically with L_c as $W_c = 1.83 + 0.23 \times \ln(1/L_c)$ in good agreement with the results of MacKinnon *et al.* [247]. This also agrees with the CTMT differing only in their coefficients) (fitting not shown here), the TMDCA clearly goes to zero faster especially in the 2D where the CTMT W_c for say $N_c = 64$ is ~ 1.8 as against only ~ 1.25 for the TMDCA. In 1D, practically zero disorder strength (~ 0.01) is enough to localize all the states for $N_c \gtrsim 100$. In 2D, due to

the logarithmic nature of the decay of the W_c with $1/N_c$, a large cluster is needed to achieve the thermodynamic W_c. Hence, the TMDCA is in better agreement with the single-parameter scaling theory which demonstrates that there is no delocalization phase in one and two-dimensional systems, respectively, for the orthogonal universality class [4], and, therefore, a vanishing static conductivity at zero temperature [290].

6.7 Conclusion

A cluster extension to the local typical medium theory via the dynamical cluster approximation for studying localization in low dimensional disordered electronic systems have been developed. The developed CTMT systematically incorporates non-local corrections to capture quantum coherence. The formalism recovers the local TMT when the cluster size is $N_c = 1$ and becomes exact as $N_c \rightarrow \infty$. As demonstrated, for the proper treatment of the lower dimensional systems, the local part of the typical density of states should be separated and treated explicitly with geometrical averaging. This way, cluster self-averaging which is manifestly more pronounced in three dimensions will be avoided. The typical medium dynamical cluster approximation not only reproduces known characteristics of the lower dimensional systems, for e.g., all states being localized for large system size $N_c \rightarrow \infty$ but opens a new avenue to study localization effects in lower dimensional model systems.

Chapter 7

Application of Typical Medium Dynamical Cluster Approximation to Three-Dimensional Disordered System

This chapter comprises of two recently published papers:

"A Typical Medium Dynamical Cluster Approximation for the Study of Anderson Localization in Three Dimensions", Phys. Rev. B Rapid Commun. **89** *081107 (2014). The list of the authors, as it appears in the manuscript are C. E. Ekuma, H. Terletska, K.-M. Tam, Z.-Y. Meng, J. Moreno, and M. Jarrell.*;

"Finite cluster typical medium theory for disordered electronic systems", (Manuscript in preparation). The list of the authors, as it appears in the manuscript are C. E. Ekuma, C. Moore, H. Terletska, K-M. Tam, J. Moreno, M. Jarrell, and N.S. Vidhyadhiraja.

My role is the development of the model, writing and debugging the code, implementation of the parallel version, running the code to generate the data and writing the manuscript. The numerical exact methods (the exact diagonalization, transfer matrix, and the kernel polynomial methods) which we benchmarked the TMDCA with is developed by my co-authors Conrad Moore and Ka Ming Tam.

7.1 Introduction

Unlike the lower dimensional systems, the non-interacting three-dimensional system intrinsically, exhibits metal-insulator transitions (MIT) at a given critical disorder strength. Over the past several decades, various mean-field models and methods have been developed and/or proposed to characterize the localization transitions in three dimensions (see Chapter 4). The hallmark of these

mean-fields is their inability to properly characterize the Anderson localization in three dimensions. As a consequence of this, a renewed search for new methods to better understand Anderson localization [4, 35] remains an active area of the study of disordered electronic systems [44].

In this chapter, I will present the results from the typical medium dynamical cluster approximation (TMDCA) as applied to the non-interacting Anderson model. To reiterate, the TMDCA is a systematic, self-consistent, causal, and computationally efficient algorithm the properly characterizes the (Anderson) localization transitions not just in three dimensions but in lower (one and two) dimensional systems. By a systematic increment of the cluster size ($N_c \to \infty$), I will demonstrate using various disorder distributions: Box, Gaussian, Lorentzian, and Alloy model (see Eqs 4.2) that the typical density of states (or the hybridization rate) is a proper order parameter for characterizing localization transitions. Furthermore, I will benchmark the TMDCA (which is for a small finite cluster) to the numerically exact methods (which requires the simulation of very large lattice cluster), and show, for instance, that the critical disorder strength obtained from the TMDCA is numerically equivalent to that from the generally more computational expensive exact numerical methods for the various disorder distributions.

To demonstrate the importance of the effective environment for a proper description of the localization transitions, I will show using the DCA its inability to capture localization transitions. Despite the systematic incorporation of spatial correlations in the DCA and such has several advantages over the CPA, it shares the same behavior with the CPA as regards properly, characterizing the localization transition in a disordered electron system. The inability of the DCA to capture Anderson localization transition will be demonstrated using the box disorder distribution.

7.2 Absence of Localization in Dynamical Cluster Approximation

The dynamical cluster approximation (DCA) unlike the coherent potential approximation (CPA) incorporates non-local spatial correlations systematically as the size of the cluster are increased. While spatial correlation is an important ingredient in the localization transition in disordered electron systems, the DCA effective medium is characterized by arithmetic averaging over the

disorder configurations. As explained above and will be demonstrated later, even a typically defined medium without a proper treatment of the typical density of states (the local part of the typical density of states needs to be separated and treated explicitly using geometrical averaging), reduces to the DCA at large cluster. In Figure 7.1 (left panel), we show the ADoS at small and large disorder strengths for the single-site ($N_c = 1$) and finite cluster ($N_c = 64$). We also show in Figure 7.1 (right panel) the probability $P(t) = \left\langle |G(l,l,t)|^2 \right\rangle$ of an electron remaining at a site say l at long time t calculated within the single-site and finite cluster DCA scheme while the insets depict the probability of an electron remaining on site l for all time ($t \to \infty$) $P(t,\eta) = \lim_{t\to\infty} |G(l,l,t)|^2 = \lim_{\eta\to 0} \frac{\eta}{\pi} \int_{-\infty}^{\infty} d\varepsilon \left\langle |G(l,l,\varepsilon+i\eta)|^2 \right\rangle$.

As explained in details in Section 7.3.1, $P(\infty,\eta)$ is expected to be nonzero for any fraction of the localized states in the spectrum of the eigenstates of the disordered system [70, 218, 264, 266].

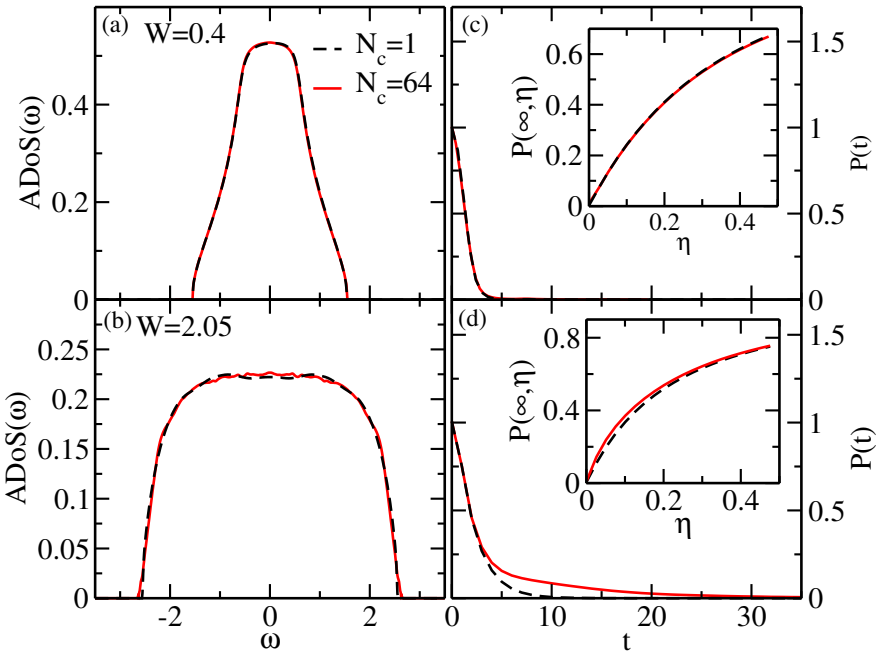

Figure 7.1: Left panel: The average density of states as calculated using the DCA for small and large disorder strength. Right panel: The probability of an electron remaining on site after some time, $P(t) = \left\langle |G(l,l,t)|^2 \right\rangle$. The insets in the plots on the right panel are the probability of an electron remaining on a site l for all time ($t \to \infty$) $P(t,\eta) = \lim_{t\to\infty} |G(l,l,t)|^2 = \lim_{\eta\to 0} \frac{\eta}{\pi} \int_{-\infty}^{\infty} d\varepsilon \left\langle |G(l,l,\varepsilon+i\eta)|^2 \right\rangle$ for the $N_c = 1$ and 64, respectively. The ADoS is not critical at the Anderson transition as manifested in the P(t) since it does still show some finite slope. However, the DCA does show some precursor of Anderson localization as manifested in the P(t) for large disorder strength only for the finite cluster size.

As it is evident from the inset of the right panel of Figure 7.1, which is the plot of $P(\infty,\eta)$ versus η, $P(\infty,\eta)$ extrapolates to zero even very close to the critical disorder strength for both $N_c = 1$ and 64, respectively.

Also observe from Figure 7.1 (left panel), the ADoS is not critical at the Anderson transition. This is manifested in the $P(t)$ plot since for a localized state, the $P(t)$ is expected to be finite. For $N_c = 1$, $P(t)$ falls quickly with time regardless of the disorder strength. However, for the $N_c = 64$, the electrons remain localized for longer times as the disorder strength is increased. This can be understood by noting that each site on the cluster is coupled to a non-interacting translationally invariant host into which electrons can escape. Hence, if a finite density of states exists at some energy, the corresponding states are guaranteed to be extended unless the hybridization rate between the host and the cluster vanishes. Indeed, this is the case in the DCA. The imaginary part of the integrated hybridization (escape) rate ($\int \Im\Gamma(\mathbf{K},\omega)d\mathbf{K}d\omega$) between the cluster and the host as a function of disorder strength W remains constant regardless of the strength of the disorder (cf. inset of Figure 7.4). Thus, the DCA is only able to capture the precursor to Anderson localization. We note that the behavior of the DCA as regards its inability to characterize the Anderson localization transitions is the same in other types of disorder distribution studied here.

7.3 Box Disorder Distribution

The box (uniform) disorder distribution is a generic disorder distribution that is centrally peaked, symmetric with a well-defined mean depicted as in Equation 4.2a. It is a characteristic of many physical phenomena. In this section, I apply the typical medium dynamical cluster approximation to the study of model systems with box disorder distribution.

7.3.1 Evolution of the Density of States for the Box Distribution

To demonstrate that the typical and not the average DoS can serve as a proper order parameter for the Anderson localization transition, we compare the algebraically averaged DoS (ADoS) and TDoS obtained from a single site TMT ($N_c = 1$) and finite clusters TMDCA ($N_c = 64$ and 125) at

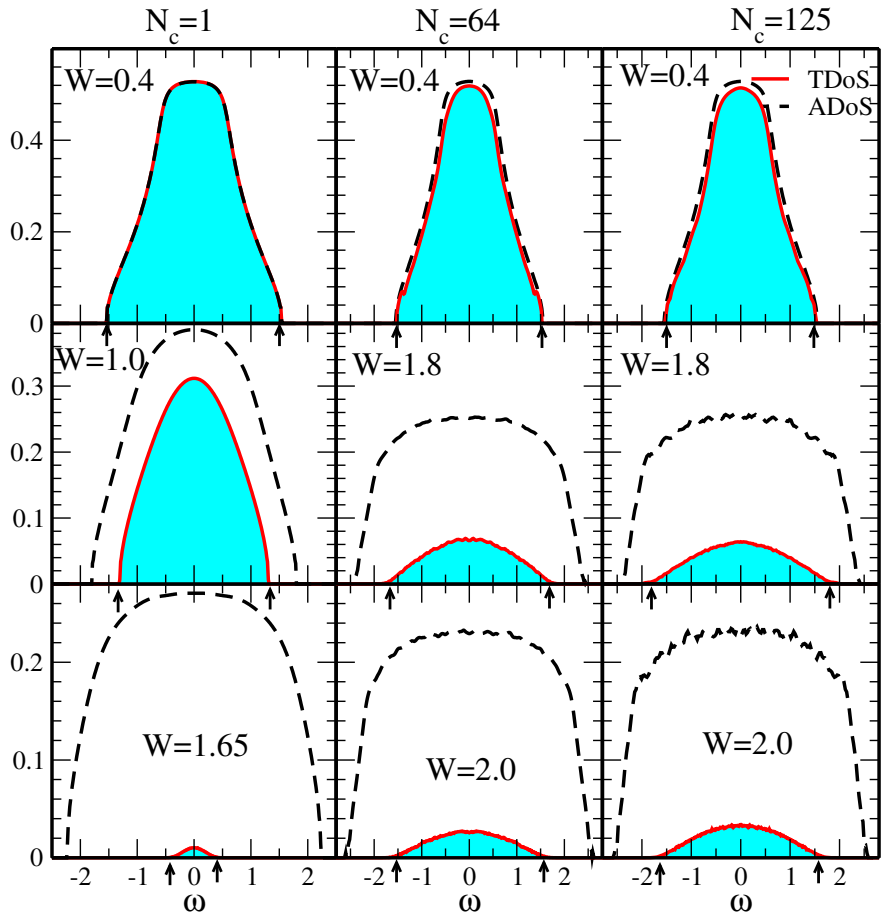

Figure 7.2: The Evolution of ADoS and TDoS at various disorder strength W for single-site TMT and TMDCA with cluster size $N_c = 64$ and 125. At low disorder, where all the states are metallic, the shape of TDoS is the same as that for the ADoS. As W increases, in the case of single-site TMT, the TDoS gets suppressed, the mobility edge also moves towards $\omega = 0$ monotonously. In the case of the TMDCA, the TDoS is also suppressed, but the mobility edge firstly moves to higher energy, only with the further increase of $W > 1.8$, the mobility edge starts moving towards the band center, indicating that TMDCA can successfully capture the reentrance behavior. Arrows indicate the position of the mobility edge, which separates the extended electronic states with localized states and the colored region indicates the area of the TDoS.

various disorder strengths W for the box disorder distribution (4.2a). As shown in Figure 7.2, for both TMT and TMDCA, the ADoS remains finite while the TDoS continually gets suppressed as the critical disorder strength is approached. Hence, the TDoS indeed is justified as a proper order parameter of for characterizing ALT. In addition, at low disorder, $W = 0.4$, for the various N_c, the ADoS and TDoS are practically the same, indicating that the TMDCA formalism at $W \ll W_c$ reduces to the DCA scheme in agreement with the analytical analysis described in Subsection 5.3.2.

Furthermore, one also observes a crucial difference between single site TMT ($N_c = 1$) and

TMDCA finite clusters: $N_c = 64$ and 125. In the former, the mobility edge (for extended states TDoS is finite) defined by the boundary of the TDoS (indicated by arrows) always gets narrower with increasing disorder strength W, while in the latter, as a function of disorder strength, the mobility edge first expands and then decreases, hence giving rise to the re-entrance behavior, which is completely missing in the single-site TMT. Observe also the quick convergence with the clusters size at the $\omega = 0$ for the finite clusters $N_c = 64$ and 125. The implications of this will be discussed further below and explored with respect to what happens to the trajectories of the mobility edge as the size of the cluster increases.

7.3.2 Benchmarking the TMDCA (DCA) with Exact Numerical Methods

One of the key verification of any newly developed formalism is how well it compares with numerically exact methods. To benchmark the TMDCA formalism with a numerical experimental technique, we utilize the kernel polynomial method [245, 275]. We show in Figure 7.3 a plot of the TDoS (ADoS) ($N_c = 64$) calculated using our TMDCA (DCA) method as compared to the

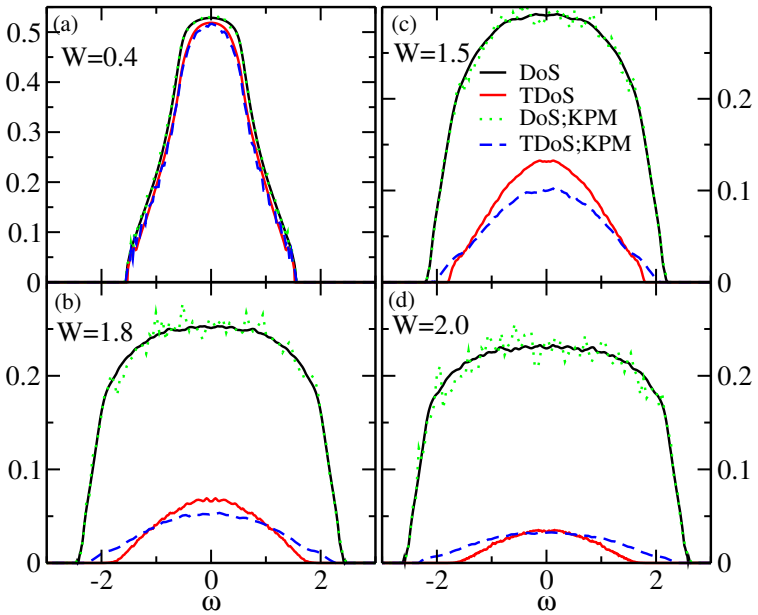

Figure 7.3: The comparison of the average (typical) density of states calculated with the DCA (TMDCA) and the Kernel polynomial method (KPM) for the box disorder at various values of the disorder strength for the cluster size N_c=64. The kernel polynomial method used 4096 moments on a 48^3 cubic lattice, and 1000 independent realizations generated with 32 sites randomly sampled from each realization.

average and typical density of states obtained using the kernel polynomial method [245, 246]. As it is evident from the plots, the agreement between the results from our method and the ones obtained using the kernel polynomial method is remarkable. This good agreement is a manifestation of the ability of our TMDCA formalism [2] to accurately characterize the Anderson localization transitions in systems with uniform disorder distribution even with relatively small system size as compared to the large lattice systems that need to be simulated in the kernel polynomial method for accurate results to be obtained.

7.3.3 Exploring the effects of Finite Cluster on Critical Disorder Strength

Here, we consider the evolution of the critical disorder strength W_c with the cluster size. Figure 7.4 shows the TDoS($\omega = 0$) at the band center as a function of disorder strength W for several cluster sizes: $N_c = 1, 64$, and 125. The critical disorder strength W_c is defined by the vanishing of the TDOS($\omega = 0$). The inset is the imaginary part of the integrated hybridization function which shares the same property as the TDoS since both vanishes at the same disorder strength. Our results show that as N_c increases, the critical disorder strength W_c systematically increases until it converges to the exact value $W_c \approx 2.10$ [131, 142, 242, 247, 270, 271, 275, 286] at cluster size $N_c \geq 12$. The cluster $N_c = 12$ is the first cluster with a complete nearest-neighbor shell based on Betts cluster classification. [291] (cf. Appendix B. From this cluster onward, W_c converges to ≈ 2.10, but the trajectory of the mobility edge continues to change until it also converges to the exact results at larger N_c. This effect is due to the systematic incorporation of coherent backscattering as the cluster size increases and will be elaborated in more detail later. To extract the order parameter critical exponent (β), we fit our data in Figure 7.4 for the largest system size considered here ($N_c = 125$) using the power law: $\text{TDoS}(\omega = 0) = a_0|W - W_c^{fit}|^{\beta}$ following the procedure as explained in Subsection 7.7. We obtain $\beta \sim 1.62 \pm 0.10$ with a corresponding critical disorder strength from the fit of $W_c^{fit} \sim 2.23 \pm 0.10$. The critical parameters from the fit are in good agreement with the recently reported value of $\beta \approx 1.67$ [271]. It is also in general agreement with the values listed in Table 7.2.

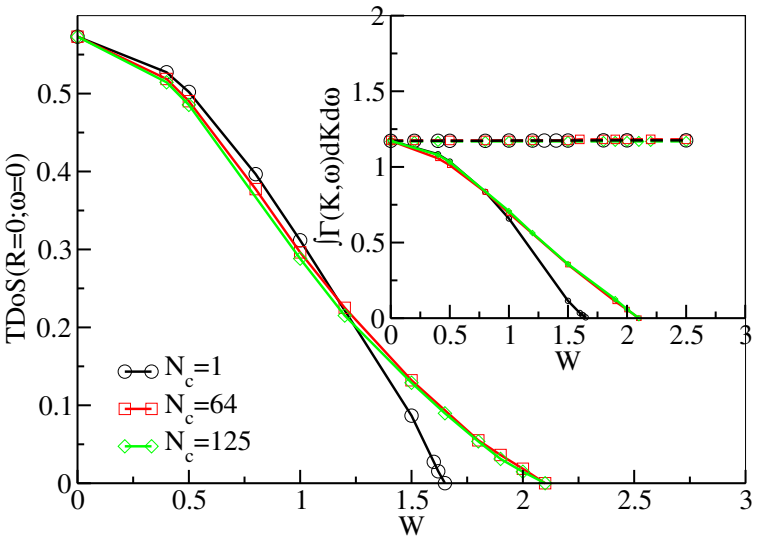

Figure 7.4: The TDoS$(\omega = 0)$ vs disorder strength W at different cluster sizes $N_c = 1, 64$, and 125 for the uniform (box) disorder distribution. The TDoS$(\omega = 0)$ vanishes at the critical disorder strength W_c. At $N_c = 1$, the critical disorder strength $W_c^{N_c=1} \approx 1.65$. As the cluster size increases, the critical strength systematically increases with $W_c^{N_c \gg 12} \approx 2.10 \pm 0.10$, showing a quick convergence with the cluster size. The inset shows the integrated hybridization function $(\int \Gamma(\mathbf{K}, \omega) d\mathbf{K} d\omega)$ as a function of disorder strength W. Observe that $\int \Gamma(\mathbf{K}, \omega) d\mathbf{K} d\omega$ vanishes at the same disorder strength as the TDoS. The dash lines are the $\int \Gamma(\mathbf{K}, \omega) d\mathbf{K} d\omega$ from the DCA. Observe that it is a constant regardless of the disorder strength. This shows that the DCA even though it incorporates spatial correlations do not describe the Anderson localization transitions. Moreover, near the critical region the TDoS$(\omega = 0)$ data can be fitted to the power-law, with TDoS$(\omega = 0) = a_0 |W - W_c|^{\beta}$. Obtained critical exponent for large enough clusters $\beta \approx 1.62 \pm 0.10$ is in good agreement with exact results. Note, the $\int \Gamma(\mathbf{K}, \omega) d\mathbf{K} d\omega$ data for $N_c = 64$ and 125 has been normalized with that of $N_c = 1$.

7.3.4 Characterizing Localization with Return Probability

Aside from the typical density of states, the localization transition in the gapless single-particle excitations of the Anderson insulator can be studied using the return probability of an electron to a site [70]. The probability of quantum diffusion (or the return probability) describes the probability of a quantum particle (or a wave) to go from site l to l' in a time t. After disorder averaging, the return probability has basically three key contributions: a) the probability of going from site l to l' without any scattering, b) the probability of going from site l to l' by an incoherent sequence of multiple scattering (known as diffusion) and c) the probability to go from site l to l' via a coherent (or enhanced) multiple scattering processes (for e.g., the *cooperon*).

To show this, we measure the probability of an electron remaining on a site say l for all time

$(t \to \infty)$ $P(t,\eta) = \lim_{t\to\infty} |G(l,l,t)|^2 = \lim_{\eta\to 0} \frac{\eta}{\pi} \int_{-\infty}^{\infty} d\varepsilon \left\langle |G(l,l,\varepsilon+i\eta)|^2 \right\rangle$. For any thermodynamically significant fraction of the localized states in the eigenstates of the disordered spectrum, $P(\infty,\eta)$ is expected to be nonzero [70, 218, 264, 266]. Since the cluster is formed by coarse-graining the real lattice problem in **K**-space, there is a one-to-one correspondence between local quantities on the cluster and real space [264]. In Fig 7.5 right panel, we show the $P(\infty,\eta)$ for the cluster sizes $N_c = 1$ and 64 for various disorder strengths. As it is evident from the plot, for relatively small disorder strength $W \sim 0.5$, $P(\infty,\eta)$ extrapolates to zero and gradually becomes nonzero as the localization transition is approached. Just like the $P(\infty,\eta)$, the finite time probability that an electron on a site l remains after some time t denoted as: $P(t) = \left\langle |G(l,l,t)|^2 \right\rangle$ is a vital parameter for detecting the localization of electrons. As shown in Fig 7.5 for $N_c = 1$ and 64 clusters, $P(\infty,\eta)$ and $P(t)$ contains

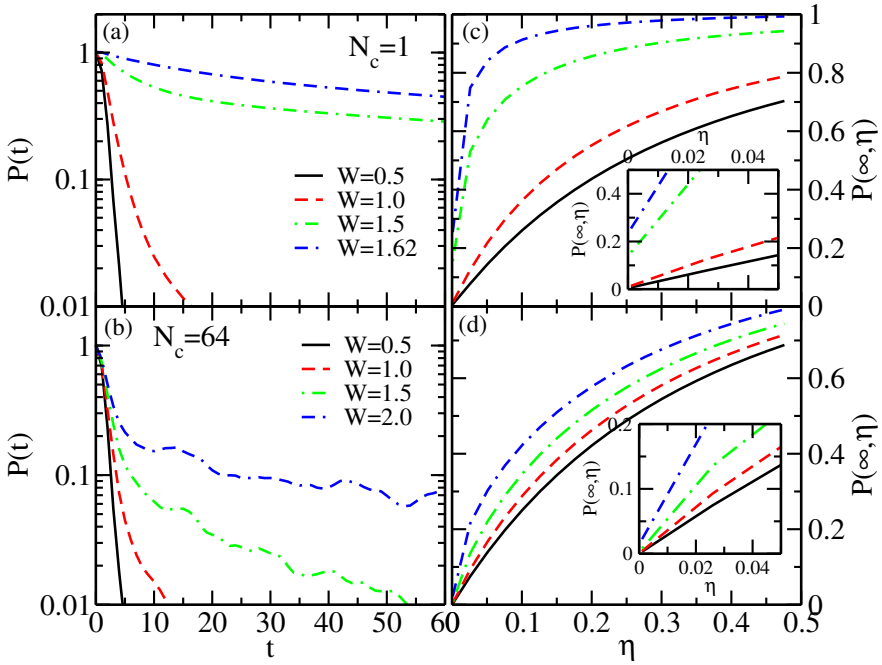

Figure 7.5: Right panels: The probability that an electron remains localized at all times $P(\infty,\eta \to 0)$ for Anderson model for $N_c = 1$ and 64 for varying disorder strengths on a semi-log plot. We used the fact that $P(t,\eta) = \lim_{\eta\to 0} P(\infty,\eta) = \lim_{\eta\to 0} \frac{-2i\eta}{N_c} \sum_l \int_{-\infty}^{\infty} d\omega d\omega' \left\langle \frac{\bar{A}(l,\omega)\bar{A}(l,\omega)}{\omega-\omega'-2i\eta} \right\rangle$, where $\bar{A}(l,\omega) = -1/\pi \Im \bar{G}(l,l,\omega)$ is the local coarse-grained (but not disorder averaged) spectra function. As $\eta \to 0$, $P(\infty,\eta)$ extrapolates to zero for small disorder strength indicating metallic behavior but does not extrapolate to zero anymore as the disorder strength is systematically increased towards the critical disorder strength leading to the transition (see the inset where this is manifestly shown). Left panels: The probability of an electron on site l remaining trapped at finite time t for $N_c = 1$ and 64 for the same parameter as $P(\infty,\eta)$.

the same information of the excitation spectra. Hence, a characteristic finite long time $P(t)$ denote localized eigenstates. In Fig 7.5 left panel, we show the $P(t)$ for the same parameters as $P(\infty,\eta)$. Again, systematic transition from a metallic regime (for small disorder) to an insulating regime (for disorder strengths close to the critical value of Anderson localization transitions in $N_c = 1$ and 64 size clusters, respectively) is observed. Unlike the DCA, the localization transition manifests clearly in the $P(\infty,\eta)$ and $P(t)$ calculated in the TMDCA since even though the density of states (ADoS) calculated within the TMDCA is finite as in the DCA (the ADoS is a conserving quantity), the hybridization rate at the same energy depends highly on the strength of the disorder (c.f. inset of Figure 7.4). In fact, it vanishes continuously with the disorder strength and goes to zero at the same point where the typical density of states also vanishes. Hence, since the hybridization rate between the cluster and the host vanishes continuously as the critical disorder strength is approached, TMDCA approach is able to capture the localization transition even when the ADoS calculated with the TMDCA is finite for the reason explained above.

7.3.5 Characterizing Localization with Probability Distribution

The probability distribution function (PDF) is another natural quantity to characterize the Anderson localization transition due to the fact that the "typical" value of a "random" variable corresponds to the most probable value of the PDF. [1, 142] Since, for a proper description of electron localization in disordered systems, one should focus on the distribution functions of the quantities of interest [35], we calculate the PDF of the cluster-momentum-resolved DoS $\rho(K,\omega=\bar{\varepsilon}_K)$ (at different momenta cells K and energy $\omega=\bar{\varepsilon}_K$) sampled over a large number of disorder configurations.

In Figure 7.6, we show the evolution of the PDF[$\rho(\mathbf{K},\omega=\bar{\varepsilon}_{\mathbf{K}})$] with W. As it is evident from the plot, for a relatively small disorder, the cells show the Gaussian distribution and gradually become log-normal (highly skewed) as the critical disorder strength is approached.

The statistical analysis of the spectra properties of the Anderson model [65, 275, 292] show that for relatively small disorder strength, the states are still delocalized and the amplitude of the wave functions associated with them are more or less the same on every site, and the distribution of the local DoS with respect to disorder configurations are Gaussian with the most probable

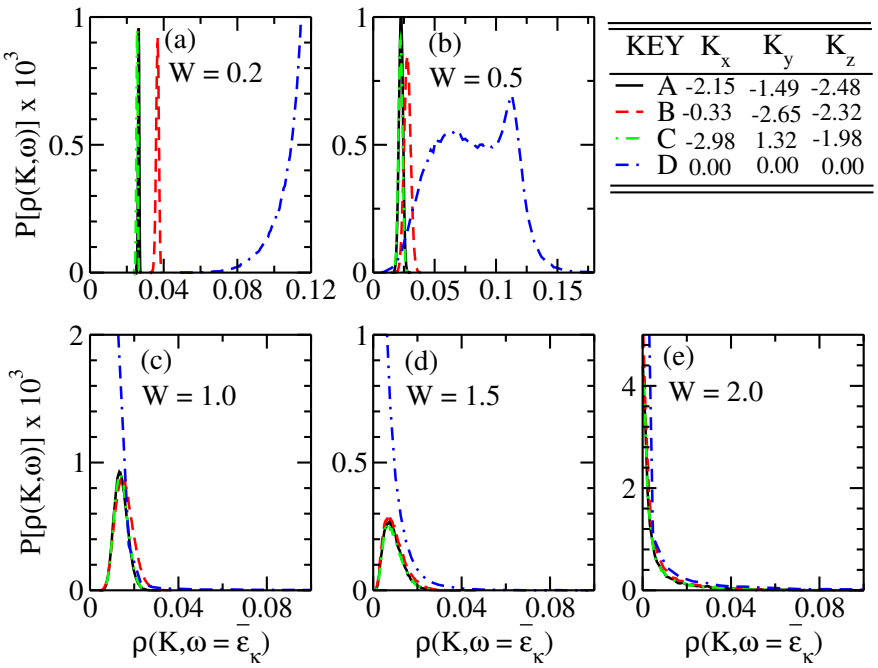

Figure 7.6: The evolution of the probability distribution of the density of states at different cluster cells with an increase of disorder strength for N_c = 38. Utilizing the irreducible wedge property and particle-hole symmetry, the original 38 cells is reduced to 4 cells. For small disorder strength, the cells show Gaussian distribution and close to the critical disorder strength $\simeq$ 2.0, all the cells show log-normal distribution.

value coinciding with the arithmetic mean (average) value. However, for sufficiently large disorder strength or in the proximity of the band tails, the spectrum consist mainly of discrete eigenvalues, and the associated eigenfunctions are exponentially localized with only substantial weight only on a few sites. The distribution is therefore extremely asymmetric (log-normal form), with a most probable value much smaller than the arithmetic mean value. At this point, most of the weight is concentrated around zero. As it is evident from Figure 7.6, we indeed observe such behavior in our results.

7.3.6 The Phase Diagram for Anderson Model

The phase diagram in the disorder-energy (W-ω) plane for the 3D is one of the most important tools for characterizing the Anderson localization transition. We show in Figure 7.7, the phase diagram of the Anderson localization transitions in the (W-ω) plane constructed from our TMDCA procedure for the box disorder distribution. Here, we show the mobility edge trajectories given

by the frequencies where the TDoS vanishes at a given disorder strength W and the band edge determined by the vanishing of the ADoS calculated within the DCA which defines the Lifshitz boundaries.

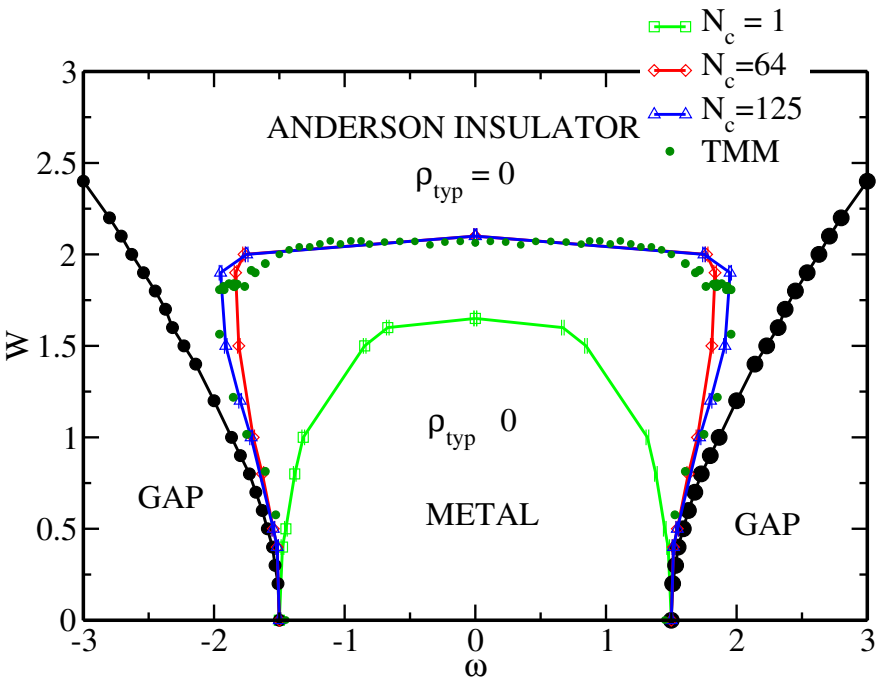

Figure 7.7: The phase diagram of the Anderson localization transition in 3D for the box disorder distribution obtained from TMDCA simulations. A systematic improvement of the trajectories of the mobility edge are achieved as the cluster size increases. At large enough N_c and within computation error, our results converge to those determined by the transfer matrix method (TMM) [242]. The TMM data includes both system sizes of length $L = 8 \times 10^4$ and $L = 5 \times 10^5$. The range of system widths used is $M = [8, 16]$ and reorthogonalization is done every 5 transfer matrix multiplications. The black line with filled circles denote the Lifshitz boundaries.

As it is evident from Figure 7.7, at $N_c = 64$ the W_c at $\omega = 0$ is the same as that for $N_c = 125$ but different from the $N_c = 1$ case. This shows that the W_c converges to ~ 2.10, while, the trajectory of the mobility edge continues to change with N_c. This may be understood from the different localization mechanisms for states at the band center and the edge [242, 248, 293]. Hence, at large enough clusters, we are able to converge to the exact result. In particular, as the cluster size N_c increases, the mobility edge trajectories are systematically reproduced, with re-entrance behavior gradually captured with the cluster size. As we increase the cluster size the DoS acquires systematically states in the band tails, which are zero in the N_c=1 case (it is well-known that single-site theories like CPA or TMT don't capture such states). According to Bulka *et al.* [242,

272] such deep trapped states dictate the physics at large energies. Hence, by making $N_c > 1$ we systematically inject additional states that tend to push the localization edge outward. States at the band center become localized mainly due to coherent backscattering while those above and below the bare band edges are initially localized in deeply trapped states. They become delocalized with increasing W due to the increasing DoS and hence increasing quantum tunneling between the deeply trapped states. They finally become localized again with increasing disorder, which explains the re-entrant behavior. Since coherent backscattering requires a retracing of the electronic path, the effective length scales captured by the cluster are doubled, such that W_c converges very quickly at the band center. On the other hand, the quantum tunneling mechanism has no path doubling and requires multiple deeply trapped states in the cluster and, therefore, converges more slowly with N_c.

7.3.7 Energy Selective Localization

We show in Figure 7.8, the scaling of the imaginary part of the typical hybridization function

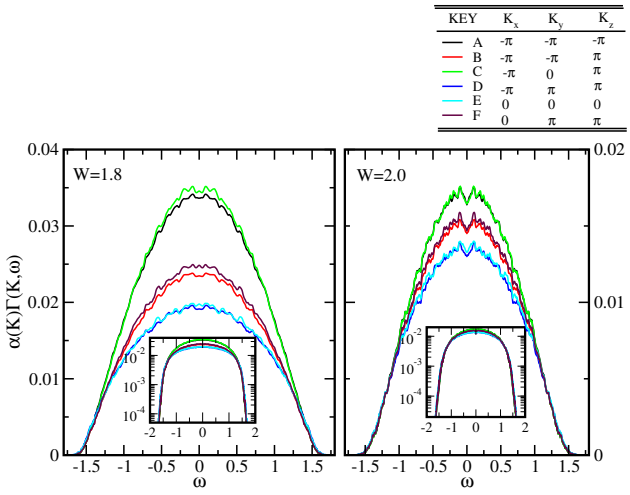

Figure 7.8: The scaling of the imaginary typical hybridization function ($\Im\Gamma(\mathbf{K},\omega)$) for 64 site cluster at disorder strengths of W = 1.8 and 2.0, respectively. The labels A–F and their associated momenta $\mathbf{K}$ correspond to each of the six distinct cells obtained using the point-group and particle-hole symmetry ($\rho(\mathbf{K},\omega) = \rho(\mathbf{Q}-\mathbf{K},-\omega)$, with $\mathbf{Q} = (\pi,\pi,\pi)$) of the cluster. Observe that the mobility edge collapses on top of each other by multiplying each of the momenta of the hybridization function with a constant such that $\Im\Gamma(\mathbf{K},\omega = \alpha(\mathbf{K})\Im\Gamma(\mathbf{K},\omega)$, where $\alpha(\mathbf{K})$ is a scaling constant, in agreement with Mott's idea of energy selective Anderson localization transitions. The insets are on a semi-log plot showing clearly that the various $\mathbf{K}$-values of $\Im\Gamma(\mathbf{K},\omega)$ are on top of each other.

($\Im\Gamma(\mathbf{K},\omega)$) for the finite cluster size of 64 at $W = 1.8$ and 2.0, respectively. The $\Im\Gamma(\mathbf{K},\omega)$ measures the escape rate of between the cluster and the host as a function of the disorder strength W. Even though different $\mathbf{K}$-cells goes to zero at different rates, they each share the same unique mobility edge. Due to the scattering from each $\mathbf{K}-$point on the cluster sites, at any energy, there will be mixing of the localized and the extended states. Since the localized and extended states cannot co-exist at the same energy, then mobility edge exists at the point where all the states in tails of the cluster sites are localized. As shown in Figure 7.8, the collapse of the tails for all $\mathbf{K}$ such that $\Im\Gamma(\mathbf{K},\omega = \alpha(\mathbf{K})\Im\Gamma(\mathbf{K},\omega)$, where $\alpha(\mathbf{K})$ is a scaling constant, essentially validates Mott's idea of energy selective Anderson localization. [39, 116]

7.4 Alloy Model

The application of the tight-binding Hamiltonian (4.1) to the study of alloy systems represent one of the most studied physical systems. This stems from the fact that the two potentials (energies) W_a and W_b depict in a natural way, the potential landscape of a binary alloy $A_{c_a}B_{1-c_a}$, with each of the sites occupied either by atom "A" or "B" of concentrations c_a and c_b (1-c_a) systems, respectively. In this section, I will present the results for a binary alloy method as obtained using the TMDCA, DCA, and their benchmark with exact numerical methods.

7.4.1 Benchmarking the TMDCA (DCA) for the Alloy Model

To explore the applicability of our method to the study of binary alloy systems, we show in Figure 7.9, the calculated typical (average) density of states from our TMDCA(DCA) procedure as compared to the TDoS(ADoS) calculated within the KPM results [106, 246, 250, 251] for various concentrations and disorder strengths. As it is evident from the plot, the importance of the TDoS is manifestly shown since for all the disorder strengths (small and large) and for varying concentrations, the ADoS remains finite around the two energies W_a and W_b, respectively, while the TDoS at a fixed concentration vanishes continuously with the strength of the disorder with smaller magnitude on the sub-band with the lowest concentration. Fixing the strength of the disorder and varying

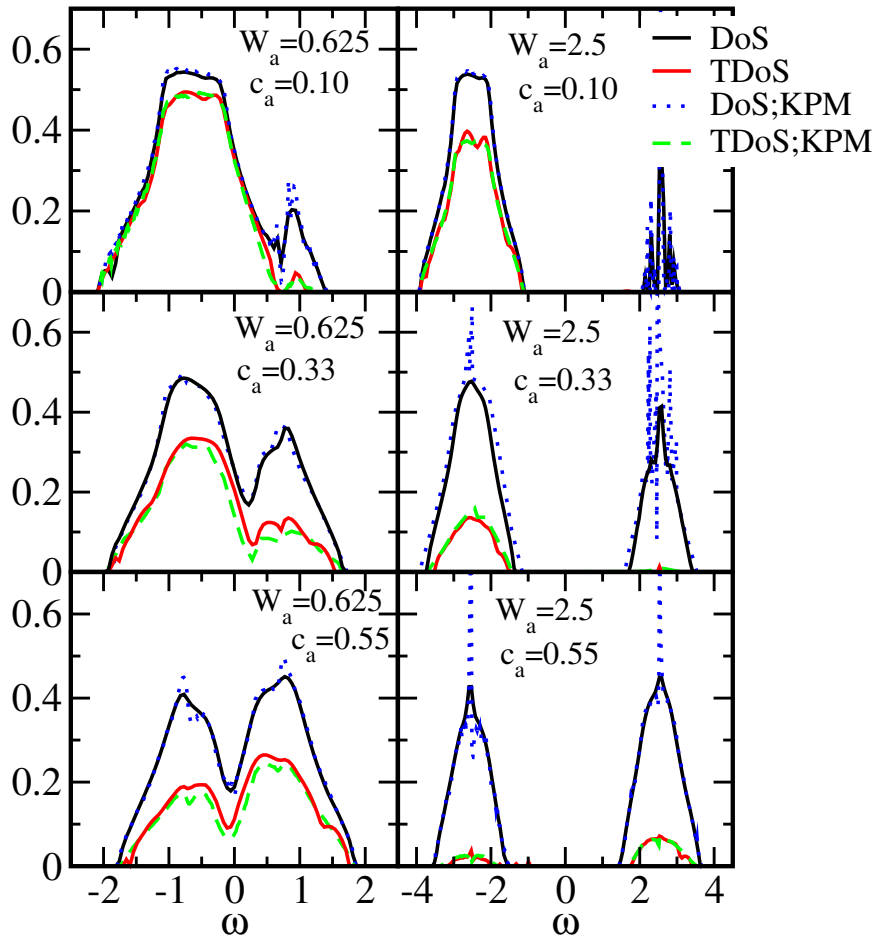

Figure 7.9: The comparison of the average (typical) density of states calculated with the DCA (TMDCA) and the Kernel polynomial method (KPM) for the diagonal disorder at various values of the local potential W_a and concentrations c_a for the cluster size N_c=125. The kernel polynomial method used 2048 moments on a 48^3 cubic lattice, and 200 independent realizations generated with 32 sites randomly sampled for each realization.

the concentration, the sub-bands with the smallest concentration have fewer states. We note that there are subtle differences between the results for $N_c = 64$ (finite cluster) and single site $N_c = 1$ (CPA) (not shown) due to the incorporation of spatial correlations in the finite cluster, which is missing in the local CPA. In fact, the TMT underestimates the extended region and misses small but important non-local features in the spectra [3].

To further benchmark our results for the binary alloy model, we show in Figure 7.9, a comparison of the average (typical) DoS calculated with the (DCA) TMDCA ($N_c = 64$) as compared with the kernel polynomial method (KPM) [245, 246]. As can be seen from the plots, our TMDCA and DCA results reproduced those from the KPM nicely showing that our formalism offers a systematic

way of studying the Anderson localization transition in binary alloy systems. Such a remarkable agreement is an indication of a successful benchmarking of the TMDCA method [2].

7.4.2 Phase Diagram in $W-\omega$ plane for the Alloy Model at $c_a = 0.5$

The mobility edges shown in Figure 7.10 were extracted from the TDoS, with the boundaries defined by the energy where the TDoS vanishes. As can be seen in Figure 7.10, the local $N_c = 1$ boundaries are narrower than those obtained for finite cluster indicating that the TMT strongly underestimates the extended state regime. The comparison of the mobility edge boundaries for the TMDCA with those obtained from the TMM calculations show quite good agreement. This again is a confirmation of a successful benchmarking of the TMDCA for treating the binary alloy model. At the center of the band and for the $c_a = 0.5$, we obtain a critical disorder strength W_c of ≈ 0.7 for the TMDCA in good agreement with the transfer-matrix method (cf. Figure 7.10).

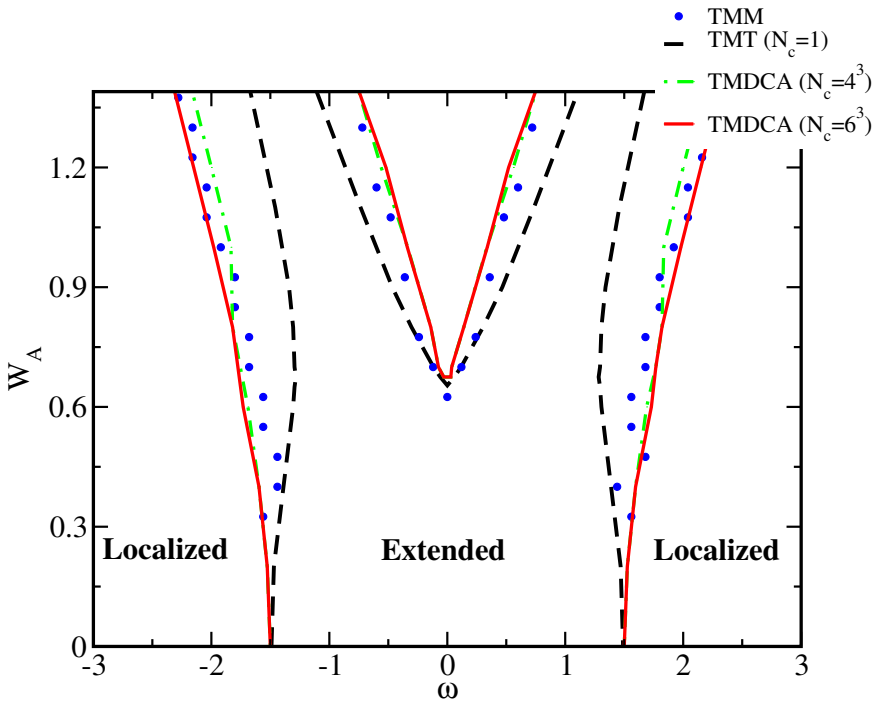

Figure 7.10: Disorder-energy (W_a-ω) phase diagram of the binary alloy system $A_{c_a}B_{1-c_a}$ for c_a = 0.5 of the Anderson localization transition in 3D. Observe the systematic improvement of the trajectories of the phase diagram for the clusters ($N_c = 125$ and 216) in basic agreement with the numerical experiment results from transfer-matrix-method (TMM).

7.5 Gaussian Disorder Distribution

The Gaussian (or normal) distribution (4.2b) is a unique distribution upon, which other disorder distributions are built and has had many physical applications including the study of molecular-doped polymers [294, 295].

7.5.1 Benchmarking the TMDCA (DCA) for the Gaussian Distribution

To further explore the versatility of our developed method, we apply it to study disordered systems with the strength of the disorder defined by the Gaussian distribution function (4.2b). Again, we use the typical density of states (TDoS) as the order parameter and the transition to the Anderson insulator is obtained at the disorder strength where the TDoS vanishes. The typical (average) density of states with those obtained from the kernel polynomial method are shown in Figure 7.11 for various values of the disorder strength. As can be seen from Figure 7.11, the TDoS at all

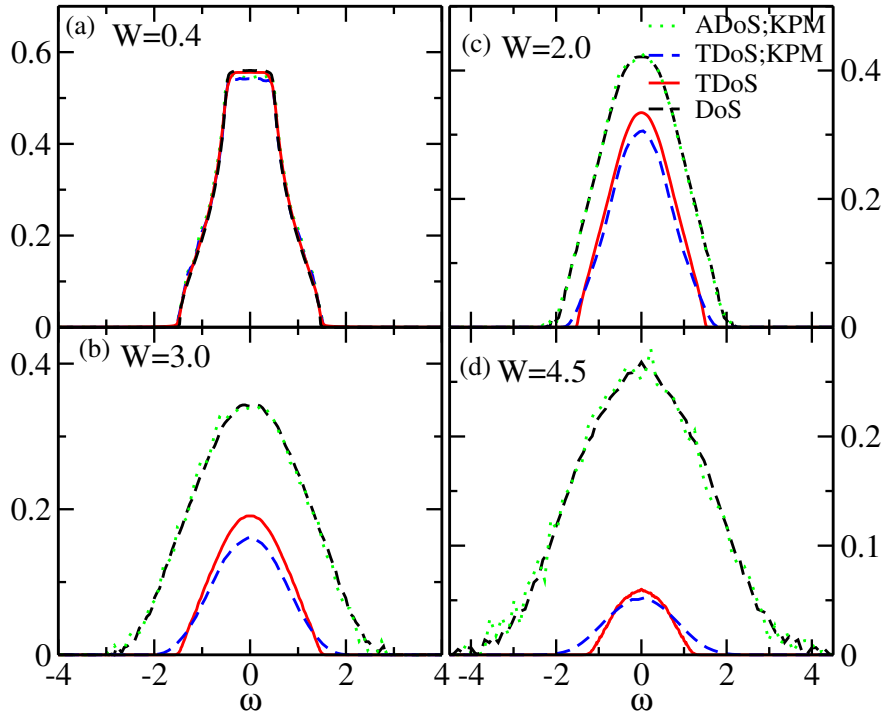

Figure 7.11: The comparison of the average (typical) density of states calculated with the DCA (TMDCA) and the Kernel polynomial method (KPM) for the Gaussian disorder at various values of the disorder strength for the cluster size N_c=64. The kernel polynomial method used 4096 moments on a 48^3 cubic lattice, and 1000 independent realizations generated with 32 sites randomly sampled from each realization.

frequencies, systematically goes to zero as the disorder strength increases while the ADoS remains finite. Again, our TMDCA formalism reproduces accurately the numerically exact results from the kernel polynomial method. We note some subtle differences between the TDoS calculated from the TMDCA and the KPM (observe that there are no noticeable differences in the average density of states from the DCA and KPM). This may be due to the effects of the broadening parameter utilized in the KPM, which contributes additional tails to the already exponential tails of the TDoS. We remark that aside the small initial broadening value ~ -0.01 used in the initialization of the TMDCA at the very first iteration, no broadening parameter is utilized.

7.5.2 Evolution of the Density of States for the Gaussian Distribution

We show in Figure 7.12, the evolution of the band center of the typical density of states (TDoS($\omega = 0$) as a function of disorder strength for the local TMT ($N_c = 1$) and the TMDCA ($N_c = 64$ and 125). This will assist to explore how the critical disorder strength W_c evolves with the system size. As can be seen from Figure 7.12, our results indicate that the critical disorder strength (defined as the W where the TDoS vanishes) systematically increases as the cluster size is increased converging to $W_c \sim 5.30$ as soon as the size of the cluster $N_c \geq 12$ in good agreement with the numerical exact value of 5.225±0.125 [272–274] and 5.32, [131] respectively. Fitting our data for the largest system size considered here ($N_c = 125$) using the power law: $\text{TDoS}(\omega = 0) = a_0|W - W_c^{fit}|^{\beta}$ following the procedure as explained in Sub-section 7.7, we obtain the order parameter critical exponent $\beta \sim 1.57 \pm 0.10$ with a corresponding critical disorder strength from the fit of $W_c^{fit} \sim 5.53 \pm 0.10$. The obtained β from our fit is in good agreement with the value we obtained for the uniform disorder distribution (c.f. Table 7.1) and in good agreement with the recently reported value of $\beta \approx 1.67$. [271] It is also in general agreement with the values listed in Table 7.2. The good agreement between the β we obtained from the uniform and Gaussian disorder distribution is a manifestation of the universal nature of the Anderson localization transition [274, 296].

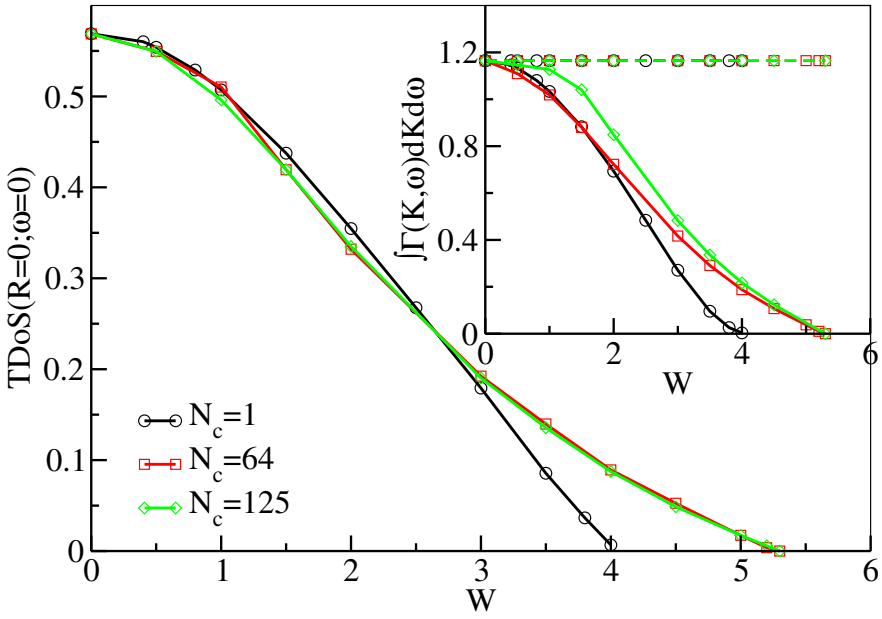

Figure 7.12: The TDoS($\omega = 0$) vs disorder strength W at different cluster sizes $N_c = 1, 64$, and 125 for the Gaussian disorder distribution. The TDoS($\omega = 0$) vanishes at the critical disorder strength W_c. At $N_c = 1$, the critical disorder strength $W_c^{N_c=1} \approx 4.0$. As the cluster size increases, the critical strength systematically increases with $W_c^{N_c \gg 12} \approx 5.30 \pm 0.10$, showing a quick convergence with the cluster size. The inset shows the integrated hybridization function ($\int \Gamma(\mathbf{K}, \omega) d\mathbf{K} d\omega$) as a function of disorder strength W. Observe that $\int \Gamma(\mathbf{K}, \omega) d\mathbf{K} d\omega$ vanishes at the same disorder strength as the TDoS. The dash lines are the $\int \Gamma(\mathbf{K}, \omega) d\mathbf{K} d\omega$ from the DCA. Observe that it is a constant regardless of the disorder strength. This shows that the DCA, even though it incorporates spatial correlations does not describe the Anderson localization transitions. Moreover, near the critical region the TDoS($\omega = 0$) data can be fitted to the power-law, with TDOS($\omega = 0$) $= a_0 |W - W_c|^{\beta}$. Obtained critical exponent for large enough clusters $\beta \approx 1.57 \pm 0.10$ is in good agreement with the numerical exact results [271]. Note, the $\int \Gamma(\mathbf{K}, \omega) d\mathbf{K} d\omega$ data for $N_c = 64$ and 125 has been normalized with that of $N_c = 1$.

7.5.3 Phase Diagram in $W - \omega$ plane for the Gaussian Distribution

To explore the trajectories of the mobility edge for Gaussian disorder distribution, we show in Figure 7.13 the phase diagram in the energy-disorder plane for various cluster sizes as compared to the TMM result. [272] For any given disorder strength W, the mobility edge is defined by the frequency where the TDoS vanishes. Unlike the critical disorder strength, which converges quickly with the cluster size $N_c \geq 12$, the trajectory of the mobility edge continues to change with N_c converging to almost the numerically exact results for $N_c = 125$. The physical reason for the quick convergence of W_c and the progressive change of the mobility edge with the cluster sizes are the same as that described above for the box disorder distribution (c.f. Section 7.3.1). As can be

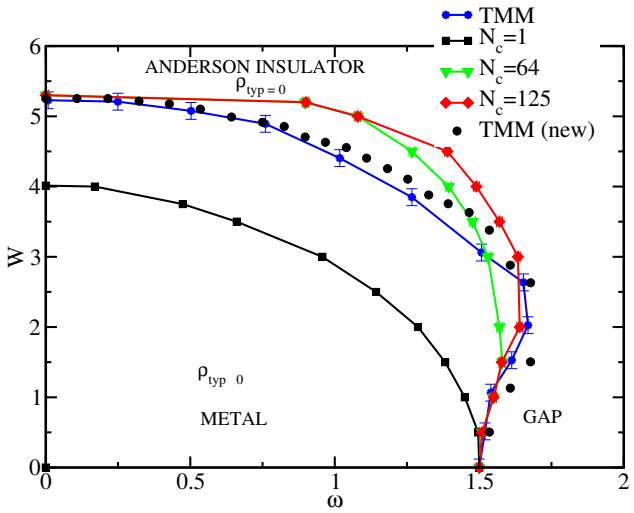

Figure 7.13: The phase diagram of the Anderson transition in 3D for the Gaussian disorder distribution obtained from TMDCA simulations. A systematic improvement of the trajectories of the mobility edge is achieved as the cluster size increases. At large enough N_c, our results converge to those determined by the TMM, which were calculated for widths $M = [2, 16]$ and for a system length of 1×10^6 and the matrix products are reorthogonalized every 5 transfer matrix multiplications. The deviation between the TMDCA and TMM results is consistent with the behavior as seen for box and Lorentzian disorder and can be attributed to the fact that a finite grid in energy is used for the TMDCA, which tends to cause the typical density of states to be larger, hence slightly overemphasizing the metallic behavior and as such, the mobility edge is slightly larger when compared to TMM in certain frequency ranges near the band edge. The effect is most pronounced here due to the small density of states near the band edge. In addition, near the reentrance regime, the TMM also has difficulty due to more difficulty in the finite size behavior (see Appendix C).

seen, the single site TMT underestimates the extended region just as in the previously presented disorder distributions. There are, however, some subtle differences between our data and the TMM data around the re-entrance regime. The cause of this difference will be discussed in Section 7.8.

7.6 Lorentzian Distribution

The Lorentzian (or Cauchy) distribution is a simple family of distributions with expected value (and other moments), which invariably, do no exist. To check the versatility of the TMDCA, I utilize it to study this generic disorder configuration.

7.6.1 Evolution of the band Center of the TDoS for Lorentzian Distribution

We next apply the TMDCA formalism to study systems with Lorentzian (or Cauchy) disorder distribution (cf. Equation 4.2c). We show in Figure 7.14, how the band center of the typical density of states (TDoS($\omega = 0$)) changes as the disorder strength is increased for the local TMT ($N_c = 1$) and the TMDCA ($N_c = 64$ and 125). As can be seen from Figure 7.14, our results depict that the critical disorder strength systematically increases as the cluster size increases converging to $W_c \sim 0.94$ for $N_c \geq 12$ in good agreement with the numerical exact value of 0.95±0.125 [272–274] and 1.07 [131], respectively. Fitting our data for the largest system size considered here ($N_c = 125$) using the power law: $\text{TDoS}(\omega = 0) = a_0|W - W_c^{fit}|^{\beta}$ (see Subsection 7.7 for the description of how the β is extracted), we can extract the order parameter critical exponent $\beta \sim 1.60 \pm 0.10$ with a corresponding critical disorder strength from the fit, $W_c^{fit} \sim 0.97 \pm 0.10$. The obtained β from our fit is in good agreement with the values listed in Table 7.2 and in good agreement with the

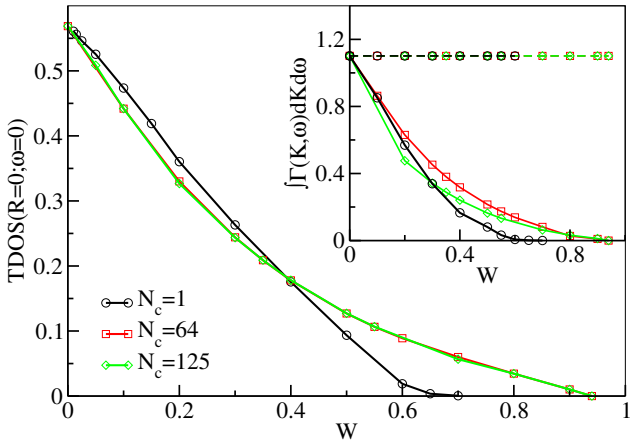

Figure 7.14: The $\text{TDoS}(\omega = 0)$ vs disorder strength W at different cluster sizes $N_c = 1, 64$, and 125 for the Lorentzian disorder distribution. The $\text{TDoS}(\omega = 0)$ vanishes at the critical disorder strength W_c. At $N_c = 1$, the critical disorder strength $W_c^{N_c=1} \approx 0.6$. As the cluster size increases, the critical strength systematically increases with $W_c^{N_c \gg 12} \approx 0.94 \pm 0.10$, showing a quick convergence with the cluster size. The inset shows the integrated hybridization function ($\int \Gamma(\mathbf{K}, \omega) d\mathbf{K} d\omega$) as a function of disorder strength W. Observe that $\int \Gamma(\mathbf{K}, \omega) d\mathbf{K} d\omega$ vanishes at the same disorder strength as the TDoS. The dash lines are the $\int \Gamma(\mathbf{K}, \omega) d\mathbf{K} d\omega$ from the DCA. Observe that it is a constant regardless of the disorder strength in agreement with the observations we had for other disorder distributions. We can fit the $\text{TDoS}(\omega = 0)$ data near the critical region to the power-law, with $\text{TDoS}(\omega = 0) = a_0|W - W_c|^{\beta}$. Obtained critical exponent for large enough clusters $\beta \approx 1.60 \pm 0.10$ is in good agreement with the numerical exact results [271]. Note, the $\int \Gamma(\mathbf{K}, \omega) d\mathbf{K} d\omega$ data for $N_c = 64$ and 125 has been normalized with that of $N_c = 1$.

recently reported value of $\beta \approx 1.67$ [271]. Again, the obtained β value of the Lorentzian disorder distribution is in good agreement with the values obtained for the box and Gaussian disorder distributions, respectively. This further illustrates the universal nature of the Anderson localization transitions. [274, 296]

7.6.2 Phase Diagram in $W - \omega$ plane for the Lorentzian Distribution

We conclude our study of the applications of the typical medium dynamical cluster approximation to the Lorentzian disorder distribution by presenting in Figure 7.15 the phase diagram in the energy-disorder plane. Unlike the box and Gaussian disorder distributions, our simulations show that the Lorentzian distribution does not have re-entrance of the mobility edge. The lack of re-entrance of the mobility edge in the Lorentzian disorder distribution may be attributed to the absence of finite variance in this form of distribution. For the single site CPA ($N_c = 1$) the critical parameters are woefully underestimated. However, we systematically converge to the numerical exact results as the size of the cluster is increased. As it is obvious from Figure 7.15, for as small as $N_c = 64$, we converge almost to the exact results of Bulka *et al.* [242]. We again see a remarkable good agreement between our effective mean-field method for the Anderson localization transitions and the numerical exact calculations.

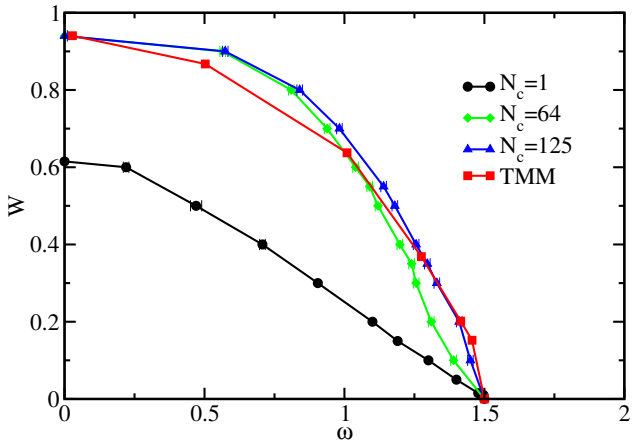

Figure 7.15: The phase diagram of the Anderson localization transition in 3D for the Lorentzian disorder distribution obtained from TMDCA simulations. A systematic improvement of the trajectories of the mobility edge is achieved as the cluster size increases. At large enough N_c and within computation error, our results converge to those determined by the transfer-matrix method [242].

7.7 Critical Parameters

The critical parameters, including the critical disorder strength W_c and the order parameter critical exponent β are reported in Table 7.1 for different cluster sizes using the box disorder distribution as a case study. W_c was determined as the W where the TDoS $(\omega = 0)$ vanishes. Observe that as N_c increases, W_c systematically increases with $W_c \approx 2.10 \pm 0.01$, with a quick convergence with N_c.

Table 7.1: The calculated and fitted critical disorder strength W_c^{cal} and W_c^{fit} and the order parameter critical exponent β obtained from our fit for the box disorder distribution. W_c is defined by the vanishing of the TDoS $(\omega = 0)$. β is obtained by fitting the TDoS$(\omega = 0)$ data with a power law, TDoS$(\omega = 0) = a_0|W - W_c^{fit}|^{\beta}$.

N_c	W_c^{cal}	W_c^{fit}	β
1	1.66±0.01	1.65±0.10	0.96±0.10
64	2.10±0.01	2.18±0.10	1.46±0.10
125	2.10±0.01	2.23±0.10	1.62±0.10

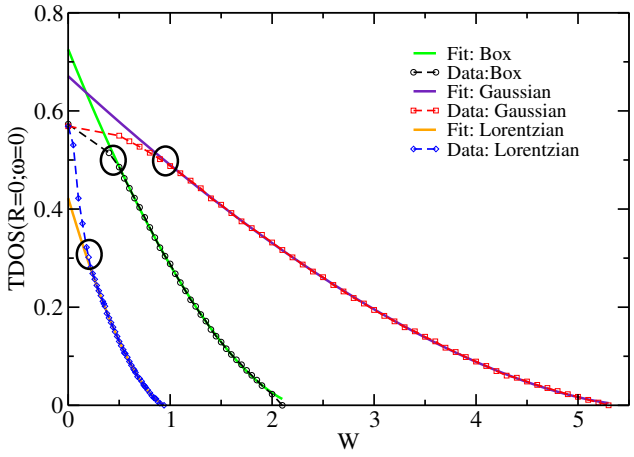

Figure 7.16: The band center of the typical density of states (TDoS$(\mathbf{K} = 0; \omega = 0)$ at various disorder strengths (W) for the 125 site cluster for the Box, Gaussian, and Lorentzian disorder distribution. The linear region of the data can be fit with a scaling ansatz: TDoS$(\Omega = 0) = a_0 \times |W - W_c|^{\beta}$, with $\beta \sim 1.62$ for the Box disorder distribution, $\beta \sim 1.57$ for the Gaussian disorder distribution, and $\beta \sim 1.60$ for the Lorentzian disorder distribution in good agreement with the recently reported value of $\beta \approx 1.67$. [142, 271] The circles in the plot depict the data point where the fit starts to deviate from the data.

The β is obtained by fitting the power law: TDoS$(\omega = 0) = a_0 \times |W - W_c^{fit}|^{\beta}$ to our data and systematically searching for the best data point away from the transition where the fit still follows

[1] The authors obtained $\alpha_o = 4.0$ such that in the hyperscaling relation $\beta = (\alpha_o - d)\nu$, β equals ν.
[2] Authors of this paper show that their quasiperiodic Kicked rotor belong to the same (orthogonal) universality class as the 'random' Anderson model.
[3] Authors of this paper reported that experiments were done on the atomic kicked rotor by a sequence of kicks to the atomic cloud and measure its dynamics.

Table 7.2: Critical parameters of the Anderson localization for various studied disorder distribution in 3D from TMDCA in comparison with numerical exact methods. Due to the energy scale used in our simulations, the box disorder distributions (Bo) are divided by a factor of 8 while the Gaussian (Ga) and the Lorentzian (Lo) disorder distributions are divided by a factor of 4, respectively. We note that the critical exponents (β and α) are independent of disorder distribution (universal) as verified by the multifractal finite size analysis [274] and the analytic results of Wegner [296]. Abbreviations used in the Table are: transfer matrix method (TMM), multifractal finite size scaling (MFSS), level statistics (LS), kicked rotor (KR), and experimental atomic waves (Exp-AW).

Author	Critical Disorder			Critical Exponent		Method
	Bo	Ga	Lo	α	β	
Present Study	2.10±0.10	5.30±0.10	0.94±0.10	–	1.57–1.62	TMDCA
Slevin *et al.* [132]	2.067	–	1.067	1.573–1.577	–	TMM
Slevin *et al.* [131, 270]	2.068–2.073	5.32	1.066	1.58	–	TMM
Slevin *et al.* [128]	2.056±0.014	–	–	1.59–1.60	–	TMM
Rodriguez [271]	2.066–2.067	–	–	1.59	1.65–168	MFSS
Rodriguez [142]	2.066–2.071	–	–	1:58±0.03	–	MFSS
Markos [297]	2.063,2.067	–	–	1.47–1.55	–	MFSS
MacKinnon [298]	2.063 ±0.05	–	–	1.54±0.08	–	TMM
MacKinnon *et al.* [247]	2.063 ±0.063	–	–	1.2±0.3	–	TMM
Bulka *et al.* [242, 272]	2.038–2.063	5.23±0.13	0.95±0.13	–	–	TMM
Milde *et al.* [222]	–	–	–	1.62±0:07	–	TMM
Shklovskii *et al.* [299]	2.0±0.063	–	–	1.50±0.15		LS
Zharekeshev *et al.* [300]	2.05	–	–	1.4±0.15	–	LS
Hofstetter [301]	2.719±0.012	–	–	1.35±0.15	–	LS
Lopez [302]	–	–	–	1.63±0.05	–	KR
Grussbach *et al.* [274]	2.02	5.23	–	1.32–1.37	1.32–1.37	MFSS [1]
Lemarié [303, 304]	–	–	–	1.58–1.60	–	KR [2]
Lemarié [303, 304]	–	–	–	1.40±0.30	–	Exp-AW [3]

The order parameter critical exponent β and the correlation length critical exponent α can be transformed from one to the other using the hyperscaling relation [271] $\beta = (\alpha_o - d)\nu$, where α_o is the Lipschitz-Hölder exponent, which gives the maximum value of the multifractal spectrum. The most recent estimates as reported in Ref. [271] are $\alpha_o = 4.048$, $\nu = 1.59$ and $\beta = 1.67$.

the actual data (scaling regime) (cf. Figure 7.16). This becomes imperative since away from the transition, the data is not expected to fit the form $\mathrm{TDoS}(\omega = 0) = a_0 \times |W - W_c^{fit}|^{\beta}$ and also close to the transition, there should be a crossover to a mean field form since the TMDCA treats the longest length scales in a mean field approximation. So, the fit may only be done between these limits. We show in Figure 7.16 a comparison plot of the fit and our data for the 125 site cluster for the box, Lorentzian, and Gaussian disorder distributions, respectively. The fit of the power law to the scaling region of the data gives the value of the β in an unambiguous manner. We note that as a natural consequence due to the strong fluctuation of the TDoS in the proximity of the critical point, there is a large error bar in our data. The obtained values of β from the various cluster sizes for instance, the box disorder distribution are shown in Table 7.1. One can see that the

obtained β systematically approaches the numerical experimental value [131, 142, 271] for large enough cluster (here, largest N_c simulated is 125) as listed in Table 7.2 for the box, Gaussian, and Lorentzian disorder distributions, respectively, and in comparison with other numerical values.

7.8 Difficulty in Extracting Mobility at Higher Disorder

As explained in the previous sections, the mobility edge is obtained by carefully, locating the frequencies where the typical density of states vanishes at a given disorder strength W, and the band edge determined by the vanishing of the average density of states calculated within the DCA. As it is obvious from the phase diagrams for the various disorder distributions (Figures 7.7, 7.13, and 7.15, respectively), there is some discrepancy between the phase diagram obtained within the typical medium dynamical cluster approximation and the transfer matrix method. This discrepancy can be attributed in part to the form of the disorder distribution. For example, the bare DoS for the Gaussian and Lorentzian disorder distributions are known to have distribution functions with exponential tails. The severity of the exponential nature of the tails associated with the various disorder distributions increases as box, Gaussian, and Lorentzian, in that order. Upon this, at these higher disorder strengths (once a mobility develops), the TDoS naturally develop tails. We note

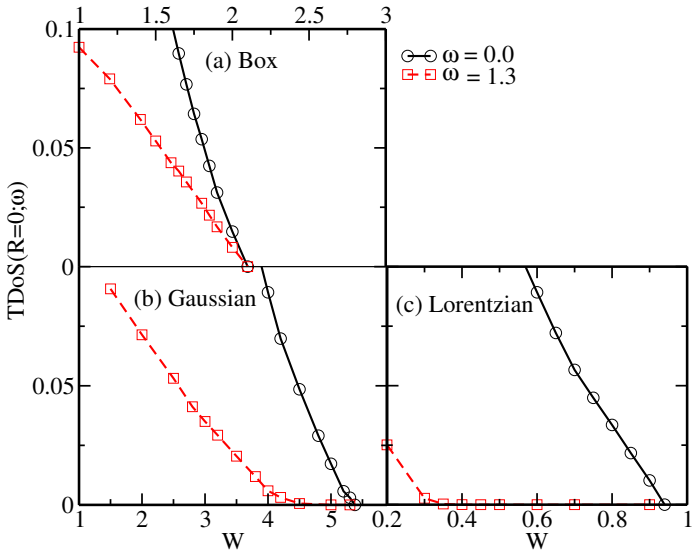

Figure 7.17: The plot of the typical density of states at $\omega = 0.0$ and 1.3 at various disorder strength for the (a) Box, (b) Gaussian, and (c) Lorentzian disorder distributions, respectively.

that in our computations, aside the initial small broadening value ~ -0.01 used in the initialization of the self-energy (needed only for the first iteration), no broadening factor is utilized. As such, these tails that emerge as disorder strength is increased towards W_c are physical tails since the top and bottom of the bands will localize first. To demonstrate this, we show in Figure 7.17, the plot of the TDoS at $\omega = 0.0$ and $\omega = 1.3$ (note the $\omega = 1.3$ frequency is arbitrary but chosen in such a way that it is close to the re-entrance region of the mobility edge) for the box, Gaussian, and Lorentzian disorder distributions, respectively. As can be seen from the plots, for the box disorder distribution, even though there are small tails, the TDoS at $\omega = 0.0$ and $\omega = 1.3$ behave alike and differ only in magnitude. There are no obvious long tails in either frequency ($\omega = 0.0$ and 1.3) that may mask the detection of the position of the mobility edge energies. However, for the Gaussian and Lorentzian disorder distributions, there are exponentially very long tails especially at $\omega = 1.3$ that make pinpointing the exact position of the mobility edge energies highly non-trivial. This should further be understood from the fact that unlike the box disorder distribution, the Lorentzian disorder distribution naturally has tails that decay very slowly at infinity, as $|x|^{-2}$, such that aside the zeroth moment (the area under the curve), all other higher moments do not even exists.

We note that this difficulty is generic not only to the TMDCA but also for any method where the extraction of the trajectories of the mobility edge is based on the TDoS. A notable example is in the kernel polynomial method, which even shows more severe discrepancy (not shown).

This deviation between the TMDCA and TMM at higher disorder strengths can also be attributed to the fact that the TMDCA just like the KPM utilizes finite frequency grid (which biases more towards the metallic regime) in contrast to the TMM, which calculates the transmission of electrons at fixed energies. Even at this, we note that the TMM also has its own short-comings around the same regime due to the strong fluctuations in Λ as can be seen in the phase diagrams for the various disorder strengths around the re-entrance regime.

7.9 Conclusions

A detailed study of the Anderson localization transitions using a new formalism: typical medium dynamical cluster approximation (TMDCA) for various disorder distributions: box, Gaussian, Lorentzian and alloy models in 3-dimensions have been presented. In all the disorder distributions studied, the TMDCA is shown to be a successful, self-consistent, preserving causality, and numerically efficient effective scheme for characterizing disordered electron systems.

With our formalism, we demonstrate that the typical DoS vanishes for localized states and is finite for states, which are extended. Employing the typical DoS as an order parameter for the Anderson localization, we have constructed the disorder-energy phase diagram, computed the critical disorder strengths (W_c), and extracted the order parameter critical exponent (β) for the various disorder distributions and benchmark them in good agreement with various numerical exact methods. We show that β for the Anderson localization transitions is a universal parameter independent of any disorder distribution in agreement with the multifractal analysis. [274] For distributions with a finite variance (box and Gaussian), we demonstrate that there are extended states outside the unperturbed band.

We further show using the DCA (which includes spatial correlations) and a variant of the typical medium (which includes spatial correlations but suffers from self-averaging), the importance of the effective medium to properly characterize the Anderson localization transitions. We further demonstrate the inability of the single site CPA and the TMT methods to accurately capture the localization and disorder effects in both the average and the typical DoS, respectively. We note that the single site TMT while being able to quantitatively capture the localization transitions, strongly underestimates the extended regions with severe underestimation of the critical parameters including the mobility edge trajectories. In contrast, the TMDCA captures nicely, the trajectories of the mobility edge with great improvement in the critical parameters. Most importantly, the TMDCA results are found to be in a quantitative agreement with exact numerical results.

The TMDCA formalism is computationally inexpensive and straightforward to implement since it requires only the computer time needed to diagonalize small clusters, average over the disor-

der configurations, and iterate to convergence. Once combined with electronic structure calculations [305] and more sophisticated many-body techniques for electron interactions, it will open a new avenue for studying localization phenomenon in real materials, as well as the competition between disorder and electron correlations.

Note that a small size cluster is needed to get a converged result in good agreement with the TMM results. As noted earlier, the TMDCA is highly inexpensive. To show this, we compare the relative CPU time needed for the largest system size simulated in the TMDCA and the TMM, respectively. For the largest cluster size utilized in the TMDCA calculations, which is $N_c = 216$, the compute-time is $\sim$ 3-4 hours (running on a single processor) as against $\sim$ 15-20 hours needed for each point in the TMM calculations for the system sizes in Figure 7.7.

Chapter 8

Application of Typical Medium Dynamical Cluster Approximation to Off-diagonal Three Dimensional Disordered System

The results presented in this chapter has been published in Phys. Rev. B **90***, 094208 (2014) [3]. This is the generalization of the local Blackman, Esterling, and Berk (BEB) method for systems with the off-diagonal disorder to finite cluster both for the DCA and the TMDCA. The list of the authors, as it appears in the manuscript are H. Terletska, C. E. Ekuma, C. Moore, K.-M. Tam, J. Moreno, and M. Jarrell.*

8.1 Introduction

Disorder which is inevitably present in most materials can dramatically affect their properties [46, 69]. There have been a number of attempts to develop systematic non-local extensions to the CPA. These include cluster extensions such as the molecular coherent potential approximation (MCPA) [306,307], the dynamical cluster approximation (DCA) [263,264,308], etc. Self-consistent mean field studies of off-diagonal disorder have been conducted by a number of authors [307,309–311]. However, all these studies have been performed at the local single-site BEB level. To include the effects of off-diagonal disorder, Gonis [306] extended the Molecular CPA, which uses a self-consistently embedded finite size cluster to capture non-local corrections to the CPA. However, he criticized the MCPA for violating translational invariance and other critical properties of a valid quantum cluster theory [2, 266]. In order to take into account such non-local effects of off-diagonal disorder models, while maintaining translational invariance, we first extend the BEB formalism using the DCA scheme [263, 264, 308] and then incorporate typical medium using the TMDCA [2].

While the CPA, DCA, and BEB have been shown to be successful, self-consistent mean-field theories for the quantitative description of the density of states and electronic structure of disordered systems, they can not properly address the physics of Anderson localization. These mean-field approaches describe the effective medium using the average density of states which is not critical at the transition [2, 70, 120, 134, 255, 283]. Thus, theories which rely on such averaged quantities will fail to properly characterize the Anderson localization. As noted by Anderson, the probability distribution of the local density of states must be considered, focusing on the most probable or the *typical* value [35, 312]. Close to the Anderson transition, the distribution is found to have very long tails characteristic of a log-normal distribution [138, 142, 313]. In fact, the distribution is log-normal up to ten orders of magnitude [257] and so the typical value [65, 269, 313, 314] is the geometrical mean. Based on this idea, Dobrosavljević *et al.* [105] formulated a single site typical medium theory (TMT) for the Anderson localization. This approximation only gives a qualitative description of the Anderson localization in three dimensions. However, it fails to properly, describe critical properties of the localization transitions including the trajectory of the mobility edge (which separates the extended and localized states), the order parameter critical exponent, and the critical disorder strengths as it neglects non-local (spatial) correlations and so does not include the effects of coherent backscattering [315]. In addition, TMT is only formulated for the diagonal disorder.

In this chapter, to go beyond the local single-site CPA-like level of the BEB formalism, we employ the DCA [263, 264, 308] scheme which systematically incorporates non-local spatial correlation effects. We first present an extension of the DCA for systems with both diagonal and off-diagonal disorder. Comparing our single site and finite cluster results, we demonstrate the effect of non-local correlations on the density of states and the self-energy. A further benchmarking with numerical exact methods is demonstrated.

Up to now, there exist no typical medium formalism for systems with off-diagonal disorder. So far, the typical medium analysis has been applied to systems with only diagonal disorder [2, 105]. In this chapter, we develop a typical medium dynamical cluster approximation formalism capable of characterizing the localization transition in systems with both diagonal and off-diagonal

disorder. We perform a systematic study of the effects of non-local correlations and off-diagonal randomness on the density of states and the electron localization. By comparing the single site and finite cluster results for the typical density of states, we demonstrate the importance of incorporating the non-local, multi-sites effects for proper and quantitative characterization of the localization transition. The results of our calculations are compared with the ones obtained with other numerical methods for finite size lattices, including exact diagonalization, kernel polynomial, and transfer matrix methods.

8.2 Formalism

The formalism that will be generalized here is already presented in Chapter 5 and will not be repeated here. I will next present the extension of the DCA and the TMDCA for the study of systems with both diagonal and non-diagonal randomness.

8.2.1 Dynamical Cluster Approximation for Off-diagonal Disorder

The simplest model widely used to study disordered systems is the single band, tight binding Hamiltonian defined by Equation 4.1. Here, the probability distribution is defined by Equation 4.2d. For the diagonal disorder case when the bandwidth of the pure host A is about the same that the bandwidth of the B system, such substitution results only in a change of the local potential V_i at the replaced site i. This corresponds to changes only in the diagonal elements of the Hamiltonian. In this case, it is assumed that the substitution of impurity atoms on average has no effect on the hopping amplitudes to the neighboring atomic sites.

For systems with off-diagonal disorder, the randomness is introduced not only locally in the random diagonal potential V_i, but also through the hopping amplitudes. To model this, BEB [316] introduced the disorder configuration dependent hopping amplitude of electrons t_{ij} as

$$
\begin{aligned}
t_{ij} &= t_{ij}^{AA}, \text{ if } \quad i \in A, \quad j \in A \\
&\quad\; t_{ij}^{BB}, \text{ if } \quad i \in B, \quad j \in B \\
&\quad\; t_{ij}^{AB}, \text{ if } \quad i \in A, \quad j \in B \\
&\quad\; t_{ij}^{BA}, \text{ if } \quad i \in B, \quad j \in A,
\end{aligned} \tag{8.1}
$$

where t_{ij} depends on the type of ion occupying sites i and j. For off-diagonal disorder BEB [316] demonstrated that the scalar CPA equation becomes a 2×2 matrix equation, with corresponding AA, AB, BA, and BB matrix elements. In momentum space, if there is only near-neighbor hopping between all ions, the bare dispersion can be written as (the under-bar denotes matrices)

$$
\underline{\varepsilon_k} = \begin{pmatrix} t^{AA} & t^{AB} \\ t^{BA} & t^{BB} \end{pmatrix} \varepsilon_k, \quad \text{where} \quad \varepsilon_k = -2t \sum_{i=1}^{d} \cos(k_i a) \tag{8.2}
$$

is the dispersion, a is the lattice constant ($a = 1$), d is the dimension and for $d = 3$, $\varepsilon_k = -2t(\cos(k_x) + \cos(k_y) + \cos(k_z))$ with $4t = 1$ as our unit of energy. t^{AA}, t^{BB}, t^{AB}, and t^{BA} are unitless prefactors.

The BEB approach by construction is local, as such, all nonlocal disorder induced correlations are neglected [316]. In order to take into account nonlocal physics, we extend the BEB formalism to a finite cluster using the DCA scheme. Here in the following, we present the algorithm and details of our nonlocal DCA extension of the BEB formalism for the off-diagonal disorder. Just as in the DCA scheme [264], the first Brillouin zone is divided into $N_c = L^d$ (d is the dimension and L is the linear cluster size) coarse-grained cells with centers $\mathbf{K}$ surrounded by points $\tilde{k}$ within the cell so that an arbitrary $k = \mathbf{K} + \tilde{k}$. For a given DCA, the $\mathbf{K}$-dependent effective medium hybridization $\underline{\Gamma(\mathbf{K}, \omega)}$ matrix in momentum space is

$$
\underline{\Gamma(\mathbf{K}, \omega)} = \begin{pmatrix} \Gamma^{AA}(\mathbf{K}, \omega) & \Gamma^{AB}(\mathbf{K}, \omega) \\ \Gamma^{BA}(\mathbf{K}, \omega) & \Gamma^{BB}(\mathbf{K}, \omega) \end{pmatrix} \tag{8.3}
$$

where underlines denote a 2×2 matrix. Since the cluster problem is usually solved in real space, we stochastically sample random configurations of the disorder potential V and calculate the corresponding cluster Green's function by inverting a $N_c \times N_c$ matrix, i.e.,

$$G_{ij} = \left(\omega\mathbb{I} - \overline{t'} - \Gamma' - V\right)^{-1}_{ij} \tag{8.4}$$

where V is a diagonal matrix for the disorder site potential. The primes stand for the configuration dependent Fourier transform (FT) components of the hybridization and hopping, respectively. I.e.,

$$\Gamma'_{ij} = \begin{cases} FT(\Gamma^{AA}(\mathbf{K},\omega)), \text{ if } \quad i \in A, \quad j \in A \\ FT(\Gamma^{BB}(\mathbf{K},\omega)), \text{ if } \quad i \in B, \quad j \in B \\ FT(\Gamma^{AB}(\mathbf{K},\omega)), \text{ if } \quad i \in A, \quad j \in B \\ FT(\Gamma^{BA}(\mathbf{K},\omega)), \text{ if } \quad i \in B, \quad j \in A \end{cases} \tag{8.5a}$$

and

$$\overline{t}'_{ij} = \begin{cases} FT(\overline{\varepsilon}^{AA}(\mathbf{K})), \text{ if } \quad i \in A, \quad j \in A \\ FT(\overline{\varepsilon}^{BB}(\mathbf{K})), \text{ if } \quad i \in B, \quad j \in B \\ FT(\overline{\varepsilon}^{AB}(\mathbf{K})), \text{ if } \quad i \in A, \quad j \in B \\ FT(\overline{\varepsilon}^{BA}(\mathbf{K})), \text{ if } \quad i \in B, \quad j \in A \end{cases} \tag{8.5b}$$

with

$$\underline{\overline{\varepsilon}(\mathbf{K})} \;\; = \begin{pmatrix} t^{AA} & t^{AB} \\ t^{BA} & t^{BB} \end{pmatrix} \tfrac{N_c}{N} \textstyle\sum_{\tilde{k}} \varepsilon_k, \tag{8.5c}$$

where Γ'_{ij} and $\overline{t}'_{ij}$ are $N_c \times N_c$ real-space matrices (where N_c is the cluster size), and e.g., $FT(\Gamma^{AA}(\mathbf{K},\omega)) = \sum_{\mathbf{K}} \Gamma^{AA}(\mathbf{K},\omega) e^{i\mathbf{K}(r_i - r_j)}$. The hopping can be long ranged, but since they are coarse-grained quantities are effectively limited to the cluster. Physically, Γ'_{ij} represents the hybridization between sites i and j which is configuration dependent. For example, the AA component of the hybridization corresponds to both A species occupying site i and j, while the AB component means that site i

is occupied by an A atom and site j by a B atom. The interpretation of the hopping matrix is the same as for the hybridization function.

In the next step, we perform averaging over the disorder $\langle(...)\rangle$ and in doing so we re-expand the Green function (Equation 8.4) into a $2N_c \times 2N_c$ matrix

$$G_c(\omega)_{ij} = \begin{pmatrix} \left\langle G_c^{AA}(\omega)\right\rangle_{ij} & \left\langle G_c^{AB}(\omega)\right\rangle_{ij} \\ \\ \left\langle G_c^{BA}(\omega)\right\rangle_{ij} & \left\langle G_c^{BB}(\omega)\right\rangle_{ij} \end{pmatrix}. \tag{8.6}$$

This may be done by assigning the components according to the occupancy of the sites i and j

$$\begin{aligned} (G_c^{AA})_{ij} &= (G_c)_{ij} \text{ if } \quad i \in A, \quad j \in A \\ (G_c^{BB})_{ij} &= (G_c)_{ij} \text{ if } \quad i \in B, \quad j \in B \\ (G_c^{AB})_{ij} &= (G_c)_{ij} \text{ if } \quad i \in A, \quad j \in B \\ (G_c^{BA})_{ij} &= (G_c)_{ij} \text{ if } \quad i \in B, \quad j \in A \end{aligned} \tag{8.7}$$

with the other components being zero. Because only one of the four matrix elements is finite for each disorder configuration (each site can be occupied by either A or B atom), only the sum of the elements in Equation 8.6 is normalized as a conventional Green function.

Having formed the disorder average cluster Green function matrix, we then Fourier transform each component to **K**-space (which also imposes translational symmetry) and construct the **K**-dependent disorder averaged cluster Green function matrix in momentum space

$$\underline{G_c(\mathbf{K},\omega)} = \begin{pmatrix} G_c^{AA}(\mathbf{K},\omega) & G_c^{AB}(\mathbf{K},\omega) \\ \\ G_c^{BA}(\mathbf{K},\omega) & G_c^{BB}(\mathbf{K},\omega) \end{pmatrix}. \tag{8.8}$$

Once the cluster problem is solved, we calculate the coarse-grained lattice Green function as

$$\begin{aligned}\underline{\overline{G}(\mathbf{K},\omega)} &= \begin{pmatrix} \overline{G}^{AA}(\mathbf{K},\omega) & \overline{G}^{AB}(\mathbf{K},\omega) \\ \overline{G}^{BA}(\mathbf{K},\omega) & \overline{G}^{BB}(\mathbf{K},\omega) \end{pmatrix} \\ &= \frac{N_c}{N}\sum_{\tilde{k}} \left(\underline{G_c(\mathbf{K},\omega)}^{-1} + \underline{\Gamma(\mathbf{K},\omega)} - \underline{\varepsilon_k} + \underline{\overline{\varepsilon}(\mathbf{K})} \right)^{-1}, \end{aligned} \tag{8.9}$$

here we use an overbar to denote the cluster coarse-grained quantities. It is important to note that each component of the Green function matrix above does not have the normalization of a conventional, i.e., scalar, Green function. Only the sum of the matrix components has the conventional normalization, so that $\overline{G}(\mathbf{K},\omega) \sim 1/\omega$, with the total coarse-grained lattice Green function being obtained as

$$\overline{G}(\mathbf{K},\omega) = \overline{G}^{AA}(\mathbf{K},\omega) + \overline{G}^{BB}(\mathbf{K},\omega) + \overline{G}^{AB}(\mathbf{K},\omega) + \overline{G}^{BA}(\mathbf{K},\omega). \tag{8.10}$$

Next, to construct the new DCA effective medium $\underline{\Gamma(\mathbf{K},\omega)}$, we impose the BEB DCA (2×2) matrix self-consistency condition, requiring the disorder averaged cluster and the coarse-grained lattice Green functions to be equal

$$\underline{G_c(\mathbf{K},\omega)} = \underline{\overline{G}(\mathbf{K},\omega)}. \tag{8.11}$$

This is equivalent to a system of three coupled scalar equations

$$\overline{G}^{AA}(\mathbf{K},\omega) = G_c^{AA}(\mathbf{K},\omega), \tag{8.12a}$$

$$\overline{G}^{BB}(\mathbf{K},\omega) = G_c^{BB}(\mathbf{K},\omega), \quad \text{and} \tag{8.12b}$$

$$\overline{G}^{AB}(\mathbf{K},\omega) = G_c^{AB}(\mathbf{K},\omega). \tag{8.12c}$$

Note $\overline{G}^{BA}(\mathbf{K},\omega) = \overline{G}^{AB}(\mathbf{K},\omega)$ automatically if $t^{AB} = t^{BA}$. We then close our self-consistency loop by updating the corresponding hybridization functions for each component as

$$
\begin{aligned}
\Gamma_n^{AA}(\mathbf{K},\omega) &= \Gamma_o^{AA}(\mathbf{K},\omega)+\xi\left(G_c^{-1}(\mathbf{K},\omega)^{AA}-\overline{G}^{-1}(\mathbf{K},\omega)^{AA}\right)\\
\Gamma_n^{BB}(\mathbf{K},\omega) &= \Gamma_o^{BB}(\mathbf{K},\omega)+\xi\left(G_c^{-1}(\mathbf{K},\omega)^{BB}-\overline{G}^{-1}(\mathbf{K},\omega)^{BB}\right)\\
\Gamma_n^{AB}(\mathbf{K},\omega) &= \Gamma_o^{AB}(\mathbf{K},\omega)+\xi\left(G_c^{-1}(\mathbf{K},\omega)^{AB}-\overline{G}^{-1}(\mathbf{K},\omega)^{AB}\right)\\
\Gamma_n^{BA}(\mathbf{K},\omega) &= \Gamma_n^{AB}(\mathbf{K},\omega)
\end{aligned}
\tag{8.13}
$$

where 'o' and 'n' denote old and new respectively, and ξ is a linear mixing parameter $0<\xi<1$. We then iterate the above steps until convergence is reached.

There are two limiting cases of the above formalism which we carefully checked numerically. In the limit of $N_c=1$, we should recover the original BEB result. Here the cluster Green function loses its $\mathbf{K}$ dependence, so that

$$
\begin{pmatrix} G_c^{AA}(\omega) & 0 \\ 0 & G_c^{BB}(\omega) \end{pmatrix} = \frac{1}{N}\sum_k \left(\underline{G_c(\omega)}^{-1}+\underline{\Gamma(\omega)}-\underline{\varepsilon(k)}\right)^{-1} \tag{8.14}
$$

which is the BEB self-consistency condition. Here we used that $\overline{\varepsilon}(\mathbf{K})=0$ for $\mathrm{N}_c=1$. The second limiting case is when there is only diagonal disorder so that $t^{AA}=t^{BB}=t^{AB}=1$. In this case the above formalism reduces to the original DCA scheme. We have verified numerically both limits.

8.2.2 Typical Medium Dynamical Cluster Approximation for Off-diagonal Disorder

To address the issue of electron localization, we use the typical medium dynamical cluster approximation (TMDCA) [2]. In Ref. [2], we confirmed that the typical density of states vanishes for states which are localized and it is finite for extended states. In the following, we generalize our TMDCA analysis to systems with off-diagonal disorder to address the question of localization and the mobility edge in such models.

First, we would like to emphasize that the crucial difference between TMDCA [2] and the standard DCA [264] procedure is the way the disorder averaged cluster Green function is calculated. In the TMDCA analysis instead of using the algebraically averaged cluster Green function in the

self-consistency loop, we calculate the typical (geometrically) averaged cluster density of states

$$\rho^c_{typ}(\mathbf{K},\omega) = e^{\frac{1}{N_c}\sum_i \langle \ln \rho_{ii}(\omega)\rangle} \left\langle \frac{-\frac{1}{\pi}\Im G_c(\mathbf{K},\omega)}{\frac{1}{N_c}\sum_i(-\frac{1}{\pi}\Im G_{ii}(\omega))} \right\rangle, \tag{8.15}$$

with the geometric averaging being performed over the local density of states $\rho_{ii}(\omega) = -\frac{1}{\pi}\Im G_{ii}(w)$ only. Using this $\rho^c_{typ}(\mathbf{K},\omega)$ the cluster averaged typical Green function is constructed via a Hilbert transform

$$G_c(\mathbf{K},\omega) = \int d\omega' \frac{\rho^c_{typ}(\mathbf{K},\omega')}{\omega-\omega'}. \tag{8.16}$$

In the presence of off-diagonal disorder, following BEB, the typical density of states becomes a 2×2 matrix, which we define as

$$\underline{\rho^c_{typ}(\mathbf{K},\omega)} = \exp\left(\frac{1}{N_c}\sum_{i=1}^{N_c}\langle \ln \rho_{ii}(\omega)\rangle\right) \times \begin{pmatrix} \left\langle \frac{-\frac{1}{\pi}\Im G_c^{AA}(\mathbf{K},\omega)}{\frac{1}{N_c}\sum_{i=1}^{N_c}(-\frac{1}{\pi}\Im G_{ii}(\omega))} \right\rangle & \left\langle \frac{-\frac{1}{\pi}\Im G_c^{AB}(\mathbf{K},\omega)}{\frac{1}{N_c}\sum_{i=1}^{N_c}(-\frac{1}{\pi}\Im G_{ii}(\omega))} \right\rangle \\ \left\langle \frac{-\frac{1}{\pi}\Im G_c^{BA}(\mathbf{K},\omega)}{\frac{1}{N_c}\sum_{i=1}^{N_c}(-\frac{1}{\pi}\Im G_{ii}(\omega))} \right\rangle & \left\langle \frac{-\frac{1}{\pi}\Im G_c^{BB}(\mathbf{K},\omega)}{\frac{1}{N_c}\sum_{i=1}^{N_c}(-\frac{1}{\pi}\Im G_{ii}(\omega))} \right\rangle \end{pmatrix} \tag{8.17}$$

Here the scalar prefactor depicts the local typical (geometrically averaged) density of states, while the matrix elements are linearly averaged over the disorder. Also notice that the cluster Green function $(\underline{G_c})_{ij}$ and its components G_c^{AA}, G_c^{BB} and G_c^{AB} are defined in the same way as in Eqs. (8.4-8.7).

In the next step, we construct the cluster average Green function $G_c(\mathbf{K},\omega)$ by performing Hilbert transform for each component

$$\underline{G_c(\mathbf{K},\omega)} = \begin{pmatrix} \int d\omega' \frac{\rho^{AA}_{typ}(\mathbf{K},\omega')}{\omega-\omega'} & \int d\omega' \frac{\rho^{AB}_{typ}(\mathbf{K},\omega')}{\omega-\omega'} \\ \\ \int d\omega' \frac{\rho^{BA}_{typ}(\mathbf{K},\omega')}{\omega-\omega'} & \int d\omega' \frac{\rho^{BB}_{typ}(\mathbf{K},\omega')}{\omega-\omega'} \end{pmatrix}. \tag{8.18}$$

Once the disorder averaged cluster Green function $G_c(\mathbf{K},\omega)$ is obtained from Equation 8.18, the self-consistency steps are the same as in the procedure for the off-diagonal disorder DCA

described in the previous section: we calculate the coarse-grained lattice Green function using Equation 8.9 which is then used to update the hybridization function with the effective medium via Equation 8.13. The above set of equations provides the generalization of the TMDCA scheme for both diagonal and off-diagonal disorder which we test numerically in the following sections. Also notice that for $N_c = 1$ with only diagonal disorder ($t^{AA} = t^{BB} = t^{AB} = t^{BA}$) the above procedure reduces to the local TMT scheme. In this case, the diagonal elements of the matrix in Equation 8.17 will contribute c_A and c_B, respectively, with the off-diagonal elements being zero (for $\mathrm{N}_c = 1$ the off-diagonal terms vanish because a given site can only be either A or B). Hence, the typical density reduces to the local scalar prefactor only, which has exactly the same form as in the local TMT scheme.

Another limit of the proposed ansatz for the typical density of states of Equation 8.17 is obtained at small disorder. In this case, the TMDCA reduces to the DCA for off-diagonal disorder, as the geometrically averaged local prefactor term numerically cancels with the contribution from the linearly averaged local term in the denominator of Equation 8.17.

Finally, we also want to mention that the developed cluster TMDCA fulfills all the essential requirements expected of a "successful" cluster theory [266] including causality and translational invariance. We note that in our formalism, instead of doing the very expensive enumeration of the disorder configurations which scales as 2^{N_c}, we instead do a stochastic sampling of the disorder configurations which greatly reduces the computational cost enabling us to study larger systems. Larger system sizes need fewer realizations. Since the convergence criterion is achieved when the TDoS($\omega = 0$) does not fluctuate anymore with iteration number, within the error bars, our computational cost does not even scale as N_c. For a typical $\mathrm{N}_c = 64$ size cluster, about 500 disorder realizations are needed to get reliable data and this number decreases with increasing cluster size.

To illustrate the generalized DCA and TMDCA algorithms described above, we present our results for the effects of diagonal and off-diagonal disorder in a generalized Anderson Hamiltonian (Equation 4.1) for a three-dimensional system with binary disorder distribution ($W_A = -W_B$) and random hopping ($t^{AA} \neq t^{BB}$, $t^{AB} = t^{BA}$) with other parameters as specified.

8.3 Application of the DCA to Diagonal and Off-diagonal Disorder

The effect of off-diagonal disorder on the average density of states (DoS) calculated within the DCA for cubic cluster ($N_c = 4^3$) is presented in Figure 8.1. The DoS we present in our results is a local density of states calculated as

$$DoS(\omega) = -\frac{1}{\pi N_c}\sum_{\mathbf{K}=1}^{N_c}\Big(\Im\overline{G}^{AA}(\mathbf{K},\omega)+\Im\overline{G}^{AB}(\mathbf{K},\omega)+\Im\overline{G}^{BA}(\mathbf{K},\omega)+\Im\overline{G}^{BB}(\mathbf{K},\omega)\Big). \quad (8.19)$$

Notice that our DCA procedure for $N_c = 1$ reduce to the original CPA-like BEB. For a fixed concentration $c_A = 0.5$, we examine the effects of off-diagonal disorder at two fixed values of the diagonal disorder potential $V_A = 0.4$ (below the split-band limit) and $V_A = 0.9$ (above the split-band limit). The off-diagonal randomness is modeled by changes in the hopping amplitudes

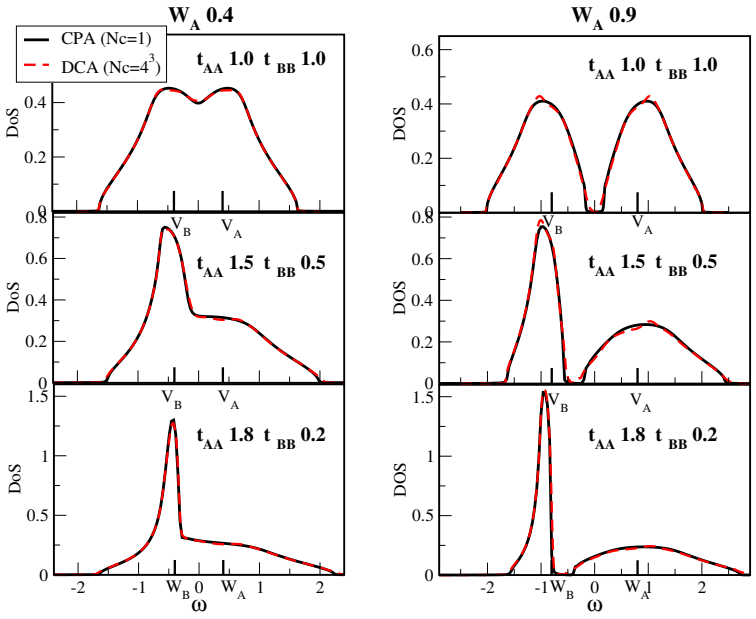

Figure 8.1: The effect of off-diagonal disorder on the average density of states calculated in the DCA scheme with $N_c = 4^3$. Our DCA results for $N_c = 1$ corresponds to a single site CPA BEB scheme. We consider two values of local disorder potential below ($W_A = 0.4$) and above ($W_A = 0.9$) the band split limit and examine the effect of changing the off-diagonal hopping strength (which amounts to a change in the non-local potential). We start with the diagonal disorder case $t^{AA} = t^{BB} = t^{AB} = 1.0$ and then consider two off-diagonal disorder cases: $t^{AA} = 1.5, t^{BB} = 0.5$ and $t^{AA} = 1.8, t^{BB} = 0.2$, respectively. We fix $t^{AB} = t^{BA} = 0.5(t^{AA} + t^{BB})$ and $c_A = 0.5$. For this parameter range of off-diagonal disorder, we do not observe a significant difference between the CPA ($N_c = 1$) and the DCA ($N_c = 4^3$) results indicating that non-local inter-site correlations are weak.

t^{AA}, t^{BB} with $t^{AB} = 0.5(t^{AA} + t^{BB})$. For a diagonal disorder case (top panel of Figure 8.1) with $t^{AA} = t^{BB} = t^{AB} = t^{BA}$ we have two subbands contributing equally to the total DoS. While as shown in the middle and bottom panels, the change in the strength of the off-diagonal disorder leads to dramatic changes in the DoS. An increase of the AA hoping results in the broadening of the AA subband with the development of a resonance peak at the BB subband. For this parameter range, both the DCA ($N_c = 64$) and CPA ($N_c = 1$) provide about the same results indicating that disorder-induced non-local correlations are negligible.

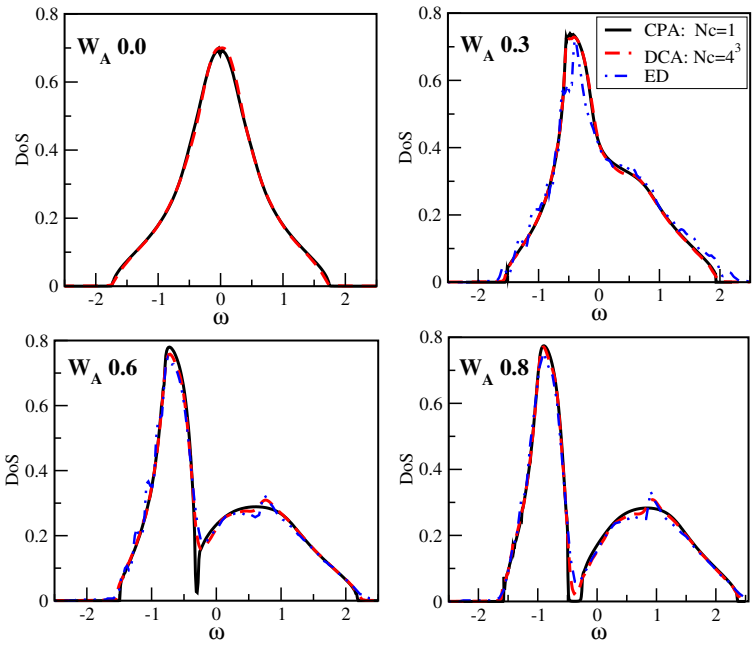

Figure 8.2: The effect on the average density of states of an increasing diagonal disorder potential W_A for a fixed off-diagonal disorder calculated with our modified DCA scheme with $t^{AA} = 1.5$, $t^{BB} = 0.5$, $t^{AB} = 0.5(t^{AA} + t^{BB})$, and $c_A = 0.5$. Results are obtained for $N_c = 1$ (corresponding to the CPA) and $N_c = 4^3$ cluster sizes. We also compare our DCA average DoS with the DoS obtained using exact diagonalization (ED) for a 12^3 cubic lattice cluster with 48 disorder realizations. For ED results, we used a $\eta = 0.01$ broadening in frequency.

In Figure 8.2 we show the average DoS calculated for fixed off-diagonal-disorder parameters and different diagonal disorder potentials V_A. We again compare the local CPA ($N_c = 1$) and the DCA ($N_c = 4^3$) results. To benchmark our off-diagonal extension of the DCA, we also compare our results with those obtained by exact diagonalization. For small V_A, there is no difference between the CPA ($N_c = 1$) and the DCA ($N_c = 4^3$) results. As local potential V_A is increased, noticeable differences start to develop. We can see that for larger V_A a gap starts to open and is more dramatic

in the CPA scheme. While in the DCA ($N_c = 4^3$) this gap is partially filled due to the incorporation of non-local inter-site correlations which are missing in the CPA. Furthermore, the DoS obtained from the DCA procedure provides finer structures which are in basic agreement with the DoS calculated with exact diagonalization for a cluster of size $12 \times 12 \times 12$. The agreement we get with ED results is a good indication of the accuracy of our extension of the DCA to the off-diagonal disorder. The additional structures observed in the DoS for $N_c > 1$, which are absent in the CPA, are believed to be related to the local order in the environment of each site [264,266]. Notice that while the DCA accounts for non-local backscattering effects which lead to the Anderson localization, the average local DoS does not capture the transition, as it is not an order parameter for the Anderson localization.

To further illustrate the important effect of the non-local contributions from the cluster, we also

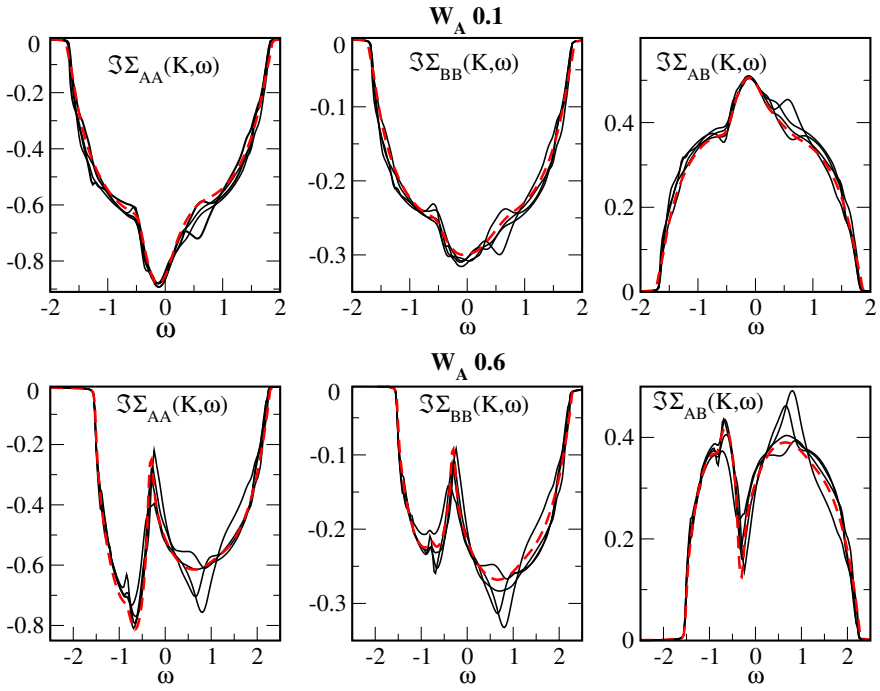

Figure 8.3: The imaginary part of the self-energy vs frequency ω for $N_c = 1$ (red dash-line) and $N_c = 4^3$ (solid lines) at various **K** momenta points: $(0,0,0)$, $(\pi,0,0)$, $(\pi,\pi,0)$, and $(\pi/2,\pi/2,\pi/2)$, for $W_A = 0.1$ (top) and $W_A = 0.6$ (bottom) diagonal disorder potential with $t^{AA} = 1.5$, $t^{BB} = 0.5$, $t^{AB} = 0.5(t^{AA} + t^{BB})$, and $c_A = 0.5$. For small disorder $W_A = 0.1$, the self-energy for $N_c = 1$ is essentially the same as that of the various **K** points of the $N_c = 4^3$ cluster, indicating that non-local effects are negligible for such small disorder. For a larger value of the disorder $W_A = 0.6$, the single site and the finite cluster data differ significantly, which illustrates that at larger disorder, the momentum dependence of the self-energy increases and becomes important.

show in Figure 8.3 the imaginary part of the self-energy $\Im\Sigma(\mathbf{K},\omega)$ for $N_c = 1$ (dash line) and for ($N_c = 4^3$) (solid lines) at different values of cluster momenta $\mathbf{K} = (0,0,0)$, $(\pi,0,0)$, $(\pi,\pi,0)$ and $(\pi/2,\pi/2,\pi/2)$ for small $W_A = 0.1$ (top) and larger $W_A = 0.6$ (bottom) disorder potentials. At small disorder $W_A = 0.1$, there is a little momentum dependence for the $N_c = 4^3$ self-energy and different $\mathbf{K}$-momenta curves practically fall on top of each other. The results for the $N_c = 1$ and $N_c = 4^3$ are essentially the same, which indicates that for small disorder the CPA still presents a good approximation for the self-energy. On the hand, for larger disorder $W_A = 0.6$ the $N_c = 1$ and $N_c = 4^3$ results differ significantly, with the $N_c = 4^3$ self-energy having a noticeable momentum dependence, indicating that non-local correlations become more pronounced for larger disorder values.

8.4 TMDCA Analysis of Diagonal and Off-diagonal Disorder

In this section, we will apply the TMDCA to the study of diagonal and off-diagonal disorder configurations.

8.4.1 Typical Medium Analysis of Diagonal disorder

To characterize the Anderson localization transition, we now explore the typical density of states (TDoS) calculated within our extension of the TMDCA presented in Subsection 8.2.2. In the typical medium analysis, the TDoS serves as the order parameter for the Anderson localization transition. In particular, the TDoS is finite for extended states and zero for states which are localized.

First we consider the behavior of the TDoS and compare it with the average DoS for the diagonal disorder. In Figure 8.4 we show our results for $N_c = 1$ (left panel) and $N_c > 1$ (right panel). To demonstrate a systematic convergence of the TDoS with increasing cluster size N_c, we present our data of the TDoS for $N_c = 1, 4^3, 6^3$. Notice that $N_c = 1$ results for TDoS correspond to the single-site TMT of Dobrosavljević *et al.* [105], and for average DoS they correspond to the ordinary CPA. As expected [2,105], for small disorder ($W_A = 0.15$) there is not much difference between the DCA

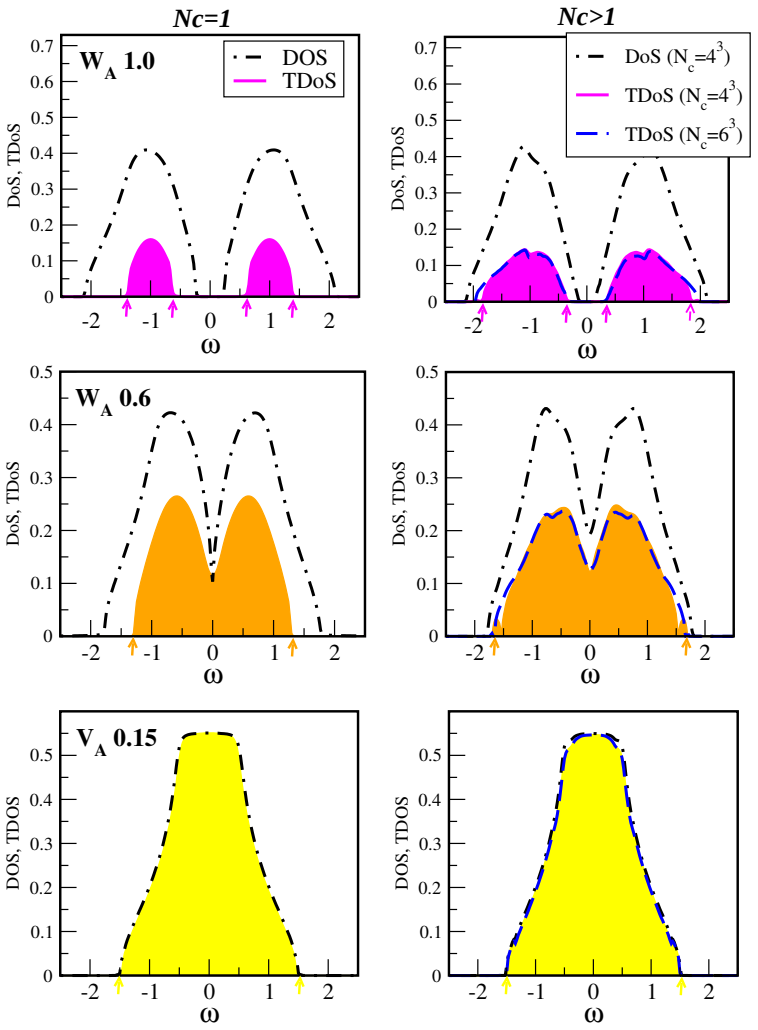

Figure 8.4: Diagonal disorder case: The average density of states (dash-dotted line) calculated within the DCA for $N_c = 1$ (left panel) and $N_c = 4^3$ (right panel) and the typical density of states shown as shaded regions for $N_c = 1$ (left panel) and $N_c = 4^3$ (right panel) and dash-line for $N_c = 6^3$ (right panel) are calculated within the TMDCA for diagonal disorder $t^{AA} = t^{BB} = t^{AB} = t^{BA} = 1, c_A = 0.5$, and various values of the local potential $W_A = -W_B$. The TDoS is presented for several cluster sizes $N_c = 1$, $N_c = 4^3$ and $N_c = 6^3$ in order to show its systematic convergence with N_c. The average DoS converges for cluster sizes beyond $N_c = 4^3$. The TDoS is finite for the extended states and zero when the states are localized. The mobility edges extracted from the vanishing of the TDoS are marked by the arrows (we show arrows for $N_c = 4^3$ only). The extended states region with a finite TDoS is always narrower for $N_c = 1$ as compared to the results of $N_c > 1$ clusters, indicating that a single site TMT tends to overemphasize the localized states.

($N_c = 4^3$) and the TMDCA ($N_c = 4^3$) or between the CPA and TMT for $N_c = 1$ results. However, there are subtle differences between the results for finite $N_c = 4^3$ and single site $N_c = 1$ clusters due to incorporation of spatial correlations. As the disorder strength, W_A is increased ($W_A = 0.6$), the typical density of states (TDoS) becomes smaller than the average DoS and is broader for the larger

cluster. Moreover, the finite cluster introduces features in the DoS which are missing in the local $N_c = 1$ data. Regions where the TDoS is zero while the average DoS is finite indicate Anderson localized states, separated by the mobility edge (marked by arrows). For $N_c > 1$ these localized regions are wider which indicates that the localization edge is driven to higher frequencies. This is a consequence of the tendency of non-local corrections to suppress localization. For even larger disorder $W_A = 1$, a gap opens in both the TDoS and the average DoS leading to the formation of four localization edges, but again the region of extended states is larger for the finite cluster, indicating that local TMT ($N_c = 1$) tends to underestimate the extended states region.

To further benchmark our results for the diagonal disorder, we show in Figure 8.5 a comparison of the average and typical DoS calculated with the DCA and the TMDCA ($N_c = 4^3$) as compared with the kernel polynomial method (KPM) [245, 246, 317, 318]. In the KPM analysis, instead of diagonalizing the Hamiltonian directly, the local DoS is expressed in term of an infinite series of Chebyshev polynomials. In practice, the truncated series leads to Gibbs oscillations. The KPM

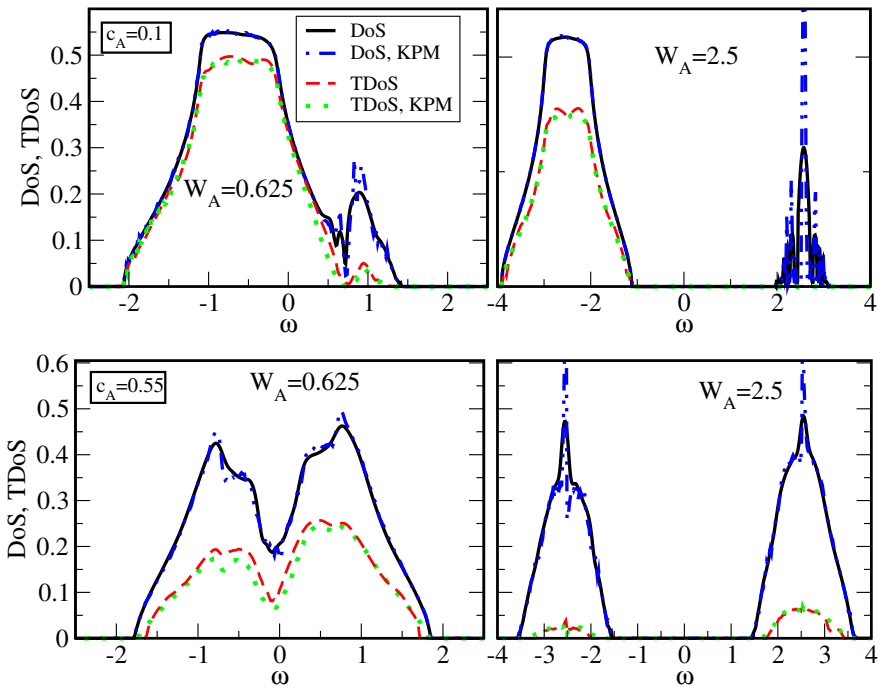

Figure 8.5: Diagonal disorder case. Comparison of the average and typical DoS calculated with the DCA/TMDCA and Kernel polynomial methods (KPM) [275] for the diagonal disorder with $t^{AA} = t^{BB} = t^{AB} = t^{BA} = 1$ at various values of local potential W_A and concentrations c_A for cluster size $N_c = 6^3$. The kernel polynomial method used 2048 moments on a 48^3 cubic lattice, and 200 independent realizations generated with 32 sites randomly sampled from each realization.

damps these oscillations by a modification of the expansion coefficients. Following previous studies on the Anderson model, the Jackson kernel is used [245]. The details of the implementation are well discussed in Ref. [245]. The parameters used in the KPM calculations are listed in the caption of Figure 8.5. As it is evident from the plots, our TMDCA results reproduced those from the KPM nicely showing that our formalism offers a systematic way of studying the Anderson localization transition in binary alloy systems. Such good agreement indicates a successful benchmarking of the TMDCA method [2].

8.4.2 Typical Medium Analysis of Off-diagonal Disorder

Next, we explore the effects of the off-diagonal disorder. In Figure 8.6, we compare the typical TDoS from the TMDCA and average DoS from the DCA for several values of the diagonal disorder strength W_A at fixed off-diagonal disorder amplitudes $t^{AA} = 1.5$, $t^{BB} = 0.5$, $t^{AB} = 1.0$. To show the effect of a finite cluster with respect to incorporation of non-local correlations, we present data for the single site $N_c = 1$ and finite clusters $N_c = 4^3$ and 5^3. The TMT ($N_c = 1$) again underestimates the extended states regime by having a narrower TDoS as compared to the $N_c > 1$. We also see that the mobility edge defined by the vanishing of the TDoS (marked by arrows for $N_c = 4^3$) systematically converges with increasing cluster size N_c. For small disorder V_A, both the DoS and the TDoS are practically the same. However, as V_A increases, significant differences start to emerge. Increasing W_A leads to the gradual opening of the gap which is more pronounced in the $N_c = 1$ case and for smaller disorder $V_A = 0.6$ is partially filled for the $N_c > 1$ clusters. As compared to the diagonal disorder case (cf. Figure 8.4), the average DoS and TDoS become asymmetric with respect to zero frequency due to the off-diagonal randomness.

In Figures 8.7 and 8.8, we present the disorder-energy phase diagram for both diagonal (Figure 8.7) and off-diagonal (Figure 8.8) disorder calculated using the single TMT ($N_c = 1$) and the non-local TMDCA ($N_c > 1$). To check the accuracy of the mobility edge trajectories extracted from TMDCA, we compare our data with those obtained with the transfer matrix method (TMM).

The TMM [106,250,251] is a well-established numerical method for calculating the correlation length and determining the mobility edge of the disorder Anderson model. Its main advantage is

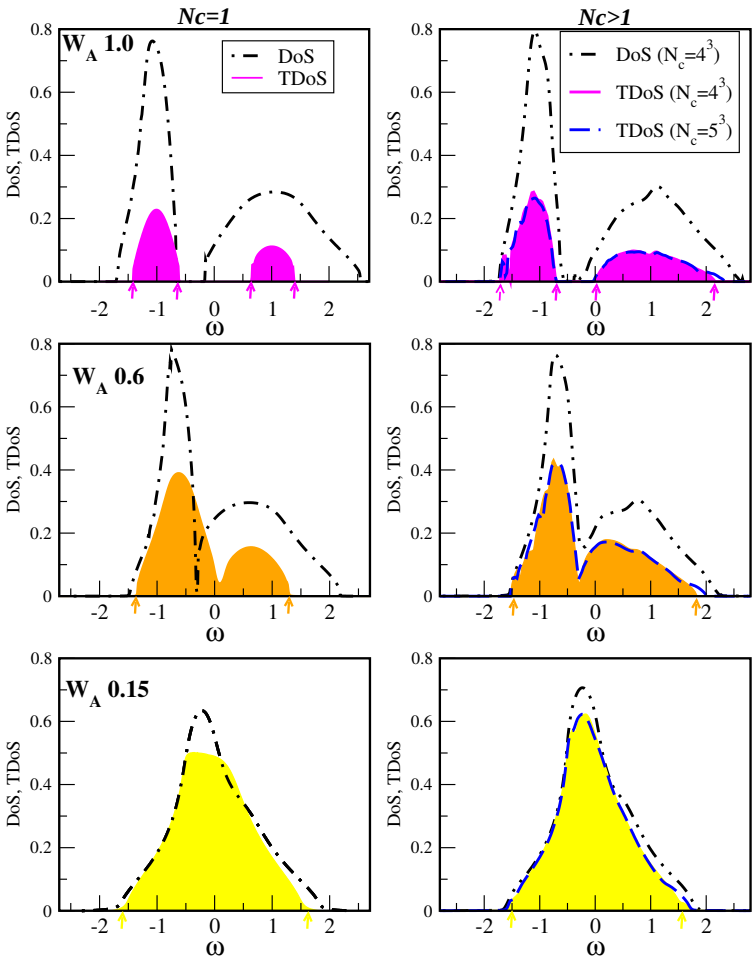

Figure 8.6: Off-diagonal disorder case: The left panel displays results for $N_c = 1$ and the right panel for $N_c > 1$. The average density of states (dash-dotted line) and the typical density of states (shaded regions) for $N_c = 1$ (left panel), $N_c = 4^3$ (right panel) and blue dash lines for $N_c = 5^3$ (left panel) for various values of the local potential W_A with off-diagonal disorder parameters: $t^{AA} = 1.5$, $t^{BB} = 0.5$, $t^{AB} = 0.5(t^{AA} + t^{BB})$, and $c_A = 0.5$. As in Figure 8.4, we show the TDoS for several cluster sizes $N_c = 1$, 4^3, and $= 6^3$ in order to show its systematic convergence with increasing cluster size N_c. The average DoS converges for cluster sizes beyond $N_c = 4^3$. The TDoS is finite for the extended states and zero for localized states. The mobility edges are extracted as described in Figure 8.4.

in its capability of capturing the effects of rather a large system sizes. Thus, TMM provides good data for a finite size scaling analysis to capture the critical points and the corresponding exponents. In our calculations, the transmission of states down a three-dimensional bar of widths $M = [6, 12]$ and length $L = 2 \times 10^4 M$ are studied by adding the products of the transfer matrices with random initial states. The multiplication of transfer matrices is numerically unstable. To avoid this instability, we orthogonalized the transfer matrix product every five multiplications using a Lapack QR

decomposition [132]. The localization edge is obtained by calculating the Kramer-MacKinnon scaling parameter Λ_M [250]. This is a dimensionless quantity which should be invariant at the critical point, that is, Λ_M scales as a constant for $M \to \infty$. [106] Thus, we determine the boundary of the localization transition vis-à-vis the critical disorder strength [223] by performing a linear fit to Λ_M v. M data: localized states will have a negative slope and vice-versa for extended states. The transfer-matrix method finite size effects are larger for weak disorder where the states decay slowly with distance and so have large values of Λ_M that carry a large variance in the data. Notice that the CPA and the DCA do not suffer such finite size effect limitation for small disorder and are, in fact, exact in this limit.

The mobility edges shown in Figure 8.7 and Figure 8.8 were extracted from the TDoS, with boundaries being defined by zero TDoS. As can be seen in Figure 8.7 and Figure 8.8, while the single-site TMT does not change much under the effect of the off-diagonal disorder, the TMDCA

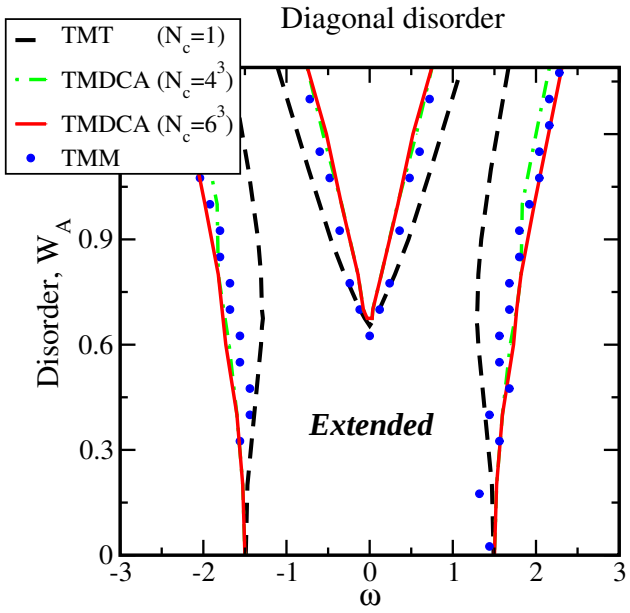

Figure 8.7: Disorder-energy phase diagram for the diagonal disorder case. Parameters used are: $t^{AA} = t^{BB} = t^{AB} = 1.0$, and $c_A = 0.5$. We compare the mobility edges obtained from the TMT $N_c = 1$ (black dash line), TMDCA with $N_c = 4^3$ (green dot-dashed line) and $N_c = 6^3$ (red solid line), and the transfer-matrix method (TMM) (blue dotted line). The single site $N_c = 1$ results strongly underestimate the extended states region when compare with TMDCA results for $N_c > 1$. The mobility edges obtained from the finite cluster TMDCA ($N_c > 1$) show good agreement with those obtained from the TMM, in contrast to single site TMT. See the text for parameters and details of the TMM implementation.

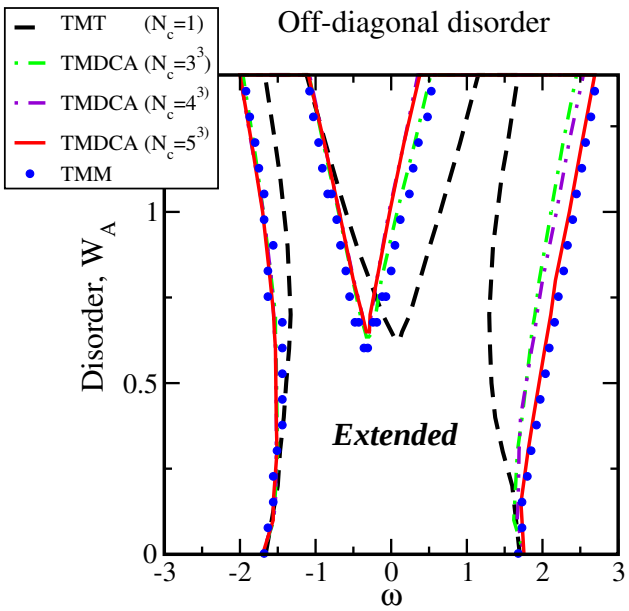

Figure 8.8: Disorder-energy phase diagram for the off-diagonal disorder case. Parameters used are: $t^{AA} = 1.5$, $t^{BB} = 0.5$, $t^{AB} = 1.0$, and $c_A = 0.5$. The mobility edges obtained from the TMT $N_c = 1$ (black dashed line), TMDCA $N_c = 3^3$ (green dot-dashed line), $N_c = 4^3$ (purple double-dot-dashed line) and $N_c = 5^3$ (red solid line), and the transfer-matrix method (TMM) (blue dotted line). The single site $N_c = 1$ strongly underestimates the extended states region especially for higher values of W_A. The mobility edges obtained from the finite cluster TMDCA ($N_c > 1$) converge gradually with increasing N_c and show good agreement with those obtained from the TMM, in contrast to single site TMT. See the text for parameters and details of the TMM implementation.

results are significantly modified. The bands for a larger cluster become highly asymmetric with significant widening of the A subband. The local $N_c = 1$ boundaries are narrower than those obtained for $N_c > 1$ indicating that the TMT strongly underestimates the extended states regime in both diagonal and off-diagonal disorder. On the other hand, comparing the mobility edge boundaries for $N_c > 1$ with those obtained using TMM, we find very good agreement. This again confirms the validity of our generalized TMDCA.

Next, we consider the effect of off-diagonal disorder for various concentrations c_A. In Figure 8.9, we show the typical and average DoS for several values of c_A calculated with the TMDCA and the DCA, respectively. As expected, when $c_A \to 0$, we obtain a pure B subband contribution (the top panel). Upon gradual increase of the c_A concentration, the number of states in the A subband grows until B-subband becomes a minority for $c_A > 0.5$ and completely disappears at $c_A \to 1$ (the bottom panel). Again, we see that a finite cluster $N_c = 5^3$ provides a more accurate description

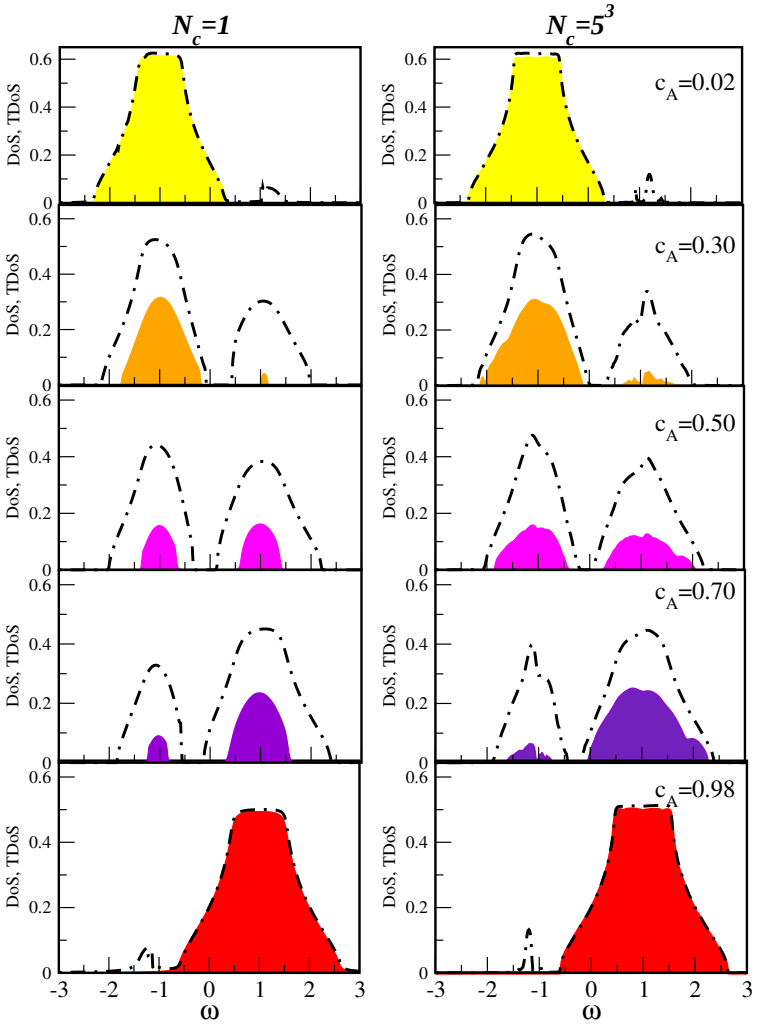

Figure 8.9: The average DoS (dot-dashed lines) and the typical DoS (shaded regions) for various values of the concentration c_A with off-diagonal disorder parameters $t^{AA} = 1.1$, $t^{BB} = 0.9$ and $t^{AB} = 1.0$, at fixed local potential $W_A = 1.0$ for $N_c = 1$ (left panel) and $N_c = 5^3$ (right panel).

(with finite details in DoS and broader regions of extended states in TDoS).

The associated contour plots for the evolution of the TDoS in the concentration range $0 \leq c_A \leq 1$ are shown in Figure 8.10. The essence of these plots is to show the overall evolution of the typical DoS for a fixed local potential and off-diagonal disorder parameters as a function of the concentration c_A. In the limit of $c_A \to 0$, only the B-subband centered around $\omega = -W_A$ survives, and for $c_A \to 1$, only the A-subband centered around $\omega = W_A$ is present. For intermediate concentrations, we clearly have contributions to the total typical density of states for both species, as expected.

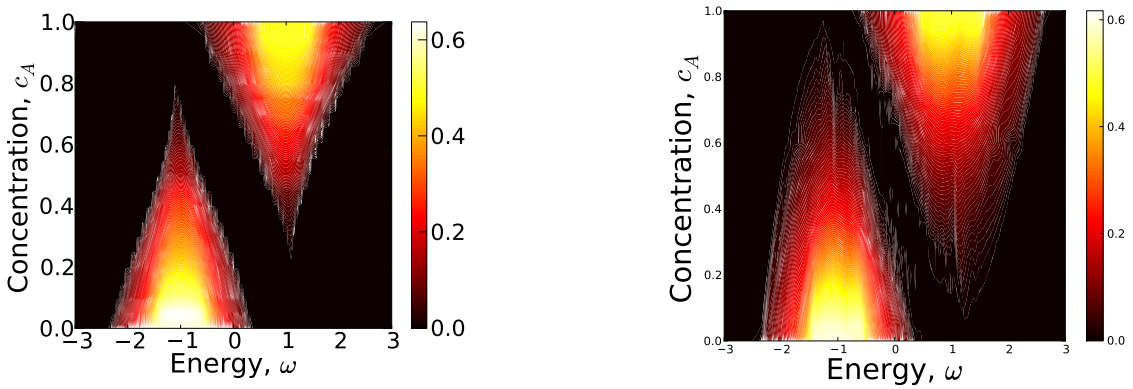

Figure 8.10: The evolution of the typical density of states for $N_c = 1$ (left panel) and $N_c = 5^3$ (right panel) with the change in the concentration $0 < c_A < 1$ at fixed diagonal and off-diagonal disorder parameters: $t^{AA} = 1.1$, $t^{BB} = 0.9$, $t^{AB} = 1.0$ and $W_A = 1.0$

Finally, we would like to comment on the possible further development of the presented scheme. After certain generalizations our current implementation of the typical medium dynamical cluster approximation for the off-diagonal disorder can serve as the natural formalism for multiband (multiorbital) systems. [319] Such an extension is crucial for studying disorder and localization effects in real materials. Further development towards this direction will be the subject of future publications.

8.5 Conclusion

A proper theoretical description of disordered materials requires the inclusion of both diagonal and off-diagonal randomness. In this chapter, we have extended the BEB single site CPA scheme to a finite cluster DCA that incorporates the effect of non-local disorder. Applying the generalized DCA scheme to a single band tight binding Hamiltonian with configuration-dependent hopping amplitudes, we have considered the effects of non-local disorder and the interplay of diagonal and off-diagonal disorder on the average density of states. By comparing our results with those from exact numerical methods, we have established the accuracy of our method. We found that non-local multi-site effects lead to the development of finite structures in the density of states and the partial filling of the gap at larger disorder. Utilizing the self-energy, we show as a function

of increasing disorder strengths, the importance of a finite cluster in characterizing the Anderson localization transition. For small disorder the single site and finite cluster results are essentially the same, indicating that the CPA is a good approximation in the small disorder regime. However, for a larger disorder we observe a significant momentum dependence in the self-energy resulting from the non-local correlations which are incorporated in the DCA.

Electron localization for off-diagonal disorder models have not been studied from the typical medium perspective. In this chapter, we generalized the TMDCA to systems with both diagonal and off-diagonal disorder. Our developed method can quantitatively and qualitatively be used to study the effects of disorder on the electron localization, effectively for systems with both diagonal and off-diagonal randomness.

We show that within the TMDCA, the TDoS vanishes for localized states and is finite for states which are extended. Employing the TDoS as an order parameter for Anderson localization, we have constructed the disorder-energy phase diagram for systems with both diagonal and off-diagonal disorder. We also demonstrate the inability of the single site CPA and the TMT methods to accurately capture the localization and disorder effects in both the average and the typical DoS, respectively. We note that the single site TMT while being able to capture the behavior of the diagonal and off-diagonal disorder, strongly underestimates the extended regions. Also the TMT is less sensitive to the off-diagonal randomness with the mobility edges being only slightly modified as compared to the diagonal case. In contrast, the finite cluster TMDCA results are able to capture the considerable changes, with a pronounced asymmetry of the extended state region, in the disorder-energy phase diagram under the effect of the off-diagonal disorder as compared to the diagonal case. Most importantly, the TMDCA results are found to be in a quantitative agreement with exact numerical results. Comparing our results with KPM, exact diagonalization, and TMM, we find good agreement with our extended DCA and TMDCA. To the best of our knowledge, this is the first numerically accurate investigation of the Anderson localization in systems with off-diagonal disorder within the framework of the typical medium analysis. We believe that the extended TMDCA scheme presents a powerful tool for treating both diagonal and off-diagonal disorder on equal footing, and can be easily extended to study localization in multi-band systems.

Chapter 9

Application of Typical Medium Dynamical Cluster Approximation to Multiband Disordered System

9.1 Introduction

Diverse theoretical and numerical methods have been developed for studying disorder and correlations in materials. For the single-band systems, many techniques/methods have been formulated for tackling the many-body impurity. These computational techniques which are of varying complexity not limited to exact numerical methods [320], quantum Monte Carlo (QMC) [321], numerical renormalization group [322], and many other schemes [104, 255, 257, 261, 323]. However, for realistic multiband systems, the impurity solver of choice have mainly being the QMC [324–326], variants of the iterative perturbation theory [327–329], configuration interaction (CI) [323], and the fluctuation exchange method (FLEX) [330]. However, due to the minus sign problem at low temperatures [331], the QMC have been severely limited, and only applicable to Ising-like exchange interactions. Note, there are other variants of the QMC formalism that do not suffer from the sign problem (at least at the single-band level), for e.g., Ref. [332], and some other versions that work with another exchange interactions, for e.g., a version of QMC with Hund's exchange correlations which work at two extreme limits: zero temperature [333] and at relatively high temperatures ($T \gtrsim 1500K$) [334]. The most realistic step in making the QMC applicable at low temperatures have been the continuous-time QMC method [332, 335], and the Hirsch-Fye solver plus a perturbation series expansion [336].

No doubt, these impurity/cluster solvers are powerful and are exact to within computational/statistical errors, they do require the diagonalization of large lattices for any reasonable accuracy to be obtained. Most importantly, most of these methods are developed in the Matsubara frequency as such, requiring the analytical continuation of the data before real frequency information can be

accessed. There is no doubt that analytical continuation may introduce uncontrollable statistical uncertainties, a typical ill-posed problem [337] but the Padé approximation [338] and maximum-entropy method [337, 339] have been reported to produce reliable real frequency data. Aside the Matsubara frequency based methods, one can work directly with other approximation methods that work in the real frequency, such as the slave bosons, noncrossing approximation (NCA), numerical renormalization group (NRG), exact diagonalization, and so on [104, 328, 340]. Each of the above impurity solvers have their advantages and disadvantages. For example, exact diagonalization can consider only a limited number of bath sites and cannot be adapted to study systems with interactions, even an interaction as simple as a single impurity coupling, NRG is only reliable at low energies, and NCA is limited to high temperatures.

For the study of localization transitions for multiband electronic systems, any of these impurity/cluster solvers can be adapted. However, efforts so far have been limited to studying other important material properties like antiferromagnetism, superconductivity, etc. But the ubiquity of disorder is such that neglecting it is at one's peril. Thus, a systematic incorporation of the effects of disorder which is always present in varying forms in materials is paramount. Within the density function theory community, variants of the supercell methods have been frequently used to study the effects of disorder in materials [341, 342]. But still, they don't characterize the localization transitions.

In this Chapter, the typical medium theory will be recast for studying localization transitions in a multiband systems, building on the successful formulated of the TMDCA for the single-band system. Since the TMDCA formalism utilizes the DCA framework, it will first be formulated within the DCA and then the TMDCA. Multiband becomes imperative as realistic materials have orbital degrees of freedom. Unlike the single-band systems, multiband systems take into account the influence of the localized electrons with orbital degrees of freedom.

9.2 Extension of the Single-band TMDCA to Multiband: Formalism

As a progress towards the application of the typical medium dynamical cluster approximation to realistic systems, here, I will outline the steps needed to generalize the single-band TMDCA to a two-band. Since the TMDCA uses the self-consistency of the dynamical cluster approximation aside the utilization of an environment characterized by the typical medium, I will first generalize the single band DCA to its multiband version and then to the TMDCA.

9.2.1 Multiband Formalism for Dynamical Cluster Approximation

For the multiband, the Hamiltonian (Equation 4.1) becomes

$$\hat{H} = \sum_{<i,j>;\alpha\beta} t_{ij}^{(\alpha\beta)} (c_{i\alpha}^{\dagger} c_{j\beta} + c_{j\alpha}^{\dagger} c_{i\beta}) + \sum_{i\alpha} (V_i^{(\alpha\beta)} - \mu) n_i^{(\alpha\beta)} - J_c \sum_i \hat{S}_i \hat{s}_i. \tag{9.1}$$

The first term provides a realistic multiband description of the host valence bands. The operators $c_i^{\dagger}(c_i)$ create (annihilate) a quasiparticle on site i. The second part denotes the disorder, which is modeled by a local potential V_i that is randomly distributed according to some specified probability distribution $P(V_i)$, where $n_i = c_i^{\dagger} c_i$ is the number operator, μ is the chemical potential, i and j are site indices, α, β label the bands ($\alpha, \beta = 1, ..., L_B$), L_B is the number of bands, and $t_{ij}^{(\alpha\beta)}$ is the hopping matrix element

$$t_{ij}^{\alpha\beta} = t_{ij}^{\alpha} \delta_{\alpha\beta} + \Upsilon \delta_{ij} \tag{9.2}$$

where $t^{\alpha}\delta_{\alpha\beta}$ is the orbital-dependent nearest-neighbor hopping and Υ is the hybridization between the two orbitals. We set $4t = 1$ as the energy unit. Observe that for $\Upsilon = 0$, Equation 9.1 reduces to multi-orbital Anderson model with distinct (decoupled) orbitals. The third part denotes the interaction between itinerant carrier spins $\hat{s}_i$ and localized impurity spins $\hat{S}_i$ ($S = 5/2$ for e.g., Mn^{2+}). J_c is the local Hund's coupling for e.g., Mn-d orbitals. For the time being, I will neglect the coupling ($J_c = 0$).

For this study, an alloy model distributions (4.2d), which can be composed of many atoms

$A_{1-x}BCDEF...G_xH$ or the familiar binary alloy model $A_{1-x}B_x$. Equation 4.2d then becomes

$$P_{MB}(\underline{V_i^{(\alpha\beta)}}) = c_a\delta(\underline{V_i} - \underline{W_A}^{\alpha\beta}) + c_b\delta(\underline{V_i} - \underline{W_B}^{\alpha\beta}). \tag{9.3}$$

where $c_b = 1 - c_a$ is the concentration, W_A and W_B is the strength of the disorder, the subscript *MB* denotes multiband, and the random potential becomes

$$\underline{V_i} = \begin{pmatrix} V_i^{\alpha\alpha} & \cdots & V_i^{\alpha\beta} \\ . & . & . \\ . & . & . \\ . & . & . \\ V_i^{\beta\alpha} & \cdots & V_i^{\beta\beta} \end{pmatrix} \tag{9.4}$$

For the single band, diagonal disorder model, the random potential is local in nature. However, as it is obvious from Equation 9.4, the random potential here is both site and band dependent, and also depends on the hopping amplitude of the electrons $t_{ij}^{\alpha\beta}$

$$t_{ij} = \begin{cases} t_{ij}^{\alpha\alpha}, \text{ if } \quad i \in \alpha, \quad j \in \alpha \\ t_{ij}^{\alpha\beta}, \text{ if } \quad i \in \alpha, \quad j \in \beta \\ t_{ij}^{\beta\alpha}, \text{ if } \quad i \in \beta, \quad j \in \alpha \\ t_{ij}^{\beta\beta}, \text{ if } \quad i \in \beta, \quad j \in \beta, \end{cases} \tag{9.5a}$$

which in momentum space (assuming only near-neighbor hopping) is nothing but a $L_B \times L_B$ matrix (underbar denotes matrix) of the form

$$\underline{\overline{\varepsilon}(K)} = \begin{pmatrix} E_0^{\alpha\alpha} + \frac{N_c}{N}\sum_{\tilde{k}}\varepsilon_k & \cdots & E_0^{\alpha\beta} + \frac{N_c}{N}\sum_{\tilde{k}}\varepsilon_k \\ . & . & . \\ . & . & . \\ . & . & . \\ E_0^{\beta\alpha} + \frac{N_c}{N}\sum_{\tilde{k}}\varepsilon_k & \cdots & E_0^{\beta\beta} + \frac{N_c}{N}\sum_{\tilde{k}}\varepsilon_k \end{pmatrix} \tag{9.5b}$$

where for a d-dimensional hypercubic lattice with a unit lattice spacing, $\varepsilon_k = -2t\sum_i^d \cos k_i$, $\mathbf{k} = (k_1, ..., k_d)$, and E_0 is a local energy which can be used to shift the bands. Following the description of the DCA framework, the first Brillouin zone is divided into $N_c = L^d$ coarse-grained cells with $\mathbf{K}$ centers surrounded by $\tilde{k}$-points within the cell such that $k = \mathbf{K} + \tilde{k}$. The DCA is characterized by a non-local hybridization matrix function $\underline{\Gamma(\mathbf{K}, \omega)}$

$$\underline{\Gamma(\mathbf{K}, \omega)} = \begin{pmatrix} \Gamma^{\alpha\alpha}(\mathbf{K}, \omega) & \cdots & \Gamma^{\alpha\beta}(\mathbf{K}, \omega) \\ . & . & . \\ . & . & . \\ . & . & . \\ \Gamma^{\beta\alpha}(\mathbf{K}, \omega) & \cdots & \Gamma^{\beta\beta}(\mathbf{K}, \omega) \end{pmatrix} \tag{9.6}$$

While the DCA is a $\mathbf{K}$-dependent formalism, the cluster problem solve is always solved in real space as to enable the incorporation of the disorder. For this, a stochastically generated random configurations of the disorder potential V is used to calculate the cluster Green function which is now an $N_c \times N_c$ matrix as

$$\underline{G}_{ij} = \left(\omega\mathbb{I} - \underline{t}'^{(\alpha\beta)} - \underline{\Gamma}'^{(\alpha\beta)} - \underline{V}^{\alpha\beta}\right)^{-1}_{ij} \tag{9.7}$$

where $\mathbb{I}$ is the identity matrix and the primes denote Fourier transform (FT) components of the hybridization and hopping matrix, respectively. I.e.,

$$\Gamma'_{ij} = \begin{cases} FT(\Gamma^{\alpha\alpha}(\mathbf{K}, \omega)), \text{ if } \quad i \in \alpha, \quad j \in \alpha \\ FT(\Gamma^{\beta\beta}(\mathbf{K}, \omega)), \text{ if } \quad i \in \beta, \quad j \in \beta \\ FT(\Gamma^{\alpha\beta}(\mathbf{K}, \omega)), \text{ if } \quad i \in \alpha, \quad j \in \beta \\ FT(\Gamma^{\beta\alpha}(\mathbf{K}, \omega)), \text{ if } \quad i \in \beta, \quad j \in \alpha \end{cases} \tag{9.8a}$$

and

$$t'_{ij} = \begin{cases} FT(\overline{\varepsilon}^{\alpha\alpha}(\mathbf{K})), \text{ if } \quad i \in \alpha, \quad j \in \alpha \\ FT(\overline{\varepsilon}^{\beta\beta}(\mathbf{K})), \text{ if } \quad i \in \beta, \quad j \in \beta \\ FT(\overline{\varepsilon}^{\alpha\beta}(\mathbf{K})), \text{ if } \quad i \in \alpha, \quad j \in \beta \\ FT(\overline{\varepsilon}^{\beta\alpha}(\mathbf{K})), \text{ if } \quad i \in \beta, \quad j \in \alpha \end{cases} \tag{9.8b}$$

where for e.g., $FT(\Gamma^{\alpha\beta}(\mathbf{K},\omega)) = \sum_{\mathbf{K}} \Gamma^{\alpha\beta}(\mathbf{K},\omega) e^{i\mathbf{K}(r_i - r_j)}$. From Equation 9.8 $\overline{\Gamma'}^{\alpha\beta}_{ij}$ and $\overline{t'}^{\alpha\beta}_{ij}$ are now $N_c \times N_c$ real-space matrices. As explained in previous chapters, Γ'_{ij} is a measure of the hybridization (escape rate) between the sites/cluster i and j and the effective medium. Hence, intuitive, the component of the bands $\alpha\alpha$ of the hybridization rate corresponds to both bands α sitting at lattice sites i and j. Similarly, the $\alpha\beta$ bands imply that the site i and j is corresponds to the band α and β, respectively. The description applies to t the $\beta\beta$ and $\beta\alpha$. The hopping matrix shares the same description above as the hybridization function.

To solve the cluster problem, we recast Equation 9.7 into an $L_B N_c \times L_B N_c$ matrix and calculate the disorder averaged cluster Green function

$$\underline{G_c(\omega)_{ij}} = \begin{pmatrix} \langle G_c^{\alpha\alpha}(\omega) \rangle_{ij} & \cdots & \left\langle G_c^{\alpha\beta}(\omega) \right\rangle_{ij} \\ . & . & . \\ . & . & . \\ . & . & . \\ \left\langle G_c^{\beta\alpha}(\omega) \right\rangle_{ij} & \cdots & \left\langle G_c^{\beta\beta}(\omega) \right\rangle_{ij} \end{pmatrix} \tag{9.9}$$

which, can be done by assigning each components according to the band indices α and β of the sites i and j

$$\begin{aligned} (G_c^{\alpha\alpha})_{ij} &= (G_c)_{ij} \text{ if } \quad i \in \alpha, \quad j \in \alpha \\ (G_c^{\beta\beta})_{ij} &= (G_c)_{ij} \text{ if } \quad i \in \beta, \quad j \in \beta \\ (G_c^{\alpha\beta})_{ij} &= (G_c)_{ij} \text{ if } \quad i \in \alpha, \quad j \in \beta \\ (G_c^{\beta\alpha})_{ij} &= (G_c)_{ij} \text{ if } \quad i \in \beta, \quad j \in \alpha \end{aligned} \tag{9.10}$$

Note, each of the diagonal bands in Equation 9.10 is normalized as a consequence of Equation 9.9 just like a conventional Green function. For example, a realistic cubic system with a perfect crystal field splitting, Equation 9.9 corresponds to

$$G_c(\omega)_{ij} = \begin{pmatrix} \left\langle G_c^{t_{2g}}(\omega)\right\rangle_{ij} & 0 & 0 & 0 & 0 \\ 0 & \left\langle G_c^{t_{2g}}(\omega)\right\rangle_{ij} & 0 & 0 & 0 \\ 0 & 0 & \left\langle G_c^{t_{2g}}(\omega)\right\rangle_{ij} & 0 & 0 \\ 0 & 0 & 0 & \left\langle G_c^{e_g}(\omega)\right\rangle_{ij} & 0 \\ 0 & 0 & 0 & 0 & \left\langle G_c^{e_g}(\omega)\right\rangle_{ij} \end{pmatrix} \tag{9.11}$$

where t_{2g} and e_g correspond to the crystal field splitting of the d-orbital into the higher and lower energy components, respectively. Having obtained the disorder averaged cluster Green functions since the DCA is a **K**-space-based formalism, a Fourier transformation is to momentum space is carried using Equation 9.10 as

$$\underline{G_c(\mathbf{K},\omega)} = \begin{pmatrix} G_c^{\alpha\alpha}(\mathbf{K},\omega) & \cdots & G_c^{\alpha\beta}(\mathbf{K},\omega) \\ . & . & . \\ . & . & . \\ . & . & . \\ G_c^{\beta\alpha}(\mathbf{K},\omega) & \cdots & G_c^{\beta\beta}(\mathbf{K},\omega) \end{pmatrix} \tag{9.12}$$

Now that we have the **K**-dependent cluster Green functions, coarse-graining over the cluster cells to obtain the lattice Green function

$$\underline{\overline{G}(\mathbf{K},\omega)} = \begin{pmatrix} \overline{G}^{\alpha\alpha}(\mathbf{K},\omega) & \cdots & \overline{G}^{\alpha\beta}(\mathbf{K},\omega) \\ . & . & . \\ . & . & . \\ . & . & . \\ \overline{G}^{\beta\alpha}(\mathbf{K},\omega) & \cdots & \overline{G}^{\beta\beta}(\mathbf{K},\omega) \end{pmatrix} = \frac{N_c}{N}\sum_{\tilde{k}} \left(\underline{G_c(\mathbf{K},\omega)}^{-1} + \underline{\Gamma(\mathbf{K},\omega)} - \underline{\varepsilon_k} + \underline{\overline{\varepsilon}(\mathbf{K})}\right)^{-1}, \tag{9.13}$$

where the overbar denotes cluster coarse-graining. Just as in Equation 9.10, the diagonal components of Equation 9.13 have the same normalization of a conventional, i.e., scalar, Green function.

Since the DCA medium is characterized by the non-local hybridization functions, we close the self-consistency loop by updating the corresponding hybridization functions for each band

$$\Gamma_n^{\alpha\beta}(\mathbf{K},\omega) = \Gamma_o^{\alpha\beta}(\mathbf{K},\omega) + \xi\left(G_c^{-1}(\mathbf{K},\omega)^{\alpha\beta} - \overline{G}^{-1}(\mathbf{K},\omega)^{\alpha\beta}\right) \tag{9.14}$$

where 'o' and 'n' denote old and new, respectively, and ξ is a linear mixing parameter $0 < \xi < 1$. The above outlined steps are iterated until convergence using the DCA self-consistency requirements that the disorder averaged cluster and the coarse-grained lattice Green functions should be equal

$$\underline{G_c(\mathbf{K},\omega)} = \underline{\overline{G}(\mathbf{K},\omega)}\,. \tag{9.15}$$

This is equivalent to a system of $\alpha \times \beta$ coupled scalar equations

$$\overline{G}^{\alpha\beta}(\mathbf{K},\omega) = G_c^{\alpha\beta}(\mathbf{K},\omega). \tag{9.16}$$

For the case when $t^{\alpha\beta} = t^{\beta\alpha}$, $\overline{G}^{\alpha\beta}(\mathbf{K},\omega) = \overline{G}^{\beta\alpha}(\mathbf{K},\omega)$ by default. At convergence, the hybridization function also converges as $\underline{\Gamma_n^{\alpha\beta}(\mathbf{K},\omega)} = \underline{\Gamma_o^{\alpha\beta}(\mathbf{K},\omega)}$.

9.2.2 Multiband Formalism for Typical Medium Dynamical Cluster Approximation

The dynamical cluster approximation incorporates all the important spatial correlations, improving upon the capabilities of the local coherent potential approximation. However, for the characterization of localization transitions, both the CPA, DCA, and other variants of the mean-field theory are not adequate due mainly to the way their effective medium are defined. As demonstrated in Chapters 7 and 6 (for the diagonal non-interacting system), Chapter 8 (for the diagonal and off-diagonal non-interacting disordered system, and will be further confirmed in Chapter 10 (for the interacting and disordered systems), the typical density of states (TDoS) if properly defined is the approximation order parameter for characterizing electron localization as it vanishes for states which are localized and it is finite for extended states.

The task here will be the generalization of the scalar TMDCA into a matrix form. For the time being, the focus will be only for two band model. Note, the original typical medium theory (TMT) as well as the TMDCA are both ad hoc. The same can be said for its generalization to a multiband system. However, in constructing the TMDCA ansatz both for the single-band and the multiband systems, important physical limits must be satisfied. Those physical limits have been carefully checked and indeed, the TMDCA (cf. Subsection 5.3.2) for both single-band and multiband are systematic. For clarity, I will repeat them here: For $\mathrm{N}_c = 1$, the TMDCA should reduce to the local TMT scheme with $\rho^c_{typ}(\omega) = \exp\langle \ln \rho(\omega)\rangle$; At weak disorder strength, $W \ll W_c$, the real space prefactor becomes $\langle \ln \rho_i(\omega, V_i)\rangle \approx \ln \langle \rho_i(\omega, V_i)\rangle$. Then $\rho^c_{typ}(\mathbf{K}, \omega)$ reduces to the DoS calculated in DCA scheme, with $\rho^c_{typ}(\mathbf{K}, \omega) \approx \langle \rho^c(\mathbf{K}, \omega, V)\rangle$; above all, it should be causal and obey all the qualities of a good cluster theory as outlined in Subsection 4.1.2.

Just as in the TMDCA analysis instead of using the algebraically averaged cluster Green function in the self-consistency loop, typical averaging is utilized. The scalar typical density of states (cf. Equation 5.11) becomes a $L_B \times L_B$ matrix

$$\underline{\rho^c_{typ}(\mathbf{K}, \omega)} = \begin{pmatrix} \exp\left(\frac{1}{N_c}\sum_{i=1}^{N_c}\left\langle \ln \rho^{\alpha\alpha}_{ii}(\omega)\right\rangle\right)\vartheta^{\alpha\alpha} & \cdots & \varphi^{\alpha\beta}(\vartheta^{\alpha\beta}) \\ . & . & . \\ . & . & . \\ . & . & . \\ \varphi^{\beta\alpha}(\vartheta^{\beta\alpha}) & \cdots & \exp\left(\frac{1}{N_c}\sum_{i=1}^{N_c}\left\langle \ln \rho^{\beta\beta}_{ii}(\omega)\right\rangle\right)\vartheta^{\beta\beta} \end{pmatrix} \tag{9.17}$$

where

$$\vartheta^{\alpha\alpha} = \left\langle \frac{-\frac{1}{\pi}\Im G_c^{\alpha\alpha}(\mathbf{K},\omega)}{\frac{1}{N_c}\sum_{i=1}^{N_c}(-\frac{1}{\pi}\Im G_{ii}^{\alpha\alpha}(\omega))} \right\rangle \tag{9.18a}$$

$$\vartheta^{\beta\beta} = \left\langle \frac{-\frac{1}{\pi}\Im G_c^{\beta\beta}(\mathbf{K},\omega)}{\frac{1}{N_c}\sum_{i=1}^{N_c}(-\frac{1}{\pi}\Im G_{ii}^{\beta\beta}(\omega))} \right\rangle \tag{9.18b}$$

$$\vartheta^{\alpha\beta} = \vartheta^{\beta\alpha} = \exp\left(\frac{1}{2N_c}\sum_{i=1}^{N_c}(\langle \ln \rho_{ii}^{\alpha\alpha}(\omega)\rangle + \left\langle \ln \rho_{ii}^{\beta\beta}(\omega)\right\rangle)\right) \tag{9.18c}$$

$$\varphi^{\alpha\beta} = \left\langle \frac{-\frac{1}{\pi}\Im G_c^{\alpha\beta}(\mathbf{K},\omega)}{\frac{1}{2N_c}\sum_{i=1}^{N_c}[(-\frac{1}{\pi}\Im G_{ii}^{\alpha\alpha}(\omega)) + (-\frac{1}{\pi}\Im G_{ii}^{\beta\beta}(\omega))]} \right\rangle \tag{9.18d}$$

$$\varphi^{\beta\alpha} = \left\langle \frac{-\frac{1}{\pi}\Im G_c^{\beta\alpha}(\mathbf{K},\omega)}{\frac{1}{2N_c}\sum_{i=1}^{N_c}[(-\frac{1}{\pi}\Im G_{ii}^{\alpha\alpha}(\omega)) + (-\frac{1}{\pi}\Im G_{ii}^{\beta\beta}(\omega))]} \right\rangle \tag{9.18e}$$

To continue the self-consistency loop, a Hilbert transform of Equation 9.18 is carried out to obtain the typical cluster Green function

$$\underline{G_c(\mathbf{K},\omega)} = \begin{pmatrix} \int d\omega' \frac{\rho_{typ}^{\alpha\alpha}(\mathbf{K},\omega')}{\omega-\omega'} & \cdots & \int d\omega' \frac{\rho_{typ}^{\beta\alpha}(\mathbf{K},\omega')}{\omega-\omega'} \\ . & . & . \\ . & . & . \\ . & . & . \\ \int d\omega' \frac{\rho_{typ}^{\alpha\beta}(\mathbf{K},\omega')}{\omega-\omega'} & \cdots & \int d\omega' \frac{\rho_{typ}^{\beta\beta}(\mathbf{K},\omega')}{\omega-\omega'} \end{pmatrix} \tag{9.19}$$

and the disorder averaged cluster Green function is easily obtained from Equation 9.19. Once the disorder averaged cluster Green function is obtained, the self-consistency loop continues just as in the DCA for the multiband case as outlined in Subsection 9.2.1. The above sets of equations provide the generalization of the TMDCA for the multiband systems.

Limiting Cases: As as explained above, the TMDCA for the multiband case must satisfy the physical limiting cases as in the single band TMDCA, viz: **i**) Assuming no hybridization of any form exists between the two bands, i.e., $t^{\alpha\beta} = 0$ and $W^{\alpha\beta} = 0$, this corresponds to two independent

bands each, being a single diagonal band since the off-diagonal bands in Equation 9.17 vanishes. For $N_c = 1$, in this diagonal picture, the typical density of states reduces to the exponential prefactor which is the exact form of the local TMT. **ii**) At weak disorder, the multiband TMDCA reduces to the DCA multiband since the the geometrically averaged local prefactor of the TDoS numerically cancels the algebraically averaged local term in the denominator of Equation 9.17. This is obvious from the fact that $exp(\langle \ln \rho_i(\omega, V_i)\rangle) \approx exp(\ln \langle \rho_i(\omega, V_i)\rangle) \Rightarrow \langle \rho_i(\omega, V_i)\rangle$. Unless stated otherwise, in the subsequent sections, only two-bands will be considered so that $\alpha, \beta = 1, 2$.

9.3 Benchmarking the Multiband TMDCA with KPM

Just as in the case of the single band typical medium dynamical cluster approximation (TMDCA), here, a comparison with numerically exact calculations using the kernel polynomial method (KPM) will be carried out. This becomes imperative as to ascertain how the TMDCA benchmarks with the KPM for various parameter regimes.

Figure 9.1 shows a comparison plot of the DCA (TMDCA) with the KPM for varying off-diagonal disorder, $W_{ab} = 0.3$ and 1.1, respectively at a fixed diagonal disorder strengths $W_a = W_b = 0.7$ and zero inter-band hopping. Since the disorder strengths on bands 1 and 2 are the same, only one band is shown for each parameter set. Observe that both the DCA and the TMDCA compare rather well with the KPM data for both limits: weak inter-band disorder ($W_{ab} = 0.3$) and strong inter-band disorder ($W_{ab} = 1.1$). Slight discrepancy is observed for the TMDCA data, however, all critical points clearly benchmark well with the typical density of states from the KPM. For the weak inter-band disorder coupling, Figure 9.1 resembles the single-band results (cf. Chapter 8, Section 8.3). This is expected since the coupling between the bands is weak and they tend to behave as two independent orbitals. However, as the disorder strength of the inter-band is increased, additional two small peaks develop between the two large bands leading to a very strong renormalization of the density of states. Observe further that the central gap opening at the band center is maintained while a secondary gap appears at approximately at $\omega = \pm 0.7$ which coincidentally, corresponds to the strength of the diagonal disorder strength on the bands.

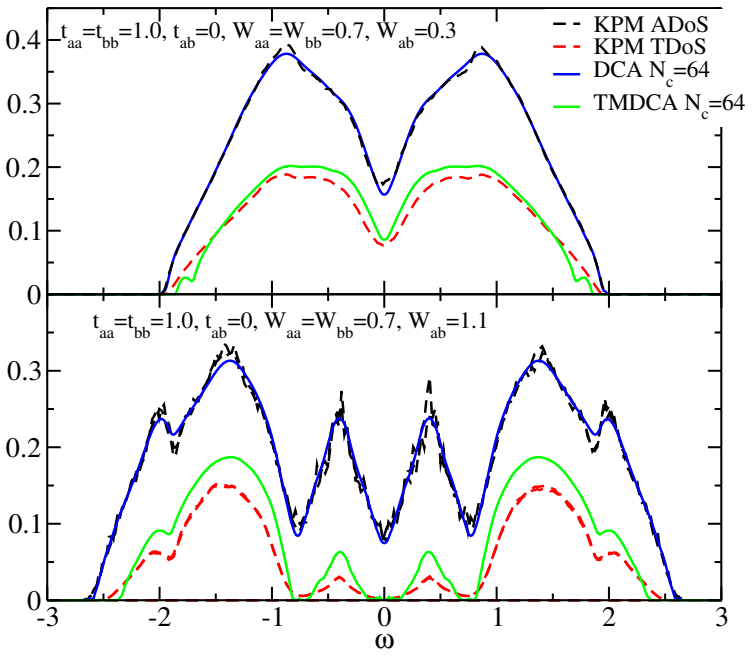

Figure 9.1: The benchmark of the (Dynamical cluster approximation) (typical medium DCA) with the kernel polynomial method at a fixed diagonal disorder strength $W_a = W_b = 0.7$ for varying off-diagonal disorder strengths, W_{ab}. Finite cluster of 64 has been used for the DCA (TMDCA).

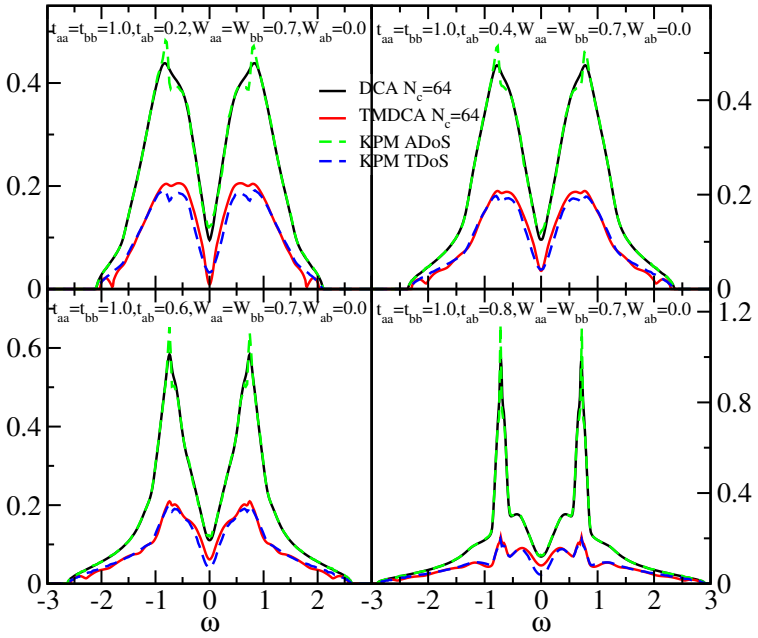

Figure 9.2: The benchmark of the (Dynamical cluster approximation) (typical medium DCA) with the kernel polynomial method at a fixed diagonal disorder strength $W_a = W_b = 0.7$ for varying off-diagonal hopping, t_{ab}. Finite cluster of 64 has been used for the DCA (TMDCA).

Some systems are inter-hopping dominated e.g., PdTe [343]. To check the applicability of the developed multiband formalism for such systems, a comparison of the DCA (TMDCA) with their KPM counterparts are depicted in Figure 9.2 for weak, intermediate, strong, and very strong inter-band hopping, respectively, at a fixed on-site disorder strengths for bands 1 and 2, respectively. Note, inter-band disorder strength is zero. Again, rather a good qualitative and quantitative benchmark with the KPM is observed. Both the ADoS and the TDoS from the DCA (TMDCA) and the KPM both show a gap at $\omega = 0$ for all parameter ranges while a secondary shoulder starts to develop at the strong inter-band hopping value.

9.4 Conclusion

In this chapter, I have presented the extension of the dynamical cluster approximation (DCA) and the typical medium DCA for applications in multi-band systems. In tandem with the objective of this dissertation, which is to develop a method that is also applicable for realistic materials study, the multi-band system becomes imperative as no system has a single-band. Various parameter regimes are explored. It should be noted that these are the extreme of the parameter regimes. Most importantly, the TMDCA results are found to be in a quantitative agreement with exact numerical results. Comparing the results from kernel polynomial, remarkably good agreement with the DCA and TMDCA are observed. The multi-band TMDCA offers a platform for doing realistic materials simulations to study electron localization since the tight band parameters can be utilized directly.

Chapter 10

Application of Typical Medium Dynamical Cluster Approximation to Interacting Disordered Electron System

10.1 Introduction

In the absence of a spontaneous symmetry breaking field, the valence band of a half-filled non-degenerate electron system may undergo a transition from a normal Fermi liquid (metal) to an insulator (MIT) either due to randomness (disorder)(W) [4, 35–37, 273] or Coulomb interactions (U) [38, 39].

A system with dominant electron correlation as compared to the kinetic energy undergoes a transition from a metal to a correlation-induced insulator. This is known as the Mott MIT [38, 39] where electrons are localized (trapped) on their individual atomic orbitals leading to the opening of a gap in the single-particle spectra. Electron localization in strongly correlated systems can also be induced by disorder (or randomness), which is inevitably present in real materials. This phenomenon is known as Anderson MIT [4, 35–37]. Here, the transition from a metal to insulator is not by the vanishing of the charge carriers but by the vanishing of the hybridization paths accompanying the quantum localization of the wave functions due to the coherent backscattering off random impurities. In contrast to the Mott MIT which is accompanied by the opening of a gap in the single-particle spectra, the Anderson insulator is gapless indicating that the single-particle excitations are essential in determining their physical properties especially at low energies.

The interplay of disorder [4, 35–37, 273] and interactions [38, 39] is an important problem in diverse fields not limited to the physics of cold atoms, photonic and bosonic systems, and optical lattices [40–43]. It has been actively studied both theoretically [17,44–50] and experimentally (see for e.g., the metal-insulator transition of doped semiconductors [39, 51–53] and some perovskite compounds [54–58]) for the past few decades.

Despite the vast theoretical and experimental studies, there are still many open questions. One of such open questions is the metal-insulator-transitions (MIT) [37, 44, 69, 104] in the presence of strong disorder and weak electron interactions and the parameter regime, which has remained one of the most challenging problems of today's condensed matter physics.

Many experimental studies [52, 55–58] show that both disorder and interaction are essential for the proper description of materials. Hence, any theoretical model formulated to understand MIT must take into account both the effects of W and U on equal footing.

Naively, since both disorder and interactions, independently lead to a MIT, one would expect their combined effects to be complimentary. In general, the opposite has been observed to be the case especially at the extreme limits (strong W and small U, and vice-versa). Interacting disordered electron systems show strong renormalization of the disorder strength [105] and hence the reduction in the critical disorder strength [313] that may inhibit the development of the quasi-coherent energy scale, already in the metallic state [102]. As such, there will be a non-trivial renormalization of the critical disorder that may be different from those of the "pure" ($U = 0$) Anderson MIT [12].

In this Chapter, I will focus on the effects of weak local interactions on disordered systems in three dimensions. The approach is an extension of the developed typical medium-dynamical cluster approximation (TMDCA) (cf. Chapter 7, which was shown to be highly successful in describing the Anderson localization transition (ALT) for non-interacting systems [2]. The typical medium approaches assume that the typical density of states (TDoS), when appropriately defined, acts as the "proper" order parameter for the ALT. Such an assumption is well justified not only for the non-interacting case [2, 105, 257] but also in the presence of interactions, as shown experimentally [52, 141]. The typical medium theory (TMT) of Dobrosavljević *et al.* [105] is a special case of the TMDCA when the cluster size $N_c = 1$. Even though the TMT cannot include weak localization effects due to coherent backscattering, it still does qualitatively predict a disorder-driven ALT, and hence incorporates 'strong localization' effects. The TMDCA incorporates non-local effects via systematic finite cluster increment and achieves almost perfect agreement with numerical exact calculations. The extension of the TMT to finite interactions show that interactions screen the

disorder [313, 344, 345]. I will show that such a conclusion is robust in the thermodynamic limit through increasing cluster size calculations.

While there have been significant efforts to understand the combined effect of disorder and interactions on the local density of states close to the Fermi level, the band edges have received scant attention. Specifically, the effect of weak interactions on the mobility edge has not been discussed thus far. This can be attributed to the difficulty in defining a proper mean-field order parameter capable of distinguishing between the delocalized and localized phases in the gapless single-particle spectra of the Anderson-Mott insulator. The presence of electron interactions will further complicate this already intricate situation due to the quantitatively different, low energy scales under this coexistence with a nontrivial density of states (DoS) of the Anderson-Mott insulators. Moreover, as the electron interaction "turns on", singular diffusion modes lead to the mixing of states with different energies.

The main result of this Chapter is that for $\mu < \omega_\varepsilon$, arbitrary small interactions lead to the masking of the sharp mobility edge that separates localized and extended states in the non-interacting regime below the critical disorder strength $W_c^{U=0}$. Thus, interactions can radically modify the spectrum of a non-interacting system even at the band edges, i.e., in the 'localized band'. However, when the chemical potential (μ) is outside the mobility edge energy (i.e., $\mu > \omega_\varepsilon$), the well-defined localization edge is restored. Nevertheless, unlike the non-interacting systems where the TDoS just shifts rigidly as one scans through μ, in the presence of interactions, there is a non-trivial decrease of the TDoS vis-à-vis the change in the filling. Further, we predict a soft-pseudogap at intermediate W just below W_c^U in agreement with experiments [54, 55]. The typical medium for interacting disordered electron system is a self-consistent, systematic formalism for treating both disorder and interactions at equal and to allow for their mutual renormalization effects.

10.2 Formalism and Method

The Anderson-Hubbard model is a minimal model for studying the interplay between electron–electron interactions and disorder. The Hamiltonian for this model is defined by Equation 4.4.

In this chapter, I utilize the box disorder configurations described by the probability distribution function (4.2a). Note, aside the internal self-consistency in obtaining the converged non-local self-energy and the cluster occupancy, the self-consistency of the TMDCA for interacting disordered system is the same as that described in Chapter 5, Subsection 5.3.2, as such, I will not repeat explicitly the whole self-consistency aside the important steps needed to implement the TMDCA for interacting disordered systems. The disorder part is treated exactly while the interaction by treating the interacting, non-local cluster self-energy ($\Sigma_c[\tilde{\mathcal{G}}](i, j \neq i)$) up to second order in the perturbation expansion of interactions, U^2. With this, a systematic incorporation of non-local spatial correlations and diagonal disorder, the initial effects of electron interactions (U) is explored.

10.2.1 The TMDCA for Interacting Disordered System: Self-consistency

The focus is on the single-particle Green's function and the associated density of states. To obtain these for the Anderson-Hubbard model(4.4), I modify the typical medium dynamical cluster approximation (TMDCA to treat both disorder and interactions with the disorder treated exactly and the interactions treated using up to the second order in the perturbation expansion of the interacting self-energy in terms of U. I refer to this as TMDCA-Second order perturbation theory (TMDCA-SOPT).

Here, an initial guess for the hybridization function ($\Gamma(\mathbf{K}, \omega) \equiv 0$) is used to form the cluster-excluded Green function $\mathcal{G}(\mathbf{K}, \omega) = (\omega - \Gamma(\mathbf{K}, \omega) - \bar{\varepsilon}_{\mathbf{K}} + \mu)^{-1}$, where $\bar{\varepsilon}_{\mathbf{K}}$ is the coarse-grained bare dispersion. $\mathcal{G}(\mathbf{K}, \omega)$ is then Fourier transformed to form the real space Green function,

$$\mathcal{G}_{n,m} = \sum_{\mathbf{K}} \mathcal{G}(\mathbf{K}) \exp(i\mathbf{K} \cdot (\mathbf{R}_n - \mathbf{R}_m)) \tag{10.1}$$

and then for a given disorder configuration $\hat{V}$, I may calculate the cluster Green function

$$G^c(V) = (\mathcal{G}^{-1} - \hat{V})^{-1}. \tag{10.2}$$

Utilizing $G^c(\hat{V})$, I then calculate the Hartree-corrected cluster Green function

$$\tilde{\mathcal{G}}_c^{-1}(\hat{V},U) = G^c(\hat{V})^{-1} + \varepsilon_d(U) \tag{10.3}$$

where $\varepsilon_d(U) = \tilde{\mu} - U\tilde{n}_i/2$ and $\tilde{n}_i = -1/\pi \int_{-\infty}^{0} \Im\, \tilde{\mathcal{G}}_c(i,i,\omega) d\omega$ is the site occupancy at zero temperature, $T = 0$. To enable the simulations both at and away from half-filling, I choose the chemical potential as $\tilde{\mu} = \mu + U/2$. Both $\tilde{\mathcal{G}}$ and $\tilde{n}_i$ are converged and then used to compute the second-order diagram shown in Figure 10.1. Thus, the full self-energy due to interactions is given as

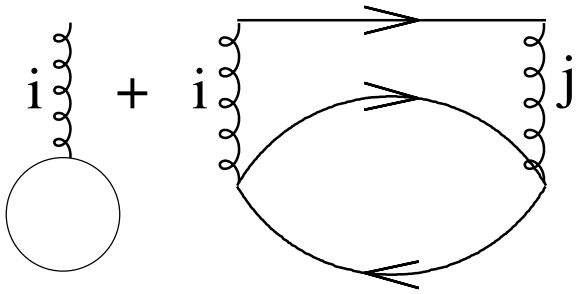

Figure 10.1: First and second-order diagrams of the interacting self-energy between sites i and j.

$$\Sigma_c^{Int}(i,j,\omega) = \Sigma_c^{H}[\tilde{\mathcal{G}}] + \Sigma_c^{SOPT}[\tilde{\mathcal{G}}], \tag{10.4}$$

where the first term is the static Hartree correction and the second term is the non-local second-order perturbation theory (SOPT) contribution. Note, the computational cost grows exponentially with each order of the perturbation series making it numerically prohibitive to include more than the second-order diagrams. However, since the focus is on the weak interaction regime $U/4t \ll 1$, I expect that higher order diagrams are suppressed by at least $\sim (U^3)$.

To check the validity of the above truncating the perturbation expansion of the self-energy in terms of U after the second order, I have carried out extensive benchmarking of the SOPT cluster solver against numerically exact quantum Monte-Carlo calculations within the DCA framework. For weak interactions and for essentially all disorder strengths, the corrections due to perturbation orders higher than the second are found to be negligible (for details, see Section 10.3).

Next, I solve the cluster problem. For a given interaction strength U and randomly chosen disorder configuration $\hat{V}$, the fully dressed cluster Green function is calculated as

$$\tilde{G}^c(\hat{V},U) = \left(\mathcal{G}^{-1} - \hat{V} - \Sigma^{Int}(U) + \frac{U}{2} \right)^{-1}. \tag{10.5}$$

The typical density of states $\rho^c_{typ}(\mathbf{K},\omega)$ is then obtained using $\tilde{G}^c(\mathbf{K},\omega,V,U)$ following the prescriptions of Ref. [2] as presented in Chapter 5, which avoids self-averaging. The disorder and interaction averaged typical cluster Green function is obtained using the Hilbert transform

$$G^c_{typ}(\mathbf{K},\omega) = \int d\omega' \frac{\rho^c_{typ}(\mathbf{K},\omega')}{(\omega-\omega')}. \tag{10.6}$$

The self-consistency loop is then closed by calculating the coarse-grained cluster Green function of the lattice

$$\overline{G}(\mathbf{K},\omega) = \int \frac{N^c_0(\mathbf{K},\varepsilon)d\varepsilon}{(G^c_{typ}(\mathbf{K},\omega))^{-1} + \Gamma(\mathbf{K},\omega) - \varepsilon_k + \overline{\varepsilon}(\mathbf{K})}, \tag{10.7}$$

where $N^c_0(\mathbf{K},\varepsilon)$ is the bare partial density of states. A schematic diagram of the typical medium dynamical cluster approximation self-consistency is shown in Figure 10.2.

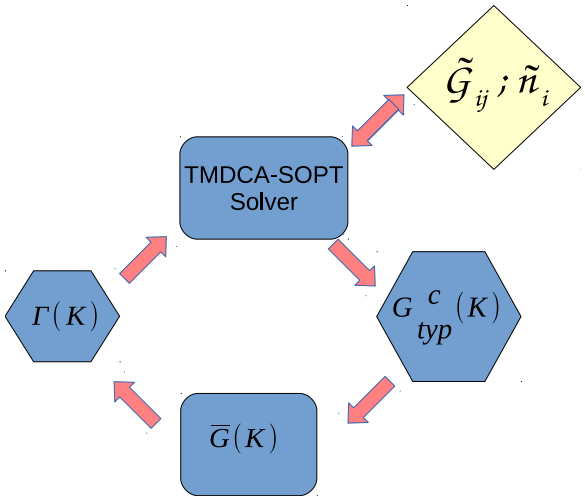

Figure 10.2: The TMDCA self-consistency for interacting disordered system.

10.2.2 Advantages of the TMDCA for Interacting Disorder System

Aside the very small computational cost and the possibility of incorporating materials specific details even for interacting disorder systems provided by the typical medium dynamical cluster approximations, there are obvious many other advantages when compared specifically to Matsubara frequency based methods. Notice that in the formulation of the typical medium dynamical cluster approximation and the average medium based dynamical cluster approximation for studying the Anderson–Hubbard Hamiltonian(4.4), instead of using the conventional Matsubara frequency approach, I instead, reformulated the formalism in real frequency. This has the major advantage of not only being capable of capturing finite temperature (T) physics, but well suited for $T = 0$, where Matsubara-based approaches cannot be used. It also avoids the rigor of analytical continuation of the major observables: the Green function and the self-energy. To achieve these, recall that the second order perturbation theory self-energy is the expansion up to the second order in U ($O\left[U^2\right]$) around the Hartree-corrected host propagator given as

$$\Sigma_c^{int}(i,j,\omega) = \Sigma_c^H[\tilde{\mathcal{G}}] + \Sigma_c^{(SOPT)}[\tilde{\mathcal{G}}] \tag{10.8}$$

where i and j are site indices. The first term of the Hamiltonian $\Sigma_c^H[\tilde{\mathcal{G}}] = U\tilde{n}_i/2$ is the Hartree term while the second term is the density-density term which in the Matsubara frequency is given by

$$\Sigma_c^{(SOPT)}[\tilde{\mathcal{G}}] = -\lim_{i\omega\to\omega^+}\left[\frac{U^2}{N_c^2\beta^2}\sum_{m,p,\mathbf{P},\mathbf{Q}}\tilde{\mathcal{G}}(\mathbf{K}+\mathbf{Q},i\omega_n+i\nu_m)\,\tilde{\mathcal{G}}(\mathbf{P}+\mathbf{Q},i\omega_p+i\nu_m)\,\tilde{\mathcal{G}}(\mathbf{P},i\omega_p)\right]. \tag{10.9}$$

However, since the cluster problem is solved in real space and for the fact that it is numerically more advantageous to work in the real frequency than in the Matsubara frequency (because analytic continuation has to be carried out from the imaginary frequency to the real frequency in order to get real frequency quantities), one can transform Equation 10.9 to its real frequency representation

as outlined in Appendix E. Equation 10.9 in real frequency (suppressing site indices) is then

$$\begin{aligned}\rho_\Sigma(\omega) &= U^2 \int d\varepsilon_1 d\varepsilon_2 \rho_{\tilde{\mathcal{G}}}(\varepsilon_1)\rho_{\tilde{\mathcal{G}}}(\omega-\varepsilon_1+\varepsilon_2)\rho_{\tilde{\mathcal{G}}}(\varepsilon_2) \\ &\times \left[n_f(-\varepsilon_1)n_f(\varepsilon_2)n_f(-\omega+\varepsilon_1-\varepsilon_2)+n_f(\varepsilon_1)n_f(-\varepsilon_2)n_f(\omega-\varepsilon_1+\varepsilon_2)\right] \quad (10.10)\end{aligned}$$

where $\rho_{\tilde{\mathcal{G}}} = -1/\pi\Im\,\tilde{\mathcal{G}}$, $n_f = 1/(e^{\beta\varepsilon}+1)$ is the Fermi function, and $\mathbf{Q}$, $\mathbf{P}$, $\mathbf{K}$ are cluster momenta. We note that $\rho_{\tilde{\mathcal{G}}}$ vanishes only for $|\omega| \geq 3B/2$ [346], where B is the full bandwidth ($12t = 3$ in our unit). The real part of the second-order term of the ISE $\Sigma_R^{SOPT}(i,j,\omega)$ on each cluster site is obtained via the Hilbert transform, and the non-local SOPT self-energy is then obtained as

$$\Sigma_c^{SOPT}(i,j,\omega) = \Sigma_R^{SOPT}(i,j,\omega) - i\pi\rho_\Sigma(i,j,\omega) \quad (10.11)$$

Note that Equation 10.10 scales as an $O\left[N^3\right]$, where N is the number of the grid points used for the integration. In my computations, this N^3 process is dramatically reduced to scale logarithmically as $N\ln N$ using fast Fourier transformation [347].

10.3 Benchmarking TMDCA-SOPT with CTQMC in Three Dimensions

To validate the TMDCA developed for characterizing interacting disordered system and check its suitability for studying the interacting disordered electron system, I compare the results for the Anderson-Hubbard model at half-filling with results from the dynamical cluster approximation (DCA) using the continuous-time quantum Monte Carlo method (CTQMC) [335, 348–351].

The quantum Monte Carlo (QMC) methods are powerful tools that enable controlled calculations of the properties of large quantum many-particle systems. Details of the CTQMC formalisms are well described in the literature (see for e.g., Refs. [321, 335, 348–352]) as such, and we will not attempt to give a detailed description of the algorithms here but will just give an overview which enables us to compare the QMC results with our Hilbert transformed imaginary frequency data. In the CTQMC, to avoid any possible time discretization error in the imaginary time axis, we adopt the recent improvements in the QMC algorithms in the continuous imaginary time [335, 348, 350, 352].

This significantly improves the quality of the data.

To make the comparison, I convert the real frequency data to Matsubara frequency using the Hilbert transformation, and obtain the local Green function and self-energy, respectively, as

$$G_{loc}(i\omega_n) = -\frac{1}{\pi}\int_{-\infty}^{\infty} d\omega \frac{\Im G_{loc}(\omega)}{i\omega_n - \omega}; \quad \Sigma_{loc}(i\omega_n) = -\frac{1}{\pi}\int_{-\infty}^{\infty} d\omega \frac{\Im \Sigma_{loc}(\omega)}{i\omega_n - \omega} \tag{10.12}$$

where $\omega_n = (2n+1)\pi/\beta$ with $\beta = 1/k_B T$ and $n \in \mathbb{Z}$ is the fermionic Matsubara frequency, T is the temperature (in a unit of $4t$), and $k_B = 1$ is the universal Boltzmann's constant.

10.3.1 Limit of Zero Disorder: Hubbard Model

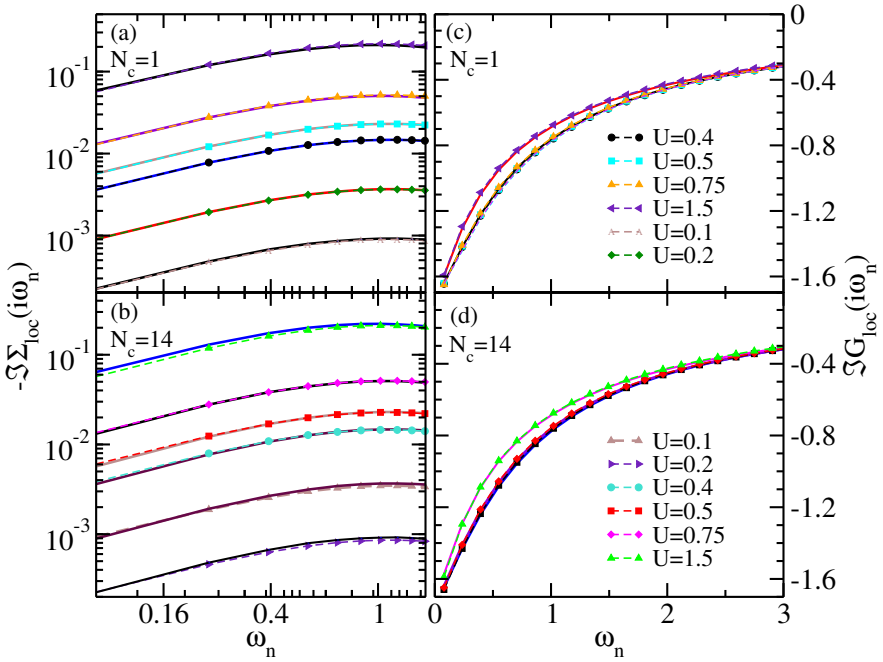

Figure 10.3: The comparison of the single-particle quantities from TMDCA-SOPT and DCA-CTQMC at $T = 0.025$ for the half-filled Hubbard model (zero disorder and the finite Coulomb interaction $U > 0$). The comparison of the imaginary part of the local self-energy for $N_c = 1$ (a) and $N_c = 14$ (b), respectively, on a log-log scale. Also shown is the corresponding comparison of the local Green function for $N_c = 1$ (c) and $N_c = 14$ (d), respectively on a linear scale. Smaller values ($U < 0.3$ for $N_c = 1$) and ($U < 0.4$ for $N_c = 14$) are not shown on the local Green functions plot for easy readability as they are too close to each other. In both cases, the dotted lines with symbols are for the TMDCA-SOPT while the solid lines depict the DCA-CTQMC results. Further, for the self-energy plots, smaller interaction strengths ($U \leq 0.5$) are on top of each other and as such, may appear indistinguishable.

At zero disorder strength, $W = 0$, the Anderson-Hubbard model (Equation 4.4) reduces to the

Hubbard Hamiltonian (Equation 4.3). As a natural consequence, the self-energy of the Hubbard model of the numerically exact CTQMC contains the most vital information for benchmarking with a mean-field theory like the TMDCA-SOPT. I show in Figs. 10.3(a) and 10.3(b) the comparison plots of the TMDCA-SOPT (using Equation 10.12) as compared with the CTQMC data for the $N_c = 1$ and finite cluster of 14, respectively, at various values of the interaction. As it is evident from the plots, the data benchmarks well up to $U \sim 2.25$ for $N_c = 1$ and $U \sim 0.75$ for $N_c = 14$ showing both quantitative and qualitative agreement between the TMDCA-SOPT and the CTQMC results. The remarkable exact agreement between the TMDCA-SOPT and CTQMC for low U (≤ 0.75), at all frequencies for both single-site and finite cluster shows that the self-energy from the TMDCA-SOPT has the correct behavior and as such, ensures that the conclusions arrived earlier about the expansion of the self-energy up to second order to be enough to quantify the weakly interacting disordered system to be numerically correct. At least for the smaller U-values (which is the regime of interest here), the good agreement with CTQMC further shows that the perturbation expansion of the self-energy up to $O\left[U^2\right]$ in U should capture all the dominant quantum fluctuations guaranteeing that quantitatively correct results are obtained. Hence, the results I will present in the subsequent sections for small interacting disordered electron system are accurate to within the computational accuracy of the formalism.

I further show in Figs. 10.3(c) and 10.3(d), the plot of the imaginary local Green function from the TMDCA-SOPT (transformed from real to Matsubara frequency using Equation 10.12) as compared to the CTQMC data for $T = 0.025$ and $W = 0$ for the $N_c = 1$ and $N_c = 14$, respectively. Again, as a confirmation of the good agreement in the local self-energy, the local Green function from the two methods are numerically the same especially for the small U-values. They are practically on top of each other up to $U \approx 1.50$ for both $N_c = 1$ and 14.

10.3.2 Limit of finite Disorder and Interaction: Anderson-Hubbard Model

To further check the applicability of the expansion of the interacting self-energy in powers of Coulomb interactions, U, up to the second-order for the study of disordered interacting electron system, I further benchmark the developed method for the Anderson-Hubbard model (Equa-

tion 4.4) with the CTQMC. This again becomes imperative as I am not aware of a prior benchmarking especially for the finite cluster.

I show in Figs. 10.4 the comparison of the developed method for fixed interaction strengths ($U = 0.1$, 0.2, and 0.5, respectively) at various disorder strengths, respectively, with the imaginary frequency data of CTQMC. As explained above, to achieve the comparison, instead of analytically continuation of the CTQMC data, I instead transform the real frequency data from the DCA-SOPT to the imaginary frequency using Hilbert transformation (10.12). As it is evident from the plots, there is almost a perfect agreement between the Hilbert transformed data (from the real to

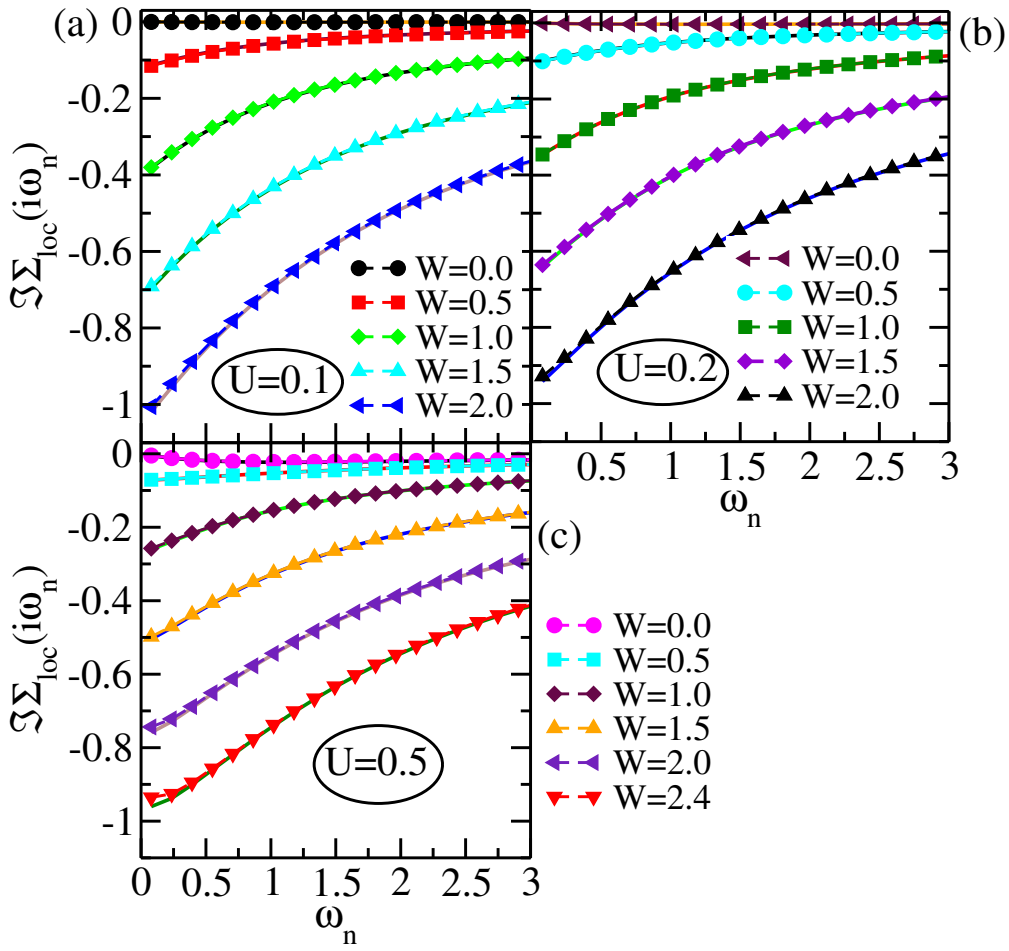

Figure 10.4: The comparison of the imaginary part of the local self-energy of the Hilbert transformed data from real to Matsubara frequency of the TMDCA-SOPT with the CTQMC data for a 14-sites cluster, respectively, at $T = 0.025$ for the half-filled Anderson-Hubbard model for a fixed U values of 0.1 (**a**), 0.2 (**b**), and 0.5 (**c**), respectively, at various disorder strengths. Here, the solid lines are for the CTQMC while the dash lines with closed symbols are for the TMDCA-SOPT.

Matsubara frequency) with the CTQMC results even for a relatively large value of the interaction strengths ($U \sim 0.5$) for all the disorder strengths up to the localization transitions. This further confirms that our truncation of the perturbation series expansion of the interacting self-energy at $O\left[U^2\right]$ (at least in the weak interaction regime) is enough to account for the quantum fluctuations in the typical environment. One can thus affirm that at least, within the weak interaction regime ($U/4t \ll 1$) in a disordered electron system that higher order diagrams in the expansion of the Σ_c^{int} are suppressed by at least $\sim (U^3)$.

10.4 Weakly Interacting Disordered System in Three-Dimensions

In three-dimensional systems for the non-interacting case, there is a broad, well-defined metal-insulator-transitions (MIT) of the gapless Anderson spectra at a given critical disorder strength $\mathrm{W}_c^{U=0}$. Here, we systematically analyze what happens to this spectra as interaction is gradually turned on. Below, we present some results for the weakly interacting disordered three-dimensional systems.

10.4.1 The DoS for Weakly Interacting Disordered System in Three Dimension

To kick start the discussion of the results obtained by applying the typical medium dynamical cluster approximation to the study of weakly interacting disordered systems, I show in Figs. 10.5(a) and (b) for a finite cluster $\mathrm{N}_c = 38$ at various disorder strengths for $U = 0.0$ and 0.1 at half-filling, the comparison of the algebraic (or average) density of states (ADoS) (obtained from the DCA, where the algebraic averaging is utilized in the self-consistency) and the typical density of states (TDoS) (obtained from the TMDCA-SOPT, where the self-consistency environment is defined by a typical medium).

At weak disorder, $W \sim 0.5$, the TDoS resembles the ADoS. However, for larger W, comparing the $U = 0.0$ results (Figure 10.5(a)) with those of $U = 0.1$ (Figure 10.5(b)), a noticeable renormalization of the spectrum is observed. There is a gradual suppression of the TDoS as the disorder strength is increased for both $U = 0.0$ and 0.1. The TDoS at $\omega = 0$ is noticeably higher when the

U is finite. This indicates a delocalizing effect of interactions which is consistent with a real space renormalization group study [34] and has been interpreted as a screening of the disorder [8, 344]. For a given disorder strength, the band edges at half-filling for the interacting case appear to be identical to that of the $U = 0$ spectrum. This seems to imply that the mobility edge is preserved when U is turned on. However, this is not the case, and this becomes clear upon examining the tails of the density of states.

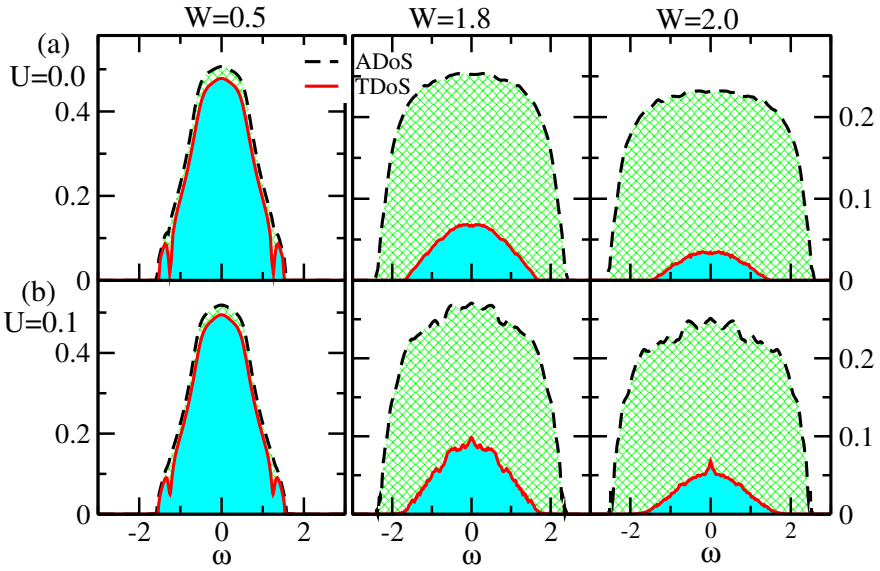

Figure 10.5: Evolution of the ADoS and TDoS at various W at $U = 0$ (**a**) and $U = 0.1$ (**b**) for the TMDCA-SOPT with $N_c = 38$ for the half-filled Anderson-Hubbard model (AHM).

10.4.2 Exploring the Mobility Edge

Figure 10.6 is the plot of the typical density of states on a log-linear scale at half-filling for the TMT ($\mathrm{N}_c = 1$) and for the finite clusters ($\mathrm{N}_c = 12$ and 38) for increasing U-values at different disorder strengths for 3D. Clearly for $U = 0$, the slopes of the TDoS for both the TMT ($\mathrm{N}_c = 1$) and TMDCA ($\mathrm{N}_c = 12$ and 38) becomes infinity signifying the existence of a sharp, well-defined mobility edge. However, for a very small $U = 0.1$ ($1/30$ of the bandwidth), and for both the TMT and TMDCA-SOPT, the slope is evidently finite up to high frequencies signifying that the sharp well-defined localization edge is replaced by an exponentially fast cross-over.

One can argue that since the tails are far away from the chemical potential, μ when $\mu = 0$, they

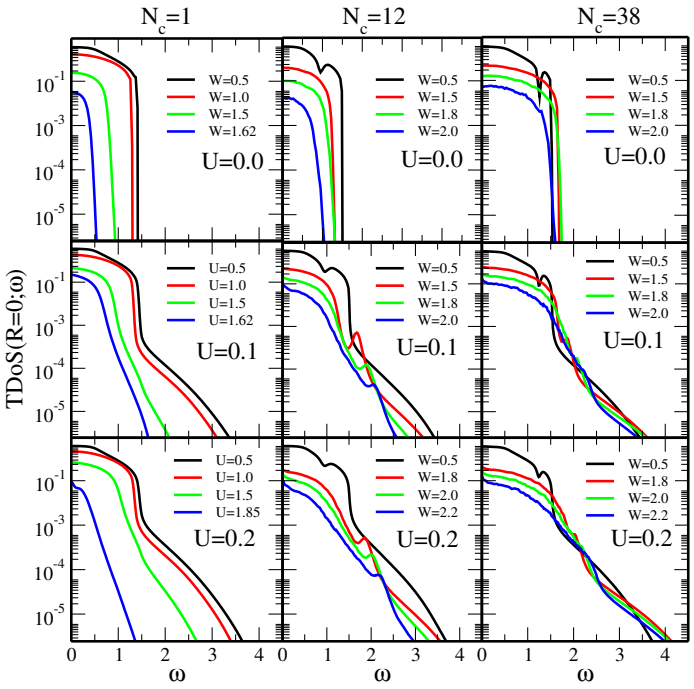

Figure 10.6: The TDoS of the Anderson-Hubbard model at half-filling for increasing U-values for the TMT ($N_c = 1$) and finite clusters ($N_c = 12$ and 38) at various disorder strengths on a log-linear plot. Observe that the $U = 0$ results have infinite slopes signifying the localization edge while for all the interactions, even for a very small $U = 0.1$ which is 1/30th the bandwidth, the slopes remain finite out to the band edge of the ADoS consistent with the mixing of the localized and extended states with different energies leading to the masking of the mobility edge.

do not generally participate in transport since only states in the proximity of the Fermi energy is excited. This can be attributed to the fact that at half-filling with finite U, interaction induces the mixing of the localized and extended states with different energies of the states at the mobility edge leading to the suppression of the sharp, well-defined mobility edge boundary with the emergence of long tails with exponentially fast crossover. This is consistent with the delocalization nature of U at $\omega = 0$ states at half-filling leading to the increase in W_c. As demonstrated in the main text, the mobility edge is well defined even in the presence of interactions as long as the chemical potential is located beyond the mobility edge energy of $U = 0$. Hence, Figure 10.6 essentially shows that at half-filling, due to the mixing of states induced by the interaction, the mobility edge energies develop tails with exponentially fast crossover which masks its detection. However, if we move the chemical potential energy outside the mobility edge energy (see the next paragraph), the sharp, well-defined mobility edge is restored.

To further explore the effect of weak interactions on the localization edge of a disordered electron system, we show in Figure 10.7, the evolution of the TDoS with $\delta = W/W_c^U$ for various values of U on a linear log plot at various μ. Clearly for $U = 0$, a sharp, well-defined mobility edge is observed (see also Figure10.5(a)). However, even for a very small $U = 0.1$ ($1/30$ of the bandwidth), and for both the TMT and TMDCA-SOPT, the sharp localization edge is replaced by an exponential tail, when $\mu < \omega_\varepsilon$. Hence, the incorporation of Coulomb interactions in the presence of disorder for $\mu < \omega_\varepsilon$ leads to long band tails that are exponentially decaying. This fingerprint can be understood from a Fermi liquid perspective.

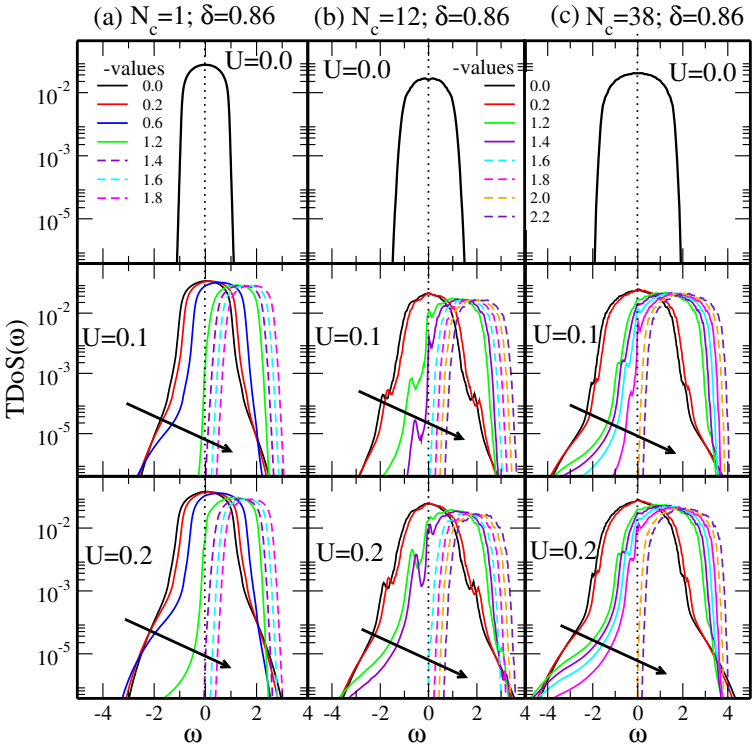

Figure 10.7: The evolution of the TDoS of the AHM for increasing U-values for the TMT ($N_c = 1$, (**a**)) and finite clusters ($N_c = 12$ (**b**) and 38 (**c**)) at fixed $\delta = W/W_c^U = 0.86$ on a log-linear plot for increasing μ-values. For $U = 0.0$, we show the plot for $\mu = 0$ only, since changing μ only involves a rigid shift of the TDoS. For $U > 0$, notice the systematic disappearance of the exponential tails (indicated by arrow) and the non-trivial decrease of the TDoS for the finite U (unlike the rigid shift in $U = 0$) as one approaches the mobility edge energy.

If we inject an electron into a Fermi liquid with an energy ω above the Fermi energy, then, we expect the particle to experience an inelastic scattering, due to U which is proportional to ω^2. One factor of ω is due to energy conservation and the other to momentum conservation with both

constrained by the Pauli principle. I.e., the inelastic scattering vanishes as $\omega \to 0$. However, if we apply the same logic to an interacting disordered system, then, we might expect the edge of the TDoS to be smeared out by these inelastic scattering processes, whenever the edge energy is above the Fermi energy but becomes sharp as the edge approaches it. Though, some argue that this reasoning fails for a disordered system, especially for a strongly disordered system since a well-defined quasiparticle no longer exists [353, 354]. As a consequence, the concept of a mobility edge would not hold and the TDoS should have pronounced exponential "tails" even when the Fermi energy approaches the top or bottom of the TDoS bands. As it is evident from Figure 10.7, the sharp mobility edge is restored as the mobility edge energy is approached in tandem with the Fermi liquid description.

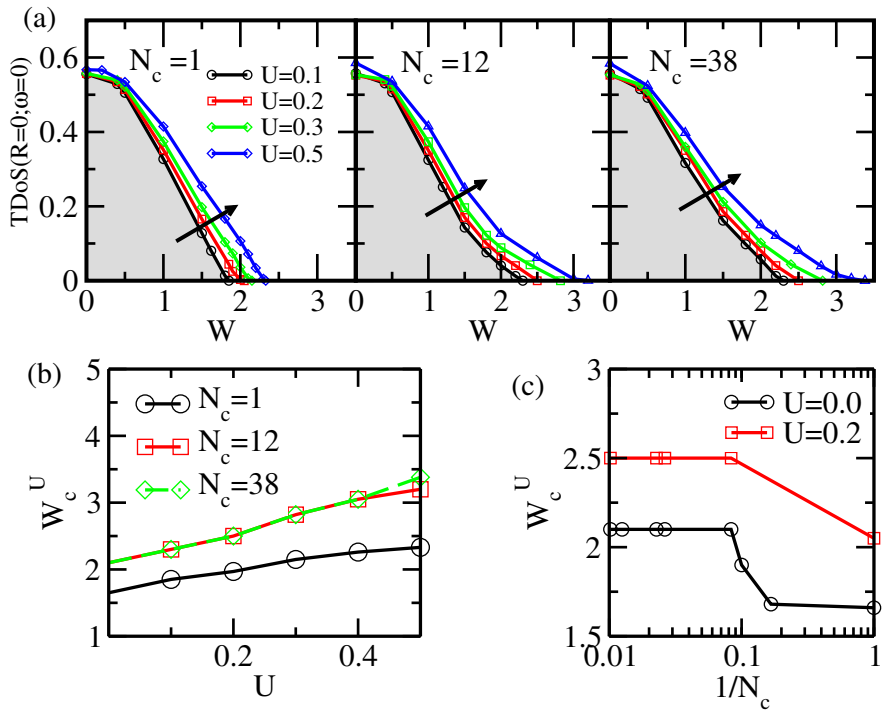

Figure 10.8: (**a**) The evolution of the TDoS (at $\omega = 0$) as a function of the disorder strength W for various interactions for $N_c = 1$, 12, and 38 at half-filling. The integral $\int \Im\Gamma(K,\omega)\, dK\, d\omega$ vanishes at the same W_c as the TDoS for a given U (not shown), signifying that the absence of the hybridization paths leads to the vanishing of the TDoS. As indicated by the arrow, increasing U pushes W_c to larger values. (**b**) The interaction dependence of the critical disorder W_c^U for different cluster sizes $N_c = 1$, 12, and 38 of the AHM at half-filling. The unit is fixed by setting $4t = 1$. The plot is generally in agreement with the results of Ref. [139]. (**c**) The W_c^U vs $1/N_c$ on a semi-log plot for $U = 0.0$ and 0.2 for the half-filled AHM. Note the systematic and fast convergence of W_c^U with cluster size for both cases.

The smearing of the TDoS edge can further be inferred from the convolutions found in the second order (and higher) diagrams (cf. Figure 10.1), which will mix states above and below the non-interacting localization edge. Consider two such states: one localized and the other extended, which are now degenerate due to this mixing. Since the inelastic scattering causes these states to hybridize with each other, both states become extended [39, 118].

10.4.3 The W-U Phase Diagram

To explore the disorder-interaction phase diagram in three-dimensional system, we show in Figure 10.8(b), the interaction U dependence of the critical disorder strength W_c^U (the ground state phase diagram) for $\mathrm{N}_c = 1$, 12, and 38 at half-filled AHM in the $W-U$ plane. For each of the N_c, we obtain a correlated metal below the lines, and above we have the gapless Anderson-Mott insulator. The trend in both the single site and finite cluster are alike (i.e., W_c^U increases with increasing U) except for the difference in W_c^U. The almost linear trend observed for the low U is in agreement with previous studies [139, 345]. We note that the $N_c = 12$ and 38 results are identical until $U = 0.4$. This is consistent with the $U = 0$ results [2] and shows that the TMDCA converges quickly as a function of cluster size, with small clusters giving essentially exact results. Figure 10.8(c) depicts the W_c^U as a function of $1/N_c$ on a semi-log plot for $U = 0.0$ and 0.2 for the half-filled AHM. Note the systematic and fast convergence of W_c with N_c for both cases.

10.4.4 Effect of Interactions on Disordered System at Half-Filling

Next, we explore the effect of interactions on the half-filled, disorder-driven localization transition. We show in Figure 10.8 the evolution of the TDoS at the band center, $\omega = 0$, for various cluster sizes. The integrated escape rate ($\int \Im\Gamma(K,\omega) dK d\omega$) (not shown) characterizes the rate of diffusion of electrons between the impurity/cluster and the typical medium. The vanishing of the hybridization paths leads to a localization transition. The TDoS vanishes at the same value of W_c^U as the integrated escape rate.

Figure 10.8 shows that an increase in U from 0.1 to 0.5 leads to a concomitant increase in W_c^U. One can say loosely that, the zero-temperature effect of correlations is an effective reduction in the

disorder strength [8, 313], leading to the increase in W_c as indicated by the arrow. For the TMT ($N_c = 1$), the W_c^U increases as 1.85, 2.05, 2.15, 2.26, and 2.33 for $U = 0.1$ – 0.5, while for the TMDCA ($N_c \geq 12$), W_c^U increases as 2.30, 2.50, 2.82, and 3.05 for $U = 0.1$ – 0.4. We note the difference in the $W_c^{0.5}$ for $U = 0.5$ for TMDCA $N_c = 12$ ($W_c = 3.20$) and $N_c = 38$ ($W_c = 3.38$) which can be attributed to finite size effects. We also note that W_c^U increases more quickly with U as one goes from single-site ($N_c = 1$) to finite clusters ($N_c = 12$ and 38). This is likely due to the effect of a finite U on the coherent backscattering, which is absent for $N_c = 1$ and is systematically incorporated as N_c increases.

10.4.5 Prediction of Soft Pseudogap in the Gapless Spectra

We further show in Figure 10.9 the evolution of the TDoS(ω) for $N_c = 12$ at $U = 0.0$ (Figure 10.9(a)) and 0.2 (Figure 10.9(b)) for various $\delta = W/W_c^U$. For finite U a soft-pseudogap, which is linear in ω (cf. Figure10.9(d)) develops (note, this is true irrespective of electron filling) at intermediate disorder strengths immediately before the system becomes localized. In Figure 10.9(c), we show that the pseudogap is robust as a function of $U < 1$. Noting that we only have short-range interaction, this soft-pseudogap cannot be attributed to excitonic effects (which are negligible here)

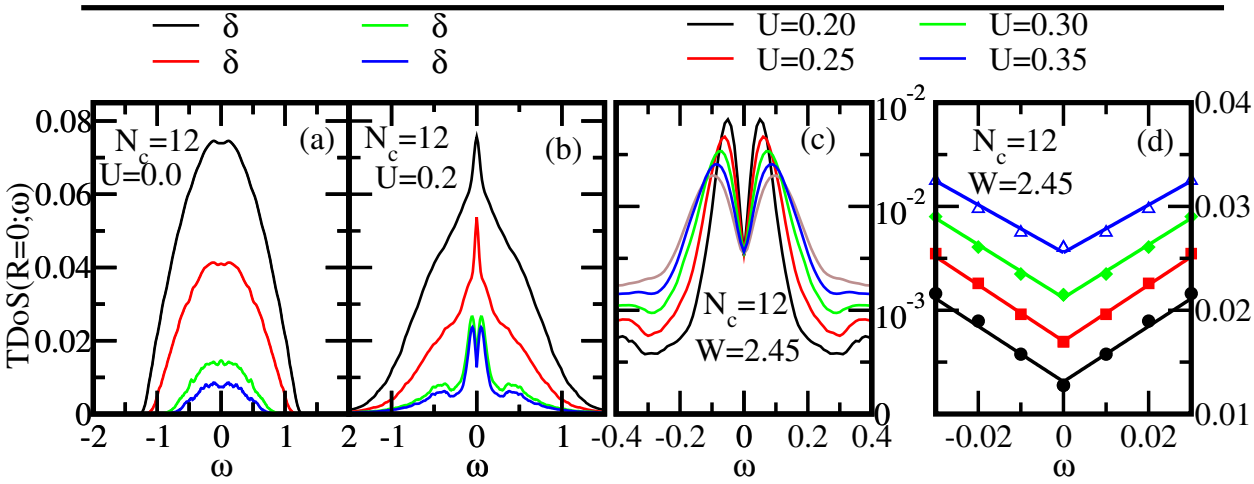

Figure 10.9: The TDoS vs energy (ω) for $N_c = 12$ ($U = 0.0$) (**a**) and $N_c = 12$ ($U = 0.2$) (**b**) at various $\delta = W/W_c^U$ showing the formation of a pseudogap at intermediate W just before $W_c^{U=0.2}$, which is absent when $U = 0$. (**c**) Shows the TDoS vs ω at a fixed W (close to $W_c^{U=0.2} = 2.50$) for various U. Note, the data has been scaled with U. (**d**) Same data as in Figure 10.9(c) showing the linear dependence of the pseudogap in ω.

as in the Efros-Shklovskii theory where the single-particle excited states are excluded from the low energies by the ground-state stability against an electron-hole excitation [148]. Also, this soft pseudogap cannot be attributed to be due to the same mechanism as in the real-space Hartree-Fock approximation and exact diagonalization results of Hiroshi *et al.* [107, 355] where the origin of their soft Hubbard gap was ascribed to a multivalley structure of energy landscape induced by electron correlations and disordered. Most importantly, unlike the Hubbard gap observed by Hiroshi *et al.* [107, 355], which occurs in the ADoS and for system sizes, $N_c > 1$, the the soft pseudogap observed here occurs only in the typical density of states irrespective of the cluster size even in $N_c = 1$ where such a single-site cannot generate a multivalley energy landscape to sustain sets of metastable states. Further, as we shown in Figure 10.10, the soft pseudogap occurs only when the second order contribution of the interacting self-energy is incorporated into the self-consistency and not in the Hartree contributions as in Refs. [107, 355], and it should be contrasted from the Altshuler-Aronov zero-bias anomaly, which is due to weak nonlocal interactions and weak disor-

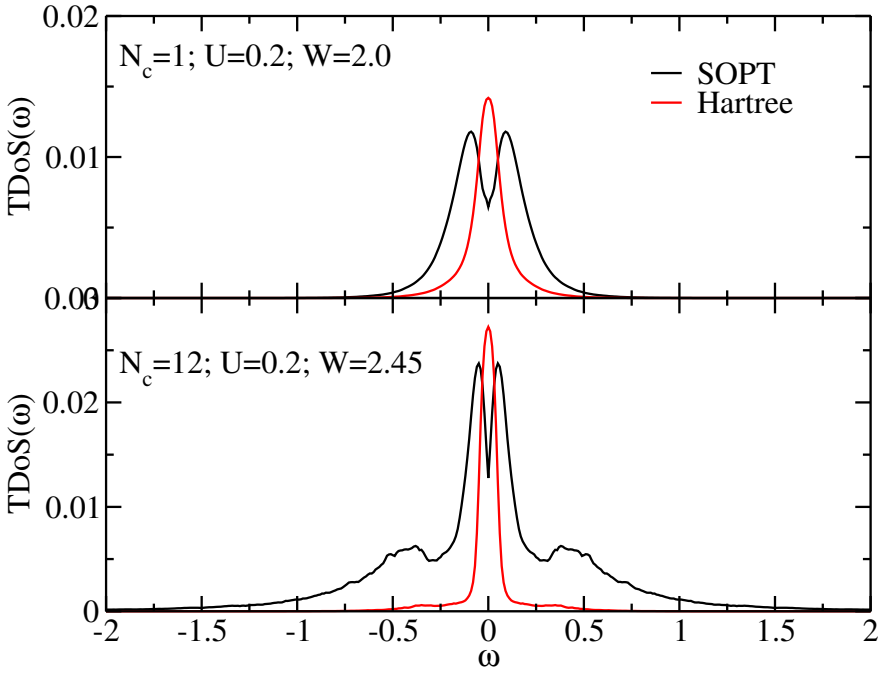

Figure 10.10: The typical density of states obtained using the Hartree and the second order contributions to the expansion of the interacting self-energy in U, respectively, for $N_c = 1$ and finite cluster $N_c = 12$ at $W = 2.0$ and $W = 2.45$ in that order. Observed that the soft pseudogap is observed in both $N_c = 1$ and 12 for the second order part but not in the Hartree contributions in contrast to the results of Ref. [107, 355].

der [108, 356]. We ascribed this soft pseudogap to the same effect where a well-defined mobility edge only exists, when the chemical potential is at or beyond ω_ε. As U suppresses localization and increases the TDoS, the phase space for scattering is drastically reduced by U leading to the opening of a soft pseudogap. Put differently, the pseudogap is due to the suppression of inelastic scattering by U due to the Pauli principle and energy conservation. It is linear (cf. Figure10.9(d)), rather than quadratic in ω as in a Fermi liquid, due to the lack of momentum conservation.

10.4.6 Effect of Interaction on the Alloy Model

The results presented above are for the box disorder distribution. The generalization of the typ-

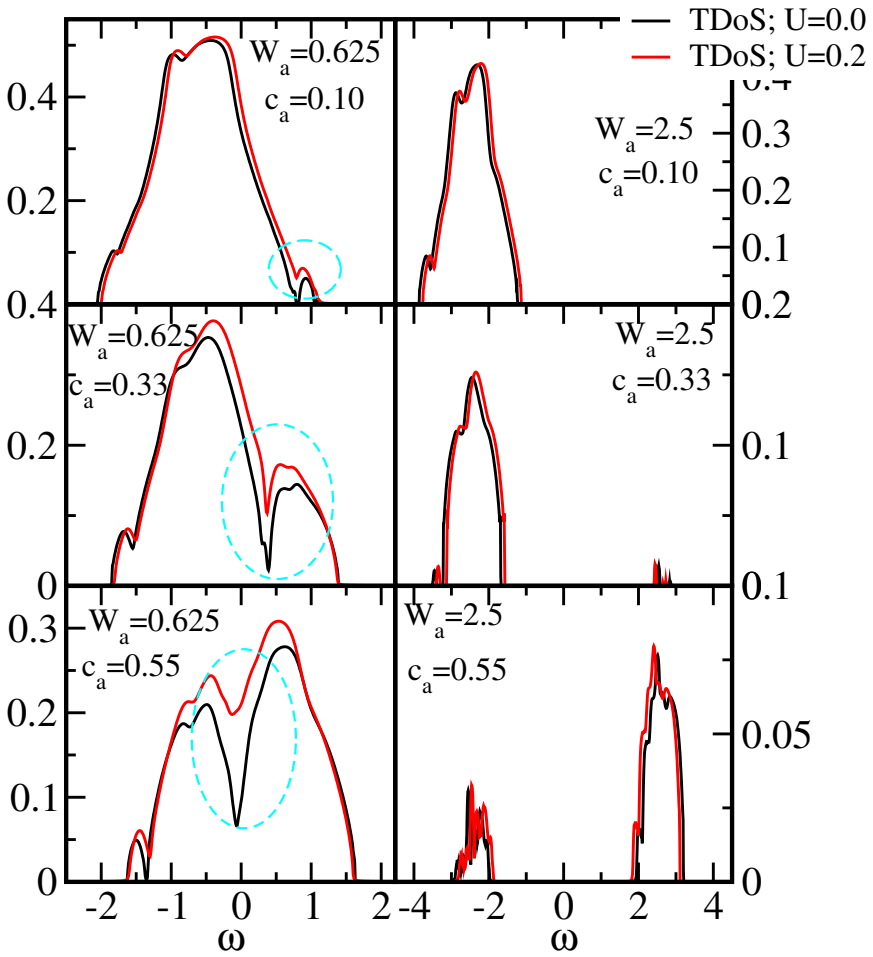

Figure 10.11: A comparison plot of the evolution of the typical density of states for the binary alloy model at various disorder strengths for $U = 0$ and 0.2 at different concentrations for the finite cluster size of 27. Observe that the TDoS($\omega = 0$) for the $U = 0.2$ is significantly larger than that of $U = 0$ showing the delocalization effect of interactions.

ical medium dynamical cluster approximation to treat disorder and interactions simultaneously can be applied for any form of distribution that one can define. As a prove of concept, we apply the TMDCA to the binary alloy model described by the probability distribution function (Equation 4.2d). The aim is to systematically, check the effects of weak interaction on the spectra of a typical binary alloy system. We show in Figure 10.11 a comparison plot of the typical density of states for the $U = 0$ and 0.2 (1/15th the bandwidth) for various disorder strengths at different concentrations c_a for the finite cluster $\mathrm{N}_c = 27$. As it is evident from the plot, just as in the case of the box disorder distributions, the presence of interactions lead to the renormalization of the effective disorder strength (delocalization effects) pushing the critical disorder strength to higher values. Note in the case of the binary alloy, the localization transition at a given band limit occurs mainly at the band center where the TDoS($\omega = 0$) goes to zero whereas there are still islands of the TDoS on both sides ($\pm\omega$) of the spectra. Surprisingly, the effects of interactions are only significant at the band center (see the left panels of Figure 10.11 as denoted by dash circles) where the TDoS($\omega = 0$) at the band center is significantly larger in the $U = 0.2$ than the $U = 0$. At both strong and weak disorder limits, the position of the mobility edge remains almost unchanged from that of the $U = 0$. This is different from the observations for the box disorder distribution where aside the renormalization of the effective disorder strength, weak interactions lead to the smearing of the sharp, well-defined mobility edge well up to high energies. For the binary alloy model, this effect is only noticeable at very low energies $\sim 10^{-4}$ (not shown).

10.5 Onset of Interaction in a Disordered Lower Dimensional Systems

The lower dimensional systems for the non-interacting disordered system is even more intriguing. This stems from the fact that there is no delocalized phase in these systems in the absent of any symmetry breaking field like spin-orbit couplings. Particularly, the two-dimensional system, which is the lower critical dimensions for the Anderson localization transitions (cf. Figure 3.3), is of interest as any external perturbation may marginally induce localized states for the weak disorder, hence, leading to the formation of delocalized phase vis-à-vis, metal-insulator transitions. In this

section, I will systematically test the effects of weak interactions to the 'fully' localized Anderson spectra within the typical medium dynamical cluster approximations.

10.5.1 Evidence of Critical Disorder Strength in Interacting Two Dimensions

As demonstrated in Chapter 6, in two-dimensional systems, an arbitrary disorder strength localizes all states in the non-interacting orthogonal universality class. Further, I showed that the cluster critical disorder strength scales logarithmically as cluster size N_c increases. To ascertain what happens in the presence of weak electron correlations, I show in Figure 10.12 a comparison plot of the typical density of states for $U = 0.0$ and $U = 0.2$ at arbitrary disorder strengths $W = 1.0$ and $W = 1.4$, respectively. Evident from the plot is the fact that even for $N_c = 128$, the largest system size simulated for $U = 0.0$ (cf. Figure 10.12(a)), no convergence as a function of cluster size is achieved. The logarithmic behavior is clearly manifest. However, for the finite U results (cf. Figure 10.12(b)), there is a clear evidence of cluster size convergence. This signifies that there is a critical disorder strength for the two-dimensional system for the interacting two-dimensional systems. This further confirms that the interacting disordered two-dimensional systems belong to a different universality class as against the traditional orthogonal universality class of the non-interacting disordered system (Anderson model).

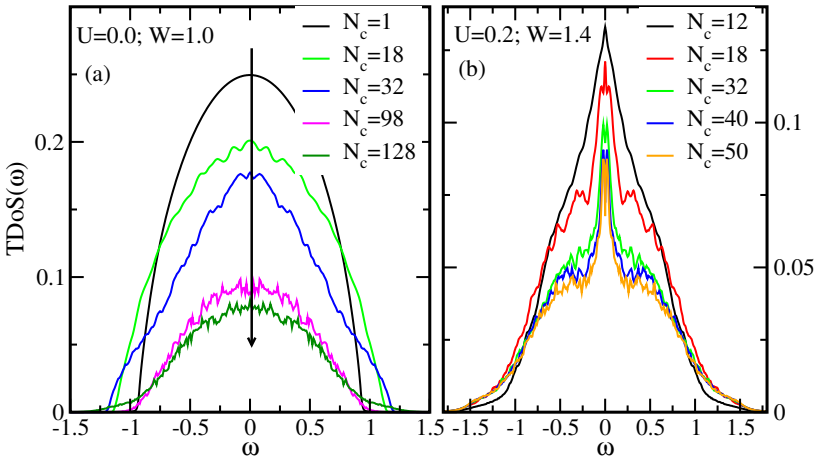

Figure 10.12: The TDoS at $W = 1.0$ $U = 0.0$ (**a**) and $W = 1.4$ $U = 0.2$ (**b**) as obtained from the TMDCA at various N_c. Observe that the TDoS for $U = 0$ even at $N_c = 128$, still changes as depicted by the arrow while for finite U, the TDoS especially at $\omega = 0$ converges rather quickly with N_c.

I further show in Figure 10.13(a) the plot of the scaling of the cluster critical disorder strengths W_c^U for $U = 0.0$ and 0.2 on a semi-log plot. As it is evident, for the $U = 0$, the plot is linear in agreement with the logarithmic trend discussed in Chapter 6. However, for finite $U = 0.2$, this is no more the case. There exists a finite critical disorder strength, which is converged as a function of cluster size. The obtained critical disorder strength at $U = 0.2$, $W_c^{U=0.2}$ is ~ 2.02.

Figure 10.13(b) shows the typical density of states for the finite cluster $N_c = 32$ at $U = 0.2$ at half-filling. Recall that in 3D, I predict a soft-pseudo-gap, which develops just below the critical disorder strength. This soft-pseudo-gap is clearly also observed in the two-dimensional system.

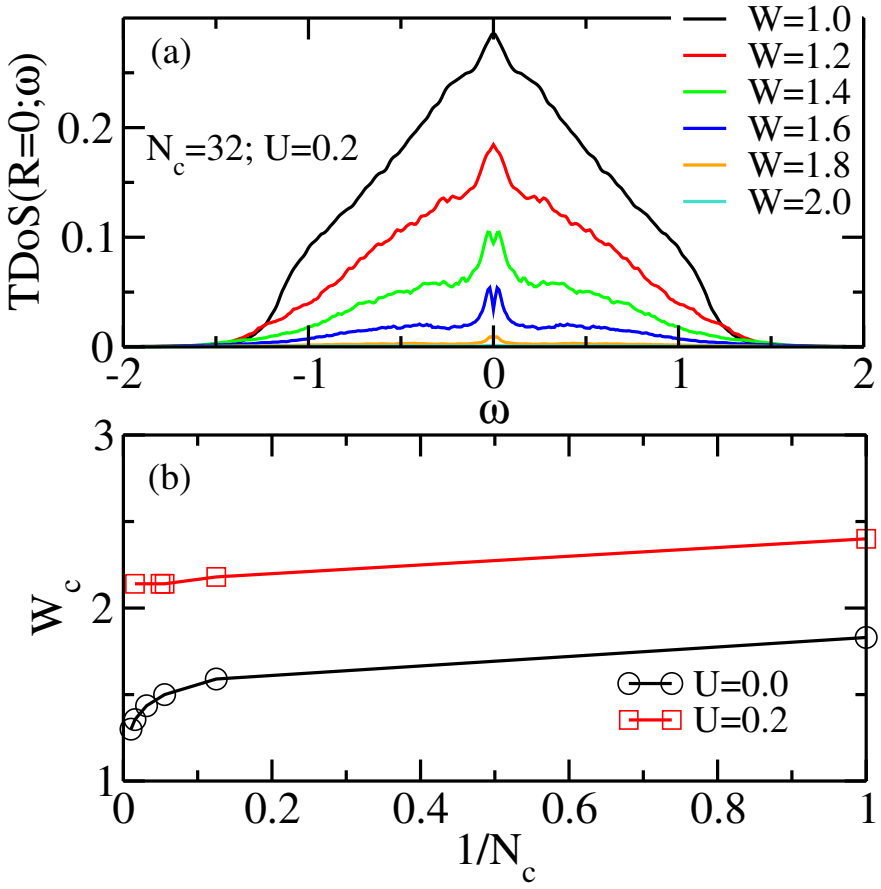

Figure 10.13: (**a**) The W_c^U vs $1/N_c$ at $U = 0.0$ and $U = 0.2$ for the half-filled AHM on a semi-log plot. Observe the systematic convergence of W_c with N_c to $W_c \sim 2.02$, while for $U = 0$, $W_c^{U=0}$ decreases logarithmically with $L_c = N_c^{1/2}$ as $W_c^{U=0} = 1.83 + 0.23 \times \ln(1/L_c)$ in good agreement with the results of MacKinnon *et al.* [247]. (**b**) Evolution of the TDoS for $U = 0.2$ at various disorder strength for $N_c = 32$ showing the emergence of a soft pseudo-gap at intermediate W close to the W_c^U.

As in the three-dimensional system, the soft-pseudo-gap only develops at finite U only in the typical medium dynamical cluster approximation as it is not observed in the dynamical cluster approximation even at finite electron-electron interactions.

10.6 Conclusions

Based on experiment, theory, and simulations, there is a growing consensus that the local density of state in a disordered system develops a highly skewed [45], log-normal distribution [52, 140, 141] with a typical value given by the geometric mean that vanishes at the localization transition, and hence, acts as the proper order parameter for the localization transitions. New mean field theories for localization, including the typical medium theory and its cluster extension, the typical medium dynamical cluster approximation have been proposed. The TMDCA is extended to weakly interacting systems using second order perturbation theory. In three-dimensions, we find that weak local interactions lead to increase in W_c, with the localization edge preserved when the chemical potential is at or beyond the mobility edge energy. For finite U we observe a soft-pseudogap for values of the disorder strength just above W_c^U. In two-dimensions, we recall that for the non-interacting systems, the cluster size (same as conductivity) decreases logarithmically with disorder strength. However, as shown in Section 10.5, this logarithmic behavior is replaced by an algebraic trend for a weakly interacting disorder system achieving a convergence with the cluster size. This implies that the interacting two-dimensional systems behaves more like a 3D system with a critical disorder strength for e.g., $U = 0.2$, $W_c^{U=0.2} \sim 2.02$. Also, the soft-pseudo gap observed in three-dimensions is present in two-dimensions.

Chapter 11

Two-Particle Formalism within the Typical Medium Dynamical Cluster Approximation

In this chapter, I will outline the steps in formulating a two-particle theory within the typical medium dynamical cluster approximation and apply it to the calculation of the direct current conductivity for various systems sizes as a function of increasing disorder strength using the box disorder distribution.

11.1 Introduction

There is wealth of experimental transport data on strongly disordered systems that have defied explanation by the conventional transport theory, which generally have been very successful in applications to good metals. Some attempts have been made to propose and/or develop a formalism for extracting some information about the conductivity in the metal-insulator-transitions in disordered electron systems, i.e., the incipient electron localization vis-à-vis the vanishing of the direct current conductivity, which determines the mobility edge and the trajectories of the mobility edge. Based on model-coupling ideas, Götze [357] develop a self-consistent localization formalism, which was applied by Prelovsek [358] to calculate the conductivity for the non-interacting electron system. An approach based on potential well analogy with the CPA was formulated [359–362] and used to calculate the conductivity in various disorder distributions [359–364]. The diagrammatic self-consistent approach of Vollhardt and Wöfle [259] was used to calculate conductivity for the Anderson model [365–368], and other various models [359, 361, 369] including in the presence of electron-electron interactions [370]. Aguair *et al.* [55] used the inverse of the typical density of states as an approximation to the resistivity and showed that the resistivity curves as a function of temperature is reminiscent of the Mooij correlations originally observed in disordered transition

metal alloys [371]. Girvin and Jonson [372] introduced an approximate scheme for calculating conductivity that becomes accurate only close to the localization transition. This method was further utilized by Dobrosavljević *et al.* [105] in their study.

It is worthwhile to note and distinguish the method proposed here from other methods of calculating conductivity already well described in literature [36, 37, 44, 259, 357, 373]. In the traditional formulation of the DMFA (or CPA) and its cluster extensions, the key ingredient in calculating conductivity is the average medium self-energy and the average, fully dressed Green function [36]. While this approach is robust in obtaining conductivity, it is important to note that it cannot characterize electron localization. This follows from the problems already well discussed in the previous Chapters due to the fact that the fluctuations of the local average Green function, which is an input in the calculation of the conductivity is so large that its *typical* value is far removed from the *average* one [374]. Thus, the local average Green function, which characterizes these mean-field environments does not have any information about the *typical nature* of the local order parameter needed to signal a phase transition. Further, the method proposed here treats the localized and extended spectra separately such that the two-particle correlation function has the information of both the localized and the extended part.

11.2 Pedagogical Concepts: Local Mean-field and Cluster Extensions

The dynamical mean-field approximation (DMFA) or its equivalent, coherent potential approximation (CPA) remains one of the most used methods for solving interacting and disordered systems, respectively. They are mean-field approaches, which are exact in infinite dimensions [375–378]. Since they are local approximations, spatial correlations are neglected while retaining local dynamical correlations. To incorporate nonlocal correlations in finite dimensions, the dynamical cluster approximation (DCA) [263, 308] remains one of the best cluster extensions of choice. As has been demonstrated, the DCA is motivated by the DMFA based on the coarse-graining of the propagators used in the construction of the generating functional and its derivatives over the entire Brillouin zone [263, 308]. However in the DCA, the momentum independent quantities as in the DMFA or

CPA are relaxed with momentum dependent and spatial correlations systematically restored. As was previously discussed in Chapter 5, the coarse-graining transformation in the TMDCA (same as the DCA) involves dividing N-points of the lattice into N_c cells of equal linear size, Δk, i.e., $N_c = L^d$ cells of linear size $\Delta k = 2\pi/L$ (cf. Figure 11.1 for a typical $N_c = 8$ cluster) such that for $N_c > 1$, nonlocal corrections of $\sim \pi/\Delta k$ is incorporated to the DMFA or CPA. Each N_c cell is represented by a cluster momentum $\mathbf{K}$ in the center of the cell such that for a quantity ζ, its coarse-grained form becomes $\overline{\zeta(\mathbf{K})} = \frac{N_c}{N}\sum_{\tilde{k}} \zeta(\mathbf{K}+\tilde{k})$, with $\tilde{k} = k - \mathbf{K}$ summed over N_c/N momenta inside the cell centered at the cluster momentum $\mathbf{K}$.

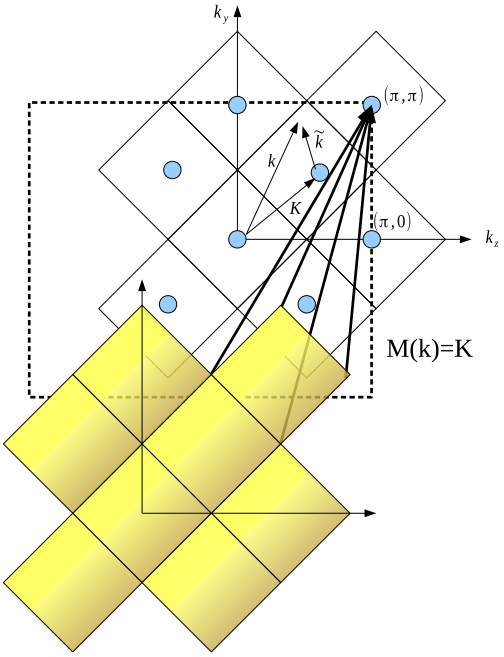

Figure 11.1: The partitioning of the first Brillouin zone (dashed line) by coarse-graining into cells of $N_c = 8$. Each cell is centered on a cluster momentum $\mathbf{K}$ (filled circles). To construct the DCA cluster, we map a generic momentum in the zone such as $\mathbf{k}$ to the nearest cluster point $\mathbf{K} = \mathbf{M}(\mathbf{k})$ (many-to-one map) denoted by gold color so that $\tilde{\mathbf{k}} = \mathbf{k} - \mathbf{K}$ remains in the cell around $\mathbf{K}$.

11.2.1 The Laue Function

As has been described in previous Chapters, the typical medium dynamical cluster approximation self-consistency is built upon the highly successful DCA algorithm with the important difference in the way the effective mean-field is defined. Unlike the DCA, which uses algebraic averaging in

the self-consistent, the TMDCA environment uses typical averaging. Hence, all the discussions of the development of a two-particle formalism for the TMDCA will overlap with the well established two-particle formalism of the DCA. As demonstrated by Müller-Hartmann [218], coarse-graining, as is done in the DCA, becomes exact in the limit of infinite dimensions ($d \to \infty$). An important property that becomes vital in formulating cluster extensions of the DMFA same as the CPA is the Laue function. For a typical Hubbard-like model, the Laue function Δ

$$\Delta(\mathbf{k}_1, \mathbf{k}_2, \mathbf{k}_3, \mathbf{k}_4) = \sum_{\mathbf{r}} \exp\left[i\mathbf{r} \cdot (\mathbf{k}_1 + \mathbf{k}_2 - \mathbf{k}_3 - \mathbf{k}_4)\right] = N\delta_{\mathbf{k}_1+\mathbf{k}_2,\mathbf{k}_3+\mathbf{k}_4} \tag{11.1}$$

implicitly characterizes the bare vertex, which expresses the momentum conservation $\mathbf{k}_1$ and $\mathbf{k}_3$ ($\mathbf{k}_2$ and $\mathbf{k}_4$) entering (leaving) each vertex. Here, $\mathbf{k}_1$ and $\mathbf{k}_2$ ($\mathbf{k}_3$ and $\mathbf{k}_4$) are the momenta entering (leaving) each vertex through the legs of G.

Following the microscopic diagrammatic derivation of the DCA [308], the systematic restoration of momentum conservation at the internal vertices, which is neglected in single site approaches require that momentum conservation be (partially) guaranteed between the cells and neglected within a cell. Taking into account the cluster and cell momenta so that $\mathbf{k}_i = \mathbf{K}_i + \tilde{k}_i$, $i = 1, 4$, then Equation 11.1 becomes

$$\begin{aligned} \Delta(\mathbf{k}_1, \mathbf{k}_2, \mathbf{k}_3, \mathbf{k}_4) &= \sum_{\mathbf{r}} e^{i(\tilde{\mathbf{k}}_1 - \tilde{k}_2 + \tilde{k}_3 - \tilde{k}_4 + \mathbf{K}_1 - \mathbf{K}_2 + \mathbf{K}_3 - \mathbf{K}_4)\cdot r} \\ &= N_c \sum_n \frac{1}{n!} \left((\tilde{\mathbf{k}}_1 - \tilde{k}_2 + \tilde{k}_3 - \tilde{k}_4) \cdot \Delta_{\mathbf{K}_1}\right)^n \delta_{\mathbf{K}_1+\mathbf{K}_3,\mathbf{K}_2+\mathbf{K}_4} \end{aligned} \tag{11.2}$$

Within the TMDCA, only the $n = 0$ (first) term of Equation 11.2 is kept [263] so that

$$\Delta_{TMDCA}(\mathbf{k}_1, \mathbf{k}_2, \mathbf{k}_3, \mathbf{k}_4) = N_c \delta_{\mathbf{M}(\mathbf{k}_1)+\mathbf{M}(\mathbf{k}_3),\mathbf{M}(\mathbf{k}_2)+\mathbf{M}(\mathbf{k}_4)} = \Delta(\mathbf{k}_1, \mathbf{k}_2, \mathbf{k}_3, \mathbf{k}_4) + O(\Delta k) \quad , \tag{11.3}$$

where $\mathbf{M}(\mathbf{k})$ is a function which maps $\mathbf{k}$ onto the momentum label $\mathbf{K}$ of the cell containing $\mathbf{k}$ (many-to-one map) (see, Figure 11.1). This choice for the Laue function guarantees the systematic restoration at the internal vertices in the TMDCA and interpolates between the exact result, Equation 11.1, which it recovers when $N_c \to N$ and the single site result, Equation 11.4, which it

recovers when $N_c = 1$. With this choice of the Laue function, the momenta of each internal Green function leg may be freely summed over the cell, i.e., each internal Green function leg $G(\mathbf{k}_1, \omega)$ in the diagram is replaced by $\overline{G}(M(\mathbf{k}_1), \omega)$. Note in the limit of infinite dimension $d \to \infty$, Equation 11.1 reduces to [218]

$$\Delta_{d\to\infty}(\mathbf{k}_1, \mathbf{k}_2, \mathbf{k}_3, \mathbf{k}_4) = 1 + O(1/d) \quad . \tag{11.4}$$

11.3 Free Energy and Two-Particle Quantities

The microscopic derivation of the DCA based on the diagrammatic expression of the grand potential enables us to access thermodynamic properties. Motivated by this, we use the free energy to construct a unique platform to gain access into the local order parameter of a disordered system. Let us take the simplest order parameter, the magnetization, m, which is the trace of the local Green function. The susceptibility follows immediately as the second derivative, and we end up with a Bethe-Salpeter equation. An order parameter within the TMDCA can intuitively be motivated by the above physical concept. The key task then will be how to formulate an appropriate order parameter in the TMDCA, which is a **K**-space formalism. We will try to answer this important question below.

Baym and Kadanoff [379, 380] demonstrated that a thermodynamically consistent approximation may be formulated by requiring that the self-energy Σ be the functional derivative of the Baym-Kadanoff generation function Φ with respect to the Green function, i.e., fulfill

$$\mathcal{G}^{-1} - G^{-1} = \Sigma = \frac{\delta\Phi[G]}{\delta G}. \tag{11.5}$$

This should be done self-consistently by carefully summing over all closed, connected, and compact graphs constructed from the fully dressed Green function G. With this, the irreducible vertices $\Gamma = \delta\Sigma/\delta G$. The second order contribution to the generating functional Φ for a Hubbard-like model is as depicted in Figure 11.2(a), becomes a functional of the local interaction and the Green function. In obtaining the self-energy Σ from a functional derivative of Φ with respect to the Green

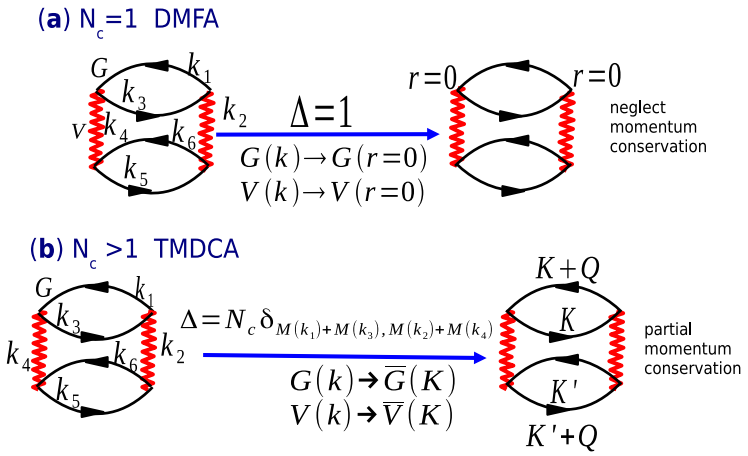

Figure 11.2: (**a**) The second order contribution to the generating functional Φ for the DMFA. As we apply the DMFA coarse-graining approximation, Equation 11.4, Φ becomes a functional of the fully dressed local Green function. (**b**) The second-order term in Φ for a Hubbard-like model. Here the undulating line represents the interaction U, and on the LHS (RHS) the solid line is the lattice (coarse-grained) single-particle Green functions. When the TMDCA Laue function is used to describe momentum conservation at the internal vertices, the momenta collapse onto the cluster momenta with each lattice Green function now replaced by the corresponding coarse-grained ones.

function G, one of the Green function lines is effectively broken. With the appropriate set of Dyson and Bethe-Salpeter equations, and the diagrammatic form of the generating functional, a complete diagrammatic formalism for accessing thermodynamic quantities can be formulated.

As demonstrated in the DCA, the unique choice of the self-energy, which guarantees that the DCA free energy is appropriately minimized is the mapping $\Sigma(\mathbf{k},\omega) = \overline{\Sigma}(\mathbf{M}(\mathbf{k}),\omega)$. Motivated by this, care must also be taken in constructing two-particle quantities. Following Ref. [263], the appropriate definition of the irreducible vertice between the lattice and the cluster should be $\mathbf{\Gamma} \approx \overline{\mathbf{\Gamma}} = \delta\overline{\mathbf{\Sigma}}/\delta\mathbf{G}$ yields an estimate for the susceptibility, which is equivalent to the result of the second derivative of the free energy with respect to an external field as will be demonstrated shortly. With this mind, *the cluster calculations should be used to provide irreducible quantities* and together with the bare real-lattice Green functions, one may construct the corresponding reducible quantities [263]. This prescription is not only motivated physically for the single-particle Green functions but can be shown to be the same for the two-particle counterparts [263].

11.3.1 Derivability of the Generating Function

The generating functional Φ can also be coarse-grained. The generating functional is the sum over all the closed, connected, compact diagrams, such as the one shown in Figure 11.2(b) given as

$$\Phi(G) = \sum_l p_l tr\left[\Sigma^l G\right] \tag{11.6}$$

The trace denotes summation over frequency, momentum, and spin, Σ^l is a set of irreducible self-energy diagrams of the lth order in interaction, G is the fully dressed Green function related to Σ via the Dyson equation (11.5), p_l is a counting factor, which measures the number of occurrences of G in each term (for a Hubbard-like model, $p_l = 1/l$). From Equation 11.9, it follows immediately that Equation 11.5 is satisfied, as required for a "Φ-derivable" theory [267].

Intuitively, the choice of the Laue function for the TMDCA Δ_{TMDCA} is the replacement of the lattice quantities with their corresponding coarse-grained counterparts denoted with overbars (cf. Figure 11.2(b)). For instance, the lattice Green function G_σ is replaced by the coarse-grained cluster Green function $\bar{G}_\sigma$. In the coarse-grained form, the external momentum label $(\mathbf{k})$ of the cluster self-energy in principle, is still the lattice momentum but the self-energy now only depends on $\mathbf{k}$ through the function $\mathbf{M}(\mathbf{k})$. With the application of the Laue function on the vertices, the corresponding TMDCA Φ functional is

$$\Phi_{TMDCA}[G] = \sum_l p_l tr\left[\bar{\Sigma}^l \bar{G}\right] \tag{11.7}$$

with the corresponding lattice quantities,

$$\frac{\delta\Phi_{TMDCA}}{\delta\bar{G}} = \bar{\Sigma} = \frac{\delta\Phi_{TMDCA}}{\delta G} \tag{11.8}$$

The second equality is true since the variation $\delta/\delta G$ corresponds to cutting a Green function line. The relation between the grand potential functional (here the free energy F_{TMDCA}) and the generating functional Φ may be expressed in terms of the linked cluster expansion [381] as

$$F_{TMDCA} = -k_B T\left(\Phi[G] - \mathrm{tr}\left[\Sigma G\right] - \mathrm{tr}\ln\left[-G\right]\right) \tag{11.9}$$

where the trace depicts a summation over cluster sites $\mathbf{X}$, superlattice wavevectors $\tilde{\mathbf{k}}$, frequency, and spin [267]. Rearranging and taking functional derivative we obtain

$$-\frac{1}{\kappa T}\frac{\delta F_{TMDCA}}{\delta G(\vec{k})} = \frac{\delta \Sigma_c}{\delta G(\vec{k})} - \mathrm{Tr}\,\frac{\delta[\Sigma G]}{\delta G(\vec{k})} + \mathrm{Tr}\,\frac{1}{G(\vec{k})}. \tag{11.10}$$

The perturbative series for Φ, Σ, and the irreducible vertices Γ in the DMFA are identical to those of the corresponding impurity model, hence, conventional impurity solvers may be used. However, care must be taken to avoid overcounting by excluding the local self-energy $\Sigma(\omega)$

$$\mathcal{G}(\omega)^{-1} = G(\omega)^{-1} + \Sigma(\omega) \tag{11.11}$$

from the local propagator $\mathcal{G}$ input to the impurity solver. This is important since most impurity solvers will sum all the diagrams equally, not just the skeletal ones. Here, $G(\omega)$ is the fully dressed local Green function. In this local approximation regime, the Hubbard model has the same diagrammatic expansion as the Anderson impurity model.

From Eqs. 11.9 and 11.10, observe that F_{TMDCA} is stationary with respect to $\mathbf{G}$ when

$$\frac{-1}{k_B T}\frac{\delta F_{TMDCA}}{\delta G(\mathbf{k})} = \bar{\Sigma}(\mathbf{M}(\mathbf{k})) - \Sigma(\mathbf{k}) = 0, \tag{11.12}$$

which implies that $\Sigma(\mathbf{k}) = \bar{\Sigma}(\mathbf{M}(\mathbf{k}))$ is the proper approximation for the lattice self-energy corresponding to Φ_{TMDCA}. The corresponding lattice single-particle propagator is then given by

$$G(\mathbf{k},\omega) = \frac{1}{\omega - \varepsilon_{\mathbf{k}} - \varepsilon - \bar{\Sigma}(\mathbf{M}(\mathbf{k}),\omega)}. \tag{11.13}$$

where $\mathbf{k} = K + \tilde{k}$. From the above formulation, it is obvious that the observables calculated from the Green function G agree with those calculated from the free energy functional, i.e., thermodynamically consistent. Since momentum and energy are conserved in the vertices, together with condition (11.5) ensures that conservation laws e.g., Ward identities are satisfied [380]. A similar procedure can be used to construct the two-particle quantities needed for calculating the conductivity or the nature of the phase diagram within the typical medium dynamical cluster approximation.

This procedure is a generalization of the response functions calculations as in single impurity solvers [382, 383].

Within the TMDCA, spatial correlations, which are important ingredient for enhancing coherent backscattering, quantum tunneling vis-á-vis deep trapped states, etc will allow for the proper characterization of electron localization. To be able to characterize electron localization using the direct current (DC) conductivity, we have to be able to compute response functions, which thermodynamically, are generally defined as second derivatives of the free energy with respect to some external fields. The quantities $\Phi_{TMDCA}(G)$, $\bar{\Sigma}$, and F_{TMDCA} depend on these fields only through G and the bare $\mathcal{G}$. Following Baym and Kadanoff [379], the approximation for Γ can be written as

$$\Gamma \approx \bar{\Gamma} \equiv \frac{\delta\bar{\Sigma}}{\delta G} \tag{11.14}$$

which is the same as that obtained from the second derivative of F_{TMDCA} with respect to the applied field. For instance, assuming an external homogeneous field h with spin σ, the magnetization, m is

$$m = \mathrm{Tr}\left[\sigma G_\sigma\right]. \tag{11.15}$$

and the susceptibility, which is the second derivative follows immediately as,

$$\frac{\partial m}{\partial h} = \mathrm{Tr}\left[\sigma\frac{\partial G_\sigma}{\partial h}\right]. \tag{11.16}$$

Recall that $G_\sigma = \left(G_\sigma^{0-1} - \bar{\Sigma}_\sigma\right)^{-1}$. Then, using this in Equation 11.16, we obtain,

$$\frac{\partial m}{\partial h} = \mathrm{Tr}\left[\sigma\frac{\partial G_\sigma}{\partial h}\right] = \mathrm{Tr}\left[G_\sigma^2\left(1+\sigma\frac{\partial\bar{\Sigma}_\sigma}{\partial G_{\sigma'}}\frac{\partial G_{\sigma'}}{\partial h}\right)\right]. \tag{11.17}$$

If we identify $\chi_{\sigma,\sigma'} = \sigma\frac{\partial G_{\sigma'}}{\partial h}$, and $\chi^0_\sigma = G^2_\sigma$, collect like terms within both traces, and sum over the cell momenta $\tilde{\mathbf{k}}$, we obtain the two-particle Dyson's equation

$$2\left(\bar{\chi}_{\sigma,\sigma} \;-\; \bar{\chi}_{\sigma,-\sigma}\right) = 2\bar{\chi}^0_\sigma + 2\bar{\chi}^0_\sigma\left(\bar{\Gamma}_{\sigma,\sigma} - \bar{\Gamma}_{\sigma,-\sigma}\right)\left(\bar{\chi}_{\sigma,\sigma} - \bar{\chi}_{\sigma,-\sigma}\right). \tag{11.18}$$

11.4 Calculation of Experimental Measurable Physical Quantities

So far, the formalisms that have been discussed above cannot be measured directly by experiment. All measurable physical quantities can be expressed theoretically as either reducible one or two-particle quantity. Both either the reducible one or two-particle parameters can be informed from the Green function, which generally is the end product of a self-consistent, converged simulation. For instance, to compare with experimental angle-resolved photoemission spectroscopy, the single-particle Green function is the needed input, which is obtained directly by solving the Dyson equation, self-consistently. For the calculation of the conductivity, the important input quantity is the irreducible vertices in the different scattering channels obtained by solving the Bethe-Salpeter equations for the lattice. Here, we will try to provide the details of how to obtain the two-particle Green function and the mapping between the lattice and cluster, counterparts.

11.4.1 Particle-hole channel

In the particle-hole channel, the two-particle Green function (neglecting spin) is

$$\begin{aligned}\chi(q,k,k') &= \int_0^\beta\int_0^\beta\int_0^\beta\int_0^\beta d\tau_1 d\tau_2 d\tau_3 d\tau_4 \times e^{i\left((\omega_n+\nu)\tau_1-\omega_n\tau_2+\omega_{n'}\tau_3-(\omega_{n'}+\nu)\tau_4\right)} \\ &\times \langle T_\tau c^\dagger_{\mathbf{k}+\mathbf{q}}(\tau_1)c_{\mathbf{k}}(\tau_2)c^\dagger_{\mathbf{k}'}(\tau_3)c_{\mathbf{k}'+\mathbf{q}}(\tau_4)\rangle.\end{aligned} \tag{11.19}$$

Here, we use the conventional notations $k=(\mathbf{k},i\omega_n)$, $k'=(\mathbf{k},\omega'_n)$ and $q=(\mathbf{q},\nu_n)$ [381], where T_τ is the time ordering operator. The two-particle irreducible vertex $\Gamma_{\sigma,\sigma'}(q,k,k')$, which is the analogue of the self-energy and $\chi_{\sigma,\sigma'}(q,k,k')$, which is the non-interacting susceptibility constructed from a pair of fully-dressed single-particle Green functions are related to each other via the Bethe-Salpeter equation (Figure 11.3):

$$\chi(q,k,k') = \chi^0(q,k,k')+\chi^0(q,k,k'')\times\Gamma(q,k'',k''')\chi(q,k''',k') \tag{11.20}$$

where the summation is for repeated indices. Applying many-to-one map, i.e., $\Gamma(q,k,k')\rightarrow\Gamma_c(q,\mathbf{M}(k),\mathbf{M}(k'))$ (frequency labels have been suppressed) as in the TMDCA and substituting

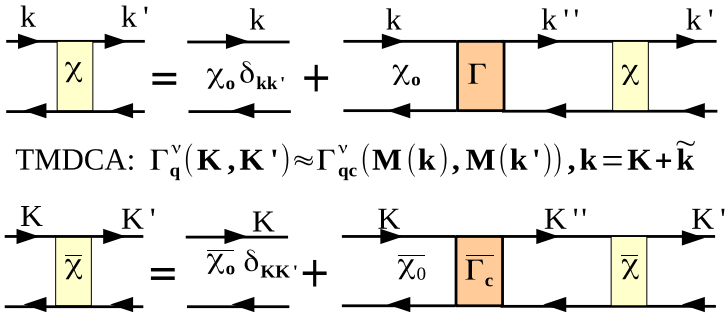

Figure 11.3: The diagrammatic representation of the Bethe-Salpeter equation for the TMDCA for the particle-hole channel. Here, the lattice irreducible vertex Γ^{ν} is approximated by the Γ^{ν}_{c} from the TMDCA cluster coarse-grained over the $\tilde{\mathbf{k}}$ momenta. With this, the remaining equation is a function of the cluster $\mathbf{K}$ only and may be solved by inversion.

in Equation 11.20 to obtain

$$\bar{\chi}(q,K,K') = \bar{\chi}^0(q,K,K') + \bar{\chi}^0(q,K,K'') \times \Gamma_c(q,K'',K''')\bar{\chi}(q,K''',K') \,. \tag{11.21}$$

Note in Equation 11.21, since we need to sum over all the k and k' to obtain the susceptibility at q, and since only the bare and dressed two-particle Green functions χ^0 and χ, respectively (see the product on the RHS of Equation 11.20), depend on the momenta, only within the cell, $\tilde{\mathbf{k}}$ and share no common momentum labels, we may freely sum over the momenta $\tilde{\mathbf{k}}$ within a cell.

The coarse-graining of the Bethe-Salpeter equation greatly reduces its complexity since each of the matrices above is sufficiently small and hence can be solved using standard techniques. Even at the reduction in the complexity, unlike coarse-graining at the single-particle level where the coarse-grained quantities are identical to those of the cluster, this is not the case at the two-particle level. For instance, $\chi_c(q,K,K') \neq \bar{\chi}(q,K,K')$. This can be understood from the fact that all the quantities obtained at the single particle level are obtained directly at the end of a converged self-consistency simulation. In contrast at the two-particle level, neither $\Gamma(q,K,K')$ nor the coarse-grained susceptibility $\bar{\chi}(q,K,K')$ are calculated during the self-consistency. They are derived quantities from an already converged TMDCA in a separate program. For instance, the coarse-grained non-interacting susceptibility $\bar{\chi}^0(q,K,K')$ is calculated in a separate program after

the TMDCA converges using the relation

$$\bar{\chi}^0[(\mathbf{q},\nu);(\mathbf{K},\omega);(\mathbf{K}',\omega')] = \delta_{\mathbf{K},\mathbf{K}'}\delta_{\omega,\omega'}\frac{N_c}{N}\sum_{\tilde{\mathbf{k}}} G(\mathbf{K}+\tilde{\mathbf{k}},\omega)G(\mathbf{K}+\tilde{\mathbf{k}}+\mathbf{q},\omega+\nu) \tag{11.22}$$

and the corresponding cluster susceptibility is calculated by the cluster solver and the vertex function is obtained by solving the cluster two-particle Bethe-Salpeter equation

$$\chi_c(q,K,K') = {\chi_c}^0(q,K,K') + {\chi_c}^0(q,K,K'') \times \Gamma_c(q,K'',K''')\chi_c(q,K''',K'). \tag{11.23}$$

Combining Eqs. 11.21 and 11.23, then, we obtain the coarse-grained susceptibility as

$$\bar{\chi}^{-1} = \chi_c^{-1} - \chi_c^{0^{-1}} + \bar{\chi}^{0^{-1}}, \tag{11.24}$$

where, for example, $\bar{\chi}$ is the matrix formed from $\bar{\chi}(\mathbf{q},\mathbf{K},\mathbf{K}')$ for fixed $\mathbf{q}$, which for our case $\mathbf{q}=0$.

11.4.2 Particle-particle channel

In the particle-particle channel, the calculation of susceptibilities is identical to the above that of the particle-hole channel, except when the susceptibility calculations are done for transitions to states of lower symmetry than the lattice symmetry. For instance, in order to obtain the pair function of the desired symmetry (s,p,d), the two-particle Green function must be multiplied by the corresponding form factors $g(\mathbf{k})$ and $g(\mathbf{k}')$ such that $g(\mathbf{k})=1$ (s wave), $g(\mathbf{k}) = cos(k_x)+cos(k_y)$ (extended s wave) and $g(\mathbf{k}) = cos(k_x)-cos(k_y)$ ($d_{x^2-y^2}$ wave). Hence, the Bethe-Salpeter equation becomes

$$\begin{aligned} g(\mathbf{k})\chi(q,k,k')g(\mathbf{k}') &= g(\mathbf{k})\chi^0(q,k,k')g(\mathbf{k}') + g(\mathbf{k})\chi^0(q,k,k'') \\ &\times \Gamma(q,k'',k''')\times\chi(q,k''',k')g(\mathbf{k}'). \end{aligned} \tag{11.25}$$

where $\chi(q,k,k')$ is the same as in Equation 11.19. Evaluating Equation 11.25 is not trivial if it is to be coarse-grained, since this will partially convolve $\chi(q,k,k')$ with *two* factors of g on the LHS and *one* factor on the RHS. Hence for the susceptibilities, or any situation where the system has

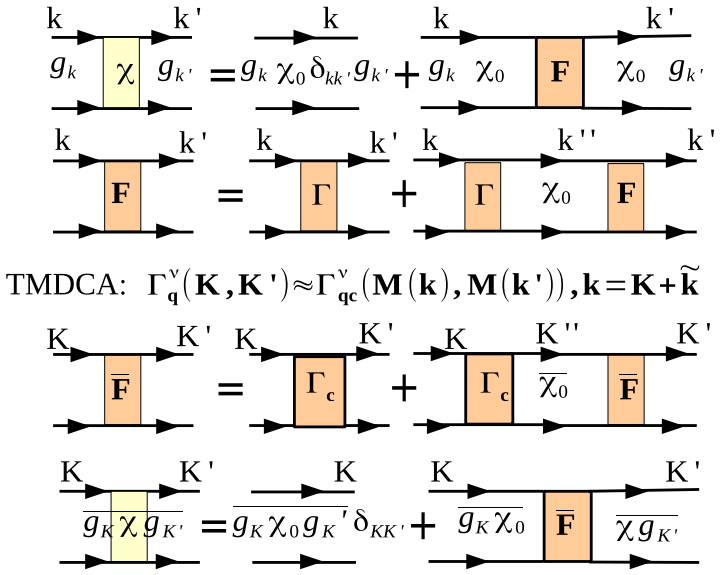

Figure 11.4: The diagrammatic representation of the particle-particle projected susceptibilities. Here the Bethe-Salpeter equation is rewritten in terms of the irreducible vertex F and the lattice irreducible vertex Γ^{ν} is approximated by the Γ^{ν}_{c} obtained from the TMDCA cluster and coarse-graining over the $\tilde{\mathbf{k}}$ momenta. After the projected bare bubbles are calculated, the remaining equation is only a function of the cluster $\mathbf{K}$ momenta only and may be solved by inversion.

a non-trivial form factor, an equivalent equation involving the reducible vertex F (instead of the irreducible vertex Γ) is adopted

$$\begin{aligned} g(\mathbf{k})\chi(q,k,k')g(\mathbf{k}') &= g(\mathbf{k})\chi^0(q,k,k')g(\mathbf{k}') + g(\mathbf{k})\chi^0(q,k,k'') \\ &\times F(q,k'',k''')\chi^0(q,k''',k')g(\mathbf{k}'), \end{aligned} \tag{11.26}$$

where

$$F(q,k,k') = \Gamma(q,k,k') + \chi^0(q,k,k'')\Gamma(q,k'',k''')\chi^0(q,k''',k') + \cdots \tag{11.27}$$

For convenient, let us define

$$\Pi_{g,g}(q,k,k') = g(\mathbf{k})\chi(q,k,k')g(\mathbf{k}') \tag{11.28a}$$

$$\Pi^0_{g,g}(q,k,k') = g(\mathbf{k})\chi^0(q,k,k')g(\mathbf{k}') \tag{11.28b}$$

$$\Pi^0_{g}(q,k,k') = g(\mathbf{k})\chi^0(q,k,k'). \tag{11.28c}$$

From here onward, the steps in the calculation of the two-particle quantities are identical to the particle-hole channel: We invert the cluster particle-particle Bethe-Salpeter equation with $g = 1$ for the cluster and extract Γ_c. Then, we coarse-grain Equation 11.27 and use Γ_c to calculate the coarse-grained $\bar{F} = \Gamma_c \left(1 - \bar{\chi}^0 \Gamma_c\right)^{-1}$. Next, we coarse-grain Equation 11.26 and use the coarse-grained $\bar{F}$ to calculate the coarse-grained $\bar{\Pi}_{g,g}$ as

$$\bar{\Pi}_{g,g}(q,K,K') = \bar{\Pi}^0_{g,g}(q,K,K') + \bar{\Pi}^0_g(q,K,K'')\bar{F}(q,K'',K''')\bar{\Pi}^0_g(q,K''',K'). \quad (11.29)$$

11.5 Calculating Conductivity in the Typical Medium DCA

We will in this section combine all the ideas developed in previous sections above to formulate a method for calculating direct current (DC) conductivity within the typical medium dynamical cluster approximation (TMDCA). In obtaining $\bar{\Pi}_{g,g}$ (cf. Equation 11.29), recall that we coarse-grained Equation 11.26, using the coarse-grained $\bar{F}$. Below, we outline the steps involved as

$$\begin{aligned} \bar{\Pi}_{g,g}(q,K,K') &= \overline{g(\mathbf{k})\chi(q,k,k')g(\mathbf{k}')} \quad (11.30) \\ &= \overline{g(\mathbf{k})\chi^0(q,k,k')g(\mathbf{k}')} \times \bar{\Gamma}_{g,g}(q,K'',K''') \frac{\left(1 - \overline{\chi^0_g}\bar{\Gamma}_{g,g}\right)^{-1}(q,K''',K'''')}{\chi^0_g(q,K'''',\mathbf{k}')g(\mathbf{k}')} \end{aligned}$$

which, reduces to

$$\bar{\Pi}_{g,g}(q,K,K') = \bar{\Pi}^0_{g,g}(q,K,K') + \bar{\Pi}^0_g(q,K,K'')\bar{F}(q,K'',K''')\bar{\Pi}^0_g(q,K''',K'). \quad (11.31)$$

In order to find the bare bubbles, we need the time-ordered lattice Green function (note $\mathbf{k} = (\mathbf{k},\omega)$) $G_l(q,\mathbf{k},\mathbf{k}',\omega)$

$$G_l(q,\mathbf{k},\mathbf{k}',\omega) = \begin{cases} G_{loc}(q,K)\delta_{K,K'}, \text{ if } \quad |\omega| > \omega_e \\ G_{ext}(q,\mathbf{k})\delta_{\mathbf{k},\mathbf{k}'}, \text{ if } \quad |\omega| < \omega_e \end{cases} \quad (11.32)$$

where G_{loc} is the localized (only on the cluster) part of the Green function, G_{ext} is the extended part of the Green function, and ω_e is the mobility edge energy.

For the non-interacting Anderson model, the scattering is purely classical, so the momentum can change by a scattering event, but the frequency does not change. This implies that if the external labels are ω and $\omega+\nu$, then, the lines will have these same labels, as such, requiring no internal frequency integration. However, if the system is an interacting disordered, a distinction needs to be made between elastic and inelastic scattering contributions. This is important since interactions will induce inelastic scattering processes.

Considering $\Pi^0_{g,g}(k,k')$, and using $q=0$, then from above, recall that

$$\Pi^0_{g,g}(K,K') = \overline{g(\mathbf{k})\chi^0(\mathbf{k},\mathbf{k}')g(\mathbf{k}')}. \tag{11.33}$$

Then,

$$\begin{aligned}\lim_{\nu\to 0^+}\Pi^0_{g,g}(K,K',\omega+\nu) &= \delta_{\mathbf{k},\mathbf{k}'}\frac{N_c}{N}\sum_{\tilde{k}\tilde{k}'}\vartheta_{K+\tilde{k},x}G_{loc}(K,\omega)\vartheta_{K+\tilde{k}',x}G_{loc}(K,\omega+\nu)\Theta(|\omega|-\omega_e)\\ &+ \delta_{\mathbf{k},\mathbf{k}'}\frac{N_c}{N}\sum_{\tilde{k}}(\vartheta_{k+\tilde{k},x})^2G_{ext}(K+\tilde{k},\omega)G_{ext}(K+\tilde{k},\omega+\nu)\Theta(\omega_e-|\omega|)\end{aligned} \tag{11.34a}$$

which, reduces to

$$\begin{aligned}\lim_{\nu\to 0^+}\Pi^0_{g,g}(K,\omega+\nu) &= \frac{N_c}{N}\left(\sum_{\tilde{k}}\vartheta_{K+\tilde{k},x}\right)^2 G_{loc}(K,\omega)G_{loc}(K,\omega+\nu)\Theta(|\omega|-\omega_e) \quad (11.34b)\\ &+ \frac{N_c}{N}\sum_{\tilde{k}}(\vartheta_{k+\tilde{k},x})^2G_{ext}(K+\tilde{k},\omega)G_{ext}(K+\tilde{k},\omega+\nu)\Theta(\omega_e-|\omega|)\end{aligned}$$

where $\Theta(x)$ is a step function. Similarly, $\bar{\Pi}^0_g(q,K,K'')$ and $\bar{\Pi}^0_g(q,K''',K')$ from Equation 11.31 can be expressed as

$$\lim_{\nu\to 0^+}\bar{\Pi}^0_g(K,\omega+\nu) = \begin{cases}\frac{N_c}{N}\sum_{\tilde{k}}\vartheta_{K+\tilde{k},x}G_{loc}(K,\omega)G_{loc}(K,\omega+\nu), \text{ if } \quad |\omega|>\omega_e\\ \\ \frac{N_c}{N}\sum_{\tilde{k}}\vartheta_{K+\tilde{k},x}G_{ext}(K+\tilde{k},\omega)G_{ext}(K+\tilde{k},\omega+\nu), \text{ if } \quad |\omega|\leqslant\omega_e.\end{cases} \tag{11.35}$$

The full charge susceptibility noting that $\overline{\Pi^0_{g,g}}$ and Π^0_g are diagonal in $\mathbf{K}$ is

$$\overline{\Pi_{g,g}}(\mathbf{k},\mathbf{k}') = N_c\delta_{\mathbf{k},\mathbf{k}'}\overline{\Pi^0_{g,g}}(\mathbf{k},\mathbf{k}') + \overline{\Pi^0_g}(\mathbf{k},\mathbf{k})\Gamma(K,K'')(1-\overline{\chi^0_g}\Gamma)^{-1}(K'',K')\overline{\Pi^0_g}(\mathbf{k}',\mathbf{k}') \qquad (11.36)$$

The DC conductivity σ_{DC} is obtained directly from Equation 11.36 by setting $g = 1$ taking the imaginary part as

$$\sigma_{DC} = \lim_{\omega\to 0^+}\frac{1}{\omega}\Im\Pi(\omega) \qquad (11.37)$$

The diagrammatic representation of the first two contributions to the conductivity is depicted in

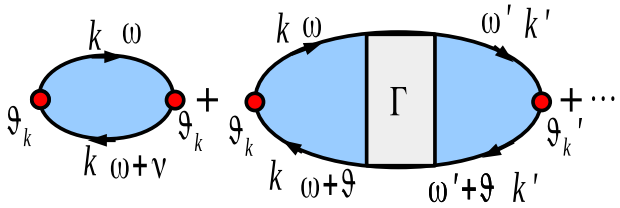

Figure 11.5: The diagrammatic representation of the first two contributions to the conductivity. The first diagram is the momentum independent part, the so-called bare bubble part, i.e., the **k**-sums on both sides can be done independently. The second diagram contains the full particle-hole vertex insertion.

Figure 11.5. In arriving at Equation 11.37, we note most important, the separation of fully dressed cluster Green (cf. Eqs. 11.34–11.35), which serves as input for the calculation of the conductivity into local and extended parts, respectively. This guarantees that the extended part, which is characterized by a well-defined dispersion, $\varepsilon_{\mathbf{K}}$ is properly represented while the dispersionless part of the spectrum is taken care of by the localized Green function, which is now local on the cluster.

11.6 Numerical Results: Conductivity for Various System Sizes

As a prove of concept, we show in Figure 11.6 for a box disorder distribution, a plot of the DC conductivity $\sigma(\omega\to 0)$ as a function of increasing disorder strengths for various cluster sizes $N_c = 1$, 12, and 38 in comparison with the numerical results of Kramer *et al.* [384]. As it is evident from Figure 11.6, the $\sigma(\omega\to 0)$ formulated within the typical medium dynamical cluster approximation characterizes the metal-insulator-transitions properly as it systematically goes to zero as the

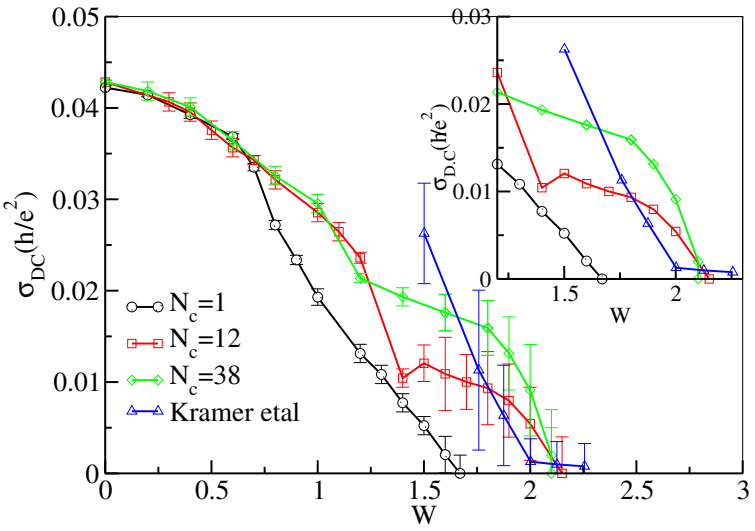

Figure 11.6: The direct current (DC) conductivity $\sigma(\omega \to 0)$ as a function of disorder strength for various cluster sizes $N_c = 1$, 12, and 38 in comparison with the equation of motion numerical results of Kramer *et al.* [384]. The inset shows the same result at reduced scale without error bars. Note, the data of Kramer *et al.* [384] have been multiplied by a factor of π.

strength of the disorder is increased towards the critical value. The $\sigma(\omega \to 0)$ goes to zero at $W_c^{U=0}$ of ≈ 1.65 and 2.1 for the single sites and finite clusters ($N_c \geqq 12$), respectively in agreement with the critical disorder strengths obtained using the typical density of states as an order parameter. Hence, $\sigma(\omega \to 0)$ clearly shows the same trend as the typical density of states and the imaginary part of the hybridization function, which all vanishes at the critical disorder strengths.

Observe further from Figure 11.6 the difference in the trend for the single site ($N_c = 1$ and finite cluster ($N_c = 12$ and 38) data at the intermediate disorder strengths. While the $N_c = 1$ monotonically goes to zero as the critical disorder strength is approached, the finite clusters first starts decreasing as the disorder strength is increased and then gets delocalized at the intermediate disorder strength before finally being localized as disorder strength is further increased towards the critical value. This fingerprint in the finite clusters is due to the re-entrance of the mobility edge, which is missing in single site approaches. As the cluster size increases, the DoS acquires systematically states in the band tails leading to increased deep trapped states at larger energies [242, 272], which are zero in the N_c=1 case. Hence, by making $N_c > 1$ we systematically inject additional states that tend to push the localization edge outward. States above and below the bare band edges are

initially localized in deeply trapped states. They become delocalized with increasing W due to the increasing DoS and hence increasing quantum tunneling between the deeply trapped states. They finally become localized again with increasing disorder, which explains the re-entrant behavior.

There is lack of numerical data on the calculation of conductivity of disordered electron systems leading to localization transitions. To benchmark our results, we compare our TMDCA results with the numerical data of Kramer *et al.* [384]. Surprisingly, as a function of increase in cluster size, we reproduce the essential features of their data. The present result is remarkable as this will enable comparison with experimental results for electron localization since it is easier to measure $\sigma(\omega \rightarrow 0)$ in experimental setting than any other order parameters characterizing localization transitions. We believe that this will motivate experiments to measure $\sigma(\omega \rightarrow 0)$ as a function of disorder strength, which can be controlled by doping the 'pure' system with varying concentrations of the dopant.

11.7 Conclusion

A two-particle formalism within the typical medium dynamical cluster approximation for calculating two-particle quantities like the conductivity are proposed. By carefully separating the Green function into extended and localized parts, it is shown that this is the appropriate way of thinking about two-particle quantities for characterizing electron localization. As a function of disorder strength, the direct conductivity $\sigma(\omega \rightarrow 0)$ calculated within the TMDCA is shown to be the appropriate two-particle order parameter characterizing the localization transitions. It is our hope that this result will spurn both numerical calculations and experimental measurements of $\sigma(\omega \rightarrow 0)$.

Bibliography

[1] C. E. Ekuma *et al.*. J. Phys. Conden. Matt. **26**(27), 274209 (2014).

[2] C. E. Ekuma *et al.*. Phys. Rev. B **89**, 081107 (2014).

[3] H. Terletska *et al.*. Phys. Rev. B **90**, 094208 (2014).

[4] E. Abrahams *et al.*. Phys. Rev. Lett. **42**, 673–676 (1979).

[5] P. Henseler *et al.*. Phys. Rev. B **78**, 235116 (2008).

[6] Y. Song *et al.*. Phys. Rev. B **77**, 054202 (2008).

[7] N. Paris *et al.*. Phys. Rev. B **75**, 165113 (2007).

[8] D. Tanasković *et al.*. Phys. Rev. Lett. **91**, 066603 (2003).

[9] M. Enjalran *et al.*. Phys. Rev. B **64**, 184402 (2001).

[10] M. E. Pezzoli and F. Becca. Phys. Rev. B **81**, 075106 (2010).

[11] D. Heidarian and N. Trivedi. Phys. Rev. Lett. **93**, 126401 (2004).

[12] K. Byczuk *et al.*. Phys. Rev. B **69**, 045112 (2004).

[13] F. Fazileh *et al.*. Phys. Rev. Lett. **96**, 046410 (2006).

[14] X. Chen and R. J. Gooding. Phys. Rev. B **80**, 115125 (2009).

[15] D. Y. Sharvin and Y. V. Sharvin. JETP Lett. **34**, 272 (1982).

[16] G. Bergmann. Phys. Rep. **107**, 1 (1984).

[17] A. Efros and M. Pollak (Eds.) *Electron-Electron Interactions in Disordered Systems*, vol. 10 of *Modern Problems in Condensed Matter Sciences* (North-Holland, Amsterdam) (1985).

[18] M. Ma and E. Fradkin. Phys. Rev. B **28**, 2990–3006 (1983).

[19] A. Punnoose and A. M. Finkel'stein. Science **310**(5746), 289–291 (2005).

[20] S. Anissimova *et al.*. Nat. Phys. **3**(10), 707–710 (2007).

[21] P. B. Chakraborty *et al.*. Phys. Rev. B **84**, 035121 (2011).

[22] P. B. Chakraborty *et al.*. Phys. Rev. B **75**, 125117 (2007).

[23] P. J. H. Denteneer *et al.*. Phys. Rev. Lett. **83**, 4610–4613 (1999).

[24] P. J. H. Denteneer *et al.*. Phys. Rev. Lett. **87**, 146401 (2001).

[25] P. J. H. Denteneer and R. T. Scalettar. Phys. Rev. Lett. **90**, 246401 (2003).

[26] G. Fleury and X. Waintal. Phys. Rev. B **81**, 165117 (2010).

[27] E. Abrahams *et al.*. Rev. Mod. Phys. **73**, 251–266 (2001).

[28] G. Fleury and X. Waintal. Phys. Rev. Lett. **100**, 076602 (2008).

[29] B. Srinivasan *et al.*. Phys. Rev. B **67**, 205112 (2003).

[30] B. L. Altshuler and A. G. Aronov. JETP Lett. **27**, 662 (1978).

[31] H.-Y. Chen *et al.*. Phys. Rev. B **84**, 045113 (2011).

[32] Y. Otsuka *et al.*. Phys. Rev. B **58**, 15314–15316 (1998).

[33] A. W. Sandvik *et al.*. Phys. Rev. B **50**, 10474–10484 (1994).

[34] M. Ma. Phys. Rev. B **26**, 5097–5102 (1982).

[35] P. W. Anderson. Phys. Rev. **109**, 1492–1505 (1958).

[36] B. Kramer and A. MacKinnon. Rep. Prog. Phys. **56**(12), 1469 (1993).

[37] F. Evers and A. D. Mirlin. Rev. Mod. Phys. **80**, 1355–1417 (2008).

[38] N. F. Mott. Proc. Phys. Soc., Sect. A **62**, 416 (1949).

[39] N. F. Mott. *Metal-Insulator Transitions, 2nd ed.* (Taylor and Francis, London) (1990).

[40] L. Sanchez-Palencia and M. Lewenstein. Nature Physics **6**, 87–95 (2010).

[41] B. Shapiro. J. Phys. A: Math. and Theor. **45**(14), 143001 (2012).

[42] M. White *et al.*. Phys. Rev. Lett. **102**, 055301 (2009).

[43] S. S. Kondov *et al.*. arXiv:1305.6072 (2013).

[44] E. Abrahams (Ed.) *50 Years of Anderson Localization* (World Scientific) (2010).

[45] R. Sapienza *et al.*. Phys. Rev. Lett. **106**, 163902 (2011).

[46] D. Belitz and T. R. Kirkpatrick. Rev. Mod. Phys. **66**, 261–380 (1994).

[47] A. Finkel'stein. JETP Lett. **37**, 517 (1983).

[48] D. Basko *et al.*. Annals of Physics **321**(5), 1126 – 1205 (2006).

[49] K. I. Wysokiński. Phys. Rev. B **60**, 16376–16381 (1999).

[50] V. Dobrosavljević and G. Kotliar. Phys. Rev. Lett. **78**, 3943–3946 (1997).

[51] N. Mott and E. Davis. *Electronic processes in non-crystalline materials*. International series of monographs on physics (Clarendon Press) (1971).

[52] A. Richardella *et al.*. science **327**, 665 (2010).

[53] S. V. Kravchenko *et al.*. Phys. Rev. B **50**, 8039–8042 (1994).

[54] K. Maiti *et al.*. Phys. Rev. B **76**, 165128 (2007).

[55] K. W. Kim *et al.*. Phys. Rev. B **71**, 125104 (2005).

[56] R. K. Sahu *et al.*. J. Solid State Chem. **184**(3), 523 – 530 (2011).

[57] A. S. Sefat *et al.*. Phys. Rev. B **74**, 104419 (2006).

[58] A. Raychaudhuri. Adv. Phys. **44**(1), 21–46 (1995).

[59] J. Rammer. *Quantum Transport Theory*. Frontiers in Physics (Perseus Books) (1998).

[60] D. Vollhardt and P. Wölfle. *Self-Consistent Theory of Anderson Localization: in, Electronic Phase Transition* (Elsevier) (1992).

[61] E. Schrödinger. Naturwissenscahften **23**, 807 (1935).

[62] E. Schrödinger. Proceedings of the Cambridge Philosophical Society **31**, 555–662 (1935).

[63] K. Busch *et al.*. Phys. Rev. B **50**, 93–98 (1994).

[64] S. Aubry. J. Phys. Colloques **50**, C3–97 – C3–106 (1989).

[65] M. Janssen. Phys. Rep. **295**, 1–91 (1998).

[66] T. Sakanoue and H. Sirringhaus. Nat. Mater. **9**(9), 736–740 (2010).

[67] J. M. Rojo and A. M. Baro. Journal of Physics C: Solid State Physics **9**(19), L543 (1976).

[68] S. van Smaalen. Acta Crystallographica Section A **61**(1), 51–61 (2005).

[69] P. A. Lee and T. V. Ramakrishnan. Rev. Mod. Phys. **57**, 287–337 (1985).

[70] D. J. Thouless. Phys. Rep. **17**, 93–142 (1974).

[71] G. Pawłowski *et al.*. Phys. Rev. B **81**, 064514 (2010).

[72] T. Shirakawa *et al.*. J. Phys. Soc. Jpn. **76**, 014711 (2007).

[73] C. Conti and A. Fratalocchi. Nat Phys **4**(10), 794–798 (2008).

[74] M. P. V. Albada and A. Lagendijk. Phys. Rev. Lett. **55**, 2692–2695 (1985).

[75] S. Gentilini *et al.*. Opt. Lett. **34**(2), 130–132 (2009).

[76] P.-E. Wolf and G. Maret. Phys. Rev. Lett. **55**, 2696–2699 (1985).

[77] D. S. Wiersma *et al.*. Nature **390**(6661), 671–673 (1997).

[78] A. A. Chabanov *et al.*. Nature **404**(6780), 850–853 (2000).

[79] S. Gentilini *et al.*. Phys. Rev. B **81**, 014209 (2010).

[80] T. Schwartz *et al.*. Nature **446**(7131), 52–55 (2007).

[81] M. Störzer *et al.*. Phys. Rev. Lett. **96**, 063904 (2006).

[82] R. Frank *et al.*. Phys. Rev. B **73**, 245107 (2006).

[83] F. Scheffold *et al.*. Nature **398**(6724), 206–207 (1999).

[84] S. E. Skipetrov and B. A. van Tiggelen. Phys. Rev. Lett. **96**, 043902 (2006).

[85] D. S. Brambila and A. Fratalocchi. Sci. Rep. **3** (2013). Article.

[86] S. John. Phys. Rev. Lett. **53**, 2169–2172 (1984).

[87] J. Bravo-Abad. Nat Phys **11**(3), 213–214 (2015). News and Views.

[88] C. Wang *et al.*. Optics Communications **336**(0), 34 – 39 (2015).

[89] A. R. McGurn *et al.*. Phys. Rev. B **47**, 13120–13125 (1993).

[90] V. D. Freilikher *et al.*. Phys. Rev. E **51**, 6301–6304 (1995).

[91] Y. A. Vlasov *et al.*. Phys. Rev. B **60**, 1555–1562 (1999).

[92] M. A. Kaliteevski *et al.*. Phys. Rev. E **73**, 056616 (2006).

[93] P. Sheng. *Introduction to Wave Scattering, Localization and Mesoscopic Phenomena*. Springer Series in Materials Science (Springer-Verlag Berlin Heidelberg) (2006).

[94] E. Akkermans *et al.*. Phys. Rev. Lett. **56**, 1471–1474 (1986).

[95] N. Ashcroft and N. Mermin. *Solid State Physics*. HRW international editions (Holt, Rinehart and Winston) (1976).

[96] C. E. Ekuma *et al.*. *Finite cluster typical medium theory for disordered electronic systems*. Manuscript in preparation.

[97] I. M. Lifshits *et al.*. *Introduction to the Theory of Disordered Systems*. Wiley, New York (Dover Publishers Incorporated) (1988).

[98] B. Kramer *et al.*. Physica A **167**(1), 163 – 174 (1990).

[99] P. A. Lee *et al.*. Rev. Mod. Phys. **78**, 17–85 (2006).

[100] D. N. Basov and A. V. Chubukov. Nat Phys **7**(4), 272–276 (2011).

[101] T. Timusk and B. Statt. Reports on Progress in Physics **62**(1), 61 (1999).

[102] M. S. Laad *et al.*. Phys. Rev. B **64**, 195114 (2001).

[103] P. Lombardo *et al.*. Phys. Rev. B **74**, 085116 (2006).

[104] A. Georges *et al.*. Rev. Mod. Phys. **68**, 13–125 (1996).

[105] V. Dobrosavljević *et al.*. EPL **62**(1), 76 (2003).

[106] B. Kramer *et al.*. Int. J. Mod. Phys. B **24**, 1841–1854 (2010).

[107] H. Shinaoka1 and M. Imada. J. Phys. Soc. Jpn. **78**, 094708 (2009).

[108] B. L. Altshuler and A. G. Aronov. *in Electron-electron interactions in disordered systems*, 1 (Elsevier, Amsterdam) (1985).

[109] D. E. Aspnes. *in Handbook of Optical Constants of Solids, edited by E. D. Palik*, 451 (Springer,Berlin) (1985).

[110] E. Akkermans and G. Montambaux. *Mesoscopic Physics of Electrons and Photons* (Cambridge University Press, Cambridge) (2007).

[111] I. M. Lifshitz. Adv. Phys. **13**, 483 (1964).

[112] P. Stollmann. *Caught by Disorder* (Birkhäuser, Boston) (2001).

[113] L. A. Pastur and A. Figotin. *Spectra of Random and almost-Periodic Operators*. Springer, Berlin (Dover Publishers Incorporated) (1992).

[114] J. Fröhlich and T. Spencer. Commun. Mathem. Phys. **88**(2), 151–184 (1983).

[115] M. Aizenman and S. Molchanov. Comm. Math. Phys. **157**(2), 245–278 (1993).

[116] N. Mott. J. Phys C: Solid State Physics **20**(21), 3075 (1987).

[117] M. H. Cohen *et al.*. Phys. Rev. Lett. **22**, 1065–1068 (1969).

[118] N. Mott. Adv. Phys. **16**(61), 49–144 (1967).

[119] R. Landauer. Philosophical Magazine **21**(172), 863–867 (1970).

[120] D. J. Thouless. J. Phys. C: Solid State Phys. **3**, 1559 (1970).

[121] J. T. Edwards and D. J. Thouless. J. Phys. C **5**(8), 807 (1972).

[122] D. C. Licciardello and D. J. Thouless. J. Phys. C **8**(24), 4157 (1975).

[123] D. C. Licciardello and D. J. Thouless. Phys. Rev. Lett. **35**, 1475–1478 (1975).

[124] F. Wegner. Z. Phys. B **25**(4), 327–337 (1976).

[125] F. Wegner. Z. Phys. B **35**(3), 207–210 (1979).

[126] N. F. Mott. Philos. Mag. **6**(62), 287–309 (1961).

[127] P. P. Edwards and C. N. R. Rao. *Metal-Insulator Transitions Revisited* (Taylor & Francis, London) (1995).

[128] K. Slevin and T. Ohtsuki. Phys. Rev. Lett. **78**, 4083–4086 (1997).

[129] A. Altland and M. R. Zirnbauer. Phys. Rev. B **55**, 1142–1161 (1997).

[130] In C. Domb and J. Lebowitz (Eds.) *Cumulative Author, Title and Subject Index Including Table of Contents, Volumes 1–19*, vol. 20 of *Phase Transitions and Critical Phenomena*, 7 – 40 (Academic Press) (2001).

[131] K. Slevin and T. Ohtsuki. Phys. Rev. Lett. **82**, 382–385 (1999).

[132] K. Slevin and T. Ohtsuki. New J. Phys. **16**(1), 015012 (2014).

[133] P. Phillips. Annual Review of Physical Chemistry **44**(1), 115–144 (1993).

[134] T. Nakayama and K. Yakubo. *Fractal Concepts in Condensed Matter Physics*, vol. 140 of *Springer Series in Solid-State Sciences* (Springer) (2003).

[135] M. Janssen. Int. J. Mod. Phys. B **8**, 943 (1994).

[136] The most probable value of a random quantity is the mode, which is the value for which its PDF becomes maximal. A property X of a given system is self-averaging if 'most' realizations of the randomness in the thermodynamic limit have the same value of X. The Anderson localization does not have this property. Close to the critical point, physical observables are not Gaussian and generally have log-normal behavior. For discussions, see A. Aharony and A. B. Harris, Phys. Rev. Lett. **77**, 3700 – 3703 (1996); S. Wiseman and E. Domany, Phys. Rev. E **52**, 3469 – 3484 (1995), E. Orlandini, M .C. Tesi, and S. G. Whittington, J. Phys. A: Math. Gen. **35**, 4219 – 4227 (2002).

[137] W. Pook and M. Janßen. Z. Phys. B **82**(2), 295–298 (1991).

[138] A. D. Mirlin and Y. V. Fyodorov. Phys. Rev. Lett. **72**, 526–529 (1994).

[139] K. Byczuk *et al.*. Phys. Rev. Lett. **94**, 056404 (2005).

[140] I. S. Burmistrov *et al.*. Phys. Rev. Lett. **111**, 066601 (2013).

[141] W. Li *et al.*. Sci. Rep. **3**, 1772 (2013).

[142] A. Rodriguez *et al.*. Phys. Rev. Lett. **105**, 046403 (2010).

[143] M. A. Paalanen *et al.*. Phys. Rev. Lett. **48**, 1284–1287 (1982).

[144] A. H. Clark. Phys. Rev. **154**, 750–757 (1967).

[145] M. Morgan and P. A. Walley. Philos. Mag. **23**, 661 (1971).

[146] N. F. Mott. Philos. Mag. **19**(62), 835 (1969).

[147] C.-T. Liang *et al.*. Solid State Communications **102**(4), 327 – 330 (1997).

[148] A. L. Efros and B. I. Shklovskii. J. Phys. C: Solid State Physics **8**(4), L49 (1975).

[149] H. Stupp *et al.*. Phys. Rev. Lett. **71**, 2634–2637 (1993).

[150] C. Sürgers *et al.*. New Journal of Physics **15**(5), 055009 (2013).

[151] Y. Zhou and S. Ramanathan. Critical Reviews in Solid State and Materials Sciences **38**(4), 286–317 (2013).

[152] H. v. Löhneysen. Annals Phys. **523**(8-9), 599–611 (2011).

[153] G. A. Thomas *et al.*. Phys. Rev. B **27**, 3897–3900 (1983).

[154] T. F. Rosenbaum *et al.*. Phys. Rev. B **27**, 7509–7523 (1983).

[155] G. A. Thomas. Phil. Mag. **B52**, 479 (1985).

[156] H. v. Löhneysen. Adv. Solid State Phys. **30**, 95 (1990).

[157] H. von Löhneysen. Phil. Trans. R. Soc. Lond. A **356**, 139 (1998).

[158] S. Waffenschmidt *et al.*. Phys. Rev. Lett. **83**, 3005–3008 (1999).

[159] S. V. Kravchenko and M. P. Sarachik. Rep. Prog. Phys. **67**, 1 (2004).

[160] V. M. Pudalov. *Metallic conduction, apparent metal-insulator transition and related phenomena in two-dimensional electron liquid*. ArXiv:cond-mat/0405315.

[161] S. V. Kravchenko *et al.*. Phys. Rev. B **51**, 7038–7045 (1995).

[162] B. Spivak *et al.*. Rev. Mod. Phys. **82**, 1743–1766 (2010).

[163] V. M. Pudalov *et al.*. Phys. Rev. Lett. **88**, 076401 (2002).

[164] D. Simonian *et al.*. Phys. Rev. Lett. **79**, 2304–2307 (1997).

[165] K. M. Mertes *et al.*. Phys. Rev. B **60**, R5093–R5096 (1999).

[166] D. Popović *et al.*. Phys. Rev. Lett. **79**, 1543–1546 (1997).

[167] V. Pudalov *et al.*. JETP Lett. **68**(5), 442–447 (1998).

[168] S. V. Kravchenko and T. M. Klapwijk. Phys. Rev. Lett. **84**, 2909–2912 (2000).

[169] A. Punnoose *et al.*. Phys. Rev. B **82**, 201308 (2010).

[170] N. J. Goble *et al.*. Phys. Rev. B **90**, 035310 (2014).

[171] Y. Hanein *et al.*. Phys. Rev. B **58**, R13338–R13340 (1998).

[172] J. Shabani *et al.*. Phys. Rev. B **90**, 161303 (2014).

[173] S. J. Papadakis and M. Shayegan. Phys. Rev. B **57**, R15068–R15071 (1998).

[174] N. P. Stepina *et al.*. Phys. Rev. B **80**, 125308 (2009).

[175] S. Das Sarma *et al.*. Rev. Mod. Phys. **83**, 407–470 (2011).

[176] T. M. Lu *et al.*. Phys. Rev. Lett. **107**, 126403 (2011).

[177] A. P. Mills *et al.*. Phys. Rev. Lett. **83**, 2805–2808 (1999).

[178] M. Y. Simmons *et al.*. Phys. Rev. Lett. **80**, 1292–1295 (1998).

[179] Y. Yao *et al.*. Phys. Rev. B **91**, 115411 (2015).

[180] B. Grbić *et al.*. Phys. Rev. B **77**, 125312 (2008).

[181] O. Gunawan *et al.*. Nat Phys **3**(6), 388–391 (2007).

[182] J. Huang *et al.*. Phys. Rev. Lett. **98**, 226801 (2007).

[183] T. Knighton *et al.*. Applied Physics Letters **104**(19), 193109 (2014).

[184] G. Fleury and X. Waintal. Phys. Rev. Lett. **101**, 226803 (2008).

[185] A. Mokashi *et al.*. Phys. Rev. Lett. **109**, 096405 (2012).

[186] E. H. Hwang and S. Das Sarma. Phys. Rev. B **87**, 075306 (2013).

[187] S. Das Sarma *et al.*. Phys. Rev. B **90**, 125410 (2014).

[188] S. Das Sarma and E. H. Hwang. Phys. Rev. Lett. **83**, 164–167 (1999).

[189] X. Liu *et al.*. Solid State Communications **209âĂŞ210**(0), 1 – 4 (2015).

[190] S. Das Sarma and E. H. Hwang. Phys. Rev. B **89**, 235423 (2014).

[191] B. L. Altshuler and D. L. Maslov. Phys. Rev. Lett. **82**, 145–148 (1999).

[192] S. J. Papadakis *et al.*. Science **283**(5410), 2056–2058 (1999).

[193] Y. Yaish *et al.*. Phys. Rev. Lett. **84**, 4954–4957 (2000).

[194] A. Finkel'stein. Z. Phys. B **56**(3), 189–196 (1984).

[195] A. Punnoose and A. M. Finkel'stein. Phys. Rev. Lett. **88**, 016802 (2001).

[196] B. L. Altshuler *et al.*. Phys. Rev. Lett. **44**, 1288–1291 (1980).

[197] R. Kotlyar and S. Das Sarma. Phys. Rev. Lett. **86**, 2388–2391 (2001).

[198] M. J. Manfra *et al.*. Phys. Rev. Lett. **99**, 236402 (2007).

[199] G. Benenti *et al.*. Phys. Rev. Lett. **83**, 1826–1829 (1999).

[200] R. Berkovits and J. W. Kantelhardt. Phys. Rev. B **65**, 125308 (2002).

[201] W. Dias and M. Lyra. Physica A **411**(0), 35 – 41 (2014).

[202] E. Wigner. Phys. Rev. **46**, 1002–1011 (1934).

[203] B. Spivak. Phys. Rev. B **67**, 125205 (2003).

[204] A. Camjayi *et al.*. Nat Phys **4**(12), 932–935 (2008).

[205] A. Amaricci *et al.*. Phys. Rev. B **82**, 155102 (2010).

[206] Y. Meir. Phys. Rev. Lett. **83**, 3506–3509 (1999).

[207] X. Chen *et al.*. Nat Commun **6** (2015). Article.

[208] L. A. Tracy *et al.*. Phys. Rev. B **79**, 235307 (2009).

[209] S. Adam *et al.*. Phys. Rev. Lett. **101**, 046404 (2008).

[210] H. G. Schlager and H. v. Löhneysen. EPL **40**(6), 661 (1997).

[211] D. Belitz and T. R. Kirkpatrick. Phys. Rev. B **58**, 8214–8217 (1998).

[212] J. S. Thakur and D. Neilson. Phys. Rev. B **58**, 13717–13720 (1998).

[213] Y. Tanaka *et al.*. Phys. Rev. B **76**, 054522 (2007).

[214] I. Lerner. Physics Letters A **133**(4âĂŞ5), 253 – 259 (1988).

[215] B. Altshuler *et al.*. Physics Letters A **134**(8âĂŞ9), 488 – 492 (1989).

[216] J. Hubbard. Proceedings of the Royal Society of London A: Mathematical, Physical and Engineering Sciences **276**(1365), 238–257 (1963).

[217] A. Georges and G. Kotliar. Phys. Rev. B **45**, 6479–6483 (1992).

[218] E. Müller-Hartmann. Z. Phys. B Condensed Matter **76**(2), 211–217 (1989).

[219] F. Gebhard. *"Metal–Insulator Transition". The Mott Metal–Insulator Transition: Models and Methods*, vol. 137 (Springer Tracts in Modern Physics) (1997).

[220] M. Ulmke *et al.*. Phys. Rev. B **51**, 10411–10426 (1995).

[221] P. W. Anderson. Science **177**, 393 (1972).

[222] F. Milde *et al.*. Eur. Phys. J. B **15**(4), 685–690 (2000).

[223] I. V. Plyushchay *et al.*. Phys. Rev. B **68**, 064201 (2003).

[224] R. D. F. Danny Porath, Gianaurelio Cuniberti. *Topics in Current Chemistry*, vol. 237, chap. Charge Transport in DNA-Based Devices, 183–227 (Springer-Verlag, Heidelberg) (2004).

[225] A. Lagendijk *et al.*. Physics Today **62**, 24 (2009).

[226] O. I. Lobkis and R. L. Weaver. J. Acoust. Soc. Am. **124**, 3528–3533 (2008).

[227] G. Roati *et al.*. Nature **453**, 895–898 (2008).

[228] I. Bloch. Nature Physics **1**, 23–30 (2005).

[229] B. Damski *et al.*. Phys. Rev. Lett. **91**, 080403 (2003).

[230] L. Sanchez-Palencia *et al.*. Phys. Rev. Lett. **98**, 210401 (2007).

[231] H. Hu *et al.*. Nature Phys. **4**, 945–948 (2008).

[232] F. Jendrzejewski *et al.*. Phys. Rev. Lett. **109**, 195302 (2012).

[233] N. Cherroret *et al.*. Phys. Rev. A **85**, 011604 (2012).

[234] E. Larose *et al.*. Phys. Rev. Lett. **93**, 048501 (2004).

[235] C. Friedrich and U. Wegler. Geophys. Res. Lett. **32**(14), L14312 (2005).

[236] J. Billy *et al.*. Nature **453**, 891–894 (2008).

[237] W. Choi *et al.*. Opt. Express **20**(18), 20721–20729 (2012).

[238] M. Ma *et al.*. Phys. Rev. B **34**, 3136–3143 (1986).

[239] A. Kocherzhenko. *Charge Transport in Disordered Molecular Systems* (Aleksey Kocherzhenko) (2011).

[240] D. Smith *et al.*. Chemical Physics Letters **50**(3), 358 – 363 (1977).

[241] T. Sasaki. Crystals **2**(2), 374–392 (2012).

[242] B. Bulka *et al.*. Z. Phys. B **60**, 13–17 (1985).

[243] R. N. Silver and H. Röder. Inter. J. Mod. Phys. C **05**(04), 735–753 (1994).

[244] R. N. Silver and H. Röder. Phys. Rev. E **56**, 4822–4829 (1997).

[245] A. Weiße *et al.*. Rev. Mod. Phys. **78**, 275–306 (2006).

[246] G. Schubert and H. Fehske. In B. K. Chakrabarti *et al.* (Eds.) *Quantum and Semi-classical Percolation and Breakdown in Disordered Solids*, vol. 762 of *Lecture Notes in Physics*, 1–28 (Springer Berlin Heidelberg) (2009).

[247] A. MacKinnon and B. Kramer. Phys. Rev. Lett. **47**, 1546–1549 (1981).

[248] B. Kramer *et al.*. In B. Kramer (Ed.) *Advances in Solid State Physics 39*, vol. 39 of *Advances in Solid State Physics*, 253–262 (Springer Berlin Heidelberg) (1999).

[249] B. Kramer and M. Schreiber. In K. H. Hoffmann and M. Schreiber (Eds.) *in Computational Physics*, 166–188 (Springer, Berlin) (1996).

[250] A. MacKinnon and B. Kramer. Z. Phys. B - Condensed Matter **53**, 1–13 (1983).

[251] P. Markoš. Acta Physica Slovaca **56**, 561–685 (2006).

[252] E. Domany and S. Sarker. Phys. Rev. B **20**, 4726–4729 (1979).

[253] L. Root and J. L. Skinner. Phys. Rev. B **33**, 7738–7742 (1986).

[254] A. Singh and W. L. McMillan. J. Phys. C **18**(10), 2097 (1985).

[255] A. Abou-Chacra *et al.*. J. Phys. C **6**, 1734 (1973).

[256] D. Vollhardt and P. Wölfle. Phys. Rev. Lett. **48**, 699–702 (1982).

[257] G. Schubert *et al.*. Phys. Rev. B **81**, 155106 (2010).

[258] P. Soven. Phys. Rev. **156**, 809–813 (1967).

[259] D. Vollhardt and P. Wölfle. Phys. Rev. B **22**, 4666–4679 (1980).

[260] D. Vollhardt and P. Wölfle. Phys. Rev. Lett. **45**, 842–846 (1980).

[261] B. Velický *et al.*. Phys. Rev. **175**, 747–766 (1968).

[262] R. J. Elliott *et al.*. Rev. Mod. Phys. **46**, 465–543 (1974).

[263] M. H. Hettler *et al.*. Phys. Rev. B **61**, 12739–12756 (2000).

[264] M. Jarrell and H. R. Krishnamurthy. Phys. Rev. B **63**, 125102 (2001).

[265] M. Tsukada. J. Phys. Soc. Jpn. **26**, 684–696 (1969).

[266] A. Gonis. *Green functions for ordered and disordered systems* (North-Holland Amsterdam) (1992).

[267] T. Maier *et al.*. Rev. Mod. Phys. **77**, 1027–1080 (2005).

[268] J. Brndiar and P. Markoš. Phys. Rev. B **74**, 153103 (2006).

[269] E. Crow and K. Shimizu (Eds.) *Log-Normal Distribution–Theory and Applications* (Marcel Dekker, NY) (1988).

[270] K. Slevin and T. Ohtsuki. Phys. Rev. B **63**, 045108 (2001).

[271] A. Rodriguez *et al.*. Phys. Rev. B **84**, 134209 (2011).

[272] B. Bulka *et al.*. Z. Phys. B **66**, 21–30 (1987).

[273] B. Kramer and M. Schreiber. In L. Garrido (Ed.) *Fluctuations and Stochastic Phenomena in Condensed Matter*, vol. 268 of *Lecture Notes in Physics*, 351–375 (Springer Berlin Heidelberg) (1987).

[274] H. Grussbach and M. Schreiber. Phys. Rev. B **51**, 663–666 (1995).

[275] G. Schubert *et al.*. *HQS@HPC: Comparative numerical study of Anderson localisation in disordered electron systems in* High Performance computing in Science and Engineering, Garching 2004 (Springer) (2005).

[276] R. T. Scalettar *et al.*. Phys. Rev. Lett. **66**, 3144–3147 (1991).

[277] A. Aspect and M. Inguscio. Phys. Today **62**, 30–35 (2009).

[278] M. Jarrell *et al.*. Phys. Rev. B **64**, 195130 (2001).

[279] E. Gross *et al.*. *Many-Particle Theory* (A. Hilger, Bristol) (1991).

[280] A. Fetter and J. Walecka. *Quantum Theory of Many-particle Systems*. Dover books on physics (Dover Publishers Incorporated) (1971).

[281] D. D. Johnson. Phys. Rev. B **38**, 12807–12813 (1988).

[282] K. Ishii. Prog. Theor. Phys. Suppl. **53**, 77 (1973).

[283] D. Thouless. Int. J. Mod. Phys. B **24**(12n13), 1507–1525 (2010).

[284] B. Wischmann and E. Müller-Hartmann. Z. Phys. B **79**(1), 91–99 (1990).

[285] J. Chabé *et al.*. Phys. Rev. Lett. **101**, 255702 (2008).

[286] Y. Song *et al.*. Phys. Rev. B **76**, 045105 (2007).

[287] D. Jung *et al.*. Inter. J. Moder. Phys.: Conference Series **11**, 108 – 113 (2012).

[288] K. Yakubo and S. Mizutaka. J. Phys. Soci. Jpn **81**(10), 104707 (2012).

[289] P. A. Lee and D. S. Fisher. Phys. Rev. Lett. **47**, 882–885 (1981).

[290] L. P. Gorkov *et al.*. JETP Lett. **30**, 228 (1979).

[291] D. D. Betts and G. E. Stewart. Can. J. Phys. **75**, 47–66 (1997).

[292] J. Fröhlich *et al.*. Commun. Mathem. Phys. **101**(1), 21–46 (1985).

[293] B. Kramer and M. Schreiber. In W. Weller and P. Ziesche (Eds.) *in Localization in Disordered Systems*, vol. 16, 96 (BSB Teubner, Leipzig) (1988).

[294] J. M. Sin and Z. G. Soos. Philosophical Magazine **83**(7), 901–928 (2003).

[295] K. Sienicki. Macromolecules **24**(1), 270–275 (1991).

[296] F. Wegner. Nucl. Phys. B **316**, 663 (1989).

[297] P. Markos. J. Phys. A **33**(42), L393 (2000).

[298] A. MacKinnon. J. Phys. Conden. Matt. **6**(13), 2511 (1994).

[299] B. I. Shklovskii *et al.*. Phys. Rev. B **47**, 11487–11490 (1993).

[300] I. K. Zharekeshev and B. Kramer. Phys. Rev. Lett. **79**, 717–720 (1997).

[301] E. Hofstetter. Phys. Rev. B **57**, 12763–12767 (1998).

[302] M. Lopez *et al.*. Phys. Rev. Lett. **108**, 095701 (2012).

[303] G. Lemarié *et al.*. Phys. Rev. A **80**, 043626 (2009).

[304] G. Lemarié *et al.*. EPL (Europhysics Letters) **87**(3), 37007 (2009).

[305] D. D. Johnson *et al.*. Phys. Rev. B **41**, 9701–9716 (1990).

[306] A. Gonis and J. W. Garland. Phys. Rev. B **18**, 3999–4009 (1978).

[307] A. Gonis and J. W. Garland. Phys. Rev. B **16**, 1495–1502 (1977).

[308] M. H. Hettler *et al.*. Phys. Rev. B **58**, R7475–R7479 (1998).

[309] H. Shiba. Prog. Theor. Phys. **46**, 77 (1971).

[310] A. Brezini *et al.*. Phys. Status Solidi B **137**, 667 (1986).

[311] F. Hamdache and A. Brezini. Phys. Status Solidi B **172**, 635 (1992).

[312] P. W. Anderson. Reviews of Modern Physics **50**(2), 191–201 (1978).

[313] K. Byczuk *et al.*. Int. J. Mod. Phys. B **24**, 1727 (2010).

[314] B. Derrida. Physics Reports **103**(1âĂŞ4), 29 – 39 (1984).

[315] A. Alvermann *et al.*. Physica B Condensed Matter **359**, 789–791 (2005).

[316] J. A. Blackman *et al.*. Phys. Rev. B **4**, 2412–2428 (1971).

[317] G. Schubert *et al.*. Phys. Rev. B **71**, 045126 (2005).

[318] G. Schubert and H. Fehske. Phys. Rev. B **77**, 245130 (2008).

[319] K. Koepernik *et al.*. Phys. Rev. B **58**, 6944–6962 (1998).

[320] M. Caffarel and W. Krauth. Phys. Rev. Lett. **72**, 1545–1548 (1994).

[321] J. E. Hirsch and R. M. Fye. Phys. Rev. Lett. **56**, 2521–2524 (1986).

[322] K. G. Wilson. Rev. Mod. Phys. **47**, 773–840 (1975).

[323] A. Go and A. J. Millis. Phys. Rev. Lett. **114**, 016402 (2015).

[324] K. Held. Adv. Phys. **56**(6), 829–926 (2007).

[325] A. Georges. AIP Conference Proceedings **715**(1), 3–74 (2004).

[326] G. Kotliar and S. Y. Savrasov. In A. Tsvelik (Ed.) *New Theoretical Approaches to Strongly Correlated Systems*, 259–301 (Kluwer Academic Publishers) (2001).

[327] L. Craco *et al.*. Phys. Rev. Lett. **90**, 237203 (2003).

[328] L.-F. Arsenault *et al.*. Phys. Rev. B **86**, 085133 (2012).

[329] M. Potthoff. Phys. Rev. B **64**, 165114 (2001).

[330] M. I. Katsnelson and A. I. Lichtenstein. Eur. Phys. J. B **30**(1), 9–15 (2002).

[331] K. Held and D. Vollhardt. Eur. Phys. J. B **5**(3), 473–478 (1998).

[332] P. Werner *et al.*. Phys. Rev. Lett. **97**, 076405 (2006).

[333] R. Arita and K. Held. Phys. Rev. B **72**, 201102 (2005).

[334] A. Koga *et al.*. Phys. Rev. B **72**, 045128 (2005).

[335] A. N. Rubtsov *et al.*. Phys. Rev. B **72**, 035122 (2005).

[336] S. Sakai *et al.*. Phys. Rev. B **74**, 155102 (2006).

[337] M. Jarrell and J. Gubernatis. Phys. Rep. **269**(3), 133 – 195 (1996).

[338] H. Vidberg and J. Serene. J. Low Temp. Phys. **29**(3-4), 179–192 (1977).

[339] R. Bryan. Euro. Biophys. J. **18**(3), 165–174 (1990).

[340] H. Kajueter and G. Kotliar. Phys. Rev. Lett. **77**, 131–134 (1996).

[341] L. Wang *et al.*. Phys. Rev. Lett. **110**, 037001 (2013).

[342] T. B. Boykin *et al.*. J. Phys.: Conden. Mat. **19**(3), 036203 (2007).

[343] C. E. Ekuma *et al.*. J. Phys. Conden. Matt. **25**(40), 405601 (2013).

[344] M. C. O. Aguiar and V. Dobrosavljević. Phys. Rev. Lett. **110**, 066401 (2013).

[345] M. C. O. Aguiar *et al.*. Phys. Rev. Lett. **102**, 156402 (2009).

[346] F. Gebhard *et al.*. Eur. Phys. J. B **36**(4), 491–509 (2003).

[347] M. Frigo and S. Johnson. In *Acoustics, Speech and Signal Processing, 1998. Proceedings of the 1998 IEEE International Conference on*, vol. 3, 1381–1384 (1998).

[348] A. N. Rubtsov and A. I. Lichtenstein. JETP Lett. **80**, 61 (2004).

[349] E. Gull *et al.*. Rev. Mod. Phys. **83**, 349–404 (2011).

[350] E. Gull *et al.*. EPL (Europhysics Letters) **82**(5), 57003 (2008).

[351] S. Fuchs *et al.*. Phys. Rev. B **83**, 235113 (2011).

[352] N. Blümer. Phys. Rev. B **76**, 205120 (2007).

[353] D. Golubev and A. Zaikin. Physica B: Condensed Matter **255**(1âĂŞ4), 164 – 178 (1998).

[354] D. S. Golubev *et al.*. EPL (Europhysics Letters) **63**(3), 426 (2003).

[355] H. Shinaoka and M. Imada. Phys. Rev. Lett. **102**, 016404 (2009).

[356] B. L. Altshuler and A. G. Aronov. Sov. Phys. JETP **50**, 968 (1979).

[357] W. Götze. Journal of Physics C: Solid State Physics **12**(7), 1279 (1979).

[358] P. Prelovšek. Phys. Rev. B **23**, 1304–1319 (1981).

[359] E. N. Economou *et al.*. Phys. Rev. B **30**, 1686–1694 (1984).

[360] E. N. Economou *et al.*. Phys. Rev. B **31**, 6483–6489 (1985).

[361] A. D. Zdetsis *et al.*. Phys. Rev. B **32**, 7811–7816 (1985).

[362] C. M. Soukoulis *et al.*. Phys. Rev. B **36**, 8649–8655 (1987).

[363] C. M. Soukoulis and E. N. Economou. *Electron States, Localized* (WILEY-VCH Verlag) (2003).

[364] C. M. Soukoulis and E. N. Economou. Waves in Random Media **9**(2), 255–269 (1999).

[365] E. Kolley and W. Kolley. Journal of Physics C: Solid State Physics **21**(36), 6099 (1988).

[366] T. Kopp. Journal of Physics C: Solid State Physics **17**(11), 1919 (1984).

[367] E. Kotov and M. Sadovskii. Z. Phys. B **51**(1), 17–23 (1983).

[368] I. Sadakata. Journal of the Physical Society of Japan **55**(11), 3991–3994 (1986).

[369] C. M. Soukoulis *et al.*. Phys. Rev. B **34**, 2253–2257 (1986).

[370] E. Kolley and W. Kolley. physica status solidi (b) **138**(1), K65–K69 (1986).

[371] J. H. Mooij. physica status solidi (a) **17**(2), 521–530 (1973).

[372] S. M. Girvin and M. Jonson. Phys. Rev. B **22**, 3583–3597 (1980).

[373] V. Dobrosavljević and G. Kotliar. Phys. Rev. B **50**, 1430–1449 (1994).

[374] E. Miranda and V. Dobrosavljevic. *Conductor Insulator Quantum Phase Transitions*, chap. Dynamical mean-field theories of correlation and disorder, 161–235 (Oxford University Press,) (2012).

[375] W. Metzner and D. Vollhardt. Phys. Rev. Lett. **62**, 324–327 (1989).

[376] P. G. J. van Dongen and D. Vollhardt. Phys. Rev. Lett. **65**, 1663–1666 (1990).

[377] C.-I. Kim *et al.*. J. Phys. Soc. Jpn **59**(7), 2414–2425 (1990).

[378] Y. Kuramoto. *Theory of Heavy Fermions and Valence Fluctuations*, vol. 62 of *Proceedings of the Eighth Taniguchi Symposium, Shima Kanko, Japan, April 10–13, 1985* (Springer Series in Solid-State Sciences) (1985).

[379] G. Baym and L. P. Kadanoff. Phys. Rev. **124**, 287–299 (1961).

[380] G. Baym. Phys. Rev. **127**, 1391–1401 (1962).

[381] A. Abrikosov *et al.*. *Methods of Quantum Field Theory in Statistical Physics*. Dover Books on Physics Series (Dover Publications) (1975).

[382] M. Jarrell. Phys. Rev. Lett. **69**, 168–171 (1992).

[383] V. Zlatic and B. Horvatic. Solid State Communications **75**(3), 263 – 267 (1990).

[384] B. Kramer *et al.*. Phys. Rev. B **23**, 6357–6370 (1981).

[385] D. D. Betts *et al.*. Can. J. Phys. **77**(5), 353–369 (1999).

[386] P. R. C. Kent *et al.*. Phys. Rev. B **72**, 060411 (2005).

Appendix A

Permission

The author has the right to use the article or a portion of the article in a thesis or dissertation without requesting permission from APS provided the bibliographic citation and the APS copyright credit line are given on the appropriate pages.*From the website of the American Physical Society (APS).*

Author's rights after publication by IOP (articles not published on an open access basis): Upon transfer of copyright, IOP and/or the copyright owner grants back to authors a number of rights. These include the right to copy the article for teaching purposes, and to include the article in research theses or dissertations. *From the website of the Institute of Physics (IOP).*

Appendix B

Generation of Cluster Geometries

Aside the three-dimensional clusters shown in Table B1 which are generally generic perfect clusters that their lattice vectors can easily be obtained, I systematically generated and utilized another cluster geometries following the grading scheme of Betts *et al.* [291]. Note, similar cluster geometries are also generated for the two dimensional systems (not shown) based on the same classification scheme [385]. In Tables B2 B3, I specify the cluster geometries and other important parameters of the generated 3D clusters. It should be noted that both in 2 and 3 dimensions, only bipartite clusters and 'fully' perfect clusters (for e.g., $N_c = 64 = 4^3$ in 3D) are used in the computations.

Table B1: Three-dimensional (3D) perfect cluster geometries as utilized in the computations. The a_i denote the cluster lattice vectors, IMP is the imperfection, and C is the cubicity.

N_c	$\vec{a}_1$	$\vec{a}_2$	$\vec{a}_3$	IMP	C	S
1	(1, 0, 0)	(0, 1, 0)	(0, 0, 1)	0	1.000	0
64	(4, 0, 0)	(0, 4, 0)	(0, 0, 4)	0	1.000	2
125	(5, 0, 0)	(0, 5, 0)	(0, 0, 5)	0	1.000	3
216	(6, 0, 0)	(0, 6, 0)	(0, 0, 6)	0	1.000	4

Table B2: Three-dimensional cluster geometries of the non-bipartite (A cluster), best bipartite (B clusters), next best bipartite (C clusters), and next-next best bipartite (D clusters). The a_i denote the cluster lattice vectors, IMP is the imperfection, C is the cubicity, B denotes Bipartite, and S is the number of complete shells.

N_c	$\vec{a}_1$	$\vec{a}_2$	$\vec{a}_3$	IMP	C	B	S
2A	(1, 0, 2)	(1, 1,-2)	(-4,-1,-2)	0	1.002	F	0
2B	(1, 1, 2)	(4,-1,-1)	(2, 0, 0)	0	1.008	T	0
2C	(1, 0, 1)	(3, 2,-1)	(2, 1, 1)	0	1.003	T	0

Continued on Next Page...

Table B2 – Continued

N_c	$\vec{a}_1$	$\vec{a}_2$	$\vec{a}_3$	IMP	C	B	S
2D	(1, 0, 3)	(3, 3,-4)	(-1,-1, 2)	0	1.003	T	0
4A	(1, 0, 2)	(4, 1, 3)	(-1,-1,-1)	0	1.006	F	0
4B	(1, 1, 2)	(4, 1, 1)	(2,-2,-4)	1	1.004	T	0
4C	(1, 1, 2)	(4, 3,-3)	(3, 3, 2)	1	1.014	T	0
4D	(1, 1, 2)	(4, 3,-1)	(0, 0, 4)	1	1.014	T	0
6A	(1, 0, 3)	(1, 1, 1)	(1,-1,-1)	0	1.002	F	0
6B	(1, 0, 3)	(4, 1,-1)	(2, 0, 0)	2	1.014	T	0
6C	(1, 1, 2)	(4, 1,-1)	(2, 0, 0)	2	1.016	T	0
6D	(1, 0, 1)	(2, 1,-1)	(1, 2, 1)	2	1.019	T	0
8A	(1, 0, 2)	(1, 2, 0)	(1,-1,-1)	0	1.005	F	0
8B	(1, 1, 2)	(3, 1, 4)	(3,-1,-2)	2	1.009	T	0
8C	(1, 1, 2)	(4,-3,-1)	(-2, 1, 1)	2	1.013	T	0
8D	(1, 1, 2)	(2, 0,-2)	(-3,-1,-4)	2	1.013	T	0
10A	(1, 0, 2)	(4, 0,-2)	(1, 1,-2)	0	1.003	F	1
10B	(1, 0, 3)	(4, 1,-3)	(-2,-1,-1)	1	1.005	T	0
10C	(1, 0, 3)	(3, 3, 4)	(1, 1,-2)	1	1.013	T	0
10D	(1, 1, 2)	(3, 2, 1)	(3,-1,-4)	1	1.018	T	0
12A	(1, 1, 2)	(4, 1,-3)	(2, 2, 0)	0	1.004	T	1
12B	(1, 1, 2)	(4, 1,-3)	(3, 3, 2)	0	1.010	T	1
12C	(1, 1, 2)	(2,-4, 2)	(-2, 1,-1)	0	1.017	T	1
12D	(1, 1, 2)	(4,-2, 2)	(1,-2,-3)	0	1.018	T	1
14A	(1, 0, 2)	(3, 1, 0)	(1,-2, 0)	0	1.002	F	1
14B	(1, 0, 3)	(2, 1, 1)	(1, 4,-3)	1	1.008	T	1
14C	(1, 1, 2)	(4,-1,-3)	(3, 2, 1)	1	1.011	T	1
14D	(1, 1, 2)	(2, 1,-1)	(1,-2, 1)	1	1.018	T	1

Continued on Next Page...

Table B2 – Continued

N_c	$\vec{a}_1$	$\vec{a}_2$	$\vec{a}_3$	IMP	C	B	S
16A	(1, 0, 2)	(0, 2, 4)	(-2,-2, 0)	0	1.004	F	1
16B	(1, 1, 2)	(4, 1, 3)	(0, 2,-2)	2	1.011	T	1
16C	(1, 1, 2)	(2,-2, 0)	(1, 1,-2)	2	1.012	T	1
16D	(1, 1, 2)	(4, 1, 3)	(2, 1,-3)	2	1.012	T	1
18A	(1, 0, 2)	(2, 2,-1)	(1,-2,-2)	0	1.003	F	1
18B	(1, 1, 2)	(2, 2,-2)	(2,-1,-1)	3	1.005	T	1
18C	(1, 0, 3)	(2, 1,-1)	(1,-2,-1)	3	1.006	T	1
18D	(1, 0, 3)	(3, 1,-4)	(2,-1, 1)	3	1.006	T	1
20A	(1, 0, 2)	(3, 2, 1)	(2,-2,-1)	0	1.011	F	1
20B	(1, 1, 2)	(4, 1, 1)	(0, 2,-2)	4	1.007	T	1
20C	(1, 0, 3)	(2, 4,-2)	(2, 1,-1)	4	1.007	T	1
20D	(1, 0, 3)	(2, 4, 0)	(1,-2, 1)	4	1.007	T	1
22A	(1, 1, 2)	(3, 1,-1)	(2,-2, 1)	1	1.014	F	1
22B	(1, 0, 3)	(2, 4, 0)	(2, 1,-1)	5	1.008	T	1
22C	(1, 0, 3)	(4, 1,-1)	(1, 2,-1)	5	1.013	T	1
22D	(1, 1, 2)	(4, 0, 2)	(2, 1,-3)	5	1.013	T	1
24A	(1, 1, 3)	(3, 0, 0)	(1, 2,-2)	1	1.075	F	1
24B	(1, 1, 2)	(3, 3, 0)	(2,-2,-2)	6	1.005	T	1
24C	(1, 0, 3)	(1, 4,-1)	(1,-2,-1)	6	1.007	T	1
24D	(1, 1, 2)	(4, 0, 2)	(0, 4, 0)	6	1.008	T	1
26A	(1, 2, 2)	(2, 2,-1)	(2,-2, 2)	1	1.053	F	1
26B	(1, 1, 2)	(3, 2,-1)	(2,-2, 2)	6	1.005	T	1
26C	(1, 0, 3)	(2, 1,-1)	(1,-3,-2)	6	1.006	T	1
26D	(1, 0, 3)	(2, 3, 1)	(2,-1,-1)	6	1.007	T	1
28A	(1, 1, 3)	(3,-1, 1)	(1, 2,-2)	0	1.063	F	1

Continued on Next Page...

Table B2 – Continued

N_c	$\vec{a}_1$	$\vec{a}_2$	$\vec{a}_3$	IMP	C	B	S
28B	(1, 1, 2)	(4, 0, 0)	(1, 2,-3)	5	1.015	T	1
28C	(1, 1, 2)	(4,-1, 1)	(2, 1,-3)	5	1.016	T	1
28D	(1, 1, 2)	(4, 0, 0)	(1,-4,-1)	5	1.017	T	1
30A	(1, 2, 2)	(2, 2,-2)	(2,-2, 1)	0	1.007	F	1
30B	(1, 1, 2)	(3,-2,-1)	(1, 1,-4)	4	1.010	T	1
30C	(1, 1, 2)	(4, 2, 0)	(3,-2, 1)	4	1.011	T	1
30D	(1, 1, 2)	(3, 1,-2)	(3,-2, 1)	4	1.012	T	1
32A	(1, 1, 3)	(2, 2,-2)	(2,-2, 1)	0	1.022	F	1
32B	(2, 0, 2)	(3, 4, 3)	(2,-2,-2)	3	1.027	T	1
32C	(1, 2, 3)	(2, 0,-2)	(2,-2, 2)	3	1.028	T	1
32D	(1, 2, 3)	(4,-2, 0)	(2, 0,-2)	3	1.040	T	1
34A	(1, 1, 3)	(3,-2, 0)	(1, 2,-2)	0	1.009	F	1
34B	(1, 0, 3)	(2, 2,-2)	(1,-3,-2)	2	1.057	T	1
34C	(1, 0, 3)	(2, 3, 1)	(2,-2,-2)	2	1.066	T	1
34D	(1, 0, 3)	(3, 2, 1)	(3,-1,-4)	2	1.067	T	1
36A	(1, 2, 2)	(3, 0,-2)	(2,-2, 2)	0	1.004	F	2
36B	(1, 0, 3)	(2, 4, 4)	(2, 2,-4)	3	1.025	T	1
36C	(1, 0, 3)	(3, 2,-1)	(2,-2,-2)	3	1.040	T	1
36D	(1, 0, 3)	(4, 2, 2)	(2,-2,-2)	3	1.052	T	1
38A	(1, 1, 3)	(3, 1,-3)	(2,-2, 1)	0	1.002	F	2
38B	(1, 2, 3)	(3,-1,-2)	(2,-2, 2)	0	1.087	T	2
38C	(1, 2, 3)	(3,-1,-2)	(2, 3,-1)	0	1.117	T	2
38D	(1, 1, 4)	(3, 2, 1)	(2,-2, 2)	0	1.144	T	2
40A	(1, 1, 4)	(2, 2,-2)	(2,-2,-1)	0	1.003	F	2
40B	(1, 2, 3)	(2, 2,-2)	(2,-2, 2)	3	1.041	T	1

Continued on Next Page...

Table B2 – Continued

N_c	$\vec{a}_1$	$\vec{a}_2$	$\vec{a}_3$	IMP	C	B	S
40C	(1, 3, 4)	(2, 2,-2)	(2,-2,-2)	3	1.075	T	1
40D	(2, 2, 2)	(3, 3,-2)	(2,-2, 2)	3	1.076	T	1
42A	(1, 2, 2)	(4, 1,-2)	(2,-3, 0)	0	1.003	F	2
42B	(1, 2, 3)	(3,-1, 2)	(2, 2,-2)	2	1.056	T	2
42C	(1, 2, 3)	(2, 1,-3)	(2,-2, 2)	2	1.057	T	2
42D	(1, 1, 4)	(3, 2,-1)	(2,-2,-2)	2	1.081	T	2
44A	(1, 2, 2)	(3, 1,-2)	(2,-4, 0)	0	1.003	F	2
44B	(1, 2, 3)	(3, 2,-1)	(2,-2, 2)	3	1.036	T	2
44C	(1, 1, 4)	(3, 1,-2)	(2,-2, 2)	3	1.072	T	2
44D	(1, 2, 3)	(2,-2, 2)	(1, 4,-3)	3	1.076	T	2
46A	(1, 2, 2)	(4, 2, 0)	(2,-4, 1)	0	1.011	F	2
46B	(1, 2, 3)	(3, 1,-2)	(2,-2, 2)	4	1.017	T	2
46C	(1, 2, 3)	(3, 2,-1)	(1,-3, 2)	4	1.049	T	2
46D	(1, 1, 4)	(3, 2,-1)	(2,-2, 2)	4	1.054	T	2
48A	(1, 1, 3)	(2, 2,-2)	(4,-2,-1)	0	1.001	F	2
48B	(1, 2, 3)	(3,-2, 1)	(2, 2,-2)	5	1.002	T	2
48C	(1, 2, 3)	(3, 1,-2)	(3,-2, 1)	5	1.033	T	2
48D	(1, 2, 3)	(3, 2,-1)	(3,-2, 1)	5	1.035	T	2
50A	(1, 1, 4)	(2,-3,-2)	(-3,-2, 0)	0	1.085	F	2
50B	(1, 2, 3)	(3, 2,-1)	(2,-3, 1)	6	1.018	T	2
50C	(1, 1, 4)	(3,-2,-1)	(2, 2,-2)	6	1.024	T	2
50D	(1, 1, 4)	(3,-2, 1)	(2, 2,-2)	6	1.026	T	2
52A	(1, 0, 4)	(3, 2,-2)	(1,-3,-1)	1	1.014	F	2
52B	(1, 2, 3)	(3, 1,-2)	(2,-3, 1)	7	1.003	T	2
52C	(1, 2, 3)	(4, 0,-2)	(2,-2, 2)	7	1.016	T	2

Continued on Next Page...

Table B2 – Continued

N_c	$\vec{a}_1$	$\vec{a}_2$	$\vec{a}_3$	IMP	C	B	S
52D	(1, 2, 3)	(2, 2,-2)	(2,-4, 0)	7	1.024	T	2
54A	(1, 2, 2)	(3, 1,-3)	(2,-2, 4)	2	1.008	F	2
54B	(1, 2, 3)	(3,-3, 0)	(2, 2,-2)	8	1.004	T	2
54C	(1, 2, 3)	(3, 3,-2)	(2,-2, 2)	8	1.010	T	2
54D	(1, 2, 3)	(3, 2,-1)	(3,-3, 0)	8	1.028	T	2
56A	(1, 2, 3)	(4, 0,-2)	(-3, 2,-2)	2	1.069	F	2
56B	(1, 2, 3)	(2, 2,-2)	(2,-4, 2)	9	1.006	T	2
56C	(1, 2, 3)	(4,-2, 0)	(2, 2,-2)	9	1.007	T	2
56D	(1, 2, 3)	(3,-4,-3)	(2, 2,-2)	9	1.015	T	2
58A	(1, 1, 3)	(4,-2, 4)	(3, 2,-2)	3	1.014	F	2
58B	(1, 2, 3)	(4, 3,-1)	(2,-2, 2)	10	1.004	T	2
58C	(1, 2, 3)	(3, 1,-4)	(2,-2, 2)	10	1.005	T	2
58D	(1, 2, 3)	(3,-3, 2)	(2, 2,-2)	10	1.011	T	2
60A	(2, 0, 3)	(2, 3,-2)	(2,-3,-2)	4	1.001	F	2
60B	(1, 1, 4)	(4,-2, 0)	(2, 2,-2)	11	1.010	T	2
60C	(1, 2, 3)	(3,-4,-1)	(2, 2,-2)	11	1.010	T	2
60D	(1, 2, 3)	(3,-3, 2)	(2, 1,-3)	11	1.011	T	2
62A	(1, 2, 4)	(3, 0,-2)	(2,-3, 2)	5	1.018	F	2
62B	(1, 2, 3)	(3, 2,-1)	(3,-3, 2)	12	1.003	T	2
62C	(1, 2, 3)	(3,-3, 4)	(2, 2,-2)	12	1.022	T	2
62D	(1, 2, 3)	(4,-3,-1)	(2, 2,-2)	12	1.025	T	2
64A	(1, 3, 3)	(2, 4,-2)	(2,-3, 2)	5	1.115	F	1
64B	(1, 2, 3)	(4, 2,-2)	(3,-2, 1)	12	1.002	T	2
64C	(1, 2, 3)	(3, 4,-1)	(3,-2, 1)	12	1.003	T	2
64D	(1, 2, 3)	(3,-2, 1)	(2, 4,-2)	12	1.003	T	2

Continued on Next Page...

Table B2 – Continued

N_c	$\vec{a}_1$	$\vec{a}_2$	$\vec{a}_3$	IMP	C	B	S
66A	(1, 2, 4)	(3,-2, 2)	(2, 1,-4)	4	1.108	F	2
66B	(1, 3, 4)	(3, 0,-3)	(2,-2, 2)	11	1.011	T	2
66C	(1, 2, 3)	(3, 0,-3)	(3,-3, 2)	11	1.026	T	2
66D	(1, 1, 4)	(3, 2,-3)	(2,-3,-1)	11	1.033	T	2
68A	(1, 2, 4)	(2, 2,-3)	(-3, 2,-2)	4	1.051	F	2
68B	(1, 3, 4)	(2, 2,-2)	(2,-4, 0)	11	1.018	T	2
68C	(1, 3, 4)	(4, 2, 0)	(2,-2, 2)	11	1.020	T	2
68D	(1, 3, 4)	(2, 4,-2)	(2,-2, 2)	11	1.022	T	2
70A	(1, 2, 4)	(3, 1,-3)	(3,-2, 2)	1	1.060	F	2
70B	(1, 2, 3)	(3, 3,-2)	(2,-4, 0)	9	1.028	T	2
70C	(1, 2, 3)	(4, 0,-2)	(3,-3, 2)	9	1.030	T	2
70D	(1, 2, 3)	(3, 3,-2)	(3,-2, 3)	9	1.034	T	2
72A	(1, 3, 3)	(3, 2,-2)	(3,-2, 2)	1	1.010	F	2
72B	(1, 2, 3)	(3,-3, 2)	(2, 4,-2)	8	1.047	T	2
72C	(1, 2, 3)	(4,-2,-2)	(3, 4,-1)	8	1.050	T	2
72D	(1, 2, 3)	(4,-1,-3)	(3,-3, 2)	8	1.050	T	2
74A	(1, 3, 3)	(3, 2,-2)	(2,-2, 4)	0	1.057	F	3
74B	(1, 3, 4)	(4,-1,-3)	(2,-2, 2)	7	1.021	T	2
74C	(1, 2, 3)	(3,-3, 2)	(2, 3,-3)	9	1.027	T	2
74D	(1, 2, 3)	(4,-2,-4)	(-3, 3,-2)	10	1.047	T	2
76A	(1, 3, 3)	(3, 2,-2)	(3,-3, 1)	0	1.010	F	3
76B	(1, 2, 3)	(3, 4,-1)	(3,-3, 2)	6	1.026	T	2
76C	(1, 2, 3)	(3,-3, 2)	(2, 2,-4)	6	1.027	T	2
76D	(1, 1, 4)	(4,-2, 2)	(3, 2,-3)	6	1.080	T	2
78A	(1, 2, 4)	(3,-2, 2)	(2, 3,-3)	0	1.043	F	3

Continued on Next Page...

Table B2 – Continued

N_c	$\vec{a}_1$	$\vec{a}_2$	$\vec{a}_3$	IMP	C	B	S
78B	(2, 3, 3)	(3, 3,-2)	(3,-3,-2)	5	1.103	T	2
78C	(1, 2, 3)	(3, 3,-2)	(3,-3, 2)	9	1.002	T	2
78D	(1, 3, 4)	(4,-1, 3)	(2, 2,-2)	9	1.016	T	2
80A	(1, 2, 4)	(3, 1,-3)	(3,-3, 1)	0	1.032	F	3
80B	(1, 1, 4)	(3, 2,-3)	(3,-3, 2)	4	1.054	T	2
80C	(1, 1, 4)	(4,-2, 2)	(2, 3,-3)	4	1.068	T	2
80D	(1, 1, 4)	(4, 3, 1)	(3,-3, 2)	4	1.079	T	2
82A	(1, 2, 4)	(3, 2,-2)	(3,-3, 1)	0	1.002	F	3
82B	(2, 0, 4)	(3, 2,-3)	(2,-3,-3)	7	1.074	T	2
82C	(1, 3, 4)	(3,-3,-2)	(-3,-2, 3)	7	1.117	T	2
82D	(1, 3, 4)	(3, 2,-3)	(3,-3,-2)	8	1.117	T	2
84A	(1, 2, 4)	(4, 1,-2)	(2,-3, 2)	0	1.007	F	3
84B	(2, 2, 4)	(3, 0,-3)	(3,-3, 2)	6	1.050	T	2
84C	(1, 1, 4)	(4,-2,-2)	(2, 3,-3)	6	1.054	T	2
84D	(1, 1, 4)	(4, 1,-3)	(3,-3, 2)	6	1.054	T	2
86A	(1, 2, 4)	(3, 2,-2)	(3,-3, 2)	0	1.007	F	3
86B	(1, 3, 4)	(2, 3,-3)	(2,-4, 0)	5	1.073	T	2
86C	(1, 3, 4)	(4, 2, 0)	(1, 4,-3)	5	1.097	T	2
86D	(1, 3, 4)	(3,-1, 4)	(2, 3,-3)	5	1.133	T	2
88A	(1, 3, 3)	(4, 2,-2)	(-3, 3,-1)	0	1.016	F	3
88B	(2, 2, 4)	(4, 2,-2)	(-3, 3, 2)	4	1.089	T	2
88C	(1, 3, 4)	(4,-2,-2)	(3, 3,-2)	4	1.102	T	2
88D	(1, 3, 4)	(3, 3,-2)	(-2, 2,-4)	4	1.104	T	2
90A	(1, 2, 4)	(3, 3,-3)	(-3, 2,-2)	0	1.014	F	3
90B	(2, 0, 4)	(3, 3,-2)	(2,-3,-3)	7	1.033	T	2

Continued on Next Page...

Table B2 – Continued

N_c	$\vec{a}_1$	$\vec{a}_2$	$\vec{a}_3$	IMP	C	B	S
90C	(2, 3, 3)	(3, 3,-2)	(3,-3, 2)	7	1.051	T	2
90D	(1, 3, 4)	(4, 0,-2)	(3,-2, 3)	7	1.059	T	2
92A	(1, 2, 4)	(4, 2,-3)	(3,-2, 2)	0	1.012	F	3
92B	(1, 3, 4)	(3,-2, 3)	(2, 4,-2)	2	1.085	T	3
92C	(1, 3, 4)	(4,-1,-3)	(3,-2, 3)	2	1.102	T	3
92D	(1, 3, 4)	(4,-1,-3)	(2, 4,-2)	2	1.119	T	3
94A	(1, 2, 4)	(3, 2,-2)	(3,-3, 4)	1	1.028	F	2
94B	(1, 3, 4)	(3,-2, 3)	(2, 3,-3)	7	1.063	T	2
94C	(2, 3, 3)	(4, 4,-2)	(3,-3,-2)	9	1.088	T	2
94D	(1, 3, 4)	(3, 2,-3)	(3,-1, 4)	9	1.103	T	2
96A	(2, 2, 4)	(4,-2, 1)	(-3,-3, 2)	0	1.035	F	3
96B	(2, 2, 4)	(4,-2, 2)	(3, 2,-3)	4	1.061	T	3
96C	(2, 2, 4)	(4,-2, 2)	(2, 3,-3)	4	1.063	T	3
96D	(2, 2, 4)	(3,-3,-2)	(-2,-2, 4)	4	1.065	T	3
98A	(2, 2, 3)	(3,-4, 2)	(2, 2,-4)	1	1.023	F	3
98B	(1, 3, 4)	(4,-1,-3)	(-3, 3,-2)	7	1.081	T	3
98C	(1, 3, 4)	(-4, 1, 3)	(-3, 3,-2)	8	1.081	T	3
98D	(2, 3, 3)	(3,-2,-3)	(-4, 4,-2)	9	1.076	T	3

The parameters of Tables B2 and B1 include the lattice vectors: $(\vec{a}_1, \vec{a}_2, \vec{a}_3)$; the lattice "imperfection" (IMP) [386]; the cubicity (C); and the number of completed shells in the cluster (S). The meaning of imperfection can be implied by understand the meaning of perfection. The perfection of a cluster is a measure of the completeness of each neighbor shell as compared to that of an infinite lattice (cf. Table B3). Hence, a perfect cluster has all neighbor shells up to the k-th shell complete; the k-th shell is incomplete, and all shells k+1 and higher are empty. The cluster imper-

fection is thus the number of sites missing on the (k-1)th and lower shells plus the number of sites occupied in shells (k+1)th and higher, IMP=$\sum_{i=1}^{k-1} |N_i - N_i^{complete}| + \sum_{i=k+1}^{\infty} N_i$, where N_i is the number of neighbors in the *i*th shell [386]. Following such criteria, all the clusters in Tables B2 and B1 are considered to be perfect, with N_c = 12 the first cluster with a complete nearest-neighbor shell while N_c = 38 is the first with a complete next-nearest-neighbor shell (cf. Tables B2 and B3). The next parameter in Tables B2 and B1 is the cubicity. It is given as $C = \max(c_1, c_1^{-1}) \times \max(c_2, c_2^{-1})$, where $c_1 = 3^{1/2} l/d$ and $c_2 = 2^{1/2} l/f$ are cluster parameters defined by the geometric mean of the lengths of the four body diagonals of the cluster, $d = (d_1 d_2 d_3 d_4)^{1/4}$, the six-face diagonals, $f = (f_1 f_2 f_3 f_4 f_5 f_6)^{1/6}$, and the edges, $l = (l_1 l_2 l_3)^{1/3}$ [386]. $C = 1$ is for a perfect cube, and $C > 1$ otherwise. Following this criterion, clusters $N_c = 1$, 64, 125, and 216 are perfect cube. A deviation from the cubicity of a perfect cube is a measure of the cubic imperfection. Finally, in the last column of Table B2, I show the number of completed shells in the cluster, for which the number of neighbors in that shell on the lattice (LS) and on the cluster (BS) is the same.

In the computations for the 3D, I utilized only 'fully' perfect clusters and bipartite Betts clusters with small imperfection and good cubicity. The same criteria are also used in selecting the clusters for the 2D. In finite size scaling, these clusters behave very regularly when compared to clusters with large imperfection and/or cubicity. For example, the choice of such good clusters are important in the study of the antiferromagnetic phase diagram of the three-dimensional Hubbard model at half-filling [386] and in the zero-temperature properties of quantum spin models [291, 385]. Furthermore, I consider bipartite clusters because they contain the wavenumber $\mathbf{Q} = (\pi, \pi, \pi)$ for 3D and $\mathbf{Q} = (\pi, \pi)$ for 2D. This allows one to impose the additional particle-hole symmetry on the cluster spectra $\rho(\mathbf{K}, \omega) = \rho(\mathbf{Q} - \mathbf{K}, -\omega)$ which reduces the noise in the statistical sampling procedure. Note, in the case of one-dimensional systems, since it is just a linear chain with just one lattice vector ($\vec{a}_1 = (\vec{a}$, infinite number of clusters can be generated with ease as such, no special handling in generating them is needed.

Table B3: Explicit description of the neighbors sites in three-dimensional clusters showing the shell number (with the nearest neighbor shell being 1, etc.), number of neighbors in that shell on the lattice (LS), and the number of neighbors in that shell on the cluster (BS) for the various clusters in Table B2. The smaller clusters with a full nearest-neighbor shell (Sh) have $N_c = 12$, the smaller clusters with a complete next-nearest-neighbor shell have $N_c = 38$, and with a complete next-next-nearest-neighbor shell have $N_c = 92$.

N_c	Sh	LS	BS	N_c	Sh	LS	BS	N_c	Sh	LS	BS	N_c	Sh	LS	BS
2A	1	6	1	2B	1	6	1	2C	1	6	1	2D	1	6	1
4A	1	6	3	4B	1	6	2	4C	1	6	2	4D	1	6	2
	–	–	–		2	18	1		2	18	1		2	18	1
6A	1	6	5	6B	1	6	3	6C	1	6	3	6D	1	6	3
	–	–	–		2	18	2		2	18	2		2	18	2
8A	1	6	6	8B	1	6	4	8C	1	6	4	8D	1	6	4
	2	18	1		2	18	3		2	18	3		2	18	3
10A	1	6	6	10B	1	6	5	10C	1	6	5	10D	1	6	5
	2	18	3		2	18	4		2	18	4		2	18	4
12A	1	6	6	12B	1	6	6	12C	1	6	6	12D	1	6	6
	2	18	5		2	18	5		2	18	5		2	18	5
14A	1	6	6	14B	1	6	6	14C	1	6	6	14D	1	6	6
	2	18	7		2	18	6		2	18	6		2	18	6
	–	–	–		3	38	1		3	38	1		3	38	1
16A	1	6	6	16B	1	6	6	16C	1	6	6	16D	1	6	6
	2	18	9		2	18	7		2	18	7		2	18	7
	–	–	–		3	38	2		3	38	2		3	38	2
18A	1	6	6	18B	1	6	6	18C	1	6	6	18D	1	6	6
	2	18	11		2	18	8		2	18	3		2	18	3
	–	–	–		3	38	3		3	38	3		3	38	3
20A	1	6	6	20B	1	6	6	20C	1	6	6	20D	1	6	6

Continued on Next Page...

Table B3 – Continued

N_c	Sh	LS	BS	N_c	Sh	LS	BS	N_c	Sh	LS	BS	N_c	Sh	LS	BS
	2	18	13		2	18	9		2	18	9		2	18	9
	–	–	–		3	38	4		3	38	4		3	38	4
22A	1	6	6	22B	1	6	6	22C	1	6	6	22D	1	6	6
	2	18	14		2	18	10		2	18	10		2	18	10
	3	38	1		3	38	5		3	38	5		3	38	5
24A	1	6	6	24B	1	6	6	24C	1	6	6	24D	1	6	6
	2	18	16		2	18	11		2	18	11		2	18	11
	3	38	1		3	38	6		3	38	6		3	38	6
26A	1	6	6	26B	1	6	6	26C	1	6	6	26D	1	6	6
	2	18	16		2	18	12		2	18	12		2	18	12
	3	38	3		3	38	7		3	38	7		3	38	7
28A	1	6	6	28B	1	6	6	28C	1	6	6	28D	1	6	6
	2	18	18		2	18	13		2	18	13		2	18	13
	3	38	3		3	38	8		3	38	8		3	38	8
30A	1	6	6	30B	1	6	6	30C	1	6	6	30D	1	6	6
	2	18	18		2	18	14		2	18	14		2	18	14
	3	38	5		3	38	9		3	38	9		3	38	9
32A	1	6	6	32B	1	6	6	32C	1	6	6	32D	1	6	6
	2	18	18		2	18	15		2	18	15		2	18	15
	3	38	7		3	38	10		3	38	10		3	38	10
34A	1	6	6	34B	1	6	6	34C	1	6	6	34D	1	6	6
	2	18	18		2	18	16		2	18	16		2	18	16
	3	38	9		3	38	11		3	38	11		3	38	11
36A	1	6	6	36B	1	6	6	36C	1	6	6	36D	1	6	6
	2	18	18		2	18	16		2	18	16		2	18	16

Continued on Next Page...

Table B3 – Continued

N_c	Sh	LS	BS	N_c	Sh	LS	BS	N_c	Sh	LS	BS	N_c	Sh	LS	BS
	3	38	11		3	38	12		3	38	12		3	38	12
	–	–	–		4	66	1		4	66	1		4	66	1
38A	1	6	6	38B	1	6	6	38C	1	6	6	38D	1	6	6
	2	18	18		2	18	18		2	18	18		2	18	18
	3	38	13		3	38	13		3	38	13		3	38	13
40A	1	6	6	40B	1	6	6	40C	1	6	6	40D	1	6	6
	2	18	18		2	18	17		2	18	18		2	18	18
	3	38	15		3	38	14		3	38	14		3	38	14
	–	–	–		4	66	2		4	66	2		4	66	2
42A	1	6	6	42B	1	6	6	42C	1	6	6	42D	1	6	6
	2	18	18		2	18	17		2	18	18		2	18	18
	3	38	17		3	38	15		3	38	15		3	38	15
	–	–	–		4	66	2		4	66	2		4	66	2
44A	1	6	6	44B	1	6	6	44C	1	6	6	44D	1	6	6
	2	18	18		2	18	18		2	18	18		2	18	18
	3	38	19		3	38	16		3	38	16		3	38	16
	–	–	–		4	66	3		4	66	3		4	66	3
46A	1	6	6	46B	1	6	6	46C	1	6	6	46D	1	6	6
	2	18	18		2	18	18		2	18	18		2	18	18
	3	38	21		3	38	17		3	38	17		3	38	17
	–	–	–		4	66	4		4	66	4		4	66	4
48A	1	6	6	48B	1	6	6	48C	1	6	6	48D	1	6	6
	2	18	18		2	18	18		2	18	18		2	18	18
	3	38	23		3	38	18		3	38	18		3	38	18
	–	–	–		4	66	5		4	66	5		4	66	5

Continued on Next Page...

Table B3 – Continued

N_c	Sh	LS	BS	N_c	Sh	LS	BS	N_c	Sh	LS	BS	N_c	Sh	LS	BS
50A	1	6	6	50B	1	6	6	50C	1	6	6	50D	1	6	6
	2	18	18		2	18	18		2	18	18		2	18	18
	3	38	25		3	38	19		3	38	19		3	38	19
	–	–	–		4	66	6		4	66	6		4	66	6
52A	1	6	6	52B	1	6	6	52C	1	6	6	52D	1	6	6
	2	18	18		2	18	18		2	18	18		2	18	18
	3	38	26		3	38	20		3	38	20		3	38	20
	4	66	1		4	66	7		4	66	7		4	66	7
54A	1	6	6	54B	1	6	6	54C	1	6	6	54D	1	6	6
	2	18	18		2	18	18		2	18	18		2	18	18
	3	38	27		3	38	21		3	38	21		3	38	21
	4	66	2		4	66	8		4	66	8		4	66	8
56A	1	6	6	56B	1	6	6	56C	1	6	6	56D	1	6	6
	2	18	18		2	18	18		2	18	18		2	18	18
	3	38	29		3	38	22		3	38	22		3	38	22
	4	66	2		4	66	9		4	66	9		4	66	9
58A	1	6	6	58B	1	6	6	58C	1	6	6	58D	1	6	6
	2	18	18		2	18	18		2	18	18		2	18	18
	3	38	30		3	38	23		3	38	23		3	38	23
	4	66	3		4	66	10		4	66	10		4	66	10
60A	1	6	6	60B	1	6	6	60C	1	6	6	60D	1	6	6
	2	18	18		2	18	18		2	18	18		2	18	18
	3	38	31		3	38	24		3	38	24		3	38	24
	4	66	4		4	66	11		4	66	11		4	66	11
62A	1	6	6	62B	1	6	6	62C	1	6	6	62D	1	6	6

Continued on Next Page...

Table B3 – Continued

N_c	Sh	LS	BS	N_c	Sh	LS	BS	N_c	Sh	LS	BS	N_c	Sh	LS	BS
	2	18	18		2	18	18		2	18	18		2	18	18
	3	38	32		3	38	25		3	38	25		3	38	25
	4	66	5		4	66	12		4	66	12		4	66	12
64A	1	6	6	64B	1	6	6	64C	1	6	6	64D	1	6	6
	2	18	18		2	18	18		2	18	18		2	18	18
	3	38	34		3	38	26		3	38	26		3	38	26
	4	66	6		4	66	13		4	66	13		4	66	13
66A	1	6	6	66B	1	6	6	66C	1	6	6	66D	1	6	6
	2	18	18		2	18	18		2	18	18		2	18	18
	3	38	34		3	38	27		3	38	27		3	38	27
	4	66	7		4	66	14		4	66	14		4	66	14
68A	1	6	6	68B	1	6	6	68C	1	6	6	68D	1	6	6
	2	18	18		2	18	18		2	18	18		2	18	18
	3	38	35		3	38	28		3	38	28		3	38	28
	4	66	8		4	66	15		4	66	15		4	66	15
70A	1	6	6	70B	1	6	6	70C	1	6	6	70D	1	6	6
	2	18	18		2	18	18		2	18	18		2	18	18
	3	38	37		3	38	29		3	38	29		3	38	29
	4	66	8		4	66	16		4	66	16		4	66	16
72A	1	6	6	72B	1	6	6	72C	1	6	6	72D	1	6	6
	2	18	18		2	18	18		2	18	18		2	18	18
	3	38	37		3	38	30		3	38	30		3	38	30
	4	66	10		4	66	17		4	66	17		4	66	17
74A	1	6	6	74B	1	6	6	74C	1	6	6	74D	1	6	6
	2	18	18		2	18	18		2	18	18		2	18	18

Continued on Next Page...

Table B3 – Continued

N_c	Sh	LS	BS	N_c	Sh	LS	BS	N_c	Sh	LS	BS	N_c	Sh	LS	BS
	3	38	38		3	38	31		3	38	31		3	38	31
	4	66	11		4	66	18		4	66	18		4	66	18
76A	1	6	6	76B	1	6	6	76C	1	6	6	76D	1	6	6
	2	18	18		2	18	18		2	18	18		2	18	18
	3	38	38		3	38	32		3	38	32		3	38	32
	4	66	13		4	66	19		4	66	19		4	66	19
78A	1	6	6	78B	1	6	6	78C	1	6	6	78D	1	6	6
	2	18	18		2	18	18		2	18	18		2	18	18
	3	38	38		3	38	33		3	38	33		3	38	33
	4	66	15		4	66	20		4	66	20		4	66	20
	–	–	–		–	–	–		5	102	2		5	102	2
80A	1	6	6	80B	1	6	6	80C	1	6	6	80D	1	6	6
	2	18	18		2	18	18		2	18	18		2	18	18
	3	38	38		3	38	34		3	38	34		3	38	34
	4	66	17		4	66	21		4	66	21		4	66	21
82A	1	6	6	82B	1	6	6	82C	1	6	6	82D	1	6	6
	2	18	18		2	18	18		2	18	18		2	18	18
	3	38	38		3	38	33		3	38	33		3	38	33
	4	66	19		4	66	22		4	66	22		4	66	21
	–	–	–		5	102	2		5	102	2		5	102	2
	–	–	–		–	–	–		–	–	–		6	146	6
84A	1	6	6	84B	1	6	6	84C	1	6	6	84D	1	6	6
	2	18	18		2	18	18		2	18	18		2	18	18
	3	38	38		3	38	34		3	38	34		3	38	34
	4	66	21		4	66	23		4	66	23		4	66	23

Continued on Next Page...

Table B3 – Continued

N_c	Sh	LS	BS	N_c	Sh	LS	BS	N_c	Sh	LS	BS	N_c	Sh	LS	BS
–	–	–	–		5	102	2		5	102	2		5	102	2
86A	1	6	6	86B	1	6	6	86C	1	6	6	86D	1	6	6
	2	18	18		2	18	18		2	18	18		2	18	18
	3	38	38		3	38	35		3	38	35		3	38	35
	4	66	23		4	66	24		4	66	24		4	66	24
–	–	–	–		5	102	2		5	102	2		5	102	2
88A	1	6	6	88B	1	6	6	88C	1	6	6	88D	1	6	6
	2	18	18		2	18	18		2	18	18		2	18	18
	3	38	38		3	38	36		3	38	36		3	38	36
	4	66	25		4	66	25		4	66	25		4	66	25
–	–	–	–		5	102	2		5	102	2		5	102	2
90A	1	6	6	90B	1	6	6	90C	1	6	6	90D	1	6	6
	2	18	18		2	18	18		2	18	18		2	18	18
	3	38	38		3	38	35		3	38	35		3	38	35
	4	66	27		4	66	26		4	66	26		4	66	26
–	–	–	–		5	102	4		5	102	4		5	102	4
92A	1	6	6	92B	1	6	6	92C	1	6	6	92D	1	6	6
	2	18	18		2	18	18		2	18	18		2	18	18
	3	38	38		3	38	38		3	38	38		3	38	38
	4	66	29		4	66	27		4	66	27		4	66	27
–	–	–	–		5	102	2		5	102	2		5	102	2
94A	1	6	6	94B	1	6	6	94C	1	6	6	94D	1	6	6
	2	18	18		2	18	18		2	18	18		2	18	18
	3	38	37		3	38	36		3	38	36		3	38	36
	4	66	32		4	66	22		4	66	22		4	66	22

Continued on Next Page...

Table B3 – Continued

N_c	Sh	LS	BS	N_c	Sh	LS	BS	N_c	Sh	LS	BS	N_c	Sh	LS	BS
	–	–	–		5	102	6		5	102	6		5	102	6
96A	1	6	6	96B	1	6	6	96C	1	6	6	96D	1	6	6
	2	18	18		2	18	18		2	18	18		2	18	18
	3	38	38		3	38	38		3	38	38		3	38	38
	4	66	33		4	66	29		4	66	29		4	66	29
	–	–	–		5	102	4		5	102	4		5	102	4
98A	1	6	6	98B	1	6	6	98C	1	6	6	98D	1	6	6
	2	18	18		2	18	18		2	18	18		2	18	18
	3	38	38		3	38	37		3	38	37		3	38	37
	4	66	34		4	66	30		4	66	30		4	66	30
	5	102	1		5	102	6		5	102	6		5	102	6
	–	–	–		–	–	–		1	146	1		–	–	–

Appendix C

Details of the Transfer Matrix Method

To enable the benchmarking of the TMDCA results, a transfer matrix method was developed. The transfer matrix method (TMM) [106, 106, 247, 247, 249–251] is an established numerical method for critical parameters in disordered quantum systems. It is based on a recursive reformulation of the Schrödinger equation. It has the advantage of capturing the effects of rather a large system sizes hence, provides quality data for a finite size scaling analysis. In the computations, the transmission of states through a quasi-1D bar of width $M = [6, 12]$ and length $L = 2 \times 10^4 M$ are studied by adding the products of the transfer matrices with random initial states. A numerical instability arises from such multiplicative process, which is reduced by orthogonalizing the transfer matrix product in steps of say five multiplications using a Lapack QR decomposition [132]. The localization edge is obtained by calculating the dimensionless Kramer-MacKinnon parameter Λ_M [250] which is universal and invariant at the critical point. I.e., Λ_M scales as a constant for $M \to \infty$ [106]. Thus, we determine the boundary of the localization transition vis-à-vis the critical disorder strength [223] by performing a linear fit to Λ_M vs. M data. Localized states will have a negative slope and positive for the extended states. The transfer-matrix method finite size effects are larger for weak disorder where the states decay slowly with distance and so have large values of Λ_M that carry a large variation in the data. The CPA and DCA are, in fact, exact in this limit as such, do not suffer this finite size effect.

Any error quoted in the TMM data are from the difference in the measured W_c from finite size scaling analysis and the crossing of the systems size M from a plot of Λ v.s. W. The finite size scaling is performed by expanding Λ near the critical point $\Lambda = f(M/\xi) \approx \Lambda_c + a_1|W - W_c|M^{1/\nu} + \cdots$, and fitting using a least squares procedure. The power of expansion used for instance in Figure 7.7 was 3.

Appendix D

Details of the Kernel Polynomial Method

To further benchmark the TMDCA results, we developed a version of the kernel polynomial method [243–246]. The kernel polynomial method [243–246] is a numerical technique for expanding the Green function of many-body quantum systems in orthogonal Chebyshev polynomials. In the kernel polynomial method analysis, instead of diagonalizing the Hamiltonian directly, the DoS is expanded in term of an infinite series of Chebyshev polynomials. In practice, the truncated series leads to Gibbs oscillations, which are damped by a modification of the expansion coefficients. Following previous studies on the Anderson model, the Jackson kernel is used [245].

Appendix E

Spectral Representation of the Second Order Term in the Self-Energy

The second order perturbation theory self-energy is the expansion up to the second order in U ($O\left[(U/B)^2\right]$) around the Hartree-corrected host propagator. Generally, it is given in the Matsubara frequency as in Equation 10.9 which we re-write below for clarity as

$$\Sigma_c^{(SOPT)}[\tilde{\mathcal{G}}] = -\lim_{i\omega\to\omega^+}\left[\frac{U^2}{N_c^2\beta^2}\sum_{m,p,\mathbf{P},\mathbf{Q}}\tilde{\mathcal{G}}(\mathbf{K}+\mathbf{Q},i\omega_n+i\nu_m)\,\tilde{\mathcal{G}}(\mathbf{P}+\mathbf{Q},i\omega_p+i\nu_m)\,\tilde{\mathcal{G}}(\mathbf{P},i\omega_p)\right]. \tag{E.1}$$

where $\mathbf{Q}$, $\mathbf{P}$, $\mathbf{K}$ are cluster momenta and β is the inverse temperature. In the TMDCA formalism, one cannot use Equation E.1 in its present form since the cluster problem is solved in real space and more significantly, it is numerically more advantageous to work in the real frequency than in the Matsubara frequency (because analytic continuation has to be carried out from the imaginary frequency to the real frequency in order to get real frequency quantities). Note further that analytic continuation process can miss important features of the observable being studied if not done carefully aside its inability to study zero-temperature physics, which coincidentally, is the regime of interest in the present study. To avoid such analytic continuation, I convert the Matsubara sums to real frequency integrals using the spectral representation to obtain Equation 10.10. Below, I will outline the steps to obtaining Equation 10.10.

To reformulate Equation E.1 in the form that is applicable to the cluster solver utilized in this work, I used spectral representation

$$\tilde{\mathcal{G}}(i\omega) = \int d\varepsilon \frac{\rho(\tilde{\mathcal{G}}(\varepsilon))}{(i\omega-\varepsilon)}, \tag{E.2}$$

where $\rho(\tilde{\mathcal{G}}(\varepsilon)) = -\frac{1}{\pi}\Im\,\tilde{\mathcal{G}}(\varepsilon)$, to convert the Matsubara sums to real frequency integrals. Using

Equation E.2 in Equation E.1 one obtains

$$\begin{aligned}
\Sigma_c^{(SOPT)}(i\omega) &= \frac{U^2}{N_c^2}\int\prod_{i=1}^{3}\left(d\varepsilon_i\rho(\tilde{\mathcal{G}}(\varepsilon))\right)\frac{1}{\beta^2}\sum_{m,p}\frac{1}{i\omega+i\nu_m-\varepsilon_1}\frac{1}{i\omega_p+i\nu_m-\varepsilon_2}\frac{1}{i\omega_p-\varepsilon_3} \\
&= \frac{U^2}{N_c^2}\int\prod_{i=1}^{3}\left(d\varepsilon_i\rho(\tilde{\mathcal{G}}(\varepsilon))\right)\frac{1}{\beta}\sum_{m}\frac{1}{i\omega+i\nu_m-\varepsilon_1}\frac{1}{\beta}\sum_{p}\left(\frac{1}{i\omega_p-\varepsilon_3}-\frac{1}{i\omega_p+i\nu_m-\varepsilon_2}\right)\frac{1}{i\nu_m-\varepsilon_2+\varepsilon_3} \\
&= \frac{U^2}{N_c^2}\int\prod_{i=1}^{3}\left(d\varepsilon_i\rho(\tilde{\mathcal{G}}(\varepsilon))\right)\left(n_F(\varepsilon_3)-n_F(\varepsilon_2)\right)\frac{1}{\beta}\sum_{m}\frac{1}{i\nu_m-(\varepsilon_1-i\omega)}\frac{1}{i\nu_m-(\varepsilon_2-\varepsilon_3)} \\
&= \frac{U^2}{N_c^2}\int\prod_{i=1}^{3}\left(d\varepsilon_i\rho(\tilde{\mathcal{G}}(\varepsilon))\right)\frac{n_F(-\varepsilon_1)n_F(\varepsilon_2)n_F(-\varepsilon_3)+n_F(\varepsilon_1)n_F(-\varepsilon_2)n_F(\varepsilon_3)}{i\omega-\varepsilon_1+\varepsilon_2-\varepsilon_3} \qquad \text{(E.3)}
\end{aligned}$$

where site labels have been suppressed, $\rho_{\tilde{\mathcal{G}}} = -1/\pi\Im\,\tilde{\mathcal{G}}$, and $n_f = 1/(e^{\beta\varepsilon}+1)$ is the Fermi function. Using the fact that $1/(x+i0^+) = \mathcal{P}(1/x) - i\pi\delta(x)$ (where '$\mathcal{P}$' is the principal value of the integral), we immediately obtain Equation 10.10 as

$$\begin{aligned}
\rho_\Sigma(\omega) &= \frac{U^2}{N_c^2}\int d\varepsilon_1 d\varepsilon_2\rho_{\tilde{\mathcal{G}}}(\varepsilon_1)\rho_{\tilde{\mathcal{G}}}(\omega-\varepsilon_1+\varepsilon_2)\rho_{\tilde{\mathcal{G}}}(\varepsilon_2) \\
&\times \left[n_f(-\varepsilon_1)n_f(\varepsilon_2)n_f(-\omega+\varepsilon_1-\varepsilon_2)+n_f(\varepsilon_1)n_f(-\varepsilon_2)n_f(\omega-\varepsilon_1+\varepsilon_2)\right] \qquad \text{(E.4)}
\end{aligned}$$

The real part of the interacting self-energy follows immediately from Kronigs-Kramer transform as

$$\Sigma_R^{SOPT}(\omega) = -\mathcal{P}\int_\infty^\infty \frac{\rho_\Sigma(\acute{\omega})}{\acute{\omega}-\omega}d\acute{\omega}. \qquad \text{(E.5)}$$

Combining the real and the imaginary part, the non-local SOPT self-energy is then obtained as

$$\Sigma_c^{SOPT}(i,j,\omega) = \Sigma_R^{SOPT}(i,j,\omega) - i\pi\rho_\Sigma(i,j,\omega). \qquad \text{(E.6)}$$

Equation E.4 is computational expensive especially since we have both spatial and frequency dependence. In fact, assuming it depends only on frequency, it scales as N^3 process (N is the size of the grid points used in the integration). This N^3 process can be reduced to N^2 process by splitting the double integral into two one dimensional integral as

$$\rho_\Sigma(\omega) = \frac{U^2}{N_c}\int d\varepsilon_1\rho_{\tilde{\mathcal{G}}}(-\varepsilon_1)\left[n_F(\varepsilon_1)\chi_1(\omega+\varepsilon_1)+n_F(-\varepsilon_1)\chi_2(\omega+\varepsilon_1)\right] \qquad \text{(E.7)}$$

with

$$\chi_1(\varepsilon) = \frac{1}{N_c}\int d\varepsilon_1 \rho_{\tilde{\mathcal{G}}}(\varepsilon+\acute{\varepsilon})\rho_{\tilde{\mathcal{G}}}(\acute{\varepsilon}) n_F(\acute{\varepsilon}) n_F(-\acute{\varepsilon}-\varepsilon) \quad \text{and} \tag{E.8a}$$

$$\chi_2(\varepsilon) = \frac{1}{N_c}\int d\varepsilon_1 \rho_{\tilde{\mathcal{G}}}(\varepsilon+\acute{\varepsilon})\rho_{\tilde{\mathcal{G}}}(\acute{\varepsilon}) n_F(-\acute{\varepsilon}) n_F(\acute{\varepsilon}+\varepsilon) \tag{E.8b}$$

In arriving at Equation E.7, particle-hole symmetry property have not been used as such, the above formulation is suitable at and away from half-filling. Utilizing the fast-Fourier transformation [347], the above N^2 process is further reduced to scale as $N \ln N$.

Vita

Chinedu Ekuma Ekuma was born and raised in the commercial city of Lagos, Nigeria. He completed his high school at Festac Grammar school, Festac Town, Lagos. Subsequently, he enrolled at the Ebonyi State University, Nigeria for his Bachelor degree in science where he graduated as the overall best graduating student with *summa cum laude* (1st Class Hons) in Industrial Physics in the 2005/2006 academy year. He went ahead to serve the compulsory one-year national youth service corps in Delta state, Nigeria. He was then appointed an Assistant lecturer in the Department of Physics, University of Port Harcourt, Nigeria and concurrently, he enrolled and obtained an MSc in the Department of Physics & Astronomy, University of Nigeria, Nigeria. In the fall of 2009 he arrived at Southern University, Baton Rouge, LA to pursue an MSc in Computational Physics after he was awarded the prestigious Ebonyi, Nigeria overseas scholarship for being the best graduating student of the 2005/2006 academic year. After successfully completing his MSc, he joined the Department of Physics & Astronomy, Lousiana State University, Baton Rouge, LA in the fall of 2010. He worked on diverse research projects under the supervision of Dr. Mark Jarrell with Dr. Juana Moreno as a conjunct advisor where he continued working towards his Ph.D.